



UNIVERSITY OF
BIRMINGHAM

**Synthesis of Precious Metal Nanoparticles Supported
on Bacterial Biomass for Catalytic Applications in
Chemical Transformations**

By

Ju Zhu

A thesis submitted to
The University of Birmingham
for the degree of
DOCTOR OF PHILOSOPHY

School of Chemical Engineering
College of Engineering and Physical Sciences
The University of Birmingham
April 2014

UNIVERSITY OF
BIRMINGHAM

University of Birmingham Research Archive

e-theses repository

This unpublished thesis/dissertation is copyright of the author and/or third parties. The intellectual property rights of the author or third parties in respect of this work are as defined by The Copyright Designs and Patents Act 1988 or as modified by any successor legislation.

Any use made of information contained in this thesis/dissertation must be in accordance with that legislation and must be properly acknowledged. Further distribution or reproduction in any format is prohibited without the permission of the copyright holder.

Abstract

Bacteria are used to ‘grow’ and scaffold precious metal nanoparticles possessing certain catalytic activities. Focusing on *Escherichia coli*, this thesis aims to investigate the catalytic behaviours of *E. coli*-supported palladium (bio-Pd/*E. coli*) or bimetallic gold-palladium (bio-AuPd/*E. coli*) in hydrogenations and oxidations operated in laboratory-scale three-phase slurry reactors. A discussion of hydrodynamics, mass transfer, reaction mechanisms and corresponding reaction performance is systematically presented for two major industrially important reactions: soybean oil hydrogenation and benzyl alcohol oxidation.

The selective hydrogenation of alkyne/alkene is studied over Pd-based catalysts in a semi-batch Baskerville autoclave reactor. Under identical operating conditions in 2-pentyne hydrogenation using isopropanol as a solvent (40 °C, 2 bar of hydrogen, 1000 rpm of stirring), 5wt%Pd/*E. coli* achieved 100% of 2-pentyne conversion in 20 mins and produced $10.1 \pm 0.7 \times 10^{-2} \text{ mol.l}^{-1}$ of desired *cis*-2-pentene; in contrast a conventional 5wt%Pd/ Al_2O_3 catalyst gave 100% of 2-pentyne conversion in 40 mins and a *cis*-2-pentene concentration of $6.5 \pm 0.4 \times 10^{-2} \text{ mol.l}^{-1}$. The solvent-free hydrogenation of soybean oil was assessed over bio-Pd/*E. coli* with the aim to reduce the *cis-trans* isomerisation. The operating conditions were optimised and mass transfer limitations minimised using 5wt%Pd/ Al_2O_3 . A maximum of $1.07 \pm 0.02 \text{ mol.l}^{-1}$ of *cis*-C18:1 was obtained, with $0.52 \pm 0.02 \text{ mol.l}^{-1}$ of *trans*-C18:1. Two kinetic models were established, with the experimental data fitted based on Langmuir-Hinshelwood kinetic expressions. Optimally in the same reactor (100 °C, 5 bar of hydrogen, 800 rpm of stirring), the use of 5wt%Pd/*E. coli* yielded *cis*-C18:1 of $1.03 \pm 0.04 \text{ mol.l}^{-1}$ and *trans*-C18:1 of $0.26 \pm 0.03 \text{ mol.l}^{-1}$ (*i.e.* ~50% less than 5wt%Pd/ Al_2O_3) after 5 hours, indicating an advantage of lower *cis-trans* isomerisation by using bio-Pd/*E. coli* catalyst.

Bimetallic bio-AuPd catalysts were tested in the solvent-free oxidation of benzyl alcohol using air in a semi-batch Parr autoclave reactor. In a dead-end operating mode, a levelling-off of reaction rate with time was attributed to the drop of oxygen partial pressure, although a constant overall pressure was maintained. Reactor modifications were developed to create a continuous air flow. The rate of benzyl alcohol oxidation was found to be zero-order with respect to oxygen at an air flow rate of 200 ml.min⁻¹ or above. Under optimised reaction conditions (110 °C, 5 bar of air, 200 ml.min⁻¹ of air flow rate, 1200 rpm of stirring), the bio-AuPd/*E. coli* catalyst exhibited a good compromise of thermal stability and activity in comparison with bio-AuPd on other strains of bacteria, and a loading of 2.5wt% Au2.5wt% Pd on *E. coli* gave better activity (TOF= 1423±20 hr⁻¹) than other bio-AuPd/*E. coli* with different metal loadings.

Thermogravimetric analysis indicated a suitable operating temperature of below 175 °C for the *E. coli*-supported catalyst. A loading of 5 wt% Pd on *E. coli* showed an average particle size of 4.31 nm estimated by TEM measurements and a crystallite size of 4.12 nm using Scherrer's equation from obtained X-ray powder diffraction data. This was smaller than an active particle diameter of 12.77 nm for 5wt% Pd/*Al*₂*O*₃ (determined by CO chemisorption).

It is concluded that biomass-supported precious metal catalyst is an environmentally attractive alternative to conventional heterogeneous catalyst for application in industrial catalytic processes.

This thesis is dedicated to my dearest father and mother, who have been morally and financially supporting me through the entire duration of my PhD study.

Acknowledgements

My deepest and heartiest thanks goes to Prof Joe Wood for his leadership in supervising my PhD research, to Prof Lynne Macaskie for her co-supervision and part of the financial support. I would like to thank them for their great patience, enthusiasm and guidance at all times during the research and writing of this thesis. Without them, this thesis would not have been written or completed.

Some people were critical to the success of this work. I am greatly indebted to Dr James Bennett and Dr Kevin Deplanche for their immense support in this work, their expertise and knowledge helped me to improve and add value to my PhD research.

I would also like to express my gratitude to Dr Iryna Mikheenko, Dr Claire Meenan, Dr Angela Murray, Scott Taylor, and Jacob Omajali from the School of Biosciences, University of Birmingham for their collaboration, willingness and enthusiasm always available to help with the bio-catalyst preparation. Mr Paul Stanley and Ms Theresa Morris from the School of Metallurgy and Materials, University of Birmingham for their unrivaled technical assistance in the catalyst characterisation. The Chemical Engineering Workshop team is also thanked for their contribution in the reactor modifications.

Thanks to the School of Chemical Engineering, University of Birmingham for the scholarships as part of my financial support. Thanks are also due to Ms Lynn Draper for the administrative support and care throughout my stay at the university.

Last but not least, very special thanks to my friends and colleagues of the Catalysis and Reaction Engineering research group: Dr Artur Majewski, Dr Yu Rong, Dr Jiawei Wang, Abdullah Al Marshed, Martin Khzouz for being such good friends and providing generous help in the successful completion of this work, without whom it would have been very hard.

Table of Contents

ABSTRACT	i
ACKNOWLEDGEMENTS.....	iv
LIST OF FIGURES	ix
LIST OF TABLES	xii
NOMENCLATURE.....	xiii
1 CHAPTER 1 INTRODUCTION.....	1
1.1 Background and Motivation	1
1.2 Objectives of the Present Study	3
1.3 Thesis Layout.....	4
2 CHAPTER 2 LITERATURE REVIEW	6
2.1 Chapter Overview	6
2.2 PGM-Based Heterogeneous Catalyst.....	7
2.2.1 Palladium in Catalysis	8
2.2.1.1 Properties of Palladium	8
2.2.1.2 History of Palladium Catalyst	9
2.2.1.3 Nanoparticulate Palladium in Heterogeneous Catalysis	10
2.2.2 Conventional Catalyst Support.....	11
2.2.2.1 Properties of Support Material	12
2.2.2.2 Functions of Catalyst Support.....	13
2.2.3 Methods of Catalyst Manufacture	15
2.2.3.1 Conventional Catalyst Preparation.....	16
2.2.3.2 Nanotechnology for Palladium Nanoparticles	19
2.2.4 Catalyst Deactivation.....	21
2.2.4.1 Chemical Poisoning.....	23
2.2.4.2 Thermal Degradation.....	25
2.2.4.3 Leaching	26
2.2.5 Promoter	28
2.2.5.1 Discovery of Gold in Catalysis	29
2.2.5.2 Supported AuPd Bimetallic Catalyst	30
2.3 Biomass-Supported Catalyst.....	33
2.3.1 Chemical Components and Cellular Structures of Microbes	34

2.3.2	Bio-Pd Catalyst.....	37
2.3.3	Bio-AuPd Catalyst.....	38
2.3.4	Advantages and Challenges of Bioreductive Synthesis of Bio-Catalyst.....	40
2.4	Reaction Mechanism on Catalyst Surfaces.....	43
2.4.1	Hydrogenation of Vegetable Oil	43
2.4.1.1	Selectivity in Catalytic Hydrogenation of Vegetable Oil.....	44
2.4.1.2	Hydrogenation of Vegetable Oil on the Catalyst Surface	46
2.4.2	Oxidation of Alcohol.....	48
2.4.2.1	Benzyl Alcohol Oxidation Using Molecular Oxygen	49
2.4.2.2	Aerobic Oxidation of Alcohol on the Catalyst Surface.....	52
2.5	Three-Phase Catalytic Reactor.....	55
2.5.1	Mechanically Agitated Slurry Reactor	56
2.5.2	Mixing and Mass Transfer.....	57
2.5.2.1	Particle Suspension	58
2.5.2.2	External Transport Limitation	58
2.5.2.3	Internal Transport Limitation	61
2.6	Conclusions and Rationale for Current Studies	63
3	CHAPTER 3 EXPERIMENTAL SETUP AND ANALYTICAL METHODS.....	65
3.1	Chapter Overview	65
3.2	Materials and Equipment	65
3.3	Bio-Catalyst Manufacture	67
3.3.1	Bacterial Growth and Metal Solutions Preparation.....	67
3.3.2	Metallisation of Bacteria	68
3.3.3	Quantitative Assays for Pd(II) and Au(III)	70
3.4	Apparatus and Procedure	71
3.4.1	Experimental Rigs	71
3.4.2	Operation Procedure for Baskerville and Parr Reactors.....	74
3.5	Qualitative and Quantitative Analytical Methods to Liquid Sample.....	77
3.5.1	Gas Chromatography.....	77
3.5.2	Assays for Residual Pd(II) and Au(III)	79
3.6	Catalyst Characterisation Techniques.....	79
3.6.1	Thermogravimetric Analysis	79
3.6.2	CO Pulse Chemisorption	80
3.6.3	Electron Microscopy	82
3.6.4	X-Ray Diffraction.....	85

4	CHAPTER 4 SELECTIVE HYDROGENATION USING BIO-PD CATALYST	87
4.1	Chapter Overview	87
4.2	Hydrogenation of 2-Pentyne	88
4.3	Hydrogenation of Soybean Oil	95
4.3.1	Conventional Catalyst 5wt%Pd/Al ₂ O ₃	97
4.3.1.1	Mixing and Mass Transfer Investigation	100
4.3.1.1.1	Particle Suspension	100
4.3.1.1.2	External Mass Transfer	101
4.3.1.1.3	Intra-Particle Diffusion	110
4.3.1.2	Kinetics Model of the Surface Reaction	111
4.3.1.2.1	Effect of Hydrogen Pressure	111
4.3.1.2.2	Kinetic models for Soybean Oil Hydrogenation	114
4.3.1.2.3	Effect of Temperature and Activation Energy	120
4.3.2	Bio-Pd Catalyst.....	122
4.3.2.1	Comparison of Bio-Pd/ <i>E. coli</i> with Pd/Al ₂ O ₃	123
4.3.2.2	Thermal Stability of Bio-Pd/ <i>E. coli</i> in Hydrogenation	126
4.3.2.3	Comparison of Bio-Pd/ <i>E. coli</i> with Bio-Pd/ <i>D. desulfuricans</i>	128
4.3.2.4	Comparison of H ₂ -Reduction with Formate-Reduction for bio-Pd/ <i>E. coli</i> ..	130
4.4	Conclusions.....	132
5	CHAPTER 5 AEROBIC OXIDATION USING BIO-AUPD CATALYST.....	134
5.1	Chapter Overview	134
5.2	Oxidation of Benzyl Alcohol	135
5.2.1	Experimental Condition Optimisation.....	138
5.2.1.1	Dead-End Reaction under Compressed Air	138
5.2.1.2	Parr Autoclave Modification	140
5.2.1.3	Stability Investigation of Bio-AuPd Catalyst.....	148
5.2.1.4	Mixing and Mass Transfer	149
5.2.1.4.1	Critical Concentration of Oxygen in Benzyl Alcohol Oxidation.....	151
5.2.1.4.2	Effect of Air Flow Rate on the Oxygen Partial Pressure	152
5.2.1.4.3	Effect of Catalyst Concentration on the Oxygen Partial Pressure	157
5.2.1.5	Effect of Temperature and Activation Energy	159
5.2.2	Bio-AuPd Catalyst Formulation	165
5.2.2.1	Effect of Biomass Strain	165
5.2.2.2	Effect of Total Metal Loading.....	171
5.2.2.3	Effect of Au:Pd Mass Ratio	176

5.3	Oxidation of Other Alcohols.....	179
5.4	Conclusions.....	180
6	CHAPTER 6 CHARACTERISATION OF CATALYST.....	182
6.1	Chapter Overview.....	182
6.2	Thermal Stability of Bio-catalyst.....	183
6.3	Examination of Bio-Catalyst by Electron Microscopy.....	188
6.3.1	Surface Morphology and Element Confirmation (SEM/BSE-EDS).....	188
6.3.2	Metal Deposition on the Bacteria (TEM).....	192
6.4	Estimation of Particle Size.....	197
6.4.1	CO Pulse Chemisorption Analysis.....	198
6.4.2	TEM Method.....	203
6.4.3	X-ray Diffraction Technique.....	205
6.5	Conclusions.....	207
7	CHAPTER 7 CONCLUSIONS AND FUTURE WORK RECOMMENDATIONS.....	209
7.1	Conclusions.....	209
7.2	Future Work Recommendations.....	216
	REFERENCE LIST.....	218
8	CHAPTER 8 APPENDICES.....	236
8.1	Kinetic Models of Hydrogenation Reactions.....	237
8.1.1	Rate Equation Derivation of 2-Pentyne Hydrogenation.....	237
8.1.2	Kinetics Models of Soybean Oil Hydrogenation.....	241
8.2	Towards Economic Bio-Catalyst Production.....	248
8.2.1	Production of Catalyst from ‘Surrogate’ and Real Wastes.....	248
8.2.2	Production of Catalyst Using ‘Second-Life’ Bacteria.....	250
8.3	Calculations.....	254
8.3.1	Agitator Reynolds Number and Power Consumption.....	254
8.3.2	Air Flow Rate Calculation in Parr Autoclave.....	255
8.4	Conferences and Additional Publications.....	257

List of Figures

Figure 2.1 Unit cell of palladium face-centred cubic (fcc) structure.	9
Figure 2.2 Top: Rapid growth of unsupported active particles. Bottom: Supported thermostable active material.	11
Figure 2.3 Major types of deactivation in heterogeneous catalysis.	22
Figure 2.4 Two conceptual models for crystallite growth due to sintering by (A) atomic migration (B) crystallite migration	26
Figure 2.5 Differences in the cell wall structure between the Gram-positive and Gram-negative bacteria.	36
Figure 2.6 Elementary reaction of hydrogenation and isomerisation of carbon-carbon double bond based on Horiuti-Polanyi mechanism.	47
Figure 2.7 General oxidation scheme for primary alcohol oxidation to acid.	52
Figure 2.8 Classification of industrial three-phase catalytic reactors.	55
Figure 2.9 Mass transport resistances of gaseous reactant in three-phase catalytic reaction system. ...	59
Figure 3.1 Simplified procedure of bio-catalyst manufacturing using bacterial cells.	70
Figure 3.2 Schematic of the Baskerville autoclave reactor for the hydrogenation reactions.	72
Figure 3.3 Schematic of the original Parr autoclave reactor for the oxidation reactions.	74
Figure 3.4 Simplified schematic of the Varian CP-3380 gas chromatography system.	77
Figure 3.5 TG 209 <i>FI</i> measuring unit for thermogravimetric analysis.	80
Figure 3.6 Micromeritics Autochem II 2920 for CO chemisorption analysis.	81
Figure 4.1 The overall integral reaction network of 2-pentyne hydrogenation.	88
Figure 4.2 Concentration profiles as the function of reaction time in 2-pentyne hydrogenation using a 2wt%Pd/ <i>E. coli</i> catalyst.	90
Figure 4.3 2-pentyne concentration profiles versus reaction time over different catalysts.	93
Figure 4.4 Simplified soybean oil hydrogenation and isomerisation network in the presence of solid catalyst.	96
Figure 4.5 Example of the evolution of products distribution during the reaction time in soybean oil hydrogenation.	98
Figure 4.6 Evolution of the initial reaction rates with stirring speed (for both <i>cis</i> -C18:3 and <i>cis</i> -C18:2 at the initial 30 mins) in soybean oil hydrogenation.	103
Figure 4.7 Comparison of the formation of <i>a)</i> <i>trans</i> -C18:1 and <i>b)</i> C18:0 at the same <i>cis</i> -C18:2 conversion under different stirring speeds.	105
Figure 4.8 <i>a)</i> A plot of $[H_2^*]/r_{H_2}$ against $1/m$; <i>b)</i> An illustrative $[G^*]/r_G$ versus $1/m$ plot for different reaction orders.	108
Figure 4.9 Effect of hydrogen pressure on initial reaction rate of hydrogen in soybean oil hydrogenation.	112
Figure 4.10 Comparison of the formation of <i>a)</i> <i>trans</i> -C18:1 and <i>b)</i> C18:0 at the same <i>cis</i> -C18:2 conversion under different hydrogen pressures.	113
Figure 4.11 The reaction scheme of soybean oil hydrogenation based on Model 1.	115
Figure 4.12 Experimental (scattered symbols) and predicted (solid lines) fatty acid composition profiles using Equations 4-15 ~ 4.18 for Model 1.	117

Figure 4.13 The reaction scheme of soybean oil hydrogenation based on Model 2.	118
Figure 4.14 Experimental (scattered symbols) and predicted (solid lines) fatty acid composition profiles using Equations 4-19 ~ 4-24 for Model 2.	119
Figure 4.15 Arrhenius plot of $\ln(k)$ versus $1/T$ showing temperature dependence of soybean oil hydrogenation over a 5wt%Pd/Al ₂ O ₃ catalyst.	121
Figure 4.16 Formation of <i>trans</i> -C18:1 versus <i>cis</i> -C18:2 conversion in soybean oil hydrogenation using 5wt%Pd/Al ₂ O ₃ under different reaction temperatures.	122
Figure 4.17 Concentration profiles as the function of reaction time in soybean oil hydrogenation using 5wt%Pd/ <i>E. coli</i>	123
Figure 4.18 Comparison of the formation of a) <i>cis</i> -/ <i>trans</i> -C18:1 and b) C18:0 at the same <i>cis</i> -C18:2 conversion by using different Pd catalysts.	125
Figure 4.19 Comparisons of a) <i>cis</i> -C18:2 conversion versus time and b) <i>trans</i> -C18:1 formation in soybean oil hydrogenation using 5wt%Pd/ <i>E. coli</i> at different reaction temperatures.	127
Figure 4.20 Comparison of a) the reactant conversion after 5 hours; comparison of the formation of b) <i>cis</i> -C18:1 and c) <i>trans</i> -C18:1 at the same <i>cis</i> -C18:2 conversion in soybean oil hydrogenation using bio-Pd/ <i>E. coli</i> and bio-Pd/ <i>D. desulfuricans</i>	129
Figure 4.21 a) Comparisons of <i>cis</i> -C18:2 conversion and <i>cis</i> -C18:3 conversion after 5 hours in soybean oil hydrogenation using 5wt%Pd/ <i>E. coli</i> prepared by different reduction methods; b) the formation of <i>cis</i> -C18:1 as a function of <i>cis</i> -C18:2 conversion.	131
Figure 5.1 Reaction schemes of aerobic benzyl alcohol oxidation.	137
Figure 5.2 Concentration profiles from the benzyl alcohol oxidation in the original Parr autoclave reactor (dead-end mode).	140
Figure 5.3 Schematic profiles of oxidation reactor before and after modifications.	142
Figure 5.4 Profiles of benzyl alcohol concentration versus reaction time in the original reactor (Parr) and the modified reactor (Parr').	143
Figure 5.5 a) Product profiles as a function of reaction time in benzyl alcohol oxidation; b) Selectivities to different products versus benzyl alcohol conversion.	145
Figure 5.6 Comparison of results from original reactor (Parr) and modified reactor (Parr') based on a) product distributions at 2 hours; b) benzaldehyde selectivity versus benzyl alcohol conversion; c) toluene selectivity versus benzyl alcohol conversion; and d) BDBA selectivity versus benzyl alcohol conversion.	147
Figure 5.7 a) Benzyl alcohol concentration profiles under different flow rates; b) Effect of the air flow rate on the benzyl alcohol consumption rate.	153
Figure 5.8 An illustration on the oxygen partial pressure changing with reaction time under different air flow rates in the modified autoclave reactor.	155
Figure 5.9 a) Evolution of the initial benzyl alcohol reaction rate by changing the catalyst loading of bio-AuPd in benzyl alcohol oxidation; b) Benzyl alcohol concentration profiles using different masses of bio-AuPd; c) A demonstration on the partial pressure changing with the reaction time when using different masses of bio-AuPd in the modified autoclave.	158
Figure 5.10 a) Benzyl alcohol concentration profiles under different reaction temperatures; b) Arrhenius plot of $\ln(k)$ versus $1/T$ showing temperature dependence of benzyl alcohol oxidation over a 2.5wt%Au2.5wt%Pd/ <i>E. coli</i> catalyst.	161
Figure 5.11 Product concentration as a function of benzyl alcohol conversion at temperature of a) 110 °C and b) 140 °C; Comparison of c) selectivity to toluene, d) BDBA formation, and e) benzoic acid formation under different reaction temperatures.	164
Figure 5.12 Benzyl alcohol conversion profiles using bio-AuPd catalysts supported on different strains of bacteria.	166

Figure 5.13 Profiles of selectivity to a) benzaldehyde, b) BDBA, c) toluene, d) benzoic acid, and e) benzyl benzoate as a function of benzyl alcohol conversion in the reactions using bio-AuPd catalysts supported on different strains of bacteria.....	170
Figure 5.14 a) and b) Comparisons of benzyl alcohol conversions over bio-AuPd/ <i>E. coli</i> catalysts with different total loadings; c) Comparison of the selectivity to toluene over bio-AuPd/ <i>E. coli</i> catalysts with loadings of 0.5wt% Au0.5wt% Pd, 1wt% Au1wt% Pd, and 2.5wt% Au2.5wt% Pd; d) Comparisons of the selectivity to benzyl aldehyde, and e) Comparisons of the selectivity to BDBA formation using 2.5wt% Au2.5wt% Pd/ <i>E. coli</i> and 25wt% Au 25wt% Pd/ <i>E. coli</i>	174
Figure 5.15 a) Benzyl alcohol conversion profiles, b) selectivity towards benzaldehyde, and c) selectivity to toluene over bio-AuPd catalyst prepared by different Au: Pd mass ratios.....	178
Figure 6.1 Weight loss curves for a) 5wt% Pd/ <i>E. coli</i> and 5wt% Pd/ <i>D. desulfuricans</i> ; b) 5wt% Pd/ <i>E. coli</i> and 2.5wt% Au2.5wt% Pd/ <i>E. coli</i> . TGA was performed in air at a heating rate of 10 °C/min from 25 °C to 1000 °C.....	185
Figure 6.2 Weight loss curves for 2.5wt% Au2.5wt% Pd bio-catalysts supported on different strains of bacteria at heating rates of 10 °C/min from 25 °C to 1000 °C.....	186
Figure 6.3 Detailed TGA analysis of a) 2.5wt% Au2.5wt% Pd/ <i>E. coli</i> , and b) 2.5wt% Au2.5wt% Pd/ <i>R. sphaeroides</i> at heating rates of 10 °C/min from 25 °C to 1000 °C.....	187
Figure 6.4 a) SEM image of <i>E. coli</i> -supported bio-catalyst powder, showing rod-shaped <i>E. coli</i> cells; b) SEM image of <i>M. luteus</i> -supported bio-catalyst powder, showing spherical-shaped <i>M. luteus</i> cells; c) SEM image of one <i>E. coli</i> -supported bio-catalyst powder, inset corresponding BSE image of the selected area; d) BSE image from dry powder of 25wt% Pd/ <i>E. coli</i> catalyst with the corresponding EDS spectrum; and e) BSE image from dry powder of 25wt% Au25wt% Pd/ <i>E. coli</i> catalyst with the corresponding EDS spectrum.....	190
Figure 6.5 BSE images of bio-catalyst powders of a) 1wt% Au1wt% Pd/ <i>E. coli</i> ; b) 2.5wt% Au2.5wt% Pd/ <i>E. coli</i> ; c) 2.5wt% Au2.5wt% Pd/ <i>M. luteus</i> ; and d) 2.5wt% Au2.5wt% Pd/ <i>A. oxydans</i>	192
Figure 6.6 a) TEM image of an ultra-thin section of native <i>E. coli</i> cell (image courtesy of Dr I. Mikheenko); b) TEM image of an ultra-thin section of 5 wt% palladium loaded <i>E. coli</i> cells showing the cell wall structure after palladisation, sectioned specimen without osmium or uranyl acetate/lead citrate stain; c) TEM image of 5 wt% palladium loaded <i>E. coli</i> cells from another separate preparation, sectioned specimen without osmium or uranyl acetate/lead citrate stain; d) TEM image of <i>M. luteus</i> whole cells loaded with 2.5wt% Au2.5wt% Pd, specimen prepared by dropping the catalyst powder in water solution onto the TEM grid; e) TEM image of 2.5wt% Au2.5wt% Pd/ <i>M. luteus</i> section (photo courtesy of Dr K. Deplanche).....	195
Figure 6.7 TEM images of whole cells (unsectioned) a) 0.5wt% Au0.5wt% Pd/ <i>E. coli</i> ; b) 1wt% Au1wt% Pd/ <i>E. coli</i> ; c) 2.5wt% Au2.5wt% Pd/ <i>E. coli</i> ; and d) 25wt% Au25wt% Pd/ <i>E. coli</i> . Specimens prepared by dropping the catalyst powder in water solution onto the TEM grids.....	197
Figure 6.8 TCD signal versus time for a) 5wt% Pd/ Al_2O_3 , and b) 5wt% Pd/ <i>E. coli</i>	199
Figure 6.9 a) TEM images of ultra-thin sections made from the 5wt% Pd/ <i>D. desulfuricans</i> catalyst powder, two images shown were used for the acquisition of particles representing two different areas from one single catalyst preparation, 155 surface particles were estimated with the inset particle size distribution; b) TEM images of ultra-thin sections made from two separate batches of freshly palladised 5wt% Pd/ <i>E. coli</i> cells, sectioned specimen without osmium or uranyl acetate/lead citrate stain, four images shown represent four different areas, 240 surface particles were estimated with the inset particle size distribution.	204
Figure 6.10 X-ray powder diffraction (XRD) analysis of monometallic Pd and bimetallic AuPd NPs formed by <i>E. coli</i> : a) 2wt% Pd/ <i>E. coli</i> , b) 5wt% Pd/ <i>E. coli</i> , c) 25wt% Pd/ <i>E. coli</i> , d) 25wt% Au25wt% Pd/ <i>E. coli</i> , e) 2.5wt% Au2.5wt% Pd/ <i>E. coli</i> , f) 4wt% Au1wt% Pd/ <i>E. coli</i> , and g) 1wt% Au4wt% Pd/ <i>E. coli</i>	206

List of Tables

Table 2.1 Important catalytic processes commercialised after 1940s.	7
Table 2.2 Physical and chemical properties of supports.	12
Table 2.3 Properties of typical catalyst supports.	12
Table 2.4 Summary of origin, mechanism and typical examples of catalyst deactivation.	22
Table 2.5 Poisons for selected catalysts in important representative reactions.	24
Table 2.6 Summary of supported AuPd bimetallic catalysts using different preparation methods.	31
Table 2.7 Characters of some bacteria.	36
Table 2.8 Fatty acid composition of some common vegetable oils.	44
Table 2.9 Some investigations on hydrogenation of fatty oils.	45
Table 2.10 Characters of three-phase reactor types with typical values are given.	56
Table 2.11 Advantages and disadvantages of agitated three-phase catalytic reactors.	57
Table 2.12 Mass transfer resistances and resistance terms.	59
Table 3.1 Commercial chemicals and materials used in this study.	66
Table 3.2 Instruments involved in this study.	66
Table 3.3 Parameters investigated and varied for different catalysts in this study.	75
Table 3.4 GC columns and oven conditions for the analysis of different substrates in this study.	78
Table 4.1 Values of fitted parameters for 2-pentyne hydrogenation using Equations 4-2 ~ 4-5.	92
Table 4.2 Comparison of the product distribution at 100% conversion of 2-pentyne over different catalysts.	94
Table 4.3 Fatty acid compositions and physical properties of untreated soybean oil.	95
Table 4.4 Parameters used for the calculation of the minimum stirring speed (N_m) in the case of soybean oil hydrogenation over 5wt%Pd/ Al_2O_3 in Baskerville autoclave reactor.	101
Table 4.5 Parameters used for the determination of the liquid-solid mass transfer coefficient k_s	109
Table 4.6 Partial differential equations in two kinetics models for hydrogenation of soybean oil.	116
Table 4.7 Values of fitted parameter using Equations 4-15 ~ 4.18 for Model 1.	117
Table 4.8 Fitted parameter values using Equations 4-19 ~ 4-24 for Model 2.	119
Table 4.9 A comparison of the component distribution in soybean oil hydrogenations using 5wt%Pd/ <i>E. coli</i> and 5wt%Pd/ Al_2O_3	123
Table 5.1 Properties of the major components presenting in benzyl alcohol oxidation.	137
Table 5.2 Comparison of the product selectivities in benzyl alcohol oxidation over ‘as-received’ and ‘pre-reduced’ 2.5wt%Au2.5wt%Pd/ <i>E. coli</i>	149
Table 5.3 Parameters used for the calculation of the minimum stirring speed (N_m) in the case of benzyl alcohol oxidation over a 2.5wt% Au2.5wt%Pd/ <i>E. coli</i> catalyst in Parr autoclave reactor.	150
Table 5.4 Comparison of the reaction conditions and the catalytic activity in benzyl alcohol oxidation in this study with those in literature.	160
Table 5.5 Details of catalyst amount used for catalytic activity comparison.	172
Table 5.6 Oxidation of different alcohols over 2.5wt%Au2.5wt%Pd/ <i>E. coli</i>	179
Table 6.1 Parameters for CO Chemisorption and the resulting data on 5wt%Pd/ Al_2O_3 catalyst.	200
Table 6.2 Summary of the characterisation data on different catalysts using different technologies.	202

Nomenclature

a	gas-liquid interfacial area per unit volume of liquid, $\text{cm}^2.\text{cm}^{-3}$
A	pre-exponential factor in Equations 4-25 and 5-4, dimensionless
B	peak width of the diffraction peak profile at half maximum height, °
d_l	stirrer diameter, cm
d_p	average diameter of catalyst particles, cm
d_T	reactor inside diameter, cm
D_G	diffusion coefficient of gas G in the liquid phase, $\text{cm}^2.\text{s}^{-1}$
E_a	activation energy of reaction, $\text{kJ}.\text{mol}^{-1}$
F	stoichiometry factor in Equation 3-1, dimensionless
F'	objective function defined in Equation 4-6
F_{air}	air flow rate, $\text{ml}.\text{min}^{-1}$
g	gravitational acceleration, $981 \text{ cm}.\text{s}^{-2}$
$[G^l]$	concentration of gas G in the bulk liquid, $\text{mol}.\text{cm}^{-3}$
$[G^s]$	concentration of gas G at the catalyst surface, $\text{mol}.\text{cm}^{-3}$
H	Henry's constant, $\text{pa}.\text{cm}^3.\text{mol}^{-1}$
k_g	gas film mass transfer coefficient, $\text{cm}.\text{s}^{-1}$
k_i', k_i	reaction rate constants of i , $\text{mol}.\text{g}^{-1}.\text{h}^{-1}$
k_L	liquid film mass transfer coefficient, $\text{cm}.\text{s}^{-1}$
k_s	mass transfer coefficient from liquid-solid interface to solid surface, $\text{cm}.\text{s}^{-1}$
K	Scherrer constant related to crystallite shape, see Equation 3-3, dimensionless
K_i	adsorption coefficient of i , $\text{m}^3.\text{mol}^{-1}$
m	mass of liquid in Equation 8-32 and 8-33, g
N_m	minimum agitation speed, rpm
N_p	power number, dimensionless
p_G	partial pressure of gas G , pa
P	power consumption per unit mass, $\text{w}.\text{g}^{-1}$
r_G	observed reaction rate of gas G per unit gram of catalyst particles, $\text{mol}.\text{g}^{-1}.\text{s}^{-1}$
R	universal gas constant, $8.314 \text{ J}.\text{K}^{-1}.\text{mol}^{-1}$
Re	agitator Reynolds number, dimensionless
R_G	overall reaction rate of gas G , $\text{kmol}.\text{cm}^{-3}.\text{s}^{-1}$
SA	surface area, $\text{m}^2.\text{g}^{-1}$
t	time, s
T	temperature, K
TOF	turnover frequency, time^{-1}
V_s	the volume of adsorbed CO, cm^3
w	mass of catalyst per unit volume of slurry, $\text{g}.\text{cm}^{-3}$

w'	percentage catalyst loading, $\text{g}(\text{catalyst}) \cdot 100\text{g}(\text{solution})^{-1}$
W_s	catalyst sample weight, g

Greek Symbols

α	parameter defined by Equation 4-12, dimensionless
β	constant (see Equations 2-1 and 2-2), dimensionless
γ	hydrogen order for <i>cis</i> -isomer to react
δ	hydrogen order for <i>trans</i> -isomer to react
ψ	correction factor for power consumption in the presence of gas bubbles
η	catalytic effectiveness factor, dimensionless
λ	distance from the centre of the catalyst at which the concentration of gas G becomes zero (see Figure 2.9)
λ'	X-ray wavelength, nm
μ	viscosity, $\text{g} \cdot \text{cm}^{-1} \cdot \text{s}^{-1}$
θ	surface coverage fraction, dimensionless
ρ	density, $\text{g} \cdot \text{cm}^{-3}$
Φ	Weisz-Prater modulus (see Equation 2-8 and 4-13), dimensionless

Acronyms

BDBA	benzaldehyde dibenzyl acetal
BOC	Brin's Oxygen Company
BSE	backscattered-SEM
COD	Crystallography Open Database
CSTR	continuous stirred-tank reactor
CTAB	cetyl trimethyl ammonium bromide
DNA	deoxyribonucleic acid
DTG	differential TGA
EDS	energy-dispersive X-ray spectroscopy
EDTA	(ethylenedinitrilo)tetraacetic acid
EXAFS	extended X-Ray absorption fine structure
FAMES	fatty acid methyl esters
fcc	face-centred cubic structure
FID	flame ionisation detector
G	transporting gas
GC	gas chromatography
GMW	gram molecular weight
HAP	hydroxyapatite
LHHW	Langmuir-Hinshelwood-Hougen-Watson

mM, M	millimole per litre, mole per litre
MCM-22	Mobil Crystalline Material-22, one type of porous silicate-based materials
MFC	mass flow controller
MOPs	3-(N-morpholino)propanesulfonic acid
MSI, SMSI	metal-support interaction, strong metal-support interaction
NB No.2	nutrient broth No.2
NA	not applicable
NAG	poly-n-acetylglucosamine
NAM	n-acetylmuramic acid
NG	not given
NP, NPs	nanoparticle, nanoparticles
OD	optical density
p.p.m.	parts-per-million
PE, PIC	pressure sensor, pressure indicator
PEGMs	polyethylene glycol monostearate
PG	pressure gauge
PG, PGMs	platinum group, platinum group metals
PVA	polyvinylalcohol
PVP	polyvinylpyrrolidone
RNA	ribonucleic acid
SEM	scanning electron microscopy; standard error of the mean
SR	safety relief bursting disc; side reaction
SRB	sulfate-reducing bacteria
STP	standard temperature pressure (273.13K and 760 mmHg)
TCD	thermal conductivity detector
TDS	thermal desorption spectroscopy
TE, TIC	temperature sensor, temperature indicator
TEM	transmission electron microscopy
TGA	thermogravimetric analysis
vol%, wt%	percentage by volume, percentage by weight
V	valve
XRD	X-ray diffraction
ZSM-5	Zeolite Socony Mobil-5

Sub- and Superscripts

<i>crit</i>	critical
<i>i</i>	component
<i>j</i>	counts of sample

Chapter 1

Introduction

1.1 Background and Motivation

In heterogeneous catalysis, chemical reactions take place at the surface of an active component. The development of metal nanoparticles (NPs) as highly desirable catalysts has attracted significant interest and research since, compared with bulk metal, the superior surface-area-to-volume ratio of metal NPs confers a high reactivity [1,2]. Moreover, chemical intermediates that underpin a wide range of chemical products are called platform chemicals. Often they are synthesised as only one product within a reaction that may also generate other products which are not desired. Therefore, developing a catalyst possessing both high reactivity and selectivity towards the desired product becomes crucial in various industrial processes [3].

The partial hydrogenation of vegetable oils is an example of a catalytic process of great importance in industry in order to raise the melting point and oxidative stability of natural unsaturated substrates [4]. This process consists of complex reaction pathways, *i.e.* the saturation, positional migration and *cis-trans* geometrical isomerisation of carbon-carbon double bonds (C=C), with a particular aim for the production of *cis*-isomers because they have been associated with, *e.g.* in health aspects, lower incidence of diseases compared with *trans*-isomers [5,6]. The catalyst of most universal choice is still nickel on different carriers, giving high activity but with a lack of selectivity towards *cis*-isomers [4]. Another example is the catalytic oxidation of primary and secondary alcohols into the corresponding carbonyl compounds which plays a central role in organic synthesis of either finished products or intermediates [7,8]. There are relatively few selective oxidation reactions that are catalysed over heterogeneous catalysts using molecular oxygen [7], instead using stoichiometric

quantities of inorganic oxidants (*e.g.* chromate or permanganate) to achieve selectivity towards aldehydes in oxidation processes [9,10] or performing in homogeneous systems to result in high product yields [11,12]. However, the disadvantages of these processes are the cost and serious toxicity issues of these reagents associated with major problems of product separation and catalyst recycling.

In the development of catalysts to improve existing catalytic systems, supported palladium NPs appear to be promising for both the partial hydrogenation of fatty oils [13,14] and the selective oxidation of alcohols [7,8]. The general routes for manufacture of monodisperse NPs are based on chemical/electrochemical reduction or thermal decomposition of palladium precursors, which usually require an appropriate reducing agent and a stabiliser to form the metal NPs that would otherwise tend to agglomerate [15,16]. Overall these synthesis methods involve rigorous experimental procedure, extreme conditions, or expensive equipment, or all three [17-19]. Alternatively, an effective and novel approach was recently established to use bacterial cells as carriers for precious metal nanoparticles (*e.g.* palladium or gold) that are held in a stable configuration on the bacterial cells [20]. This stability of NPs could potentially lead to a catalyst of certain activity and with superior selectivity towards products of interest [21-23]. In addition, the catalyst material can be recovered at the end of the reaction by filtration or centrifugation and recycled. The precious metal can be easily and economically recovered from the used catalyst by incineration, sonication or microwaving the biomass [24], following multiple reaction cycles [25].

An exemplar case is the sulfate-reducing bacterium *Desulfovibrio desulfuricans* which reduces soluble Pd(II) to Pd(0) [20]. Palladised *D. desulfuricans* cells had high catalytic activity in the production of hydrogen from hypophosphite [26], the dehalogenation of polychlorinated biphenyls [27] and the reduction of Cr(VI) to Cr(III) in batch suspension [28] or flow-through reactor [29] systems. Creamer *et al.* [30] reported that a 5 wt%Pd loading on

D. desulfuricans produced palladium particles of ~5 nm diameter which were found to be active in the hydrogenation of itaconic acid. Bennett *et al.* [24] investigated the selectivity of 5wt%Pd/*D. desulfuricans* in the hydrogenation of 2-pentyne and found better alkene/alkane and *cis/trans* selectivities in comparison with a conventional 5wt%Pd/ Al_2O_3 catalyst. A comparison of the catalytic activity of ‘bio-Pd’ on various bacteria in the reduction of Cr(IV) showed that the Gram-negative species *D. desulfuricans* and *Escherichia coli* gave the most active catalytic NPs. *E. coli* was selected as the candidate for further development due to ease of growth at scale, lack of production of catalyst poisons (*e.g.* H_2S) and the well-developed molecular genetics of this organism to enable future strain development for targeted applications [31].

The work presented in this study focuses on the use of *E. coli* as the support to produce two classes of bionano-catalysts (*i.e.* bio-Pd/*E. coli* and bio-AuPd/*E. coli*). The resulting *E. coli*-supported catalysts were tested for catalytic activities and selectivities in the hydrogenation of alkyne/alkene and oxidation of alcohols in three-phase slurry reactors. The specific details are addressed in the objectives of this work.

1.2 Objectives of the Present Study

Given the range of knowledge reported above, the following objectives were set for the present study:

- i) To manufacture the bio-catalysts using a bacterial strain of *Escherichia coli*.
- ii) To evaluate hydrogenation reactions over Pd-based catalysts in a 500 ml Baskerville autoclave reactor.
 - a) To compare the catalytic performance of bio-Pd/*E. coli* with Pd/ Al_2O_3 in 2-pentyne hydrogenation; to study the reaction kinetics of this simple hydrogenation.

- b) To investigate the mass transfer in soybean oil hydrogenation (solvent free) and optimise the reaction conditions using conventional Pd/Al₂O₃ catalyst; to interpret reaction results and establish kinetics models for experimental data.
 - c) To test bio-Pd/*E. coli* in the soybean oil hydrogenation under optimised reaction conditions and compare the reactivity and selectivity with the conventional Pd/Al₂O₃ catalyst.
- iii) To test bio-AuPd catalysts in the solvent-free oxidation of alcohols in a 100 ml Parr autoclave reactor.
- a) To operate the selective oxidation of benzyl alcohol under solvent-free conditions using compressed air with the aim of establishing a green catalytic process.
 - b) To modify the reactor and study the hydrodynamics of the reaction system.
 - c) To study the influence of catalyst formulation on the reaction performance.
 - d) To evaluate the catalytic activity of AuPd/*E. coli* against a range of different alcohols.
- iv) To characterise the bio-catalysts evaluated in this study using different techniques, and relate observed features to the catalytic properties described from objectives ii) ~ iii).

1.3 Thesis Layout

Given the range of objectives stated above, the structure of the present thesis is set as the following 8 chapters.

Chapter 1 gives an introduction and background information about current work, along with objectives of this study.

Chapter 2 presents a literature review, which introduces the application of platinum group metals (PGMs) in manufacturing heterogeneous catalysts and current conventional manufacturing methods. Biological synthesis of metal NPs using bacterial cells as the catalyst supports is described in detail. Two major types of catalytic reactions, *i.e.* hydrogenation and oxidation, on the catalyst surface are described. This chapter also includes a description of the use of an agitated slurry reactor for three-phase catalytic reactions.

Chapter 3 is a compilation of the list of materials and instruments used in this work and descriptions of the catalyst manufacturing, experimental systems, operating procedures, and analytical methods employed. This chapter also provides detailed information about the characterisation techniques used and their significance.

Chapter 4 presents investigations of Pd-based catalysts in 2-pentyne hydrogenation and soybean oil hydrogenation in a three-phase Baskerville autoclave reactor.

Chapter 5 studies the catalytic activity of biomass-supported AuPd catalysts in the aerobic oxidation of alcohols in a three-phase Parr autoclave reactor.

Chapter 6 discusses characterisation results of biomass-supported Pd and AuPd catalysts based on various techniques.

Finally, Chapter 7 brings the results together in final conclusions, which attempt to place the work in context at the cutting edge and identify the fundamental questions that should be addressed in future work. References are added at the end of the thesis.

Additional methodology and method validations are addressed in the appendices in Chapter 8. It also includes a list of conference presentations, reproduction of posters gave at conferences, and a manuscript accepted for publication subjected to minor referee's comments. The Health and Safety Risk Assessments needed as part of health and safety regulations are included.

Chapter 2

Literature Review

2.1 Chapter Overview

This chapter opens with an introduction about the application of platinum group metals (PGMs) in manufacturing heterogeneous catalysts in §2.2. Typical industrial heterogeneous catalysts may consist of three main components: active metal, support and secondary metal (co-catalyst or promoter). The active metal, being palladium (Pd) as a specific focus in this study (§2.2.1), is responsible for the principal chemical reaction. Conventional materials for catalyst supports are introduced in §2.2.2, along with manufacturing methods ranging from conventional synthesis to novel nanotechnology being summarised in §2.2.3. Despite the high catalytic activity of Pd-based catalyst, current challenges of catalyst deactivation are reviewed and mechanisms of deactivation are explained in §2.2.4. This section also includes a discussion on the role of metal promoter gold on palladium catalyst in §2.2.5.

Thereafter a bioreductive synthesis of metal nanoparticles (NPs) using bacterial cells as the catalyst supports (bio-Pd or bio-AuPd NPs) is introduced in §2.3. An introduction of cellular structures and components of bacterial cells which are able to perform the reduction of Pd(II) to Pd(0) is given in §2.3.1. Subsequently, the use of bio-Pd or bio-AuPd NPs in some catalytic reactions are reviewed in §2.3.2 and §2.3.3 respectively. In addition, the overall advantages and challenges of this biological synthesis method are presented in §2.3.4.

The application of supported Pd catalyst in both hydrogenation and oxidation and reaction mechanisms are presented in §2.4. An agitated slurry reactor is selected for this study and is described in §2.5, with particular emphasis upon mass transfer effects in this three-phase catalytic reaction system (gas-liquid-solid). Towards the end of the chapter, some conclusions and rationales for the current work are presented in §2.6.

2.2 PGM-Based Heterogeneous Catalyst

Platinum group (PG) metals include ruthenium, rhodium, palladium, osmium, iridium and platinum. These are extracted and refined from primary ores by complex processing [32,33], and have high technological importance due to their excellent resistance to corrosion and high-temperature, stable electrical conductivity and outstanding catalytic activity [34]. These properties have been exploited for a variety of industrial applications such as jewellery, glassmaking, electrical/electronics, automotive and chemical industries [33]. For example a large chemical sector use of PG metals is in catalysts [35] for many catalytic processes of the petrochemical and chemical manufacturing industries. PG metals, although more expensive initially (in comparison with nickel, cobalt and iron catalysts), often display greater activity and product selectivity which makes it possible to carry out commercially important reactions at appreciably lower temperatures and pressures than those necessary with base metal catalysts [36]. Also PG metals could readily be recovered and recycled, making their use much more commercially attractive [36]. Table 2.1 shows the applications of some PGM-based catalysts which were realised on an industrial scale since the 1940s.

Table 2.1 Important catalytic processes commercialised after 1940s [3].

Year	Process	Catalyst	Products
1939-1945	dehydrogenation	Pt/Al ₂ O ₃	toluene from methylcyclohexane
1946-1960	oxidation (Wacker process)	PdCl ₂ -CuCl ₂	acetaldehyde from ethylene
1961-1970	reforming	bimetallic catalysts (Pt, Sn, Re, Ir)	gasoline
1971-1980	automobile emission control	Pt-Rh-CeO ₂ -Al ₂ O ₃ (three-way catalyst)	removal of NO _x , CO, CH _x
	carbonylation (Monsanto process)	organic Rh complex	acetic acid from methanol
1981-1985	hydrocarbon synthesis (Shell)	Pt/SiO ₂	middle distillate from CO+H ₂
	environmental control (combustion process)	Pt/Al ₂ O ₃ (monoliths)	deodorization
1986-present	dehydrogenation of C ₃ , C ₄ alkanes (Star and Oleflex processes)	Pt(Sn)-zinc aluminate, Pt/Al ₂ O ₃	C ₃ , C ₄ olefins

Among the six PG metals, palladium is the most widely used, *e.g.* in reforming reactions in the petroleum refining industry, hydrogenation and dehydrogenation reactions in the pharmaceutical industry, and both organic and inorganic oxidation reactions [32]; herein is the focus in the present study.

2.2.1 Palladium in Catalysis

Palladium (Pd), with an atomic number of 46 on the periodic table, is a soft silver-white metal. It is the least dense and has the lowest melting point of the PG metals. Given the widespread use of palladium in many industrial catalytic processes, it is interesting to review the properties of palladium and to consider why Pd-based catalysts are so active and crucial for industrial applications.

2.2.1.1 Properties of Palladium

Palladium has a face-centred cubic (fcc) structure with a lattice parameter of $a = 0.3890$ nm at room temperature (298 K) [37] (Figure 2.1). Graham [38] first noted the adsorption of hydrogen gas by palladium in 1866 and produced an alloy of palladium with metallic hydrogen. Upon hydrogen adsorption the lattice undergoes an isotropic expansion while retaining its fcc structure [37]. At the molecular level, as a result, hydrogen fills the palladium metal forming a palladium hydride (PdH_x , x value varies depending on the formed crystalline phase), which despite its name is not an ionic hydride but rather is metallic palladium that contains a substantial quantity of hydrogen within its crystal lattice [39].

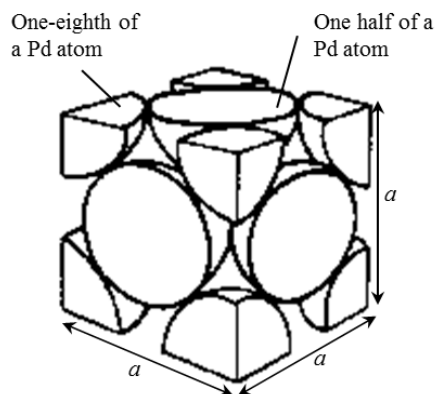


Figure 2.1 Unit cell of palladium face-centred cubic (fcc) structure. a , the lattice parameter, refers to the constant distance between unit cells in a crystal lattice [37].

At room temperature and pressure, palladium is known to have a remarkable adsorption capacity for hydrogen, being able to adsorb up to 900 times its own volume of hydrogen [40]. This therefore makes palladium highly suitable for use in hydrogen storage [41,42], gas sensing applications [43,44] and also as an efficient catalyst with industrial importance [45].

2.2.1.2 History of Palladium Catalyst

The discovery of the great activity of palladium in the catalysis of chemical reactions (*e.g.* combustion of hydrogen and oxygen, production of sulphuric and nitric acids) is owed to the early research of the Davy, Dobereiner, Faraday, and Kuhlmann [36,46] in the early 19th century. After almost 40 years with no further progress in the application of catalysis in industry, palladium black became of research interest in a number of catalytic reductions in 1912 and was investigated by Zelinsky for converting cyclohexane into benzene at about the same time [36]. During this early period, however, palladium blacks often showed a low or a varying activity [36]. These early forms of finely divided palladium catalyst were largely superseded by supported catalyst from the late 20th century, to make more effective use of the metal and to enable a wider range of reaction conditions to be met. The application of supported palladium catalyst on a range of suitable carriers (*e.g.* alumina, asbestos, silica gel and activated charcoal) then started to burgeon from the 1970's in many key industrial processes [33,36].

Since, in heterogeneous catalysis, a chemical reaction proceeds at the surface of active metal atoms, the catalytic activity of solids is therefore usually proportional to the surface area of the active component of the catalyst per unit weight or per unit volume [1,2]. It is apparent that small particles expose increased numbers of low-coordinate surface metal atoms [3], in other words smaller particles provide larger surface area per unit weight and thus more efficient activity. This has led to intense interest recently in developing Pd nanoparticles [15,47], due to the high surface-area-to-volume ratio, as a desirable type of catalytic material for use in industry.

2.2.1.3 Nanoparticulate Palladium in Heterogeneous Catalysis

Nanodimensional materials (in the 1~100 nm size domain) are seen as a bridge between atomic and bulk materials and have been shown to exhibit a variety of unique chemical, physical, electronic (and catalytic) properties that are different from those of bulk material [17,48,49]. For example, palladium is a paramagnetic metal and the bulk metal is considered to be on the verge of ferromagnetism [50] while nanoscale Pd-clusters are ferromagnetic [51]. Ferromagnetism has been demonstrated in high purity Pd nanoparticles (NPs) with radii of between 2 and 6 nm [52,53]. As to the impact on catalysis, Mikheenko [22] manufactured ferromagnetic Pd NPs (~5 nm at loading of 5 wt%Pd) *via* use of sulphate-reducing bacteria and found the catalytic activity of the resulting bio-Pd(0) NPs was comparable with that of a commercial catalyst (5wt%Pd/C) in the hydrogenation of itaconic acid.

For catalytic applications, there are conflicting needs to maintain the nanoparticle format for high reactivity whilst stabilising the active metal NPs. The transition and noble metals typically have high surface free energies [3,54] and therefore a pronounced tendency for small particles or crystallites to reduce their surface areas by particle growth [1], which occurs either by coalescence (the fusing of two or more smaller particles to form a larger one) or by ripening (the growth of large particles by migration of material from smaller ones) [55].

Accordingly, intervention is required to preserve and stabilise the nanosized particles, which can be achieved by dispersing active metals on high surface area supports.

2.2.2 Conventional Catalyst Support

The primary aim of applying a catalytically active component to a support is to spread out an expensive catalyst ingredient (usually only a minor percentage), such as a precious metal, in order to achieve a greater effective utilisation of the metal *via* providing a larger active surface area compared with a bulk metal system (*e.g.* a palladium black) [56], meanwhile to stabilise the active component against particle growth [57]. As indicated in Figure 2.2, the growth of small particles alone leads to a low active surface area, whereas application of the active component on a support can stabilise the active surface area.

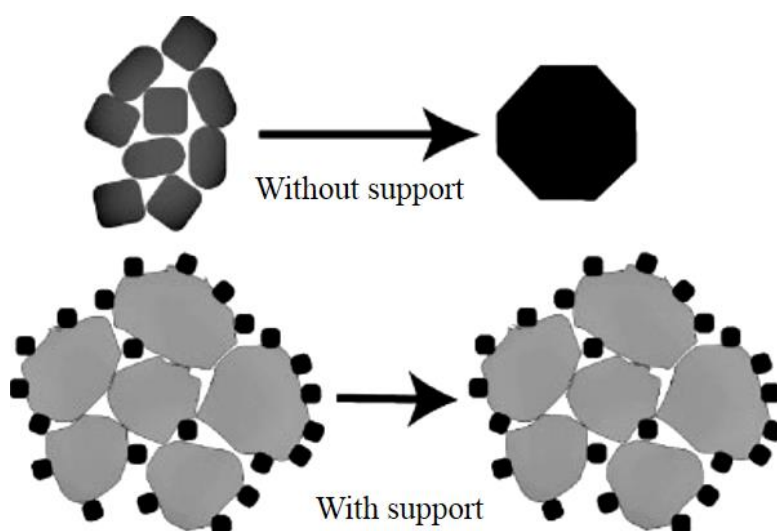


Figure 2.2 Top: Rapid growth of unsupported active particles. Bottom: Supported thermostable active material (Taken from Geus *et al.* [1]).

It is well known that the nature of the support (*e.g.* inertness, surface area, pore size distribution) influences the metal particle size, charge and morphology, forming specific active sites at the metal-support boundary [58]; ultimately this would result in differences in catalytic properties of the resulting metal particle. Therefore, in the development of a novel catalyst, much research and trials are required to find the most appropriate support.

2.2.2.1 Properties of Support Material

Materials suitable for the use as a catalyst support are usually solids with a high surface area [59]. The desirable physical and chemical characteristics to be considered in the choice of a support are listed in Table 2.2.

Table 2.2 Physical and chemical properties of supports [56].

Physical properties		Chemical properties	
i	mechanical strength	i	inert to undesired reactions
ii	optimised bulk density	ii	stable under reaction and regeneration conditions
iii	high active surface area	iii	high specific activity/selectivity
iv	optimised catalyst porosity	iv	stabilise the catalyst against sintering
v	optimised metal crystal and particle size	v	minimise catalyst poisoning

There are many types of catalyst support but the most frequently used support materials are alumina, silica, titania, magnesia, zeolites, silica-alumina and various forms of carbon (charcoal, activated carbon) [60]. Table 2.3 summarises some typical oxide and carbon supports and a comparison of their important properties.

Table 2.3 Properties of typical catalyst supports [3].

Support	Crystallographic phases	Properties	Applications
Al ₂ O ₃	mostly α - and γ -Al ₂ O ₃	SA up to 400 m ² .g ⁻¹ thermally stable	catalyst for three-way converters; steam reforming
SiO ₂	amorphous	SA up to 1000 m ² .g ⁻¹ thermally stable	hydrogenation and other
TiO ₂	anatase, rutile	SA up to 150 m ² .g ⁻¹ limited thermal stability	selective catalytic reduction
MgO	fcc	SA up to 200 m ² .g ⁻¹	steam reforming
Zeolites	faujasites, ZSM-5	Highly defined pore system shape selective	bifunctional catalysts
Silica-alumina	amorphous	SA up to 800 m ² .g ⁻¹ medium strong acid sites	dehydrogenation; bifunctional catalysts
Carbon	charcoal, activated carbon	SA up to 1000 m ² .g ⁻¹ unstable in oxide environment	hydrogenation

α -Al₂O₃: polymorphic phase; γ -Al₂O₃: cubic lattice; fcc: face-centred cubic structure; ZSM: Zeolite Socony Mobil-5; SA: surface area, m².g⁻¹.

In addition, support materials can be obtained in a variety of forms [56], such as spheres, granules, extrudates, cylinders and powders, the selection of which depends on the nature of the reaction and on the type of applied reactor [3].

2.2.2.2 Functions of Catalyst Support

The support material may or may not take part in the catalytic reaction. In some cases the support may actively interfere with or promote the catalytic process, *e.g.* zeolites and silica-alumina supported bifunctional catalysts [1,3,60]. Other than playing a direct role in the catalysis, the support is more often considered to be more or less catalytically inert [3], simply maintaining a high surface area to disperse small quantities of active valuable metals. For example, in catalytic converters, a ceramic honeycomb acts as a high surface area support for the catalyst such as Pt, Rh and Pd for changing pollution gases from the engine to environmentally acceptable emissions [61]. The stabilisation of the active metal NPs on the surface is achieved *via* favourable metal-support interactions (MSI). The metal-support interactions (MSI) may influence the electronic properties of the active phase particles relative to the bulk metal and are responsible for the dispersion and size of the particles [3], eventually revealing the individual catalytic performance in the chemical reactions.

Nohair *et al.* [62] used various oxide supports (SiO_2 , $\alpha\text{-Al}_2\text{O}_3$, $\gamma\text{-Al}_2\text{O}_3$, TiO_2 , MgO , ZnO , CeO_2 , CeZrO_2) to deposit 0.3 wt% palladium ($\text{Pd}_{0.3}$) and found the mean Pd particle sizes ranged from 1.3~3.6 nm; meanwhile they observed the $\text{Pd}_{0.3}/\text{SiO}_2$ (mean particle size of 1.7 nm) tended to be more active in sunflower oil hydrogenation than the $\text{Pd}_{0.3}$ catalysts supported on MgO , ZnO , CeO_2 , and CeZrO_2 (mean particle sizes of 2.4 nm, 3.5 nm, 3.6 nm, and 3.2 nm respectively) while slightly less active than $\text{Pd}_{0.3}$ catalysts supported on the two aluminas (mean particle sizes of 1.6 nm using $\alpha\text{-Al}_2\text{O}_3$, and 1.3 nm using $\gamma\text{-Al}_2\text{O}_3$ respectively). Similarly, Fernandez *et al.* [63] prepared Pd catalysts for the hydrogenation of

sunflower oil using 4 different supports (α -Al₂O₃, γ -Al₂O₃, ZSM-5 and MCM-22) and reported a metal loading in the range 0.7~1 wt% giving a main Pd particle size of 1.9~4.5 nm. With similar metallic particle sizes of 4 nm, the MCM-22 supported catalyst was slightly more active than α -Al₂O₃, γ -Al₂O₃ and ZSM-5 supported ones. Also, they found the particle size distribution was broader for Pd/ α -Al₂O₃ catalyst than that for Pd/ γ -Al₂O₃. The Pd/ γ -Al₂O₃ catalyst using Pd(C₅H₇O₂)₂ as palladium precursor, with a metal loading of 0.78 wt% and a 60% dispersion (~2.9 nm), showed a specific activity higher than the other Pd catalysts in the hydrogenation of sunflower oil under the same reaction conditions. It is apparent that the nature of the support materials played an important role, and the smaller active particles (*i.e.* higher surface area) deliver better catalytic activities.

Moreover, the nature of the support could also affect the product selectivity. Palladium supported on mesoporous silica was reported to give higher reaction rates but lower selectivity to *cis*-alkene than that supported on amorphous silica in the liquid-phase hydrogenation of phenyl alkyl acetylenic compounds [64]. More recently Enache *et al.* [65] investigated the effect of inorganic supports for bimetallic AuPd catalysts in liquid phase benzyl alcohol oxidation, in which they suggested that the more acidic nature of the Al₂O₃ and Fe₂O₃ supports led to enhanced ester formation as compared with TiO₂. Additionally, the heterogeneous catalyst has the complexity that active sites could be associated with just the exposed metal sites or the metal sites adjacent to the support [66], *i.e.* at the periphery of the nanoparticles. The detailed surface chemistry of the Pd NPs can influence the selectivity observed in the reactions, for example the number of edge or corner atoms, and defects in the Pd crystal structure [67] and the relative surface concentrations of the precursors [66].

Some other research suggested that carbons (charcoal, activated carbon) are potential highly effective supports since they possess outstanding surface areas of 800~1200 m².g⁻¹ [3,68] due to a considerable number of pores, superior to most of the oxide supports (Table 2.3).

Palladium catalysts supported upon activated carbon have played an important part in low pressure liquid phase hydrogenation reactions in the pharmaceutical industry to produce vitamins, cortisone and dihydrostreptomycin among other products [36]. Pd/C was found to adsorb less hydrocarbon/coke than Pd/Al₂O₃ during an alkyne hydrogenation reaction [69]. A carbon support offers many other advantages such as stability in both acidic and basic environments [70,71]; moreover it can be simply burnt off when the catalyst becomes deactivated to easily recover the precious metals [71]. Unlike metal oxides, carbon supports are electronically inert but extremely conductive to provide a means for conduction of the electrons for the electrocatalytic reactions in fuel cells; however the detachment and agglomeration of active metal particles (*e.g.* Pt) caused by carbon corrosion remains a problem [72].

The effect of the support material on catalytic activity and selectivity of a metal can be significant and complex. Careful control of the dispersion of precious metal as stable active particles needs to be performed in order to maximise the utilisation of active metal. On the other hand, the broad application of supported catalysts in industrial catalysis has led to the development of numerous preparation methods applicable on a technical scale.

2.2.3 Methods of Catalyst Manufacture

A variety of techniques have been established to deposit an active species onto to a support material, such as ion exchange, impregnation, anchoring, grafting, deposition-precipitation [57] and recent applications of novel nanotechnology [15]. In the following sections, only the most common preparation methods and recently developed novel nanotechnology for supported active nanoparticles will be considered.

2.2.3.1 Conventional Catalyst Preparation

There are two main steps in conventional catalyst preparation, namely depositing the precursor in a divided form upon the support and transforming it into the required active component(s) [57]. Ion exchange and impregnation are the two most frequently employed methods [57,73] to deposit the active component, particularly for preparing catalysts consisting of one or several precious metal(s) at small loading [1]. When several active components are required, *e.g.* supported bimetallic catalysts, they can be deposited consecutively or simultaneously [57].

Deposition of Active Component

i) Ion Exchange

Ion exchange is an operation which consists of replacing an ion in an electrostatic interaction with the surface of a support by another ion species [57]. The support containing ion *A* is plunged into an excess volume (much larger than the pore volume) of a solution containing ionic form of the active metal *B*. Ion *B* gradually penetrates into the pore space of the support and takes the place of ion *A*, which passes into the solution, until an equilibrium is established corresponding to a given distribution of the two ions between the solid and the solution. The solid is then washed, and finally separated by filtration or centrifugation. This technique is usually influenced by the number of available adsorption sites on the support, the concentration of ions, the pH and the adsorption strength [74]. This process is very effective with the use of zeolites, such as ZSM-5 or Y-type faujasite since they are known to exchange ions efficiently; however often only low loadings can be achieved.

ii) Impregnation

The impregnation technique is to fill the pores of the support with a solution of the catalyst precursor, *e.g.* a metal salt of sufficient concentration to achieve the desired loading [3,60].

By this technique, the whole precursor is expected to be retained on the support since no intermediate washing step is involved [57], thus there is no risk of loss of active precursor through the washing step [1] and no waste water is produced. With precious metals, for example noble metals on activated carbon, impregnation is therefore the procedure of choice since it eliminates waste [3].

Impregnation is usually followed by drying, the rate of which needs to be carefully controlled depending on the desired distribution, as some redistribution of the active species can occur as the liquid fronts move within the pore structure and create concentration gradients [56]. Reasonable results can be achieved with a powdered, finely divided support that is continuously and intensively kneaded during evaporation of the liquid, but the distribution of the active component in the dried support is generally not homogeneous [1,56]. Similar to the ion exchange technique, high loadings can often not be achieved by pore-volume impregnation, as the required amount of active precursor cannot be dissolved in a liquid volume equal to the pore-volume of the support [1].

Formation of the Final Catalysts

The catalyst activation is defined as the transformation of a solid precursor to the material immediately active for the desired reaction [75] which, depending on the reaction to be catalysed, can be found in the ionic, oxidic, sulfided, or metallic state [57]. This process is crucial for catalyst activity, product selectivity, catalyst life and its resistance to deactivation [76]. A typical procedure is the transformation of hydroxides to oxides by calcination followed by the reduction of metal oxides to dispersed metal particles.

i) Calcination

After active metal deposition, the catalysts are calcined to convert the salts and hydroxides to oxides. The temperature of calcination should not substantially exceed the reduction

temperature used to activate the catalyst [56]. Typically the higher the calcination temperature used in preparation, the more difficult it will be to activate the catalyst by reduction. The calcination step plays an important role in the case of oxides used as catalysts and supports, *e.g.* Al_2O_3 , TiO_2 , silica-alumina, and many other oxides or mixed oxides [76].

The group of Hutchings [7,77,78] reported the effect of calcination on the stability and reactivity of supported AuPd catalysts. The non-calcined materials, both of $\text{AuPd}/\text{Al}_2\text{O}_3$ and AuPd/TiO_2 catalysts, were highly unstable due to loss of metals during use. In contrast, catalysts that were pre-calcined at 400 °C prior to use were very stable and did not leach any Au or Pd into solution. The use of lower temperatures than 400 °C, even for a longer time, led to catalysts that leach Au and Pd on use. It was suggested that the chemical composition of metal particles in those catalysts was strongly influenced by the heat treatment process used; both of the calcined and non-calcined catalysts contained small Pd particles, however only the non-calcined sample exhibited any pure Au particles [78]. Furthermore, Edwards *et al.* [78] noticed the presence of a very few large (~70 nm) metal particles in the non-calcined sample, suggesting that either these large particles were a direct byproduct of the impregnation synthesis process or they formed over time even in the absence of elevated-temperature calcination. For catalytic activity, catalysts that were calcined (400 °C) were significantly less active than non-calcined catalysts in the direct synthesis of H_2O_2 .

ii) Reduction

In the majority of cases, the final step in the preparation of catalytically active metal is the reduction of its oxide forms [76]. This activation procedure usually takes place under a reducing gas (*e.g.* hydrogen), which can be either part of the manufacturing process or employed as catalyst pre-activation before use. For example the AuPd/TiO_2 catalyst for alcohol oxidations [79], became oxidised after a long term in storage. Hence the catalyst needs to be reactivated before use by reduction, *i.e.* passing hydrogen over the AuPd/TiO_2

catalyst sample with careful control of the temperature, to regenerate the reduced active component.

To give better control of the final active form, the operating temperature of this process is crucial and the presence of water seems always to be detrimental [80,81]. In general a higher temperature always brings about a higher degree of reduction [76], but this is always accompanied by a loss in dispersion of the metal. Extremely high temperatures may lead to the overgrowth of the particles due to the so-called strong metal-support interactions (SMSI) effect [82], or alloying of the active metal with some reduced metallic element of the support, for example nickel with silicon [83,84].

There are also many other conventional catalyst preparation processes such as deposition-precipitation [1], or a more recent study on the use of colloidal methods [85]. The careful control of metal deposition on the support by conventional methods is generally achieved by adjusting the quantity of support, pH, time of crystallisation, calcination procedure and concentrations of metal ions in solutions [73]. In modern heterogeneous catalysis, the overwhelming applications of active metal nanoparticles require reliable preparations of the nanomaterials, which remains an area of active research.

2.2.3.2 Nanotechnology for Palladium Nanoparticles

As the intrinsic properties of the metal nanoparticles (NPs) are mainly determined by their size, shape, composition and crystallinity [86,87], the preparation of metal NPs with well-controlled particle sizes and shapes [88,89] of a high monodispersity is a key technology. The formation of active metal NPs can be achieved *via* various synthetic strategies, of which the general routes are based on chemical or electrochemical reduction or thermal decomposition of precursors of the active components [15,16]. Appropriate reducing agents (*e.g.* H₂O₂ and NaBH₄) are required to reduce metal salts into their zero-valent metallic form while

stabilisers (*e.g.* organic ligands, surfactants, polymers and dendrimers) are required to prevent the particles from aggregating [15].

Yu *et al.* [90] prepared a series of palladium colloids using H_2PdCl_4 as the precursor and polyvinylpyrrolidone (PVP) as the stabiliser at room temperature, at different pH conditions by the addition of NaOH into the mixture. The average diameter of Pd colloids was found to decrease with increasing pH. It was suggested that adding a suitable amount of base (molar ratio of NaOH to metal: 6~8) promoted the reduction rate, leading to smaller particle size formation (~1.9 nm). Berger *et al.* [91] also synthesised Pd NPs by a polyol-based method at 140 °C, using different palladium precursors (PdCl_2 and K_2PdCl_4) and stabilisers (PVP: polyvinylpyrrolidone and CTAB: cetyl trimethyl ammonium bromide). Pd NPs synthesised from PdCl_2 in the presence of PVP by a reduction reaction with ethylene glycol in an argon atmosphere had a spherical shape and 7.5 nm average size with a size distribution in the range of 5~10 nm. By using a mixture of PVP and CTAB, Pd NPs synthesised from K_2PdCl_4 resulted in polyhedral shapes with an average size of 8.4 nm (for those obtained in air), and 6.3 nm (for those synthesised in an argon atmosphere), respectively.

Seed-mediated growth method is another popular synthetic strategy since it can take place at room temperature in the presence of air and water. Many noble metal NPs in the form of spheres [92,93], cubes [94], rods [95-97], plates [98,99] and even core/shell nanostructures [100,101] have been successfully synthesised using this method. Chen *et al.* [45] reported a seed-mediated growth route to the synthesis of Pd NPs from H_2PdCl_4 as the precursor, while a colloidal gold (~3 nm) solution needed to be pre-prepared as the seed solution. The synthesised Pd NPs were polyhedral in shape maintaining a uniform distribution with sizes from 33 nm to 110 nm depending on the amount of gold seeds.

It appears that the size and morphology of Pd NPs strongly depends on the reaction conditions like pH, temperature, and the type of metallic precursor and stabiliser. Preparation

of the stabilisers can be complicated, as in the case of complex ligand synthesis, which requires specialist equipment or the use of an inert atmosphere [24]. In addition, these synthetic strategies require the use a series of reductants, which are usually toxic and expensive chemical agents [102]. Overall, the current preparation of supported metal NPs involves rigorous experimental procedure, extreme conditions, or expensive equipment, or all three [17-19].

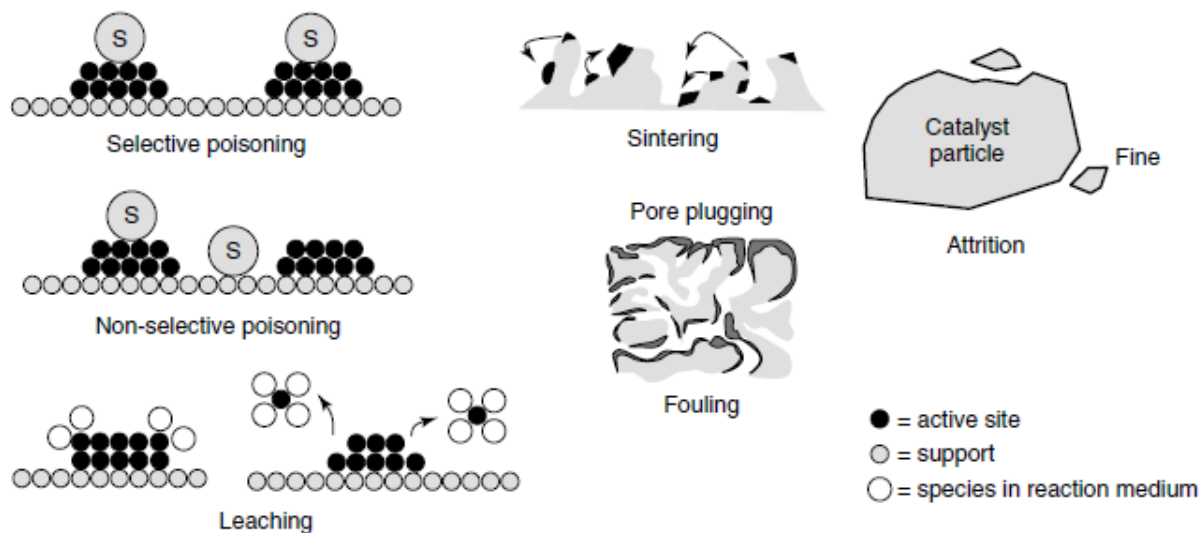
2.2.4 Catalyst Deactivation

Another major challenge of using platinum group metal (PGM)-based catalysts, Pt and Pd in particular, is that they can deactivate quickly under certain reaction conditions [103]. Catalyst deactivation is a problem of great technical, economic and ecological concern in industrial chemical processes [104-107]; for PGM-based catalysts this is a major reason that limits their applications in the fine chemicals industry [108]. Therefore, in most academic laboratories involved in heterogeneous catalysis, mastering catalyst stability has now become nearly as important as controlling activity and selectivity. In practice, it is inevitable that all the catalysts undergo mechanical, physical and/or chemical deactivation with, as a consequence, a loss in both activity and (but not always) a decrease in selectivity to the desired product [109]. Depending on the commercial process (reactors or reaction conditions such as temperature, pressure and reactant composition), deactivation can be rapid or slow [105,107]. It is therefore very important to understand the causes and mechanisms of catalyst deactivation to aid the development, design and operation of commercial processes.

The causes of deactivation of solid catalysts and their mechanisms were reviewed in recent papers by Moulijn *et al.* [105] and Bartholomew [107], based on which the five major types of causes of deactivation are listed in Table 2.4. It appears that with most of them (except type 4), chemical steps play a major role. A schematic representation of the deactivation phenomena inside a catalyst particle taken from Moulijn *et al.* [105] is shown in Figure 2.3.

Table 2.4 Summary of origin, mechanism and typical examples of catalyst deactivation [105,107,109].

Type	Origin	Mechanism	Examples
1	Chemical poisoning	Strong chemisorption of species on catalytic sites which block sites for catalytic reaction. Reversible or irreversible.	<i>Metals:</i> S compounds, CO, polyaromatics, coke <i>Acid oxides:</i> bases, polyaromatics
2	Fouling/coking	Physical deposition of species from fluid phase onto catalytic surface and in catalyst pores, by simple deposition (fouling) or by catalytic or thermal transformation of feed components (coking). Only reversible by oxidative regeneration.	<i>Metals:</i> coke (e.g. Pt), carbon (e.g. Ni) <i>Acid oxides:</i> deposit of heavy feed components, catalytic or thermal coke
3	Thermal degradation	Thermally induced loss of catalytic surface area, support area and active phase support. Irreversible.	<i>Metals:</i> sintering <i>Acid oxides:</i> e.g. dealumination then collapse of the zeolite framework under hydrothermal conditions
4	Mechanical damage	Loss of catalytic material due to abrasion, loss of internal surface area due to mechanical induced crushing of catalyst particle. Irreversible.	Fracture, erosion, e.g. in fluidised beds i) from collisions of particles with each other or with reactor walls ii) or due to high fluid velocities
5	Leaching	Leaching of active species, e.g. by dissolution in reaction medium. Most common in liquid phase synthesis of fine chemicals. Often reversible	Dissolution of metal framework (e.g. Cr in CrS-1) component of metallosilicate molecular sieves

Figure 2.3 Major types of deactivation in heterogeneous catalysis (Taken from Moulijn *et al.* [105]).

The purpose of this general review, which is essentially based on some review papers [104-107,109], is to selectively present the possible causes of supported palladium NPs deactivation (*i.e.* Type 1, 3 and 5 in Table 2.4) that would most likely occur in this study and

the means which are used to prevent, limit and cure this deactivation. To illustrate this presentation, examples will be chosen, if feasible, in the field of PGM-based or, more closely, Pd-based catalytic processes.

2.2.4.1 Chemical Poisoning

Poisoning of a catalyst is caused by the strong chemisorption of reactants, products or impurities on catalytic active sites [105,107,109]. Mechanisms by which a strongly adsorbed poison may affect catalytic activity involves some or all of the following [107]: i) physically blocking adsorption/reaction sites; ii) electronically modifying the surface atoms; iii) restructuring the catalyst surface; iv) blocking access of adsorbed reactants to each other; and v) preventing or slowing the surface diffusion of adsorbed reactants. Depending upon the strength of poison adsorption, poisoning may be reversible or irreversible. If the chemisorption is weak, reactivation may occur; if it is strong, deactivation results.

Bartholomew [107] (Table 2.5) listed a number of common poisons for selected catalysts in important representative reactions. It is apparent that PGM metals (*e.g.* Pd and Pt), very relevant to this work, may be widely affected by a broad range of poisons in both hydrogenation and oxidation processes.

Reaction rate profiles for oxidation over PGM-based catalysts are surprisingly given the problem of catalyst deactivation [103] which makes their application in oxidations being relatively rare in comparison with their widespread application in hydrogenations. It was found that the deactivation of Pt and Pd catalysts in liquid phase oxidation can be caused by over-oxidation of the metal to form oxides on the surface due to strongly adsorbed oxygen [103,108,110,111], in other words, the oxygen that is essential for the reaction is also responsible for deactivation of the catalyst. Grunwaldt *et al.* [112] studied the formation of surface PdO by measuring the Pd-O distance using Extended X-Ray Absorption Fine

Structure (EXAFS) which revealed that Pd was oxidised on a Pd/Al₂O₃ catalyst used for cinnamyl alcohol oxidation in organic solvent at 65 °C. A similar result was reported by Keresszegi *et al.* [113] using the same technique for Pd/Al₂O₃ during 1-phenylethanol oxidation at 55~80 °C and 1 bar (air) in a continuous-flow fixed-bed reactor. Gogova *et al.* [114] reported that deactivation by over-oxidation was reversible for Pd/C catalyst in glucose oxidation in a continuous stirred-tank reactor (CSTR) by replacing dioxygen with dinitrogen for a short amount of time at 30 °C and atmospheric pressure, during which the metal oxide surface was thought to be re-reduced *in situ* by the alcohol groups of glucose.

Table 2.5 Poisons for selected catalysts in important representative reactions [107].

Catalyst	Reaction	Poisons
Silica-alumina, zeolites	Cracking	Organic bases, hydrocarbons heavy metals
Nickel, platinum, palladium	Hydrogenation dehydrogenation	Compounds of S, P, As, Zn, Hg, halides, Pb, NH ₃ , C ₂ H ₂
Nickel	Steam reforming of methane, naphtha	H ₂ S, As
Iron, ruthenium	Ammonia synthesis	O ₂ , H ₂ O, CO, S, C ₂ H ₂ , H ₂ O
Cobalt, and iron	Fischer-Tropsch synthesis	H ₂ S, CO, S, As, NH ₃ , metal carbonyls
Noble metals on zeolites	Hydrocracking	NH ₃ , S, Se, Te, P
Silver	Ethylene oxidation to ethylene oxide	C ₂ H ₂
Vanadium oxide	Oxidation selective catalytic reduction	As, Fe, K, Na from fly ash
Platinum, palladium	Oxidation of CO and hydrocarbons	O ₂ , Pb, P, Zn, SO ₂ , Fe
Cobalt and molybdenum sulfides	Hydrotreating of residue	Asphaltenes, N compounds, Ni, V

It was suggested that [70,103,113,115-119] adjusting the reaction conditions (*e.g.* by using compressed air or low oxygen partial pressure) could protect the catalyst from being deactivated. The presence of inert gas, such as nitrogen, could have an effect on the hydrodynamics and decrease the gas holdup of the reactant gas [120], as a result oxygen dissolved in the reactant mixture would be totally consumed. It is worth noting that the ability

to perform oxidation reactions in air (as an inexpensive and environmentally acceptable reagent) without strong oxidising agents, could be attractive for future green industrial applications. On the other hand, alloying materials to create bimetallic catalysts can also be used to increase the stability and thus longevity of heterogeneous catalysts [70,103,121]. For instance, the synthesis of bimetallic catalysts for benzyl alcohol oxidation is focused on AuPt and AuPd catalysts [103], which is detailed in §2.2.5.2.

2.2.4.2 Thermal Degradation

One typical process of catalyst deactivation which belongs to the category of thermal degradations is high-temperature-induced sintering. The activity losses result from [107]: i) loss of catalytic surface area due to crystallite growth of the catalytic phase; ii) loss of support area due to support collapse; and iii) loss of catalytic surface area due to pore collapse on crystallites of the active phase. Sintering is strongly dependent on the temperature and atmosphere [105]: the rate of sintering increases with increasing temperature, the presence of oxygen or steam can accelerate the process while under hydrogen the rate is relatively slow.

The metal crystallite growth on a support can go *via* three principal mechanisms [107]: i) crystallite migration, ii) atomic migration, and iii) (at very high temperatures) vapour transport. The last type of mechanism is least likely to occur in this study since low temperatures (50~160 °C) were used in most cases. A conceptual model of the first two types is illustrated in Figure 2.4. Thermal degradation can occur in all stages of the life cycle of the catalyst. It might occur due to local heating during preparation (calcination), reduction (fresh or passivated catalyst), reaction (hot spots, maldistribution) or regeneration (coke burn-off) [105].

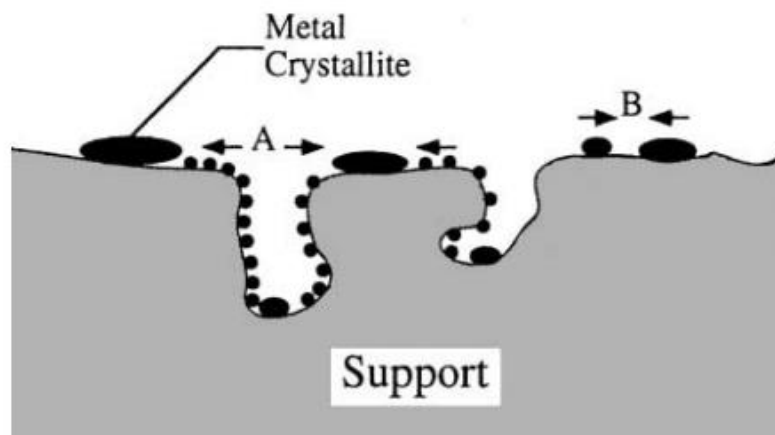


Figure 2.4 Two conceptual models for crystallite growth due to sintering by (A) atomic migration (B) crystallite migration (Taken from Bartholomew [107])

Herzing *et al.* [122] synthesised a series of AuPd/ Al_2O_3 catalysts by impregnation and the catalysts were subjected to a variety of heat treatments from 200 °C to 400 °C. It was observed that the nature and size distribution of the AuPd particles was highly dependent upon both the heat treatment temperature and the atmosphere. ‘As-synthesised’ particles were homogeneous alloys, but subsequent calcination in air produced metal particles which showed a progressive enrichment of Pd at their surface. The change from homogeneous alloy to Pd(rich shell)-Au(rich core) morphology and increase in average particle size induced by the calcination treatment was accompanied by a significant decrease in the activity of the catalyst.

Sintering is irreversible or difficult to reverse [107], which is slow at moderate reaction temperatures. The key to prevent sintering processes is to maximise catalytic activity enough to enable operation at temperatures low enough that sintering rates are negligible [123].

2.2.4.3 Leaching

Leaching, which occurs essentially during the liquid-phase synthesis of functionalised organic molecules, results from the presence in the reaction medium of highly polar species, often bearing complexing and/or solvolytic moieties which favour the dissolution of the

active components of the catalyst (this is typically the case with metal sites) [109]. With precious metal catalysts it is essential that the metals are not lost from the catalyst during use. However, typical noble metal catalysts are known to have leaching rates of 5~10% per year or higher, which represents a substantial economic burden on any catalytic process [105]. A very typical example is heterogeneous catalytic hydrogenation of unsaturated oil in food processing, in which nickel is the catalyst of choice, but traces of nickel appear in the product. Leaching of palladium is much slower, which might be a good reason to replace nickel with palladium, although being more expensive for the latter [105].

The support material itself may also be subjected to leaching if the reaction medium is corrosive. For instance, corrosion and leaching of alumina will occur at both high ($\text{pH} > 12$) or low pH ($\text{pH} < 3$) [105]. Therefore, for reactions carried out at high or low pH , carbon should be considered as the catalyst support, not alumina.

Leaching causes not only the loss of catalyst activity of the solid catalysts, but also the loss of the active metal to the product phase which results in contamination of the product [24,105], from which the dissolved metal may lead to the formation of an active homogeneous catalyst [7]. Leaching can be minimised by the addition of sophisticated ligands to the surface of the support but this makes the catalyst immobilisation procedure more time-consuming and expensive [124]. Alternatively, the addition of a second metal component as the metal promoter has received substantial research interest. Alloying two metals for alcohol oxidation catalysts has been shown to inhibit the leaching of active component from the support or to prevent catalyst deactivation [125], for example the alloying of Pd and Au to prevent the leaching of Pd from the catalyst support [126].

In summary, supported palladium is a promising heterogeneous catalyst, but the drawback of utilising palladium individually is that frequently poor selectivity and deactivation are often observed [111]. The main challenges of the application of PGM-based catalysts are to

improve the selectivity and stability of the catalyst without deactivating the catalyst. Extensive research has therefore investigated ways to improve their resistance to deactivation. One way of achieving this goal is with the help of promoters, which can prevent the PGM-based catalysts from over-oxidation and leaching.

2.2.5 Promoter

Since heterogeneous catalysts have been used industrially, commercial catalysts tend to involve multiple promoters to enhance the activity, selectivity, lifetime and structural integrity of the catalyst [127]. The promotion in heterogeneous catalysis by adding another metal atom results from a number of effects [127,128]: i) by geometric modifications between the metal components to selectively block specific surface sites; ii) by electronic effects (caused by intra-atomic bond length or lattice constants changes) which aid the adsorption, dissociation, and desorption processes on a metal catalyst surface; and iii) by elimination of non-desired gas phase reactions. Ultimately the formed bimetallic surface could exhibit chemical and catalytic properties that are very different from those of the surfaces of the individual metals [129,130], which is why many bimetallic catalysts have been studied [131,132]. However, the overall catalytic activity of the resulting bimetallic catalyst not only depends on the matching of geometric and electronic modifications occurring in metal particles but also on the support, the substrate and the specific reaction conditions [71]. Synergistic effects normally describe the enhanced activity and selectivity of the promoted catalyst as the results of a complex synergy of all the effects involved.

In the case of palladium, a wide range of metals have been used as promoting elements. For example, the combination of chemically produced Pd and Fe is a very well-documented bimetallic catalyst for reduction reactions [133,134]. Other transition metals like Cu, Ni, and Ag have also been used as promoting elements for Pd catalysts [135-137]. Recently, the combination of Pd and Au has become widely applied for oxidation reactions [7], which is

relevant to this study. In this section, the discovery of gold in heterogeneous catalysis and the addition of gold upon the supported palladium catalyst, forming an AuPd bimetallic surface, are considered and described.

2.2.5.1 Discovery of Gold in Catalysis

Gold (Au), with an atomic number of 79 on the periodic table, is a very stable transition metal. Bulk gold is an immutable, ductile metal hardly tarnishing in air or water and thus is prized for its great beauty and value in coinage, jewellery, and other arts rather than for the depth of its chemistry [7].

For many years researchers had tried to use Au as a catalyst but it was found to be relatively inactive, which often related to its large particle size [71]. However, when prepared in nanocrystalline form, as a collection of a few hundreds of atoms, it displays remarkable activity as a heterogeneous catalyst for a broad range of redox reactions [7,77]. Bond and co-workers [138] showed that nanocrystalline Au could be effective for the hydrogenation of dienes, however Au was not shown to be more effective than well dispersed Pd or Pt and, as these catalysts were well established, Au was not viewed as a viable alternative. Subsequently, Haruta [139,140] made the unexpected discovery that Au nanoparticles (NPs) could act as effective catalysts for the oxidation of CO at temperatures as low as $-76\text{ }^{\circ}\text{C}$. In the 1980s Hutchings [141] demonstrated that cationic Au had outstanding catalytic properties in acetylene hydrochlorination. These two key discoveries have led to a burgeoning interest in gold catalysis. In recent years, highly dispersed supported Au NPs have been found to be active for a range of reactions [142], including the preferential oxidation of CO in the presence of H_2 , CO_2 and H_2O for fuel cell applications [143], the oxidation of alcohols [144], the epoxidation of alkenes [145-148] as well as the hydrogenation of unsaturated aldehydes [149], the hydrogenation of alkynes in the presence of alkenes [150], the hydrosilylation of alcohols and aldehydes [151] and the hydrogenation of N-O bonds [152].

Of particular note relevant to this study is the ability of Au, when alloyed with Pd NPs forming mixed ensembles of reactive sites at the alloy surface on the catalyst support, to catalyse selective oxidation reactions, *e.g.* aerobic oxidation of an alcohol to an aldehyde under solvent-free conditions [65] in which Pt and Pd catalysts suffer deactivation caused by over-oxidation of the metal to form oxides on the surface (discussed in §2.2.4.1).

2.2.5.2 Supported AuPd Bimetallic Catalyst

The combination of Au and Pd in an alloy nanoparticle configuration (or chemical ordering) has now been demonstrated on many supports such as CeO₂ [153], carbon [71,125,154], Al₂O₃ [155,156], Fe₂O₃ [157,158], SiO₂ [159] and TiO₂ [65,66,78] as well as bacterial biomass [160,161] (to be introduced in §2.3.3). Various configurations of the bimetallic particles were obtained depending on the preparation conditions. The mechanism behind the formation of specific bimetallic ensembles is not well-understood yet. Some theoretical studies suggest the Au(shell)-Pd(core) segregation is energetically favoured due to the slightly higher cohesive energy of Pd and the lower surface energy of Au [162,163]. However some experimental research obtained inverted Au(core)-Pd(shell) structures [65,157,161]. Deplanche *et al.* [161] suggested that pre-formed Pd(0) atoms or clusters have a reduction effect on Au(III) to generate Pd(II) ions which then relocate around Au(0) NPs and are reduced to Pd(0) *via* H₂ on the surface of Au NPs. Other experimental studies have reported that AuPd mixed configurations [66,160] can also be formed. Table 2.6 summarises the AuPd particles have been synthesised by various methods.

Table 2.6 Summary of supported AuPd bimetallic catalysts using different preparation methods.

Loading, wt%		Support	Precursor	Stabiliser and reductant	Preparation method	Compositions of the metal particles and particle size	Reference
Au	Pd						
0.2	1.0	CeO ₂	HAuCl ₄ ·4H ₂ O aqueous solution Pd(II) acetate acetone solution	NA	Surface redox reaction between the Ce(III) oxide support and noble metal ions (protected under N ₂) under sonication in an ultrasonic water bath	CeO ₂ support: nanorods with 10~20 nm in diameter and 50~300 nm in length AuPd particles: nanoparticles with size ~2.6 nm, may be the mixture of Au and Pd atoms	Zhang <i>et al.</i> [153]
0.63	0.65	SiO ₂	HAuCl ₄ ·3H ₂ O aqueous solution Ethanol solution of PdCl ₂	PVP	Simultaneous reduction of Pd and Au precursors by ethanol in the presence of the polymer Calcination in air at 673K	3.5 nm for the non-calcined sample 6.2 nm for the sample after calcination, both PdO and AuPd alloys are present	Venezia <i>et al.</i> [159]
0.73	0.27	Activated carbon	NaAuCl ₄ ·2H ₂ O aqueous solution Na ₂ PdCl ₄ aqueous solution	PVA NaBH ₄	Sol-immobilisation technique, sequential deposition of Au sol and Pd sol	Alloyed phases of a single composition Average size of 3.4 nm	Dimitratos <i>et al.</i> [125] Prati <i>et al.</i> [71]
0.5	0.5	Carbon	PdCl ₂ aqueous solution HAuCl ₄ ·3H ₂ O aqueous solution	NA	Simultaneous impregnation method Calcination in static air at 673K	AuPd alloy nanoparticles Average size of ~6 nm with a broad range between 2 and 14 nm	Lopez-Sanchez <i>et al.</i> [154]
				PVA NaBH ₄	Sol-immobilisation technique, simultaneous deposition of mixture of the two metal sols	AuPd alloy nanoparticles with a narrower particle size range between 4 and 7 nm	
2.5	2.5	Fe ₂ O ₃	PdCl ₂ aqueous solution HAuCl ₄ ·3H ₂ O aqueous solution	NA	Simultaneous impregnation <i>via</i> an incipient wetness method Calcination in static air at 673K	Au(rich core)-Pd(rich shell) metal alloy A bimodal metal particle size distribution: smaller particles in range of 4~10 nm larger particles in range of 30~70 nm	Edwards <i>et al.</i> [157]
5.9	3.2	γ-Fe ₂ O ₃	HAuCl ₄ aqueous solution Na ₂ PdCl ₄ aqueous solution	PEGMs 2-propanol	Sonochemical method	Au(core)-Pd(shell) structure Average particle size of 8.3 nm	Nitani <i>et al.</i> [158]

Table 9.6 *continued.*

Loading, wt%		Support	Precursor	Stabiliser and reductant	Preparation method	Compositions of the metal particles and particle size	Reference
Au	Pd						
2.5	2.5	γ -Al ₂ O ₃	Pd(NO ₃) ₂ ·6H ₂ O aqueous solution AuCl ₄ ·3H ₂ O aqueous solution	NA	Impregnation or co-precipitation Calcination in static air at 673K and reduction in flowing H ₂ at 673K	Metal nanoparticles present as AuPd alloys with a size range of 2~9 nm	Landon <i>et al.</i> [156]
1	1	γ -Al ₂ O ₃	solutions of H ₂ PdCl ₄ and HAuCl ₄	NA	Sequential impregnation of Au and Pd salt <i>via</i> an incipient wetness method	Au(core)-Pd(shell) configuration After calcination, the grain size of the Au increased from 5.5 to 8.4 nm	Nutt <i>et al.</i> [164]
2.5	2.5	γ -Al ₂ O ₃	HAuCl ₄ ·3H ₂ O aqueous solution PdCl ₂ aqueous solution	NA	Simultaneous impregnation Calcination in static air at 673K	Au(core)-Pd(shell) morphology Particles size in range of 2~10 nm	Solsona <i>et al.</i> [165]
2.5	2.5	TiO ₂	PdCl ₂ aqueous solution HAuCl ₄ ·3H ₂ O aqueous solution	NA	Simultaneous impregnation <i>via</i> an incipient wetness method Calcination in static air at 673K	Au(core)-Pd(shell) structure A bimodal metal particle size distribution: most of the particles in range of 1~8 nm while minority larger particles in range of 40~70 nm	Edwards <i>et al.</i> [78] Enache <i>et al.</i> [65] Miedziak <i>et al.</i> [85]
0.65	0.35	TiO ₂	PdCl ₂ aqueous solution HAuCl ₄ ·3H ₂ O aqueous solution	PVA NaBH ₄	Sol-immobilisation method	Homogeneous alloys Particle sizes in range of 1~11 nm with a mean diameter of 4 nm	Meenakshisundaram <i>et al.</i> [66] Miedziak <i>et al.</i> [85]
5	5	<i>Desulfovibrio desulfuricans</i>	Na ₂ PdCl ₄ aqueous solution HAuCl ₄ ·nH ₂ O aqueous solution	NA	A two-step microbial method combined with successive reduction of Pd and Au particles onto the biomass	Homogeneous mixing and complex segregations Particles sizes in range of 4~40 nm in diameter	Tran <i>et al.</i> [160]
5	5	<i>Escherichia coli</i>				Ordered Au(core)-Pd(shell) nanostructures	Deplanche <i>et al.</i> [161]

PVP: polyvinylpyrrolidone; PVA: polyvinylalcohol; PEGMs: polyethylene glycol monostearate; NA: not applicable.

In terms of the catalytic application in oxidation reactions by using gold to alloy with palladium, Au could act as a diluent to isolate Pd monomer sites (*i.e.* to reduce the oxygen coverage), thereby enhancing the durability of Pd catalyst (*i.e.* resistance to over-oxidation) [166,167]. It was suggested that the addition of Au to Pd decreased the binding energy of oxygen to the surface and drastically reduced the oxygen coverage, as found by thermal desorption spectroscopy (TDS) [168,169]. A range of supported AuPd NPs has been tested for the oxidation of benzyl alcohol [65,66,125,153,154,170] and a synergistic enhancement in the activity and selectivity has been suggested over both the Au- and Pd- only catalysts [65,125,170]. Thus there is a growing trend in the potential use of supported bimetallic AuPd NPs [71], of which the structure of bimetallic combinations is crucial in order to obtain the necessary synergistic interactions that lead to increases in catalytic activity. However most of the physico-chemical syntheses (Table 2.6) produce metal particles which can be relatively non-uniform and can show variations in morphology depending on the support and particle composition making any correlation difficult and often not reliable. Such irreproducibility limits commercial production and implementation.

2.3 Biomass-Supported Catalyst

A promising alternative for chemical synthesis is to exploit the bioreductive deposition of metals by bacteria, in which the sulphate-reducing bacterium (SRB) *Desulfovibrio desulfuricans* was the first reported species with Pd-reducing capacities [20]. When Pd(II) was added to a *D. desulfuricans* culture together with H₂ or formate as the electron donor, nanoscale deposits of Pd(0) were observed at the outer surface of the bacterial cells [20,171], which makes them available for applications as catalyst.

2.3.1 Chemical Components and Cellular Structures of Microbes

Bacterial cells, typically a few micrometres in length with a wide range of shapes ranging from spheres to rods and spirals, are composed of mainly polymeric organic materials and inorganic components in an organised configuration. Taking *Escherichia coli* as an example, the polymeric organic molecules comprise ~96% of the dry weight of the cell; small molecules and inorganic ions (Fe^{2+} , Mn^{2+} , Cu^{2+} , NH_4^+ , SO_4^{2-} , PO_4^{3-} etc.), which are constituents of the cytoplasm, comprise the remaining 4% [172]. There are four fundamental types of polymeric organic materials (made up of monomeric subunits) that occur in all forms of cells: polysaccharides are composed of carbohydrate (sugar) molecules; lipids are composed of fatty acids; proteins are composed of amino acid molecules; and nucleic acids (DNA and RNA) are made up of molecules called nucleotides. It is the arrangement or sequence in which the subunits are put together that often determines the exact properties that the polymeric organic materials will have. Some molecules can be substituted, for example glucose in the form of poly-n-acetyl glucosamine (NAG) is a key component of peptidoglycan found extensively at bacterial surfaces and the component which confers structural rigidity along with n-acetyl muramic acid (NAM), with chains of NAG and NAM forming a peptidoglycan network. Bacteria fall into two fundamental types, namely Gram-positive (+) and Gram-negative (-) types (Table 2.7), presenting major differences in cell envelope composition and structure (Figure 2.5).

The Gram-positive cell envelope comprises a cytoplasmic membrane and a very thick peptidoglycan layer (20~80 nm, embedded with teichoic acids and lipoteichoic acids). Gram-positive bacteria lack an outer membrane but adjacent to the thick peptidoglycan layer, are often found an attached outermost S-layer (depending on species, the S-layers have a thickness between 5 and 25 nm and possess identical pores with 2~8 nm in diameter [173]). In contrast, the Gram-negative bacteria possess a more complex double-membrane structure

(the cytoplasmic membrane and an outer membrane) separated by a periplasmic space, which contains a thinner peptidoglycan layer (2~3 nm, a single layer of peptidoglycan) and many proteins responsible for various biological activities (*e.g.* substrate binding or hydrolysis, reception of extracellular signals and hydrogenase in some species [30,174]). The outer membrane, composed of phospholipids and lipopolysaccharides (which face into the external environment) allows for transport of many ions across through the porins channels. For both Gram-positive and Gram-negative bacteria, particles of approximately 2 nm can pass through the peptidoglycan [175].

Table 2.7 Characters of some bacteria.

Species (Abbreviation)	Shape and size	Biology and biochemistry	Rationale
<i>Gram-negative (-)</i>			
<i>Rhodobacter sphaeroides (R. sphaeroides)</i>	rod-shaped	facultative anaerobe	purple non-sulfur bacteria, photosynthetic, metal resistant [176]
<i>Escherichia coli (E. coli)</i>	rod-shaped, 2.0~4.0 μm length	facultative anaerobe	purple sulfur bacteria, hydrogen producing through fermentation, metal-reducer, hydrogenase activity [177,178]
<i>Desulfovibrio desulfuricans (D. desulfuricans)</i>	rod-shaped, 3.0~5.0 μm length	obligate anaerobe	purple sulfate-reducing bacterium, metal-reducer, high hydrogenase activity [20,26]
<i>Gram-positive (+)</i>			
<i>Arthrobacter oxydans (A. oxydans)</i>	rod-shaped	obligate aerobe	metal resistant, accumulates metal
<i>Micrococcus luteus (M. luteus)</i>	spherical, 0.5~3.5 μm diameter	obligate aerobe	metal-reducer, accumulates high amounts of metals
<i>Bacillus shaericus (B. sphaericus)</i>	rod-shaped	obligate aerobe	shown to make pd(0) nanoparticles [30]

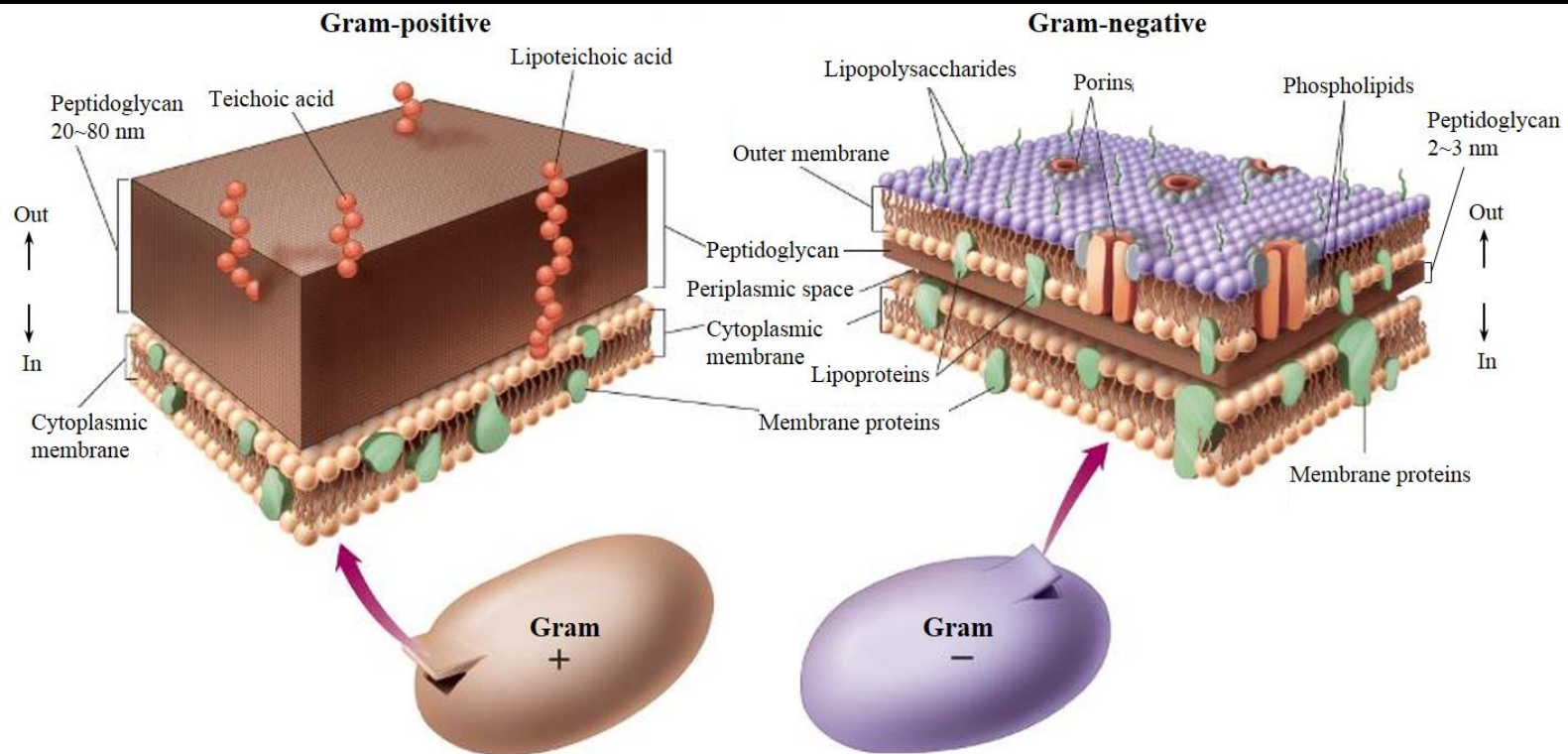


Figure 2.5 Differences in the cell wall structure between the Gram-positive and Gram-negative bacteria (Adapted from [179]).

2.3.2 Bio-Pd Catalyst

Previous studies of bio-Pd observed differences in Pd(II) sorption and Pd(II) reduction ability between different bacterial strains [23]. The fundamentally different biochemical support matrices were noted by Creamer *et al.* [30] whom observed the difference of Pd(0) deposition on *D. desulfuricans* (Gram-negative) and *B. sphaericus* (Gram-positive). In the Transmission Electron Microscopy studies by Deplanche *et al.* [31], biogenic Pd(0) NPs showed strain-specific size distributions, which were consistently larger on Gram-positive cells than those on Gram-negative strains. Within the same Gram-negative catalogue, *R. sphaeroides* and *D. desulfuricans* also showed different Pd(0) NPs deposition behaviours [176].

During the manufacturing process of Pd(0) NPs on Gram-negative bacteria, hydrogenases are believed to be responsible for the reduction of Pd(II) to Pd(0) and act as a focus for the initial formation of Pd(0) ‘seeds’ [177], taking the well understood mechanism of bio-Pd manufacture in *D. desulfuricans* [30] as an example. Initially, the soluble Pd(II) coordinates to oxygen and amine groups [180], which are on or near a hydrogenase enzyme that mediates the reduction of Pd(II) to Pd(0) *via* oxidation of H₂ (or formate). A more detailed study by Mikheenko *et al.* [181] used a molecular approach to construct strains of *D. fructosovorans* (Gram-negative) deficient in its periplasmic hydrogenases and they observed relocation of the Pd(0) deposits to the cytoplasmic membrane, the site of the remaining hydrogenases. Similar findings were recently reported with hydrogenases-deficient *E. coli* mutants [177]. After the nucleation of Pd(0), further cluster growth then occurs to make cell-bound deposits of catalytically active Pd NPs being stabilised by the architecture of the bacterial matrix. In addition, the average Pd(II) accumulation capacity (per gram of cell dry weight) of Gram-negative strains without added electron donor (‘biosorption’) was found to be ~7 times greater than Pd(II) uptake by the Gram positive strains [31]. Since the bioreduction of Pd(II) by *D. desulfuricans* and *E. coli* leads to apparently homogeneous coverage of small (5~10

nm) Pd(0) NPs on the cell surface [31], these two strains become the most studied organisms and bio-Pd produced by *D. desulfuricans* and *E. coli* have shown their remarkable catalytic activity in a wide variety of reactions [24,26,30,31,177,182-184].

The catalytic potential of this biomineralised Pd(0) (bio-Pd) was first demonstrated by Yong *et al.* [26] in a simple reaction involving the formation of H₂ from sodium hypophosphite using bio-Pd/*D. desulfuricans* catalyst. This was followed by the demonstration of remarkable catalytic properties of bio-Pd in a number of test reactions including the remediation of metallic pollutants (*e.g.* Cr(VI)) [31,177,185] and xenobiotics (halogenated aromatics and flame-retardants) [27,171,182,184]. Being particularly relevant to the current study, bio-Pd catalyst has demonstrated certain activities in hydrogenation reactions [24,30]. In the hydrogenation of itaconic acid [30], 5wt%Pd/*D. desulfuricans* gave an initial rate of $1.1 \times 10^{-2} \text{ mol.g(Pd)}^{-1}.\text{s}^{-1}$, which compared well with a commercial 5wt%Pd/graphite catalyst ($1.3 \times 10^{-2} \text{ mol.g(Pd)}^{-1}.\text{s}^{-1}$). An advantage in selectivity using 5wt%Pd/*D. desulfuricans* was also revealed in the hydrogenation of 2-pentyne [24]. At 92% 2-pentyne conversion, 5wt%Pd/*D. desulfuricans* gave a *cis/trans* ratio of 2.5 and pentene/pentane ratio of 3.3, as opposed to respective values of 2.0 and 2.0 with 5%Pd/*Al₂O₃*. On the other hand, Deplanche *et al.* [170] used *E. coli* as the support for 5 wt%Pd and tested in benzyl alcohol oxidation with molecular oxygen. However a levelling-off of the reaction rate after 2.5 hours was observed, indicating the potential of deactivation of bio-Pd due to the over-oxidation of Pd metal (see §2.2.4.1). This leads to the postulation that using gold to alloy biomass-supported palladium NPs could enhance the overall catalytic property.

2.3.3 Bio-AuPd Catalyst

De-Corte *et al.* [186,187] synthesised bio-AuPd catalyst by co-precipitation of Pd and Au onto the metal-respiring bacterium *Shewanella oneidensis* (Gram-negative). TEM images revealed that aggregates of AuPd bimetallic NPs were precipitated mainly on the outer parts

of the *S. oneidensis* cells giving a bimetallic crystalline structure [186]; no zones with pure Pd or pure Au were present within one aggregate as shown by the EDX elemental line-scan across an AuPd aggregate. The bimetallic bio-AuPd/*S. oneidensis*, compared to the monometallic bio-Pd/*S. oneidensis*, resulted in a greatly improved catalytic activity with more reproducible results in dehalogenation of environmental contaminants [186] and in Suzuki cross-coupling reactions (iodobenzene and phenylboronic acid) [188]. However using this simultaneous reduction of Pd and Au supported on cells of *S. oneidensis*, the authors have not yet been able to obtain bimetallic Au(core)-Pd(shell) structures [186,189], which was thought to be responsible for the high reaction rate in dehalogenation reactions [190].

More relevant to this study, a two-step method combining a successive reduction of Pd(II) and Au(III) onto the bacterial cells was developed as the manufacturing method. The synthesis relies on the ability of bacterial cells to firstly reduce Pd(II) ions enzymatically from a precursor using H₂ as an electron donor [177]. The resulting fine layer of Pd(0) leads to an increase in the rate of Au(III) reduction under H₂ and results in the incorporation of Au atoms into the Pd seeds [161]. Deplanche *et al.* [161] presented this to be a facile, size-controlled and cost-efficient method to synthesise Au(core)-Pd(shell) nanostructures using *E. coli*. Following the sequential reduction of Pd(II) and Au(III), *E. coli* cells exhibited complete coverage of both the cell surface and the periplasmic space by metal NPs, with some cells showing a small number of intracellular NPs. Characterising the bio-AuPd nanoparticle by comprehensive techniques (high-resolution TEM, energy dispersive X-ray elemental mapping, cyclic voltammetry, X-ray absorption spectroscopy techniques and XRD) revealed a non-random alloy with an Au(core)-Pd(shell) structure. Bio-AuPd catalyst material possessing Au(core)-Pd(shell) nanostructure, to the best of the author's knowledge, has not been studied extensively in the application in organic chemical synthesis reactions, which becomes one of the major research objectives in this study.

2.3.4 Advantages and Challenges of Bioreductive Synthesis of Bio-Catalyst

Biological synthesis of supported metal nanoparticles (bio-Pd or bio-AuPd in this study) is an innovative method for manufacturing heterogeneous catalysts potentially useful in a wide range of chemical reactions. This section discusses the advantages of this biological synthesis method, together with some challenges which need to be fulfilled in order to create a stable, sustainable and applicable biocatalyst.

Advantages

Using microorganisms as the supports for bio-Pd or bio-AuPd catalysts can have several advantages over chemically produced catalysts, such as imparting reliable size control on the metal particle, while the method is environmentally benign and often cheaper than chemical methods [161].

i) A reliable route to produce Pd(0) NPs on the cell surface.

The bacterial cells are support materials with extremely high specific surface areas [188], on which the precipitation of the metals occurs within minutes. For example, discrete Pd(0) NPs of ~5 nm diameter were synthesised on *D. desulfuricans* [30] and stabilised against agglomeration [25]. Offering particle size and shape control, being the most attractive requirement in industrial application, this microbial method has been reported as an effective route for synthesising nanoparticles [161,176,191,192].

ii) Fewer toxic and expensive chemical agents (reductants and stabilisers) involved.

The bacterial cells serve both as stabilising and as reducing agents for the metal NPs [188]. Bacterial strains like the facultative anaerobe *Escherichia coli* (the focus in this study), is fast and easy to grow (aerobically) since it is less sensitive to O₂ than strict anaerobes, and is well characterised in physiological and biochemical terms as well as having a very well defined molecular biology and hence being the laboratory ‘workhorse’ for studies in molecular

engineering. *E. coli* displays a remarkable flexibility in its respiratory electron transport processes that allows for growth on a wide range of substrates [193,194]. Additionally, *E. coli* possesses significant metal-reducing capacity and, in the case of Tc(VII) reduction, studies using mutants revealed similarities in the reducing mechanism between *E. coli* and sulphate-reducing bacteria (SRB) such as *D. desulfuricans* [195,196]. Hydrogenases, the primary route for metal reduction described in this study, are enzymes associated with anaerobic (not aerobic) metabolism. Hence, practically, aerobically-pregrown cells are exposed to a period of anaerobiosis in order to upregulate hydrogenase production prior to metal reduction.

Hydrogen, as the electron donor in most circumstances, is a clean and low-cost species for the reduction of metal salts into their zero-valent metallic forms. As hydrogen is mostly produced electrochemically, its cost is very dependent on the energy price. It could be promising when fermenting bacteria are used, since biogenic hydrogen can be delivered *in situ* and this cost can be omitted.

iii) A potential win-win technique: catalytic application of biorecovered Pd.

While precious metals (*e.g.* Pd and Pt) are available to a very limited extent, there is an increasing demand to use them as catalyst [47]. Since biological reduction of metals is well documented [20], it could be attractive to synthesise bio-Pd from a Pd-containing scrap leachate and subsequently apply it as a catalyst in order to obtain a closed cycle of Pd. The bioreduction process is sensitive enough to recover metal at parts-per-million (p.p.m.) concentrations, which is often below the economic threshold of traditional recovery methods, thus biorecovery provides a clean alternative to traditional reclaiming treatments [177]. Such bio-recovered Pd(0) has been found to be catalytically active [29].

Challenges

A major limitation for the use of bionanomaterial would be the long-term stability, which needs to be further investigated [47]. If bio-nanocatalysts are used in advanced synthetic organic chemistry, which is often performed at high temperature, the bacterial biomass may disintegrate, causing the detachment of active components. Even worse, poisoning of the catalyst may occur *via* the disintegration of bacterial biomass at high temperature application, during which the sulphur will be released *via* breakdown of sulphur-amino acids (an essential component of microbial biomass). Sulphur is known to have a strong affinity for the Pd metal and may block the active sites of the catalyst *via* formation of strong Pd-S bonds and layers of sulphur around the Pd clusters [197,198]. De-Corte *et al.* [47] suggested that sulphur poisoning was the reason for a very rapid loss of catalytic activity of the bio-Pd catalyst in dehydrogenation reactions at 250 °C.

Another challenge could exist in the concept of sustainable recycling and production of bio-Pd for catalytic application (as stated in advantages iii) from real waste scrap leachates. It is probable that the success of both the biorecovery and the catalytic application are very dependent on the composition of metal-containing wastes. The scrap can contain compounds, such as Cu(II) (a known hydrogenase inhibitor), which inhibit the biorecovery process and other metals present on the bacteria after the recovery process might decrease the catalytic activity of Pd [47].

Therefore, more in-depth understanding of the mechanisms behind this biotechnology of nanoparticle-formation is urgently required. However, the production process of biomass-supported catalysts has great potential for improvement; it can be further optimised, which will make these catalysts even more competitive with chemically produced catalysts.

2.4 Reaction Mechanism on Catalyst Surfaces

Given that palladium has the reputation of being one of the most active and selective metals in catalysis, nanoparticles of palladium have been heavily studied in a wide range of catalytic applications including hydrogenation of various organic reactants [199,200] and liquid phase oxidation of alcohols [201,202]. These selective redox processes are the key synthetic steps for the preparation of many pharmaceuticals, agrochemicals and commodity chemicals, which commonly require a partial reaction product, rather than the finished products of total hydrogenation or oxidation [77]. To achieve very high selectivity in a particular reaction, it is thus important to understand the reaction mechanisms, *i.e.* all the parallel and consecutive reactions that are active in the overall transformation, to assist catalyst design and fine tuning. This section focuses on the examples of vegetable oil hydrogenation and alcohol oxidation reactions over heterogeneous catalysts and reaction mechanisms on the catalyst surface.

2.4.1 Hydrogenation of Vegetable Oil

Being the most used feedstocks in industrial oleochemical hydrogenation reactions, vegetable oils (*e.g.* palm oil, rapeseed oil, soybean oil, and sunflower oil) are composed of natural fatty triglycerides which are derived from glycerol and three molecules of natural fatty acids [4,13,203]. The fatty acids distributing in natural triglycerides vary depending on the source, but are mostly with an even number of carbon atoms from 6 to 22 in their chains (C₆~C₂₂). Unsaturated fatty acids (mainly C₁₈~C₂₂) are those that contain single or up to six non-conjugated carbon-carbon double bonds (C=C), correspondingly known as oleic acid (C₁₈:1), linoleic acid (C₁₈:2), linolenic acid (C₁₈:3), gadoleic acid (C₂₀:1) and erucic acid (C₂₂:1). It is also noted that unsaturated C=C bonds in natural fatty acids appear exclusively in a *cis* configuration [4,203], which means that adjacent hydrogen atoms are on the same side of the C=C bond. Typical compositions of some vegetable oils are given in Table 2.8. The highest average degree of multiple unsaturated double bonds can be found in soybean oil

(23.8 wt% C18:1, 53.2 wt% C18:2, 7.8 wt% C18:3), or sunflower oil (18.6 wt% C18:1, 68.2 wt% C18:2, 0.5 wt% C18:3) [204].

Table 2.8 Fatty acid composition of some common vegetable oils [204].

C-chain:double bonds ^a	Fatty acid	Composition (wt%) in different vegetable oils					
		Coconut	Palm	Canola	Rape seed	Soybean	Sunflower
C6:0	Capronic	0.5					
C8:0	Caprylic	8.0					
C10:0	Caprinic	6.4					
C12:0	Lauric	48.5	0.3				0.5
C14:0	Myristic	16.2	1.1		0.1	0.1	0.2
C16:0	Palmitic	7.7	45.1	3.9	2.8	11.0	6.8
C18:0	Stearic	3.2	4.7	1.9	1.3	4.0	4.7
C18:1	Oleic	8.3	38.8	64.1	23.8	23.8	18.6
C18:2	Linolic	1.0	9.4	18.7	14.6	53.2	68.2
C18:3	Linoleic		0.3	9.2	7.3	7.8	0.5
C20:0	Arachidic		0.2	0.6	0.7	0.3	0.4
C20:1	Gadoleinic			1.0	12.1		
C22:0	Behenic			0.2	0.4	0.1	
C22:1	Erucic				34.8		

^a C denotes carbon; the first number, *e.g.* 18, represents the total carbon number of the acyl groups; the second number, *e.g.* 3, represents the total number of double bonds.

Natural unsaturated triglycerides and fatty acids need to be modified in most cases through partial or complete catalytic hydrogenation (saturation) of the C=C bonds to raise the melting point and oxidative stability [4], before they can be used as base stocks in either industrial or consumer products, such as frying oils, shortenings, margarines, soap stock, industrial oils and greases [13].

2.4.1.1 Selectivity in Catalytic Hydrogenation of Vegetable Oil

In a typical industrial application, the oils are hydrogenated in three-phase reactors in the presence of a heterogeneous catalyst at about 50~220 °C and 5~7 atm of hydrogen, in 1~3 h depending on the catalyst and oil [205-208]. Some studies are summarised in Table 2.9. This catalytic process consists of complex reaction pathways, *e.g.* the sequential saturation of

multiple C=C bonds (*i.e.* hydrogenation of triene to diene to monoene, and finally to saturated fat), positional migration and *cis-trans* geometrical isomerisation of single C=C bond, thus yielding a variety of products. It is noted here that a *trans* configuration, by contrast with *cis* configuration, means that the two adjacent hydrogen atoms are bound to *opposite* sides of the C=C bond.

Table 2.9 Some investigations on hydrogenation of fatty oils [206,208].

Substrate	Catalyst	Pressure, atm	Temperature, °C	Reactor type
Castor oil	Ni	1.3~5	130~200	stirred-tank
Methyl oleate	Pt/C	2.2~5.5	160~180	stirred-tank
Soybean oil	Ni	0.34~1.35	160~210	stirred-tank
Rapeseed oil	Raney Ni	2.55	60	stirred-tank
Groundnut oil	G-111 Ni	3.8~9.3	100~160	stirred-tank
Soybean oil	Ni	2.4~4.2	140~180	stirred-tank
Soybean oil	Pd/charcoal	1~5	80~160	stirred-slurry
Soybean oil	CuO-Cr ₂ O ₃ -MnO ₂	1	185~215	continuous slurry (bubble column)
Sunflower-seed oil	Ni-spherosil	2.2~3.4	138~238	agitated-slurry (autoclave)
Rapeseed oil	Ni	0.3~10	140~220	stirred-slurry
Soybean oil	Raney Ni, copper chromite Ni-Cu, Cu-Al, Pd-Al, Cu-Cr, Al alloys	2.2~8.5	110~190	fixed-bed, continuous downflow
Soybean oil	Copper chromite	2	155	agitated-slurry
Soybean oil	Nickel flakes, nickel on kieselgur, copper chromite	1.5~4.8	180~200	bubble column, continuous upflow
Soybean oil	Copper chromite	2	170~200	agitated-slurry
Cottonseed oil	Ni	3	139~169	agitated-slurry
Soybean oil	Ni	1	170	agitated-slurry

In terms of the products from this type of hydrogenation process, *trans*-isomers of unsaturated fatty acids and the terminal product (saturated fatty acid) are highly undesirable in food applications since they have been linked to the incidence of coronary artery disease [209] and cardiovascular disease [210]. In contrast, diets higher in monounsaturated fatty acid, especially oleic acid (*cis*-C18:1), has been associated with good aspects to lower the

incidence of diseases [5,6]. Thus *cis*-C18:1 becomes a highly desirable product in the partial hydrogenation process. To selectively produce *cis*-isomers has been challenging due to the overall complex reaction network, which leads to the importance of understanding its mechanism.

2.4.1.2 Hydrogenation of Vegetable Oil on the Catalyst Surface

Though partial hydrogenation of fatty oils is one of the oldest industrial processes and a large number of papers, patents and books have been published on the subject, only a few papers have been devoted to the kinetics of this reaction [13,206]. Instead, simplified reaction systems are usually studied, for example using pure methyl esters of unsaturated fatty acids [203,211,212]. The results of these studies can be extended with difficulty to the interpretation of the behaviour of natural oils, that is, mixtures of polyunsaturated fatty acids. The total immiscibility between the fatty acids and their derivatives could influence the selectivity and reaction rate in and around the solid catalyst [4]. Herein the elementary reaction step of hydrogenation of edible oil on the catalyst surface is described, as the fundamental principle of kinetics investigation (Appendix §8.1.2) for hydrogenation of soybean oil in this study.

For a hydrogenation reaction between unsaturated oil and hydrogen at the presence of a catalyst, the unsaturated double bond (C=C) is firstly adsorbed on the catalyst surface as well as hydrogen becoming dissociated into atomic hydrogen. The subsequent addition of hydrogen atoms to the C=C bond is considered as a two-step addition, which is well-known to follow the Horiuti-Polanyi mechanism [213]. The schematic reaction sequence of hydrogenation and isomerisation of C=C bonds on the active site is established in Figure 2.6.

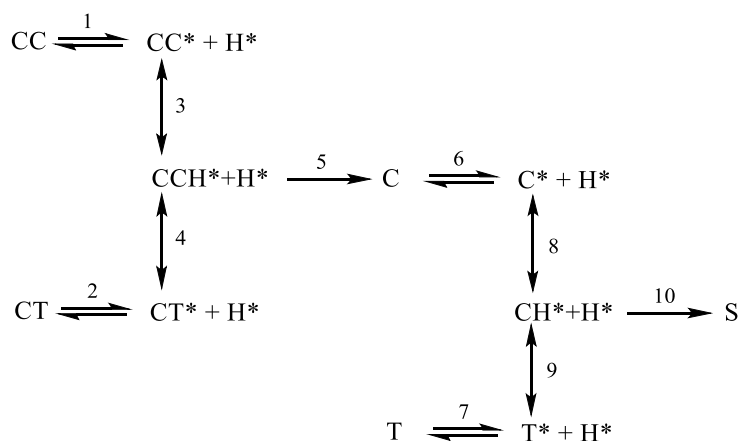


Figure 2.6 Elementary reaction of hydrogenation and isomerisation of carbon-carbon double bond based on Horiuti-Polanyi mechanism. C= one *cis* form of double bond, while T= one *trans* form of double bond, *= one active site, H*= one adsorbed hydrogen atom, CCH*/CH*= one half-hydrogenated surface intermediate, and S= saturated compound.

In the above reaction scheme, the addition of the first hydrogen atom (H^*) to one of the carbon atoms linked to the double bond on the active site (CC^*) forms a half-hydrogenated surface intermediate (CCH^*), which is considered as reversible with characteristic equilibrium constant. As a consequence, the double bond remains to be a single bond in the resulting half-hydrogenated surface intermediate (CCH^*), of which the easy rotation at the surface leads to the loss of its geometrical *cis* or *trans* configuration. Accordingly, the release of a hydrogen may result in the original *cis*-bond (step 3) or in the formation of a *trans*-bond (step 4). Like the diene CC^* , the *cis*-monoene C is adsorbed onto the catalyst surface (C^*) in step 6 and reacts with a hydrogen atom to form a half-hydrogenated surface intermediate (CH^*) in step 8. Unlike the CCH^* , this half-hydrogenated fatty acid CH^* has no residual double bond left so it is only loosely attached to the catalyst surface. Therefore it is likely to dissociate (steps 8 and 9) and leave the surface as a *cis*-monoene (step 6) or a *trans*-monoene (step 7). The saturation of one double bond (to form C in step 5, or S in step 10) is accomplished by a successive addition of the second hydrogen atom to the other carbon atom that was originally linked to the double bond. The second hydrogen insertion can be regarded as an irreversible reaction, because dehydrogenation occurs above 670 K only [214]. In addition, the positional migration of double bond along the carbon chain, merely one position

only, may occur *via* the π -allyl intermediate, which is mainly present at low hydrogen pressure [215,216]. It is suggested that the characteristics of the double bonds from the 8, 9, or 10 position can be assumed to be similar due to the always comparable surroundings and, under most conditions, the migration products are only minor, compared to *cis-trans* isomerisation products [203]. Thus the *cis-trans* geometrical isomerisation is a major consideration in this study.

2.4.2 Oxidation of Alcohol

The selective oxidation of primary and secondary alcohols into the corresponding carbonyl compounds plays a central role in organic synthesis of either finished products or intermediates [7,8]. For example, aromatic aldehydes are highly valuable both as intermediates for pharmaceuticals, agrochemicals and as direct components for the flavour and perfume industries [10,65,217]. Due to their applications, these aromatic aldehydes have to be obtained with high selectivity.

There are many synthetic routes to produce aromatic aldehydes. In contrast to hydrogenation reactions which are often conducted catalytically with molecular hydrogen, there are relatively few selective oxidation reactions that are catalysed using molecular oxygen [7], instead using stoichiometric quantities of inorganic oxidants, *e.g.* chromate or permanganate, to achieve selectivity towards aldehydes in oxidation processes [7,9,218,219]. These reagents are expensive and have serious toxicity issues associated with them [9,10,65] as well as often resulting in a poor atom efficiency of the overall process [7]. In response, many homogeneous systems able to catalyse liquid phase oxidation have been used successfully, resulting in high product yields [85]. However, the disadvantage of the use of homogeneous systems is widely known to be associated with separation and catalyst recycling. From both economic viewpoint and environmental concern, atom efficient heterogeneous catalytic systems that employ clean oxidants such as air or molecular oxygen in combination with the

utilisation of heterogeneous catalyst are more desirable [8,160] for the fine chemicals industry and, even more demanding, using mild solvent-free reaction conditions [7].

2.4.2.1 Benzyl Alcohol Oxidation Using Molecular Oxygen

Oxidation of primary alcohols with molecular oxygen to aldehydes in the liquid phase over heterogeneous catalysts is a fundamentally important laboratory and commercial procedure [65]. A variety of different metal loaded heterogeneous catalysts, having ease of recovery and recycling and amenability to continuous processing, has been developed in the last decade. Benzyl alcohol is chosen in this section as a model alcohol to summarise some new developments, such as the use of supported Pd, Au and bimetallic (AuPd) catalysts.

Pd Catalyst in Benzyl Alcohol Oxidation

Mori *et al.* [220] studied oxidation of benzyl alcohol under atmospheric O₂ pressure by nanoparticles of Pd on a variety of materials, including hydroxyapatite (HAP), carbon, Al₂O₃ and SiO₂. The highest conversion (99%) and selectivity to aldehyde (99%) after 1 hour was observed when using HAP-supported Pd catalyst. The other supports examined (Al₂O₃, SiO₂ and C) produced the aldehyde with less than 50% selectivity; among which the most selective catalyst was Pd/SiO₂ (47%) though the conversion was only 71%. Pd/Al₂O₃ catalyst achieved a benzyl alcohol conversion of 96%, though the selectivity was the lowest (38%). The Pd/C catalyst produced the lowest conversion (46%) and low selectivity (42%) under the identical reaction conditions. The above reactions were all performed in the presence of trifluorotoluene as a solvent.

Chen *et al.* [221] proposed that the interaction between the Pd precursor and the support plays a key role in tuning the mean size of the Pd NPs. Using SiO₂-Al₂O₃ mixed oxide as the support, they synthesised Pd NPs with mean sizes ranging from 2.2 to 10 nm. It was found that the intrinsic turnover frequency (TOF) per surface Pd atom depended significantly on the

mean size of Pd particles and showed a maximum at a medium mean size (3.6~4.3 nm), revealing that the aerobic oxidation of benzyl alcohol catalysed by the supported Pd NPs was structure-sensitive. The optimised catalysts (Pd particle sizes of 4.3 nm and 3.6 nm) demonstrated high TOF (2.53 s^{-1} and 2.45 s^{-1} , respectively) as well as high selectivity to the aldehyde (98% selectivity with 73% conversion and 98% selectivity with 99% conversion, respectively, in 10 h) in solvent-free conditions.

Au catalyst in Benzyl Alcohol Oxidation

Rossi, Prati and co-workers [222-224] were the first to demonstrate clearly that supported Au NPs can be very effective catalysts for the oxidation of alcohols. To some extent this observation is counterintuitive since extended Au surfaces do not chemisorb oxygen, nor do they corrode. Large Au particles are unable to chemisorb reactant molecules unless the particles are small enough to be deficient in the complete metal coordination character [225].

The effects of added base and support have been investigated thoroughly for benzyl alcohol oxidation over Au catalysts. Much of the literature on alcohol oxidation over Au catalysts describes results obtained in the presence of a homogeneous base (typically NaOH), which is considered to be essential for the first hydrogen abstraction [7]. Guo *et al.* [226] reported successful aerobic oxidation of benzyl alcohol over unsupported bulk Au performed in aqueous NaOH and found the product distribution was strongly dependent on the reaction temperature and concentration of NaOH. At a reaction temperature of 333K, benzyl benzoate was obtained as the major product at lower concentrations of base ($\leq 0.6 \text{ M NaOH}$) while benzoic acid was produced at higher concentrations (1.2 M NaOH). For benzyl alcohol oxidation at 363K, mainly aldehyde was produced over a range of NaOH concentrations.

As an alternative to a homogenous base, some groups investigated the effect of acid and base sites on the support ('solid base') in Au catalysis for benzyl alcohol oxidation [227-229]. In

the oxidation of primary alcohols without additional homogeneous base [228], a maximum benzyl alcohol conversion of only 7.1% was obtained over an Au/Fe₂O₃ catalyst (87.6% selectivity to benzaldehyde) after 3 h at 373 K and 200 kPa O₂. The highest selectivity to aldehyde (100%) was obtained using Au/CeO₂ along with a benzyl alcohol conversion of 3.4%. Maintaining the selectivity to aldehyde of 100%, however the lowest conversion was observed over Au/TiO₂ (0.65% conversion in 3 h). Fe₂O₃ supported Au catalyst gave the highest selectivity (12%) to benzyl benzoate, which was formed by subsequent oxidation of benzaldehyde to the corresponding benzoic acid by a standard acid-catalysed mechanism. Among the examined supported Au catalysts, the strongest acidic sites on Au/Fe₂O₃ was revealed by temperature programmed desorption of NH₃.

Bimetallic AuPd catalyst in Benzyl Alcohol Oxidation

As introduced in §2.2.5.2, a breakthrough was made with the discovery that alloying of multiple metals has the potential to enhance reaction rate, alter product selectivity, and/or help slow or prevent catalyst deactivation. Synthesis of bimetallic catalysts for benzyl alcohol oxidation is focused on Au, Pt and Pd catalysts, which were found active under more environmental friendly conditions such as in aqueous solution or even under solvent-free condition [103].

Dimitratos *et al.* [125] used gold to promote PGM (platinum group metal) catalysts supported on activated carbon for the selective oxidation of various primary alcohols under mild conditions (333 K, 152.0 kPa O₂). When water was used as solvent in place of organic solvent (toluene) for benzyl alcohol oxidation, a positive synergistic effect was observed in the case of Pd with the addition of Au. It was found that TOF increased from 30 h⁻¹ for 1wt%Pd/C catalyst to 160 h⁻¹ for 0.73wt%Au0.27wt%Pd/C catalyst.

Enache *et al.* [65] synthesised a bimetallic AuPd/TiO₂ catalyst by adding Au to Pd nanoparticles. An improved selectivity to aldehyde was obtained in solvent-free benzyl alcohol oxidation under mild conditions (373 K, 100 kPa O₂), which was 92% at 75% conversion for bimetallic 2.5wt% Au2.5wt% Pd/TiO₂ compared with a 54% selectivity at 51% conversion for monometallic 5wt% Pd/TiO₂. It was suggested that the enhancement of activity of AuPd/TiO₂ was due to Au altering the electronic structure of Pd [65]. Characterisation by Electron Microscopy and X-ray photoelectron spectroscopy revealed that the formed AuPd nanocrystals on TiO₂ were made up of an Au-rich core with a Pd-rich shell. Other materials such as Al₂O₃ and Fe₂O₃ were also used to synthesise bimetallic AuPd catalysts; though the selectivity to the aldehyde was lower (87% at 83% conversion on Al₂O₃, 67% at 63% conversion on Fe₂O₃) possibly due to acid sites on the support promoting ester (benzyl benzoate) formation.

It is suggested that Pd is largely responsible for the transformation of benzyl alcohol by the AuPd catalyst [230]. The reaction rate of benzyl alcohol oxidation over AuPd bimetallic catalysts was found to be zero order in O₂ pressure in the range 100~3000 kPa [66,71,231,232]. In addition to the synergistic effect on the catalytic activity, alloying Au and Pd for alcohol oxidation catalysts has been shown to inhibit the leaching of metal (Pd) from the support or to prevent catalyst deactivation [125].

2.4.2.2 Aerobic Oxidation of Alcohol on the Catalyst Surface

The aerobic oxidation of primary and secondary alcohols forms the corresponding carbonyl compounds. For example, as outlined in Figure 2.7, a primary alcohol proceeds first to an aldehyde and subsequently to a carboxylic acid.

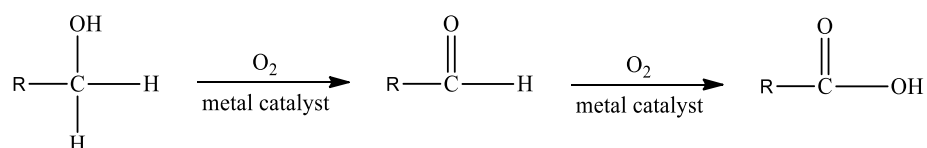


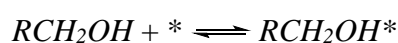
Figure 2.7 General oxidation scheme for primary alcohol oxidation to acid.

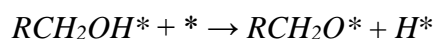
The precise reaction pathway for the oxidation of alcohols using dioxygen is still under dispute as several different mechanisms have been proposed [70,233-236]. There are still too many uncertainties as to the complex nature and coverage of the adsorbed species on the metal surface (*e.g.*, the origin of adsorbed oxygen species, O₂ or OH⁻ or H₂O, or the type of adsorbed reactant alcohol, RCH₂OH or RCH₂O⁻ or RCH₂O [117]) which depend upon many factors such as pH, oxygen availability, substrate concentration and nature of the metal [70]. However, there is a general agreement on the dehydrogenation mechanism, *via* β-hydride elimination from the metal alkoxide to form a metal hydride [8,103], for which the active site is considered to be the reduced metal such as Pd(0) [230]. As to the oxygen adsorption on the active site, molecular O₂ is suggested to be adsorbed dissociatively on most metal surfaces, such as Pt and Pd, whereas associatively on the surface of Au [103]. The role of adsorbed oxygen is ultimately to remove electrons from the metal surface, oxidise metal-hydride bonds, and regenerate hydroxide ions [103,237,238].

This section presents the mechanism of aerobic oxidation of an primary alcohol to an aldehyde over a heterogeneous catalyst as the representative based on the latest review by Davis *et al.* [103], who proposed three steps: i) the alcohol adsorbs on the metal surface, producing an adsorbed metal-alkoxide; ii) β-hydride elimination occurs to produce a carbonyl species and a metal-hydride; and iii) the metal-hydride is oxidised by dioxygen to regenerate the metal surface.

Metal-alkoxide formation

The alcohol (RCH₂OH) adsorbs dissociatively on the metal surface (*), the O-H bond is broken producing an adsorbed metal alkoxide (RCH₂O*) and a metal-hydride (H*) [220,221,239,240]. The corresponding path is as follows:

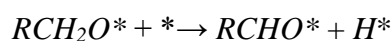




The formation of metal alkoxide may be affected by the nature of the metal or the nature of substrates adsorbed on the metal [103].

β -hydride elimination

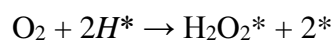
After the formation of the metal-alkoxide (RCH_2O^*), a β -hydride elimination occurs on the metal surface to produce a carbonyl species ($RCHO^*$) and a metal hydride (H^*) [220,221,240-243]. The β -hydride elimination step can be described as:



At this point, O_2 does not play a role in the mechanism, yet O_2 is required for the oxidation to proceed. Isotopic labelling studies indicated that oxygen atoms from dioxygen are not directly incorporated in the acid products, but are essential for the oxidation of aldehyde to acid. The β -hydride elimination step has been proposed to be the likely rate-determining step in alcohol oxidation [220,221,241].

Oxidation of metal-hydride and regeneration of catalyst surface

The third step in alcohol oxidation to aldehyde is the oxidation of the metal-hydride species (H^*) generated from the β -hydride elimination step to regenerate either the metal-hydroxide (OH^*) or metal surface (*), which can be described as:



The oxidation of the metal-hydride (H^*) likely proceeds through a peroxide intermediate (OOH^*) to yield a water molecule (H_2O) and one half of an O_2 molecule [220].

2.5 Three-Phase Catalytic Reactor

Because of the good heat transfer, temperature control and catalyst utilisation, three-phase catalytic reactors are usually employed in many heterogeneous hydrogenation and oxidation reactions [206]. The ‘global’ classifications of three-phase catalytic reactors used in industry can be summarised in Figure 2.8 as follows:

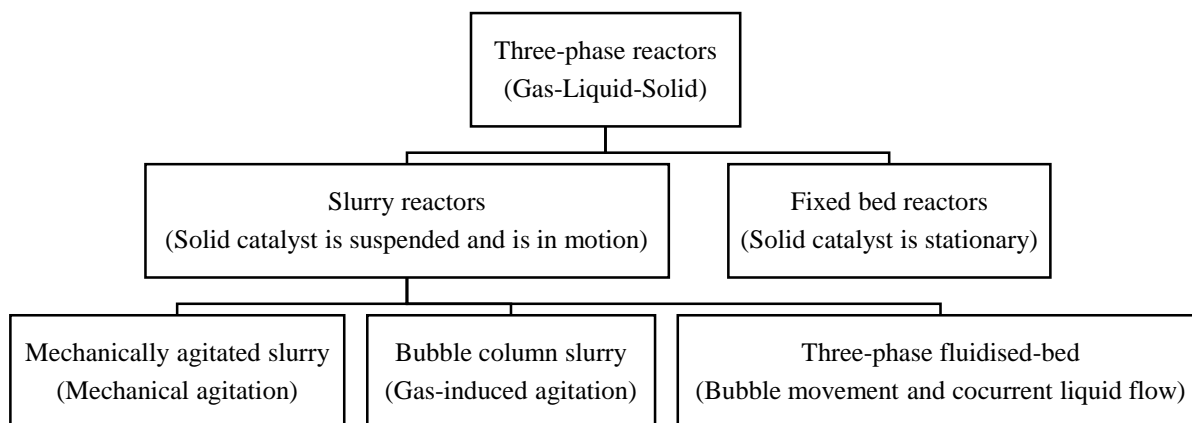


Figure 2.8 Classification of industrial three-phase catalytic reactors [3,206].

It is of primary importance to select the proper reactor to obtain the required information. A rational choice from the variety of reactor types available requires knowledge of chemical reaction kinetics, thermodynamics, heat and mass transport, reactor hydrodynamics and the properties of the reaction mixture throughout the reaction [244]. Furthermore, the criteria for the selection of a reactor for catalyst testing are different from those for the selection of an industrial reactor. Laboratory reactors are small-scale reactors. Scaling down as far as possible is desirable for reasons of lower equipment costs, lower materials consumption, less waste formation, lower utility requirements, reduced demands on laboratory infrastructure and increased intrinsic safety (reduced hazards of toxic emissions, explosions and fires). However, a small-scale laboratory reactor requires an accurate experimentation and the use of representative (catalyst) samples. Table 2.10 lists characteristic properties of the reactors discussed in Figure 2.8, which can serve as guidelines for preliminary reactor selection.

Table 2.10 Characters of three-phase reactor types with typical values are given. (Adapted from Diepen and Moulijn [244])

Characterises	Catalyst in suspension			Fixed bed	
	mechanically agitated	bubble column	three-phase fluidised-bed	trickle-bed	3-phase monolith
Reactor					
Catalyst	mobile small particles 1~200 μm		mobile particles 0.1~5 mm	spheres, extrudates, <i>etc.</i> 1.5~6 mm	blocks with channels covered with catalyst layer 10~150 μm
Mode of operation	(semi)batch or continuous		continuous	continuous (+ quasi batch), cocurrent downward	
Liquid hold-up ($\text{m}_l^3\text{m}_r^{-3}$)	0.8~0.9	0.8~0.9	0.2~0.8	0.05~0.25	0.1~0.5
Fraction of catalyst ($\text{m}_{\text{cat}}^3\text{m}_l^{-3}$)	0.01~0.1	0.01~0.1	0.1~0.5	0.55~0.6	0.07~0.15
a_l ($\text{m}^2\text{m}_l^{-3}$)	1000~2000	600~1000	500~1000	100~1000	500~1000
$k_l a_l$ (s^{-1})	0.15~0.5	0.05~0.25	0.05~0.3	0.01~0.3	0.05~0.7
$k_s a_s$ (s^{-1})	0.1~0.5	≈ 0.25		0.06	0.03~0.09
$\eta \approx$	1	1	< 1	< 1	< 1

a_l = gas-liquid interfacial area per unit volume of liquid; a_s = liquid-solid interfacial area per unit volume of liquid; k_l = mass-transfer coefficient from gas-liquid interface to bulk liquid $\approx 10^{-4}$ - $4 \times 10^{-4} \text{m}^3\text{m}_l^{-2}\text{s}^{-1}$ for all systems; k_s = mass transfer coefficient from liquid-solid interface to solid surface ($\text{m}_l^3\text{m}_s^{-1}\text{s}^{-1}$).

This section is limited to the mechanically agitated slurry reactor, since it is the most suitable type for the determination of the reaction kinetics of a three-phase reaction system on the laboratory scale [206,244] if after careful investigations of improving the mass transfer.

2.5.1 Mechanically Agitated Slurry Reactor

The mechanically agitated slurry reactor can be operated both batchwise and semi-continuously. Most laboratory units are dead-end autoclaves equipped with a gas-inducing impeller with only feed of the reactant gas by keeping the pressure constant (semi-batch operation) [245]. The cylindrical vessels are equipped with different types of stirrers or turbines to keep the solid catalyst suspended in the form of fine particles in the liquid phase. The products are removed from the vessel after some time and separated from the catalyst.

Table 2.11 lists some practical advantages and disadvantages of commonly used slurry reactors.

Table 2.11 Advantages and disadvantages of agitated three-phase catalytic reactors [3,206,244,245].

Advantages		Disadvantages	
i)	highly active catalysts can be used	i)	often poor gas-liquid mass transfer
ii)	small particles with catalyst effectiveness approaching unity	ii)	potential non-uniform distribution of the catalyst particles in the reactor
iii)	good temperature control	iii)	catalyst attrition
iv)	high liquid-solid mass transfer rates	iv)	catalyst/product separation difficult
vi)	low pressure drop	vi)	operation at high pressure (>30 bar) can be costly
vii)	ease of design and scale-up	vii)	hard to detect catalyst deactivation

For a three-phase catalytic reaction taking place, gaseous reactant (*e.g.* hydrogen or oxygen) needs to be dissolved in the liquid phase, followed by the adsorption of both gaseous and liquid reactants on the catalyst surface and the successive surface reaction. This involves a number of mass transfer steps. It is useless to try and improve the reaction rate by using a more active catalyst or increasing the catalyst load, when the overall rate of reaction is determined by mass transfer, *i.e.* when the latter is slow compared with the intrinsic rate of reaction. Therefore, mass-transfer characteristics must be considered in the choice and design of three-phase reactors, based on which certain efforts can be made to improve the mixing and minimise the mass transfer resistance [244].

2.5.2 Mixing and Mass Transfer

With the goal of obtaining intrinsic catalyst properties (reaction kinetics) from experimental data without this being obscured by the mass transfer rates, the following conditions are suggested to be fulfilled [245]: i) Effective contact between reactants and catalyst; ii) Absence of mass and heat transport limitations inside and outside the catalyst particles; and iii) Good description of reactor characteristics, with well-defined residence time distributions under isothermal conditions (ideal systems).

2.5.2.1 Particle Suspension

Proper agitator selection is very important to provide good contact between the phases [244]. The catalyst particles must be kept uniformly suspended in the reaction medium for maximum utilisation of the catalyst, *i.e.* no catalyst should settle at the bottom in an ideal operation. This requires a minimum degree of agitation [244], which is relevant to the system geometry (stirrer diameter d_I), properties of the catalyst (catalyst loading w' , mean diameter of catalyst particles d_p , density ρ_p) and the liquid substrate at the operating conditions (viscosity μ_L , density ρ_L). A correlation (Equation 2-1) proposed by Zwietering *et al.* [246] is globally used to calculate the minimum agitation (N_m) required to ensure complete suspension in a stirred vessel, so that proper operating conditions can be chosen.

$$N_m = \frac{\beta d_p^{0.2} \mu_L^{0.1} g^{0.45} (\rho_p - \rho_L)^{0.45} w'^{0.13}}{\rho_L^{0.55} d_I^{0.85}} \quad 2-1$$

where, β is a dimensionless constant for a given system geometry. Nienow [247,248] has shown that an approximate value of β is given by:

$$\beta = 2 \left(\frac{d_T}{d_I} \right)^{1.33} \quad 2-2$$

2.5.2.2 External Transport Limitation

In the three-phase catalytic reaction systems, the liquid substrate is usually present at much higher concentrations (*e.g.* pure liquid phase reactant in this study) than the gas dissolved in the liquid; gas reactant is the 'limiting' reactant. Therefore, the transport rate of gas (noted as G) from the gaseous phase to the liquid phase and then to the catalyst particle is of predominant significance. There are five major mass transfer resistances (see Table 2.12) during the transportation of G from the bulk gas-phase to the catalyst surface; each step reduces the effective concentration of gas reactant as reflected in Figure 2.9.

Table 2.12 Mass transfer resistances and resistance terms [4].

Steps in Figure 2.9	Mass transfer resistance of gaseous reactant G	Inverse resistance term
1	Diffusion in the bulk gas phase	$k_g a$ (s^{-1})
2	Mass-transfer in the gas-liquid interface	$k_L a$ (s^{-1})
3	Convective (diffusive) transport across bulk	D ($m^2 \cdot s^{-1}$)
4	Mass transfer in the liquid-solid film	$k_s a_s$ (s^{-1})
5	Diffusion of reactants into porous network of the catalyst	η

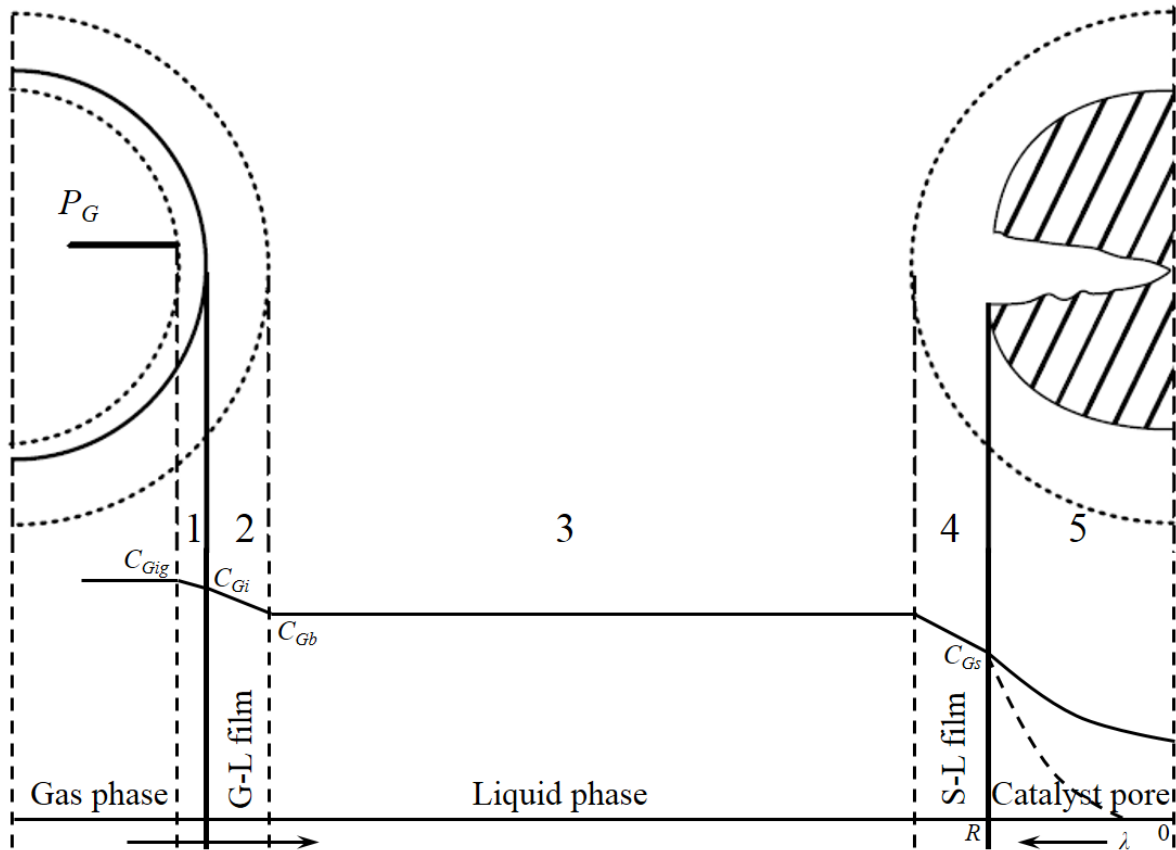


Figure 2.9 Mass transport resistances of gaseous reactant in three-phase catalytic reaction system [4].

Steps 1~4 are often grouped as external mass transfer resistance of the gaseous reactant G , accordingly step 5 as the internal mass transfer resistance.

Diffusion in gas phase

The gaseous reactant G is initially present in the reactor as gas bubbles, its concentration in the interior of these bubbles being C_{Gg} and on the gas-side of the gas-liquid interface being C_{Gig} . The diffusion rate of G in the gas bubble is determined by gas film mass transfer

coefficient k_g , gas-liquid interfacial area per unit volume of liquid a , and concentration difference ($C_{Gg}-C_{Gig}$), which can be expressed as:

$$r_G = k_g a (C_{Gg} - C_{Gig}) \quad 2-3$$

This part of the diffusion resistance is negligible for a sparingly soluble gas, such as hydrogen, and for pure gas feeds (*i.e.* no inert dilutes) [13,206]. For instance, Fernandez *et al.* [249] reported that in the hydrogenation of sunflower oil with constant pure hydrogen feed, the diffusion of hydrogen in the gas bubble was not considered since the diffusivity in gases is much greater than in liquids.

Mass-transfer in the gas-liquid interface

The rate of mass transfer between gas and liquid is determined by the volumetric liquid-side mass-transfer coefficient ($k_L a$) and concentration difference of gaseous reactant G between liquid-side of the gas-liquid interface and the liquid bulk ($C_{Gi}-C_{Gb}$) [244]. The rate of gas-to-liquid mass transfer is given as:

$$r_G = k_L a (C_{Gi} - C_{Gb}) \quad 2-4$$

Assuming equilibrium between the phases at the interfaces, the concentration of G on the liquid side of the interface can be obtained by Henry's law (H is Henry's constant):

$$C_{Gi} = C_{Gig} / H \quad 2-5$$

The volumetric liquid-side mass-transfer coefficient ($k_L a$) may be affected by the operating variables, mainly dependent on agitation speed N , operating temperature T , stirrer type and diameter d_I , and viscosity of the liquid (μ_L) [120]. Empirical gas-liquid mass transfer correlations have been thoroughly investigated for different conditions for agitated slurry reactors in the literature [250-254].

It was suggested that the poor gas-liquid mass transfer, is often, but not always, the limiting step in a heterogeneous catalytic process [244,245]. The agitation test appears useful to check for the presence of interphase gradient at the gas-liquid interphase, at which the mass transfer resistance can be minimised by an adequate stirring speed [260,261].

Diffusion in the bulk liquid phase

The resistance to the diffusion of reactant gas G in the liquid substrate can be neglected taking into account that near perfect mixing occurs when the applied agitation speed is above the estimated minimum agitation (N_m) [249].

Mass transfer in the liquid-solid film

The 4th step of mass transfer in Figure 2.9 is the transport of reactant gas G onto the catalyst surface through a liquid-solid film. Likewise, the rate of reactant transport depends on the external specific surface area of the catalyst particles a_s , the liquid-solid mass transfer coefficient k_s , the catalyst loading w and the reactant concentration difference between the liquid bulk and the catalyst surface ($C_{Gb}-C_{Gs}$). The transport rate can be expressed as:

$$r_G = k_s a_s (C_{Gb} - C_{Gs}) \quad 2-6$$

The measurement techniques for $k_s a_s$ in mechanically agitated slurry reactors have been reviewed by Ramachandran *et al.* [206], and there are many semi-empirical formulae based on the Reynolds and Schmidt number that can be used to estimate its value [235,255-259]. For a three-phase catalytic operation, mass transport at the liquid-solid interface can be improved by establishing a high relative particle-liquid velocity [249].

2.5.2.3 Internal Transport Limitation

The concentration of reactants may not be uniform throughout the catalyst particle due to internal transport resistance, if the porous catalyst support was used to distribute active metal particles [255]. When the diffusion in the interior of the catalyst particles is rate determining,

not only are the rates often reduced but selectivities are also affected [244]. The rate of internal diffusion and reaction depends on the catalyst loading w , the intrinsic reaction rate k_{int} , the reactant concentration on the catalyst surface C_s and the internal effectiveness factor η_c . Accordingly the following rate equation can be expressed:

$$r_G = wk_{int}C_s\eta_c \quad 2-7$$

The catalytic effectiveness factor η ($0 \leq \eta \leq 1$) is defined as the ratio of reaction rate per unit volume of catalyst and the maximum reaction rate in the catalyst particle based on C_s . When $\eta \rightarrow 1$, the reactor operates at maximum efficiency, while in the presence of intraparticle transport resistance, η will be less than unity. To determine if the reaction is intrinsically limited or diffusion rate limited, a generalised criterion- the dimensionless Weisz-Prater modulus Φ [260,261] can be applied:

$$\Phi = \frac{(-r_G)\rho_p d_p^2}{D_{\epsilon,G}[G^I]} \quad 2-8$$

Where r_G is the observed reaction rate of gas G per unit gram of catalyst particles, ρ_p is the catalyst density, d_p is the mean diameter of catalyst particles, $[G^I]$ is the initial concentration of gas reactant G in the bulk liquid, and $D_{\epsilon,G}$ is the effective diffusivity of G in the liquid [261]. It was suggested that the use of very small catalyst particles (mainly smaller than 200 μm) can minimise the intraparticle concentration gradients [206].

2.6 Conclusions and Rationale for Current Studies

Some of the following conclusions can be made from the above discussion:

- Pd has been widely used in heterogeneous catalysis due to its outstanding catalytic activities, particularly in the form of nanoparticles on appropriate support materials.
- Physico-chemical synthesis to stabilise Pd NPs on conventional support materials (*e.g.* oxide and carbon) usually requires toxic and expensive chemical agents or a rigorous experimental procedure in order to obtain nanoparticles with uniform sizes and shapes. Deactivation remains as a problematic issue for the use of supported Pd catalysts, which could be caused by chemical poisoning, thermal degradation and leaching of palladium. Alloying Au to Pd to form bimetallic AuPd catalyst was found to have a synergistic enhancement in the activity and selectivity.
- Bioreductive synthesis of Pd NPs supporting on bacterial cells appears to be a promising method to manufacture bio-Pd catalysts with reliable size-control and certain catalytic activities in some applications (*e.g.* remediation of metallic pollutants, hydrogenations and organic chemical synthesis reactions).
- There are desirable requirements to minimise the yield of *trans*-isomers in hydrogenation of vegetable oils and replace stoichiometric oxidants with environmentally-friendly alternatives (*e.g.* oxygen with heterogeneous catalyst) in the oxidation of alcohols; supported Pd or AuPd NPs have the potential to fulfil this need. A good choice for operating and studying the intrinsic mechanism of these reactions is an agitated slurry reactor, in which a perfect mixing needs to be ensured and reaction is not under mass-transfer control.

Based on the literature review provided, it is clear that challenges exist in manufacturing and application of palladium catalysts in heterogeneous catalysis. The work in this thesis

highlights the potential roles of bio-catalysts in organic chemical synthesis reactions using three-phase autoclave reactors. The first part of the work will examine the bio-Pd catalyst in partial hydrogenation of soybean oil, with particular attention paid to minimising the production of *trans*-isomers. The second part of the work will investigate bio-AuPd catalysts in the oxidation of alcohols under solvent-free conditions using compressed air as a green oxidant. Detailed characterisation analysis will also be presented to understand the properties of bio-catalysts and relate these to the catalytic activities observed.

Chapter 3

Experimental Setup and Analytical Methods

3.1 Chapter Overview

This Chapter describes four experimental procedures or methods: i) the preparation of bio-catalyst, ii) the experimental rigs and the standard operating procedure of the chemical reactions, iii) the methodologies for sample analyses, and iv) the techniques for catalyst characterisation. Firstly section §3.2 provides a full list of the commercial materials used in this study, including the information of supplier and specification. It also provides a table giving a brief specification of the instruments employed throughout this work. This is followed by the introduction of the microbial method of manufacturing bio-catalyst in §3.3, describing the lab work carried out with the strain of *Escherichia coli*. The bio-catalysts supported on the other strains reported in the later results chapters were provided by Drs I. Mikheenko and K. Deplanche from the School of Biosciences, University of Birmingham. The setups of two lab-scale semi-batch autoclaves are then described in §3.4, along with detailed instructions of the operating procedure, catalyst pre-reduction, and sampling method. The analytical method, performed using gas chromatography (GC), which has been developed to identify and quantify the products liberated during the reactions is presented in §3.5. Finally, the techniques employed to characterise the bio-catalysts are detailed in §3.6.

3.2 Materials and Equipment

A full list of all the commercial chemicals and materials used in this study is provided in Table 3.1. All the chemicals were used as received without further purification, unless otherwise stated. Table 3.2 presents a list of the major instruments employed for various uses, such as separations, analysis of chemicals and characterisation of catalysts.

Table 3.1 Commercial chemicals and materials used in this study.

Material	Supplier	Specification
<i>For chemical reaction</i>		
2-pentyne	Alfa Aesar, UK	>98% (hydrogenation reactants)
soybean oil	Sigma-Aldrich, UK	
benzyl alcohol, 1-phenylethanol, 1-octanol, 2-octanol, and 1,4-butanediol	Sigma-Aldrich, UK	>99.9% (oxidation reactants)
methyl linolenate, methyl linoleate, methyl oleate, methyl elaidate, methyl stearate, methyl palmitate	Sigma-Aldrich, UK	>99% (GC analytical standards)
benzaldehyde, benzoic acid, benzyl benzoate		
boron trifluoride/methanol	Sigma-Aldrich, UK	10 w/w% (derivatisation reagent)
sodium chloride, sodium hydroxide	Sigma-Aldrich, UK	>99% (reagents)
2-propanol, n-heptane, hexane, and methanol	Sigma-Aldrich, UK	>98% (solvents)
<i>For bio-catalyst preparation</i>		
nutrient broth no. 2 (NB no. 2)	Oxoid, UK	general media for bacteria
sodium fumarate, glycerol	Sigma-Aldrich, UK	≥99% (cellular respiration)
MOPS: 3-(n-morpholino)propanesulfonic acid-NaOH buffer (20 mM, pH 7.0)	Sigma-Aldrich, UK	≥99.5% (biological buffer)
palladium(II) sodium chloride (Na ₂ PdCl ₄)	Sigma-Aldrich, UK	>99.9%
gold(III) chloride hydrate (HAuCl ₄ ·nH ₂ O)		>99.9%
Tin(II) chloride, thiamine hydrochloride, hydrochloric acid, concentrated nitric acid, (Ethylenedinitrilo)tetraacetic acid (EDTA)	Sigma-Aldrich, UK	analytical reagents
phloxine B	Sigma-Aldrich, UK	stains and dyes
<i>Gas</i>		
compressed air	BOC, UK	gas reactant, GC
hydrogen		>99.9% (gas reactant, GC)
nitrogen		>99.9% (inert gas)
hydrogen/argon		10 vol/vol% (chemisorption)
CO		>99.9% (chemisorption)
Helium		>99.9% ^a (GC carrier gas)
<i>Commercial catalyst</i>		
2 wt% Pd/Al ₂ O ₃ , 5 wt% Pd/Al ₂ O ₃	Johnson Matthey	powder, Type 335 ^b
<i>Others</i>		
Sieve	Endecotts Ltd	Aperture size: 63 μm
TEM grids	Agar Scientific, UK	copper ^c
γ-DEX™ 225 (30m×0.25mm×0.25μm)	Sigma-Aldrich, UK	GC capillary columns ^d
SP™-2560 (75m×0.18mm×0.14μm)	Sigma-Aldrich, UK	
RTX-1701 (30m×0.25mm×0.25μm)	Restek, USA	

^a Helium was further purified using a moisture, hydrocarbon and oxygen trap; ^b Type 335 specification: D50:45 (average size of 45 μm with distribution percentage reaches 50%); ^c Holey carbon film supported by a 300 mesh copper TEM grid, grid thickness: 20~30 nm; ^d column specification: Length(m)×Internal Diameter(mm)×Film Thickness(μm).

Table 3.2 Instruments involved in this study.

Instrument	Manufacture	Note
A&D analytical balance	A&D Instruments Ltd.	Series: HR-200
IEC Centra Mid bench centrifuge	DJB Labcare Ltd.	
Ultraspec III UV/VIS spectrophotometer	Pharmacia Biotech, Inc.	optical density (OD) measurement
JEOL 1200EX2 TEM	JEOL, Inc.	Lanthanum hexaboride (LaB6) filament
Emscope SC 500 sputter coater	Emscope	carbon coating
Philips XL-30 Environmental SEM	FEI Company	Oxford Inca 300 EDS system
Equinox 3000 Powder X-Ray diffractometer	Inel, USA	CuK α radiation
TG 209 FI	NETZSCH	ceramic crucible, Proteus analysis
Autochem II 2920 analyser	Micromeritics	thermal conductivity detector (TCD)
Accupyc II 1340 Pycnometer	Micromeritics	density measurement
Varian CP-3380 Gas Chromatography	Varian, Inc.	Flame Ionisation Detector (FID)

3.3 Bio-Catalyst Manufacture

The novel biochemical method to synthesise biomass-supported monometallic Pd or bimetallic AuPd nanoparticles (NPs) is based on the sacrificial hydrogen strategy. The detailed preparation procedure using *Escherichia coli* (the major strain of bacteria investigated in this work) is described in the following section.

3.3.1 Bacterial Growth and Metal Solutions Preparation

Specially-grown E. coli

Escherichia coli MC4100 (provided by Prof J.A. Cole, University of Birmingham, UK) precultures were grown overnight at 37 °C under anaerobic respiratory conditions (NB no. 2 supplemented with 0.4% sodium fumarate (wt/vol) and 0.5% glycerol (vol/vol)) [177]. The precultures were then inoculated into 2 litre Durham bottles, which were filled to the brim with medium (NB no. 2) and sealed with rubber stoppers, degassed *via* a syringe through the stopper, and grown anaerobically in the same way as above for overnight. The cells were harvested by centrifugation (7000 rpm, 4 °C, 10 min), washed three times in degassed MOPS-NaOH buffer (20 mM, pH 7.0), re-suspended in a known volume of the same buffer under N₂, and stored at 4 °C as concentrated cell suspensions until use.

The cell concentration, g(dry weight).l⁻¹, was estimated from optical density (OD) measurements using spectrophotometer at 600 nm by reference to a pre-determined OD₆₀₀ to dry weight conversion, an OD₆₀₀ of 1 corresponding to a biomass concentration of 0.482 g.l⁻¹ for *E. coli* [23].

'Second-life' E. coli

The fermenting bacteria *E. coli* was harvested from a 4-litre fermentation bioreactor after 3 weeks of hydrogen production [262], the primary process. The harvest 'second-life' *E. coli* cells were divided for two different treatments to active cells before palladisation: (A)

Incubated under H₂ at 30 °C (30 min), then H₂ substituted by N₂; and (B) Transferred into anaerobic respiratory medium (NB no. 2 with 0.4% sodium fumarate (wt/vol) and 0.5% glycerol (vol/vol)), left overnight at 30 °C.

Pd (II) and Au (III) solutions

An aqueous Pd(II) solution (2 mM) was made by dissolving an appropriate amount of sodium tetrachloropalladate (Na₂PdCl₄) in HNO₃ (0.01 M), to a pH of 2.3 as this was previously shown to be optimal for production of active catalyst using whole cells [26]. Similarly, aqueous Au(III) solution (2 mM) was made by dissolving an appropriate amount of hydrogen tetrachloroaurate (HAuCl₄.nH₂O) into distilled water and adjusting the pH to 2.3.

3.3.2 Metallisation of Bacteria

Preparation of bio-Pd

The above harvested resting cell suspension was palladised following a standard procedure as described below. A calculated volume of the resting cell suspension was transferred anaerobically into an appropriate volume of degassed (vacuum pump) 2 mM Pd(II) solution, the amount of each depending on the final Pd loading required, *e.g.* weight of Pd:dry weight of cells being 1:19 or 1:3 to give loadings of 5 wt% and 25 wt% Pd on biomass respectively. The cell/Pd(II) mixture was left to stand at 30 °C for 30 mins to allow the biosorption of Pd(II) complexes [263]. After that H₂, as the electron donor, was sparged through the suspension (200 ml.min⁻¹, 20 min) for reduction [20]. In some cases sodium formate was added; this is noted where appropriate. Reduction of cell surface-bound Pd(II) to Pd(0) was confirmed by observing the colour of the mixture changing from yellow to grey during H₂ sparging [170]. The Pd loaded cells were allowed to settle overnight under gravity. Thereafter, the black bio-Pd(0) precipitate was harvested by centrifugation (4000 rpm, 4 °C, 15 min), while the complete removal of Pd(II) from the solution was confirmed by assaying

the cell/Pd mixture supernatant for residual Pd(II) by the SnCl₂ method to be described in §3.3.3. The solid was washed three times in distilled water and one final wash in acetone. The washed bio-Pd(0) was then re-suspended in a small volume (~5 ml) of acetone, left to dry in air and finally finely ground to approximately 63 µm particle diameter (estimated by sieve) in an agate mortar.

Preparation of bio-AuPd

Overall, the procedure of bio-AuPd preparation is a successive reduction of Pd(II) and Au(III) on bacterial biomass. The black bio-Pd(0) precipitate, after washing in distilled water three times, was re-suspended in a known volume of distilled water. The bio-Pd(0) suspension was degassed and then transferred anaerobically into a bottle containing an appropriate amount of 1 mM Au(III) solution saturated with hydrogen by bubbling gas (200 ml.min⁻¹, 1 h), the amount of each again was adjusted based on the final ratio of Pd:Au (w:w) required (*i.e.* 1:4, 2.5:2.5, and 4:1). The mixture was then allowed to react overnight in a rotary shaker (150 rpm, 30 °C) during which the suspension developed an intense purple/dark red colour from yellow [160], indicating the formation of colloidal gold Au(0). The AuPd loaded bacterial cells were allowed to settle overnight under gravity, and the supernatant was assayed for residual Pd(II) and Au(III) to ensure complete removal of both metal species (methods refer to §3.3.3). The final material bio-AuPd precipitate was recovered as the same process described above for bio-Pd, washed three times in distilled water, once in acetone and left to dry in air, followed by grinding into fine powder. Figure 3.1 depicts simplified procedure of metallisation steps during the bio-catalyst preparation.

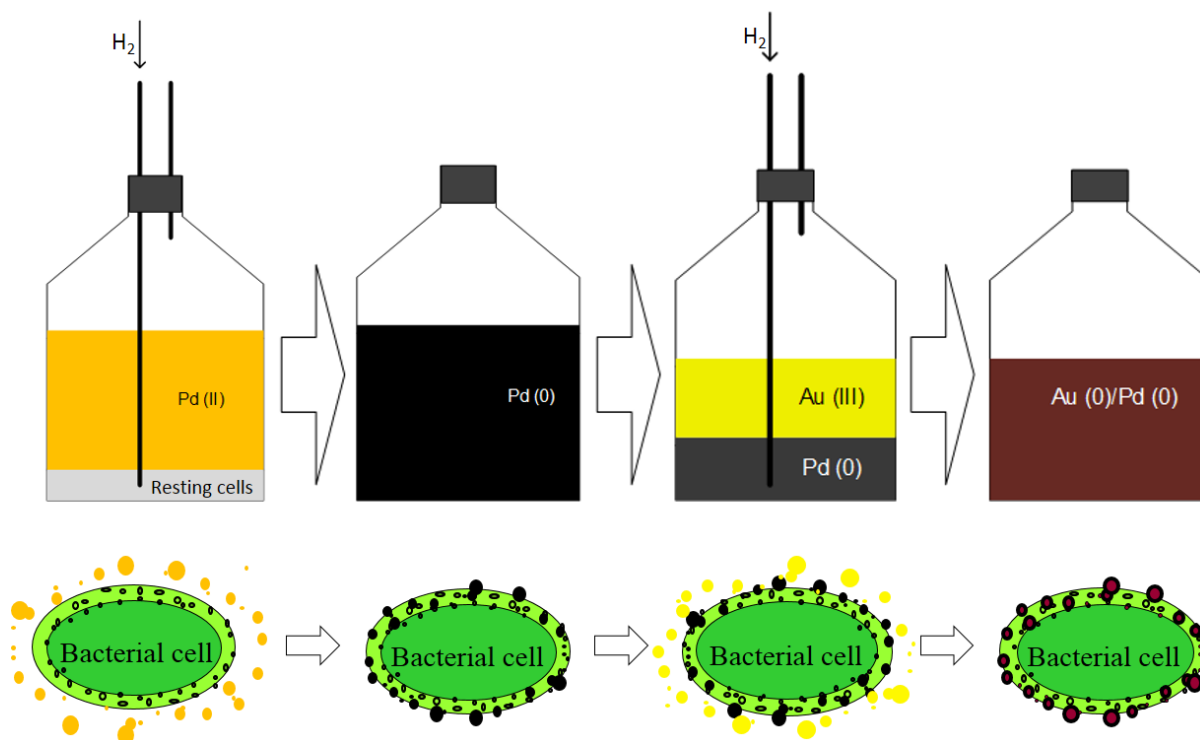


Figure 3.1 Simplified procedure of bio-catalyst manufacturing using bacterial cells.

3.3.3 Quantitative Assays for Pd(II) and Au(III)

Before harvesting metallised biomass, the concentration of free Pd(II) or Au(III) ions in the cell/Pd in samples supernatants was monitored in order to confirm the complete reduction of Pd(II) and Au(III) using the following methods.

Assay of Pd(II)

Complete removal of residual Pd(II) from the cell/Pd mixtures supernatants was confirmed by carrying out the spectrophotometric SnCl₂ method [264]. The Sn(II) reagent was made by dissolving 29.9 g of SnCl₂ powder into 500 ml of concentrated HCl. For Pd(II) assay, 0.2 ml of sample was well mixed into 0.8 ml of SnCl₂ solution in a 1.5 ml plastic cuvette and the absorbance at 463 nm was determined after one hour of incubation at 30 °C against a blank prepared in the same way (distilled water *in lieu* of sample). The system obeyed Beer's law over the range 5~80 ppm Pd(II).

Assay of Au(III)

Removal of Au(III) from the sample supernatants was monitored by the thiamine-phloxine assay as described by Fujita *et al.* [265]. The following were added to 1 ml of test solution in an assay tube and mixed well: 0.5 ml of 0.5% (w/v) methylcellulose, 1 ml of 10 mM thiamine, 2 ml of EDTA-citrate buffer (0.05 mM EDTA, 0.1 mM citric acid pH 4.6), 1 ml of 1 mM phloxine and 4.5 mL of distilled water. Assay tubes were incubated in a water bath (20 min; 40 °C) and absorbance at 570 nm was recorded against a blank prepared in the same way (distilled water *in lieu* of sample). The system obeyed Beer's law over the range 0.2~20 ppm Au(III).

3.4 Apparatus and Procedure

This section covers the employment of two autoclaves throughout this study, *i.e.* one 500 ml Baskerville autoclave reactor for hydrogenation and the other 100 ml Parr autoclave reactor for oxidation reactions.

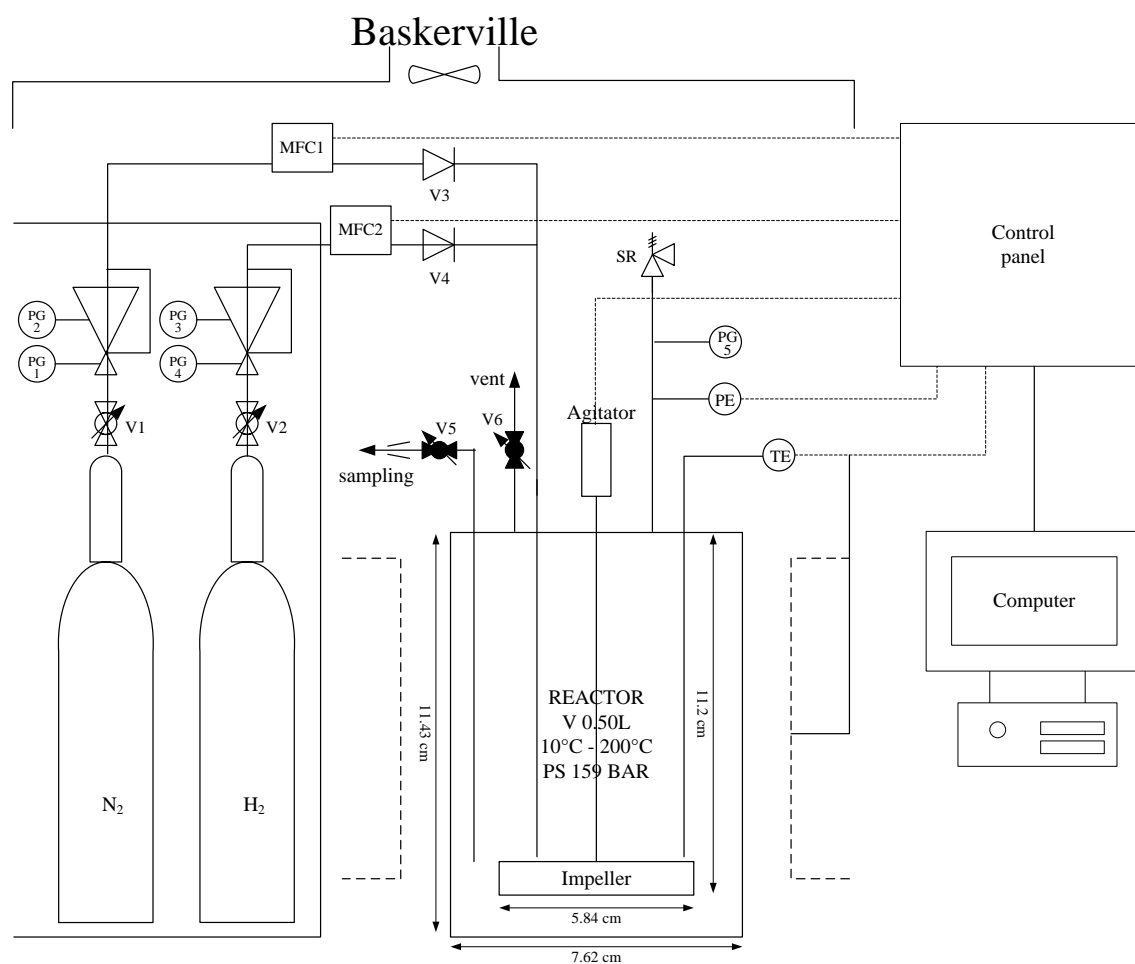
3.4.1 Experimental Rigs

Baskerville Reactor for Hydrogenation Reactions

The hydrogenations were all carried out in a 500 ml stainless steel autoclave reactor (max pressure 159 bar, temperature range 10 to 200 °C) manufactured by Baskerville Reactors and Autoclaves Ltd, Manchester, UK. Figure 3.2 shows a schematic of this reactor setup.

The 500 ml autoclave (cylindrical, flat-bottomed vessel, diameter×height: 7.62×11.43 cm) is a typical gas-sparging type reactor equipped with a gas inlet pipe reaching near to the bottom of the reactor for the purpose of gas dispersion into the slurry phase. The agitator (50~1500 rpm) used for mixing is a four-bladed impeller (5.84 cm diameter). The sampling line, from which aliquots could be removed during the reaction, is a small diameter (0.32 cm) dip-pipe

reaching near to the bottom of the reactor. A thermocouple is fitted to monitor the real-time temperature of the slurry, together with a heating jacket around the vessel that can be programmed to a desired set-point for the control of the temperature in the unit. In addition, a venting line for gas releasing and a safety relief bursting disc (SR, set at 16 bar) are located on the top of the reactor head. During the experiments, the heat flow, gas uptake, pressure and temperature in the reactor and temperature of the heating jacket were all monitored and recorded by a computer through an interface control system (Eurotherm Instruments, Inc.).



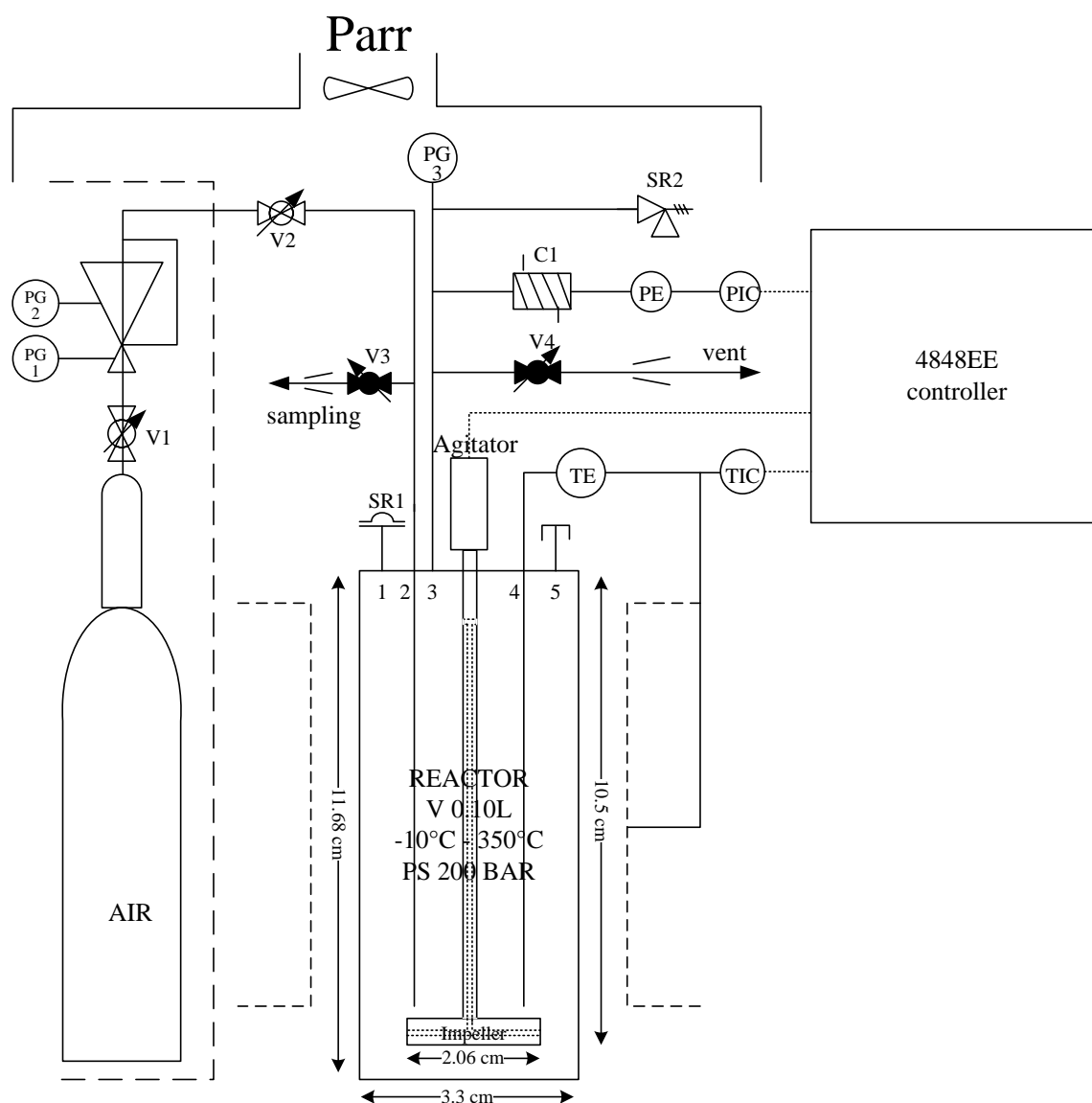
Valves:		Gauges:	
V1, V2	gas cylinder regulator	PG1 ~ PG5	mechanical pressure gauge
V3, V4	as inlet non-return valve	Indicators:	
V5	sampling valve	TE, PE	temperature sensor, pressure sensor
V6	gas release valve		
Others:			
MFC1, MFC2	mass flow controller		
SR	safety relief bursting disc (set at 16 bar)		

Figure 3.2 Schematic of the Baskerville autoclave reactor for the hydrogenation reactions.

Parr Reactor for Oxidation Reactions

Catalyst testing in aerobic oxidation was conducted in another stainless steel autoclave reactor (max pressure 60 bar, temperature range 10 to 350 °C) manufactured by Parr Instrument Company, Illinois, US. Figure 3.3 shows a schematic of the original Parr autoclave used in this study. During the course of the experimental study it was necessary to make a number of modifications to the Parr reactor which are further described in detail in the results chapter §5.2.1.2.

This 100 ml autoclave is a cylindrical and flat-bottomed vessel with the inside dimensions of 3.30 cm(diameter)×11.68 cm(height). An efficient gas entrainment impeller is equipped to maximise the gas dispersion into a liquid system. This is obtained with a specially designed hollow four-bladed impeller (2.06 cm diameter) attached to a hollow stirring shaft through which gas is continuously recirculated from the head space above the liquid through the impeller into the liquid phase. As with all impellers, the speed of the stirrer creates a vacuum at the tip of the impeller. Gas enters openings near the top of the shaft and is pulled through dispersion ports located at the tips of the impellers. In the present Parr system with dispersion ports located at the very tips of the impellers, increased stirring speed leads to higher vacuum and associated increase of driving force for this very effective gas dispersion system. The liquid sampling valve is attached to the same fitting as the gas inlet valve and connected to the same dip tube. With this arrangement, incoming gas is always introduced below the surface of the liquid and the operator is provided with a means for clearing the dip tube to be sure that any sample taken during a run will be representative of the charge.



Valves:		Indicators:	
V1	gas cylinder regulator	TE	temperature sensor
V2	gas inlet control valve	TIC	temperature indicator
V3	sampling valve	PE	pressure sensor
V4	gas release valve	PIC	pressure indicator
Others:			
PG1, PG2, PG3	mechanical pressure gauge		
SR1	relief valve (set at 40 bar)		
SR2	safety rupture disc (set at 70 bar)		
C1	original built-in condenser		

Figure 3.3 Schematic of the original Parr autoclave reactor for the oxidation reactions.

3.4.2 Operation Procedure for Baskerville and Parr Reactors

A standard procedure of the reactor operation is described in this section with specific reaction conditions listed individually in the corresponding results chapters.

Reactor Operating

Typically, the autoclave reactor was charged with a weighed mass of catalyst and a known volume of solvent-free (unless otherwise stated) liquid substrate. After filling, the reactor was closed and purged with nitrogen three times in order to remove either the dissolved oxygen in the liquid or the remaining oxygen in the headspace of the reactor. Then the mixture was programmed to heat up to the desired reaction temperature with a gentle stirring speed (~500 rpm). Thereafter the reaction was initiated by switching from a nitrogen gas flow to a reactant gas flow (*i.e.* hydrogen for hydrogenation and air for oxidation). For a typical semi-batch operation, gas reactant was through-flow and the reactant gas consumed was automatically replenished to maintain the set point of the pressure by the controller. Thus the reaction proceeded isothermally under a constant pressure throughout the set reaction time, during which liquid samples were taken periodically. The total reaction time depended on the operating conditions, the catalyst activity and the catalyst amount. After each experiment, the reactor was allowed to cool down to minimise the amount of vapour. Residual liquid chemicals were stored in waste drums prior to professional disposal. Table 3.3 illustrates the range of different variables used for the different catalysts studied.

Table 3.3 Parameters investigated and varied for different catalysts in this study.

Substrate	Hydrogenation in Baskerville		Oxidation in Parr	
	2-pentyne	soybean oil	benzyl alcohol	1-phenylethanol, 1-octanol 2-octanol, 1,4-butanediol
Solvent	isopropanol	solvent-free	solvent-free	solvent-free
Catalyst	Pd/Al ₂ O ₃	Pd/Al ₂ O ₃ bio-Pd ^a	bio-AuPd ^a	bio-AuPd
Stirring speed (<i>N</i> , rpm)	1000	500~1200	1200	1200
Agitator Reynolds number (Re) ^b	25241	3681~8834	1619	-
Power consumption (<i>P</i> , w.g ⁻¹) ^c	0.132	0.016~0.228	0.004	-
Pressure (<i>p</i> , bar)	2, hydrogen	3~7, hydrogen	5, air	5, air
Flow rate (<i>F</i> , ml.min ⁻¹)	NA	NA	0~350	200
Temperature (<i>T</i> , °C)	40	100-150	100~140	140~160

^a Various strains of bacteria used as the catalyst support, as detailed in individual sections. ^b Turbulence was assumed for both hydrogenation system (Re>2300) and oxidation system (a gas entrainment impeller as described in §3.4.1), detailed calculation refers to Appendix §8.3.1. ^c calculation refers to Appendix §8.3.1. NA: not applicable.

Catalyst Pre-reduction

Catalyst pre-treatment usually consists of activating a catalyst prior to its use in a chemical reaction. For example, catalyst after long-term storage may be covered with impurities such as moisture or adsorbed O₂ or become otherwise oxidised [266]. Reduction under a flow of H₂ at a sufficiently high temperature to achieve reduction is necessary to regenerate the active sites, or reduced atoms of active metals, which are responsible for the catalytic activity.

In-situ pre-reduction to the catalyst before reaction was carried out if solvent was used in the reaction system, *i.e.* 2-pentyne hydrogenation. After charging the required amount of catalyst and solvent into the reactor, a flow of hydrogen (500 ml.min⁻¹) was bubbled through the system for 20 min with a gentle stirring of 500 rpm. The reactor was then opened again and the substrate was added into the catalyst/solvent mixture for the subsequent reaction.

Ex-situ activation of the catalyst was carried out in the case of bio-AuPd catalyst used for the solvent-free oxidation. The catalyst was placed in a dry and clean glass vial, which after sealing and applying a vacuum was half-immersed into an oil bath with constant temperature of 120 °C for reducing the active metal. The *ex-situ* pre-reduction started by continuously flowing H₂ through the ‘catalyst bed’ in the vial for 1 hour. The reduced catalyst was kept under nitrogen until required for use.

Sampling method

Liquid samples from the reactor were taken periodically, *via* a sampling valve, ensuring that the volume purged before sampling was higher than the tube volume. In the case of soybean oil hydrogenation, liquid samples taken were subjected to derivatisation. The derivatisation of fatty acids to fatty acid methyl esters, which offer excellent stability, and provide quick and quantitative samples for GC analysis, is performed using an alkylation derivatisation reagent. A typical derivatisation procedure was as follows: 2 ml of 0.5 M sodium hydroxide in

methanol was added into the liquid sample (~0.2 ml) in a test tube, which was then placed in a water bath at 60 °C for 15 mins; After cooling, 2 ml of boron trifluoride/methanol (10 w/w%) were added and the mixture was kept under temperature of 60 °C for a further 10 mins; 2 ml of a saturated solution of NaCl and 1 ml hexane were added sequentially and the tube was shaken to aid separation and dissolution of the fatty acid methyl esters (FAMES) in the hexane layer top. After allowing the tube to stand for a few minutes and the layers to settle, the hexane layer was extracted and placed in a small, clean vial and kept in a cool dark place until further composition analysis.

3.5 Qualitative and Quantitative Analytical Methods to Liquid Sample

3.5.1 Gas Chromatography

The compositions of the reaction mixtures were analysed using a Varian CP-3380 Gas Chromatograph equipped with a Flame Ionisation Detector (FID) (Figure 3.4). The FID uses hydrogen and air to partially burn the organic constituents that are carried by helium through a retention column. This produces ionic sub-compounds that are detectable by the FID and the resulting signals shown at different retention times are proportional to the quantity injected into the GC, with retention time corresponding to individual components.

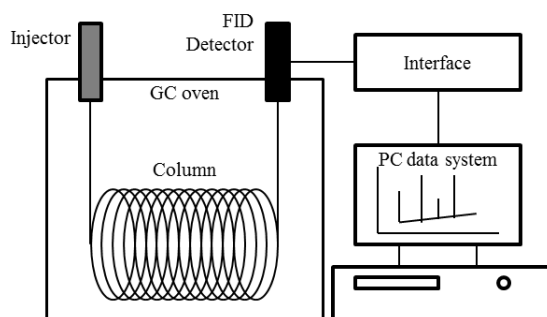


Figure 3.4 Simplified schematic of the Varian CP-3380 gas chromatography system.

An optimised chromatographic separation begins with the column. The selection of the proper capillary column is of crucial importance, and should be based on four significant

factors: stationary phase (match to the polarity of the sample), column I.D. (dependent on the size of the sample), film thickness (dependent on the volatility of the sample), and column length (to increase the resolution when needed). An appropriate oven method then needs to be developed to keep the column at the right temperature or temperature ramp, allowing the elution of different substrates to be sufficiently separated from each other to obtain distinct peaks but within a reasonable amount of run time. Thereafter known chemical standards can be injected in the GC to determine the corresponding retention time, which allows the identification of the compounds from experimental samples. By injecting a standard containing a series of known concentrations, a calibration plot between the signal versus the analyte concentration can be established which permits the quantifications of the analyte concentrations in the experimental samples. Hence, the qualitative and quantitative analysis of chemicals can be established. The following Table 3.4 summarises the specific columns and oven methods established for the sample analysis throughout this study.

Table 3.4 GC columns and oven conditions for the analysis of different substrates in this study.

	2-pentyne hydrogenation	Soybean oil hydrogenation	Alcohol oxidation
<i>GC Column</i>			
capillary column	30 m γ -DEX TM 225	75 m SP TM -2560	30m RTX-1701
<i>Carrier gas flow rate</i>			
helium, ml.min ⁻¹	30.0	24.0	33.3
<i>Injector</i>			
temperature, °C	200	250	230
injection volume, μ l	0.1	0.5	0.1
<i>Detector</i>			
temperature, °C	220	265	230
range	11	11	11
<i>Oven Conditions</i>			
equilibrium time	-	5.0 min at 200 °C	0.5 min at 130 °C
isothermal temperature and time	40 °C for 10 min	-	-
ramp rate	-	4 °C/min	20 °C/min
2 nd isothermal temperature and time	-	240 °C for 15 min	240 °C for 7 min

3.5.2 Assays for Residual Pd(II) and Au(III)

In order to check if the active metal components, *i.e.* Pd(II) and Au(III), leach from the catalyst particles into the bulk mixture during the course of the reaction, assays were conducted to the supernatant liquid (after centrifugation) using the same methods as described in §3.3.3.

3.6 Catalyst Characterisation Techniques

The morphology of the catalyst, dispersion of the active metal particles and the interaction with the support are known to be strongly related to the catalyst activity and selectivity toward different products. To obtain the information of the catalyst characteristics, this section describes the characterisation techniques employed in this study.

3.6.1 Thermogravimetric Analysis

Thermogravimetric analysis (TGA) is used to record small and precise changes in weight as a function of programmed temperature ramps under certain gas atmospheres (*e.g.* H₂, N₂, or air, depending on the application). TGA is commonly employed to determine characteristics of materials such as polymers, to determine the absorbed moisture content of materials, degradation temperatures and levels of inorganic and organic components. If a species is thermally stable, over a certain temperature range there will be negligible mass change corresponding to little or no slope in the TG trace. However unstable materials will show a mass loss with temperature due to degradation reactions occurring. Hence TGA is a very useful technique to obtain the limit of upper temperature for use of a material, where beyond this temperature the material will begin to degrade.

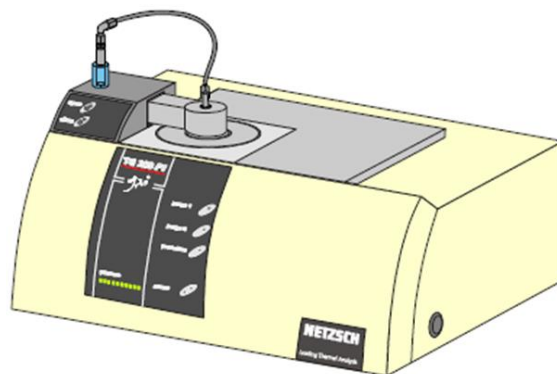


Figure 3.5 TG 209 *F1* measuring unit for thermogravimetric analysis.

In this study air was chosen as the oxidising atmosphere to perform thermogravimetric analysis of combustion behaviour [267], which provides a useful indication of the catalyst's physical stability in the oxidation reaction environment. A thermal analyser instrument TG 209 *F1* Iris developed by NETZSCH was employed for all the thermal studies (Figure 3.5). The bio-catalyst powder is evenly spread over the bottom of the ceramic crucible and precisely weighed with an analytical balance (Table 3.2). TGA was performed in an atmosphere of flowing air ($50 \text{ ml}\cdot\text{min}^{-1}$) at a linear heating rate of $10 \text{ K}\cdot\text{min}^{-1}$, covering the temperature range from ambient to 1000 K. The temperature program and the corresponding curve of weight (percentage) against temperature are recorded by the computer data system. After the complete curve is obtained, results processing such as curve smoothing and peak detection are performed by using the *Proteus* software to find the exact points of inflection. Based on the TGA analysis, the reaction temperatures were selected carefully during the bio-catalyst catalytic testing, for example to avoid using temperatures at which the catalyst may degrade.

3.6.2 CO Pulse Chemisorption

CO Pulse Chemisorption technique uses the principle of gas molecular chemical adsorption on catalyst sites to determine information on active surface area, percent metal dispersion, and active metal particle size by applying measured doses of carbon monoxide to the sample.

Figure 3.6 shows the Micromeritics Autochem II 2920 analyser equipped with a thermal conductivity detector (TCD) used for CO Pulse Chemisorption in this study.



Figure 3.6 Micromeritics Autochem II 2920 for CO chemisorption analysis.

This characterisation technique involves firstly the cleaning the metal surface by purging hydrogen over the sample while ramping the temperature, which should reach a value high enough to remove any contaminants or moisture (informed by TGA, §3.6.1) but not so high as to cause sintering or fusing of the sample. The temperature was then lowered to room temperature (25 °C) under an inert gas (*e.g.* helium, argon, or nitrogen), and known pulses of analytical gas (*i.e.* CO) measured by the injection loop were applied to the cleaned catalyst sample either until each active site has reacted and no more adsorption is detected or otherwise for a prescribed maximum number of pulses (20). The gas flow is monitored by the TCD and when few consecutive pulses contain the same amount of initially administered gas, the catalyst surface is said to be saturated, *i.e.* a monolayer is formed on the catalyst surface. The quantity of molecules chemisorbed is the difference between the total amount of reactant gas injected and the sum amount that did not react with the active sites of the sample as measured by the detector. It is worth noting here that the chemisorption is not

recommended to be used for bimetallic catalyst samples such as Au-Pd/ TiO_2 since different metals have different binding energies and stoichiometric factors for an analytical gas.

In this study, the catalyst powder was precisely weighed and well dispersed on the top of quartz wool in the clean sample tube, through which the gas flows downwards. Approximately the same amount of sample was used for each analysis for comparing data from sample to sample. The CO chemisorption analysis was performed under the following temperature program. The catalyst metal surface was first cleaned by being heated to 100 °C (10 °C/min) under hydrogen (10 vol/vol% H_2/Ar , 50 ml.min⁻¹), then allowed to cool to room temperature and subsequently CO gas was introduced by pulse-dosing, flushing with pure helium in between.

The percent metal dispersion, metallic surface area and active particle size can be determined from the following equations calculated by the software of the Micromeritics Autochem II 2920:

$$Dispersion, \% = 100 \left(\frac{V_s F}{22414 \times W_s} \right) GMW \quad 3-1$$

$$SA_{Metallic} = \left(\frac{V_s}{SW \times 22414} \right) \times (SF_{calc}) \times (6.123 \times 10^{23}) \times (SA_{calc}) \quad 3-2$$

where V_s is the volume of adsorbed CO (cm³ at STP), F is the stoichiometry factor, W_s is the sample weight (g), the gram molecular weight (GMW) is a weight average of the number of moles of each active metal, and the SA_{calc} is the calculated specific surface area (per gram of metal).

3.6.3 Electron Microscopy

The techniques of electron microscopy are particularly useful for characterisation of bio-catalysts, since they provide direct images of surfaces of the biomass, identification of the

element, and structural information of the active phases. This section includes the application of scanning electron microscopy (SEM), backscattered-SEM (BSE), energy dispersive X-ray analysis (EDS), and transmission electron microscopy (TEM).

SEM-EDS

A scanning electron microscope (SEM) is a type of electron microscope that images a sample by scanning it with a high-energy beam of secondary electrons in a raster scan pattern. The electrons interact with the atoms that make up the sample producing images that reflect the information about the specimen's surface topography of a surface layer 5~50 nm thick. For specimens with thick surface coatings, no information is provided regarding the underlying base. Back-scattered electron (BSE) is another type of signal produced by an SEM and used to image compositional contrast. The intensity of the BSE signal is strongly related to the atomic number (Z) of the chemical composition, by almost linear monotonic increase. In other words, heavy elements (high atomic number) backscatter electrons more strongly than light elements (low atomic number), and appear brighter in the BSE image [268]. In addition, SEM always includes an Energy-dispersive X-ray spectroscopy (EDS) capability, which is a powerful analytical technique used for the elemental analysis or chemical characterisation of a sample. It relies on the investigation of an interaction of a source of X-ray excitation and a sample. Its characterisation capabilities are due to the fundamental principle that each element has a unique atomic structure allowing X-rays that are characteristic of an element's atomic structure to be identified uniquely from one another.

In this study dried samples of catalyst powder were mounted onto a microscope stub, and coated with an ultrathin layer of electrically conducting material (graphite) by high-vacuum evaporation (Emscope SC 500 sputter coater; Table 3.2), then examined on a Philips XL-30 Environmental SEM fitted with an Oxford Instruments Inca energy dispersive X-ray spectroscopy (EDS) system, operating at an accelerating voltage of 10 kV. The

backscattering detector was used to allow for visualisation of metallic nanoparticles on the biomass and elemental analysis of the metals (Pd and Au) was determined by EDS. Detector controlling, analysing and processing were performed using INCA software.

TEM

Transmission electron microscopy (TEM) is capable of imaging at a significantly high resolution (usually ~20 nm) for examining material features as small as a single column of atoms. The principle behind the technique is that a beam of electrons is transmitted through an ultrathin specimen which interacts with the specimen as it passes through, leading to the generation of a corresponding image at a detector. The specimen must be of sufficiently low density to allow electrons to travel through it. These thin samples can be produced in different ways depending on the material under analysis, the desired information to obtain from the specimen, and the availability of equipment. For instance, dry materials that have dimensions small enough to be electron transparent, such as powders or nanotubes, can be quickly prepared by the deposition of a dilute sample containing the specimen onto support grids or films and in use after drying. On the other hand, samples like biological material contains large quantities of water which must be removed since the TEM works in vacuum, thus an ultrathin sectioning method is usually employed using fixed, dehydrated samples. To avoid disruption as a result of the loss of water, the material was preserved with fixatives to maintain the original stable structures. The material is then dehydrated in alcohol or acetone. After that, the specimen is embedded in plastic that polymerises into a solid hard plastic block. The block is cut into thin sections by a diamond knife in an instrument called ultramicrotome. Each section is only 50~100 nm thick. The thin sections of the sample are placed on a copper grid. The slice of tissue can then be studied under the electron beam.

In this study the TEM specimens of catalyst were prepared in the two ways (*i.e.* whole cells and sections) as mentioned above. More specifically, the former simple method is to disperse

the dried catalyst powder in ultra-high purity water. A drop of the suspension is then allowed to evaporate on a holey carbon film supported by a 300 mesh copper TEM grid. For viewing the detailed cells structure in sections, the later complex sectioning procedure is applied to prepare the specimen using freshly harvested metal-loaded bacteria. The pellets of metal-loaded bacteria were rinsed twice with distilled water, fixed in 2.5% (wt/vol) glutaraldehyde, centrifuged, re-suspended in 1.5 ml of 0.1 M cacodylate buffer (pH 7) and stained in 1% osmium tetroxide in 0.1 M phosphate buffer, pH 7 (60 min). Cells were dehydrated using an ethanol series (70%, 90%, 100%, 100%, 100% dried ethanol, 15 min each) and washed twice in propylene oxide (15 min, 9500g). Cells were embedded in epoxy resin and the mixture was left to polymerise (24 h; 60 °C). Sections were cut from the resin block with a diamond knife in ultramicrotome, and placed onto a copper grid.

A JEOL 1200EX2 TEM operating at accelerating voltage of 80 kV was employed to view the specimens. The TEM images were acquired in Gatan Digital Micrograph and subsequently processed with the aid of Image J software. For the measurement of the particle size distribution, at least 100 individual surface metal particles were examined for each catalyst.

3.6.4 X-Ray Diffraction

X-ray diffraction (XRD) is a non-destructive analytical technique which reveals information about the crystallographic structure, chemical composition, and physical properties of materials and thin films. The atomic planes of a crystal cause an incident beam of X-rays to be refracted at specific angles, from which the generated pattern allows the identification of the structure when compared to a database of XRD patterns. The crystal size can be calculated from the width of the peaks, by application of the Scherrer's equation [269] as:

$$L = \frac{K \lambda'}{B \cos \theta} \quad 3-3$$

where λ' is the X-ray wavelength in nanometer (nm), B is the peak width of the diffraction peak profile at half maximum height resulting from small crystallite size in radians and K is the Scherrer constant related to crystallite shape.

In this study X-ray powder diffraction patterns were acquired using an Equinox 3000 Powder X-Ray diffractometer. The catalyst powder is packed into the sample cup tightly so that the powder is level with the top of sample cup. The analysis was conducted by directing monochromatic high-intensity CuK α radiation ($\lambda' = 0.154056$ nm) at the powder specimen. The software Match! is employed to process the obtained data, and the powder pattern was compared to references in the Crystallography Open Database (COD).

Chapter 4

Selective Hydrogenation Using Bio-Pd Catalyst

4.1 Chapter Overview

This chapter describes the evaluation of the catalytic performance of both conventional palladium catalyst ($\text{Pd}/\text{Al}_2\text{O}_3$) and biomass-supported palladium nanoparticles (bio-Pd) for two hydrogenation reactions of industrial significance. Reactions were all carried out in a 500 ml Baskerville autoclave reactor (as described in §3.4.1) in a semi-batch manner with a through-flow of hydrogen gas. Firstly in §4.2, the liquid phase hydrogenation of 2-pentyne, which may include reactions of both the saturation of carbon-carbon triple-/double-bond and the *cis-trans* isomerisation of double-bond, was studied. Several systematic studies have been previously published by group members *e.g.* Bennett *et al.* [24,270]. In their work a 5wt%Pd/*D. desulfuricans* bio-catalyst was investigated and revealed a higher selectivity towards *cis*-2-pentene although a lower initial reaction rate (~70% slower) in comparison with a conventional 5wt%Pd/ Al_2O_3 catalyst, showing *cis/trans* ratios of 2.5 and 2.0 at a 2-pentyne conversion of 92% respectively. The work reported here extends earlier studies to explore the potential for using *Escherichia coli* as the bio-Pd catalyst support.

The other substrate used for hydrogenation investigation was soybean oil (§4.3), which is a complex mixture of fatty acids usually of different degrees of unsaturation. The chemistry of soybean oil hydrogenation is similar to, but more complicated than 2-pentyne hydrogenation, being a saturation reaction of multiple carbon-carbon double bonds simultaneously involving geometric (*cis-trans*) and positional isomerisations. Enhancing the production towards the desirable *cis*-monoene (*i.e.* *cis*-C18:1) in this catalytic process remains a problematic issue in industry. Herein, the primary objective is to investigate the catalytic performance of the bio-catalyst for the partial hydrogenation of soybean oil, with a specific aim of improving the

production of *cis*-isomer. This is the first time that the bio-Pd catalyst has been tested in soybean hydrogenation.

Finally conclusions were drawn in §4.4 to summarise the catalytic performance of bio-Pd, as a novel heterogeneous catalyst, in the hydrogenation of both 2-pentyne and soybean oil.

4.2 Hydrogenation of 2-Pentyne

The reaction network of 2-pentyne hydrogenation is shown in Figure 4.1, including the saturation of the carbon-carbon triple bond (step 6), the saturation (step 8 and step 9) and the *cis-trans* isomerisation (step 7) of the formed double bond. The *cis*-isomer is the specifically sought in industrial hydrogenations such as olefin metathesis [271].

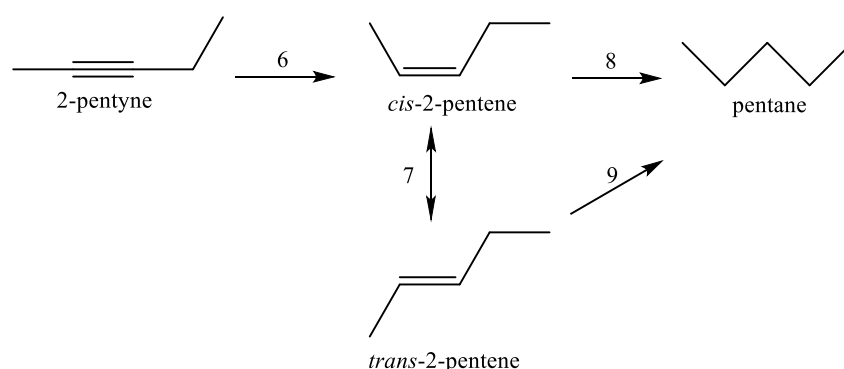


Figure 4.1 The overall integral reaction network of 2-pentyne hydrogenation. Reaction step numbers shown maintain consistent with those in the kinetic study in Appendix 8.1.1.

In this section, the reaction conditions employed were optimum conditions determined by Bennett *et al.* [270] for minimising the mass transfer limitations, which were a temperature of 40 °C, a constant hydrogen pressure of 2 bar, and a stirring speed of 1000 rpm. For all the 2-pentyne hydrogenation experiments, the amount of the substrate used was 4 ml of 2-pentyne in 150 ml of isopropanol as a solvent. The Pd loading was maintained identically as 0.375 mg(Pd).ml(2-pentyne)⁻¹ for each test. The catalyst weight, if of a variable Pd loading (*e.g.* 2wt%, or 5wt%), was adjusted in order to keep constant the weight of Pd among the various experiments. Reactant and product profiles over the course of the reaction were followed by

withdrawing liquid samples for the analysis by gas chromatography (column and oven method refer to Table 3.4 in §3.5.1). Results are all presented from at least triplicate experiments as mean \pm standard error of mean, unless otherwise stated. Error bars are within the dimensions of the symbols if not shown. Each catalyst was sampled from the same preparation, unless otherwise stated. The catalytic activity of the Pd catalyst was mainly evaluated by estimating the conversion of 2-pentyne, which was defined as the fraction of the 2-pentyne that has been consumed with respect to the original amount after corresponding reaction time as follows:

$$\text{2-pentyne conversion \%} = \frac{[\text{2-pentyne}]_0 - [\text{2-pentyne}]_t}{[\text{2-pentyne}]_0} \times 100\% \quad 4-1$$

where $[\text{2-pentyne}]_0$ and $[\text{2-pentyne}]_t$ correspond to the concentrations at initial time ($t=0$) and subsequent time (t) respectively.

The typical concentration profiles for 2-pentyne hydrogenation using 2wt%Pd/*E. coli* under the aforementioned conditions (40 °C, 2 bar, and 1000 rpm) are shown in Figure 4.2. Complete hydrogenation of 2-pentyne was achieved within 40 mins. *Cis*-2-pentene was observed as the major product during the initial 30 mins, suggesting a preferentially *syn*-addition of hydrogen onto the triple bond ($\text{C}\equiv\text{C}$) (step 6 in Figure 4.1). Meanwhile, the other two identified products, *trans*-2-pentene and pentane, were formed slowly at roughly equal rates by observing very close concentration profiles on the plot. It is noted that the concentration of *cis*-2-pentene, reaching a maximum value of $18.11 \pm 0.36 \times 10^{-2} \text{ mol.l}^{-1}$ (~66.7 wt% of the mixture) at ~30 mins, and began to fall at >90% of 2-pentyne conversion. Simultaneously a continuing increase in both the *trans*-2-pentene and pentane was observed. This implies that the reaction path is the hydrogenation of 2-pentyne to *cis*-2-pentene followed by its deposition and re-adsorption for further hydrogenation to pentane or *cis-trans* isomerisation to *trans*-2-pentene. The adsorption of alkyne on the palladium surface is

suggested to be stronger than that of the corresponding alkene [272-276] thus could prevent the re-adsorption of the product alkene [271,277]. In other words, *cis*-2-pentene is able to compete for the metal active sites only when most of the 2-pentyne is consumed from the solution, to be further hydrogenated to pentane or converted to its *trans*-isomer. As a consequence, *cis*-2-pentene was not consumed in the presence of 2-pentyne (0~30 mins in Figure 4.2), while it underwent ready hydrogenation and isomerisation in the absence of the 2-pentyne (after ~30 mins). The mole balance of the liquid substances was conserved during the course of the reaction.

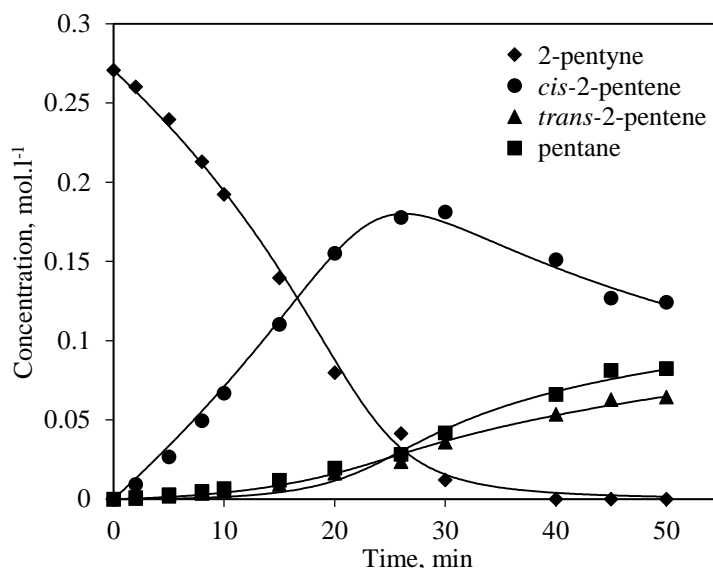


Figure 4.2 Concentration profiles as the function of reaction time in 2-pentyne hydrogenation using a 2wt%Pd/*E. coli* catalyst. Reaction conditions were: 75 mg of 2wt%Pd/*E. coli*, 4 ml of 2-pentyne, 150 ml of isopropanol (solvent), $T = 40\text{ }^{\circ}\text{C}$, $p_{H_2} = 2\text{ bar}$, $N = 1000\text{ rpm}$. Discrete symbols are experimental data points averaged from two experiments with a reproducibility of within 10%. Lines shown represent the kinetic model in Equations 4-2 ~ 4-5.

The kinetics of 2-pentyne hydrogenation in the present system were studied with the reaction rate equations derived based on a Langmuir-Hinshelwood type relationship. By taking into account the *cis-trans* isomerisation of 2-pentene, which was considered following the well-known Horiuti-Polanyi mechanism [213] (details in §2.4.1.2), the overall reaction rates of the key components during the course of the 2-pentyne hydrogenation were derived in Equations 4-2 ~ 4-5 accordingly (procedure of the equation derivation refers to Appendix §8.1.1):

$$\frac{\partial \text{Py}}{\partial t} = -wk_{\text{Py}}'K_{\text{Py}}[\text{Py}]\theta_*^3 \quad 4-2$$

$$\frac{\partial \text{cis-Pe}}{\partial t} = w\left\{k_{\text{Py}}'K_{\text{Py}}[\text{Py}]\theta_*^3 - (k_7K_{\text{Pe}}[\text{cis-Pe}] - k_{-7}K_{\text{Pe}}[\text{trans-Pe}])\theta_* - k_{\text{Pe}}'K_{\text{Pe}}[\text{cis-Pe}]\theta_*^3\right\} \quad 4-3$$

$$\frac{\partial \text{trans-Pe}}{\partial t} = wK_{\text{Pe}}\left\{(k_7[\text{cis-Pe}] - k_{-7}[\text{trans-Pe}])\theta_* - k_{\text{Pe}}'[\text{trans-Pe}]\theta_*^3\right\} \quad 4-4$$

$$\frac{\partial \text{Pa}}{\partial t} = wk_{\text{Pe}}'K_{\text{Pe}}([\text{cis-Pe}] + [\text{trans-Pe}])\theta_*^3 \quad 4-5$$

in which, vacant active site fraction $\theta_* = \frac{1}{K_{\text{Py}}[\text{Py}] + K_{\text{Pe}}([\text{cis-Pe}] + [\text{trans-Pe}]) + K_{\text{Pa}}[\text{Pa}] + 1}$

Py, cis-Pe, trans-Pe, and Pa denote 2-pentyne, cis-2-pentene, trans-2-pentene, and pentane correspondingly; w denotes the catalyst loading per unit volume of liquid; rate constants k_{Py}' and k_{Pe}' incorporate hydrogen concentration and hydrogen adsorption coefficient; k_7 and k_{-7} represent the reversible rate constants of cis-trans isomerisation (step 7 in Figure 4.1); and K_i ($i = \text{Py}, \text{cis-/trans-Pe}, \text{Pa}$) denotes the adsorption coefficient of each component.

To solve for the above model parameters k_i' , k_i and K_i , the following objective function, F' , which represents the sum of the squares of the difference between experimental and calculated concentration for each component was minimised:

$$F' = \sum_{i=1}^{n_{\text{comp}}} \sum_{j=1}^{n_{\text{obs}}} (C_{i,j,\text{observed}} - C_{i,j,\text{regression}})^2 \quad i = \text{Py}, \text{cis-/trans-Pe}, \text{ and Pa}; j = 1, 2, 3 \dots \quad 4-6$$

All the model parameters were simultaneously estimated using a Solver function of MS Excel software. A constraint was imposed that the coefficients must be greater than or equal to zero. The procedure was successful for all the components in 2-pentyne hydrogenation system as shown by the fitted lines in Figure 4.2 being a good match to the experimental data points. Table 4.1 lists the predicted values of the kinetic and adsorption parameters. Hydrogenation rate constants estimated by the model indicate a 7.6-fold faster hydrogenation of the carbon-

carbon triple bond (C≡C) than that of the carbon-carbon double bond (C=C), which were $22.3 \times 10^{-3} \text{ mol.g}^{-1}.\text{s}^{-1}$ and $2.9 \times 10^{-3} \text{ mol.g}^{-1}.\text{s}^{-1}$ respectively. Values of *cis-trans* isomerisation rate constants (k_7 and k_{-7}) were predicted lower than those of hydrogenation rate constants (k'_{Py} and k'_{Pe}), suggesting a lower level of isomerisation than hydrogenation in the present reaction system. A stronger adsorption of 2-pentyne than that of 2-pentene, and a very weak adsorption of pentane on the active site are revealed by the model-predicted values of adsorption coefficients ($K_{\text{Py}} > K_{\text{Pe}} \gg K_{\text{Pa}}$). Very few values of the rate constant and adsorption coefficient of 2-pentyne in a similar hydrogenation process are reported in the literature for the purpose of comparison. However, it is still worth to note that in the hydrogenation of 2-butyne-1,4-diol using isopropanol as solvent over a Pd/A. *oxidans* bio-catalyst by Wood *et al.* [278], adsorption coefficients of 2-butyne-1,4-diol and 2-butene-1,4-diol were reported as $31.28 \text{ m}^3.\text{mol}^{-1}$ and $0.00 \text{ m}^3.\text{mol}^{-1}$. In another study of 2-methyl-3-butyne-2-ol hydrogenation over a Pd/CaCO₃ catalyst under solvent free conditions by Bruehwiler *et al.* [279], the estimated adsorption coefficients of 2-methyl-3-butyne-2-ol and 2-methyl-3-buten-2-ol were rather small, which were $1.03 \times 10^{-3} \text{ m}^3.\text{mol}^{-1}$ and $10^{-5} \text{ m}^3.\text{mol}^{-1}$ respectively. Although the above variance from the literature due to the use of different substrates, catalysts and reaction conditions, it is evident that the adsorption strength of alkyne on a palladium surface is stronger than that of alkene.

Table 4.1 Values of fitted parameters for 2-pentyne hydrogenation using Equations 4-2 ~ 4-5.

Catalyst	Rate constant $\times 10^{-3} \text{ mol.g}^{-1}.\text{s}^{-1}$				Adsorption coefficient $\times 10^{-3} \text{ m}^3.\text{mol}^{-1}$		
	k'_{Py}	k_7	k_{-7}	k'_{Pe}	K_{Py}	K_{Pe}	K_{Pa}
2wt%Pd/ <i>E. coli</i>	22.3	0.2	0	2.9	28.48	12.20	0.002

One of the objectives of this study is to compare the catalytic performance of bio-Pd/*E. coli* in 2-pentyne hydrogenation with that of the conventional catalyst Pd/Al₂O₃. Figure 4.3 shows a comparison of 2-pentyne consumption profiles over four different catalysts, which are

2wt%Pd and 5wt%Pd on both *E. coli* and Al_2O_3 , under identical reaction conditions (40 °C, 2 bar, and 1000 rpm). It can be observed from Figure 4.3 that under the same reaction conditions, the 2-pentyne consumption rates decreased in the order of catalysts: 5wt%Pd/*E. coli* > 2wt%Pd/ Al_2O_3 > 2wt%Pd/*E. coli* close to 5wt%Pd/ Al_2O_3 .

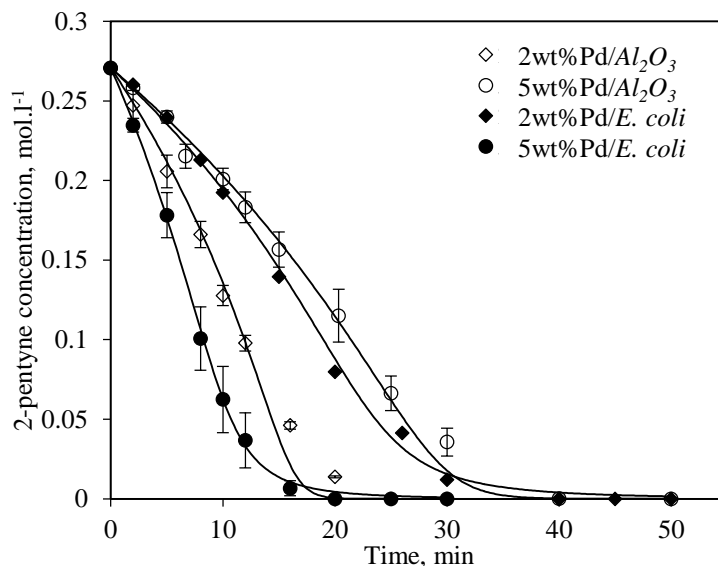


Figure 4.3 2-pentyne concentration profiles versus reaction time over different catalysts. Reaction conditions were: 30 mg of 5 wt%Pd (or 75 mg if 2 wt%Pd), 4 ml of 2-pentyne, 150 ml of isopropanol (solvent), $T= 40\text{ }^{\circ}\text{C}$; $p_{H_2} = 2\text{ bar}$, $N= 1000\text{ rpm}$. Discrete symbols are experimental data points. Where error bars are shown these were calculated as mean \pm standard error of the mean from at least three experiments. Where no error bars are shown (2wt%Pd/*E. coli*) the data were averaged from two experiments with a reproducibility of within 10%. Lines shown represent the kinetic model in Equation 4-2.

Increasing the Pd loading from 2 wt% to 5 wt% upon Al_2O_3 , the catalytic activity decreased; whereas with *E. coli* support over the same range of Pd loadings an increase in catalytic activity was observed. For the conventional Pd/ Al_2O_3 catalyst, it is suggested that a lower Pd loading leads to a higher metal dispersion [280] with Pd particles possessing smaller size and larger surface area per unit mass of metal. 2wt%Pd/ Al_2O_3 and 5wt%Pd/ Al_2O_3 catalysts in the present work were examined by CO pulse chemisorption analysis with metallic surface areas of $57.85\text{ m}^2.\text{g}(\text{metal})^{-1}$ and $39.32\text{ m}^2.\text{g}(\text{metal})^{-1}$ respectively (details to be presented in §6.4.1). At the same Pd loading in each test, *i.e.* $0.375\text{ mg}(\text{Pd}).\text{ml}(2\text{-pentyne})^{-1}$, 2wt%Pd/ Al_2O_3 provided larger surface area than 5wt%Pd/ Al_2O_3 for reaction to take place, thus showing a faster 2-pentyne consumption rate over 2wt%Pd/ Al_2O_3 than that over 5wt%Pd/ Al_2O_3 .

However this was not the case with bio-Pd/*E. coli* catalysts, in which Pd particle seeds were suggested to be localised by hydrogenases (within the cell wall structure of Gram-negative bacteria) [177,181]. At a relatively low loading of 2 wt%Pd, most of Pd particles may be encased within the *E. coli* cell membrane or surface layers. As the increase of Pd loading leads to the growth of Pd particles, there could be an increasing possibility of them rupturing the membrane and some of the metallic surface becoming exposed to the exterior environment. This ruptured particle growth was observed in the Electron Microscopy images as to be detailed in §6.3; as a result the increased availability of active metal surface in 5wt%Pd/*E. coli* led to the faster rate of reaction as compared to 2wt%Pd/*E. coli*.

Table 4.2 Comparison of the product distribution at 100% conversion of 2-pentyne using different catalysts. Reaction conditions were: 30 mg of 5 wt%Pd (or 75 mg if 2 wt%Pd), 4 ml of 2-pentyne, 150 ml of isopropanol (solvent), $T= 40\text{ }^{\circ}\text{C}$; $p_{H_2} = 2\text{ bar}$, $N= 1000\text{ rpm}$.

Catalyst	Product concentration, $\times 10^{-2}\text{ mol.l}^{-1}$		
	<i>cis</i> -2-pentene	<i>trans</i> -2-pentene	pentane
1 2wt%Pd/ Al_2O_3	7.34 \pm 0.53	10.29 \pm 0.60	9.44 \pm 0.48
2 5wt%Pd/ Al_2O_3	6.52 \pm 0.46	9.62 \pm 0.38	10.94 \pm 0.79
3 2wt%Pd/ <i>E. coli</i>	15.11	5.36	6.61
4 5wt%Pd/ <i>E. coli</i>	10.09 \pm 0.52	6.20 \pm 0.54	9.96 \pm 0.64

Table 4.2 compares the product distribution when the 2-pentyne reached 100% conversion using these four catalysts. It is apparent that, at an equal Pd loading, the *E. coli*-supported catalyst selectively produced a higher amount of *cis*-2-pentene and a much lower yield of the unwanted *trans*-2-pentene than the Al_2O_3 -supported catalyst. The better selectivity towards *cis*-2-pentene over bio-Pd/*E. coli* can be attributed to a smaller average size of Pd particles as compared to Pd/ Al_2O_3 at an equivalent Pd loading, *e.g.* 4.31 nm for 5wt%Pd/*E. coli* and 12.77 nm for 5wt%Pd/ Al_2O_3 respectively (details to be presented in §6.4).

In summary, it can be concluded that in 2-pentyne hydrogenation ($T= 40\text{ }^{\circ}\text{C}$; $p_{H_2} = 2\text{ bar}$; $N= 1000\text{ rpm}$), promising reaction rates and lower yield of *trans*-pentene by using bio-Pd/*E. coli*

catalyst were obtained in comparison with the Pd/Al₂O₃ catalyst. Based on this, the more complicated hydrogenation of soybean oil was conducted to assess whether the bio-Pd catalyst could be used beneficially in place of existing catalyst, as reported in the following section.

4.3 Hydrogenation of Soybean Oil

Commercial soybean oil purchased from Sigma-Aldrich (UK) was used in this study, which mainly contains linolenic acid (*cis*-C18:3), linoleic acid (*cis*-C18:2), oleic acid (*cis*-C18:1), stearic acid (C18:0), and palmitic acid (C16:0). The chemical composition of each component determined by gas chromatography (GC) and some of the physical properties are presented in Table 4.3.

Table 4.3 Fatty acid compositions and physical properties of untreated soybean oil.

<i>Chemical properties</i>			
Fatty acids	Trivial name	C-chain:double bonds ^a	Composition, wt% ^b
hexadecanoic acid	palmitic	C16:0	10.6~10.8
octadecanoic acid	stearic	C18:0	4.2~4.4
<i>cis</i> -9-octadecenoic acid	oleic	<i>cis</i> -C18:1	22.4~24.6
<i>trans</i> -9-octadecenoic acid	elaidic	<i>trans</i> -C18:1	<0.1
<i>cis,cis</i> -9,12-octadecadionic	linoleic	<i>cis</i> -C18:2	53.4~55.3
<i>cis,cis,cis</i> -9,12,15-octadecatrienoic acid	linolenic	<i>cis</i> -C18:3	6.8~7.4
<i>Physical properties</i>			
	Correlation	Reference	
viscosity, μ , kg.m ⁻¹ .s ⁻¹	$\log_{10} \mu = -3.073 + 46.6 \times 10^6 \times T^{-3}$	Haighton <i>et al.</i> [281]	
density, ρ_L , kg.m ⁻³	$\rho_L = 1108 - 0.65 \times T$	Bailey [282]	
vapour pressure, p , MPa	$\log_{10} p^s = -1145 \times T^{-1} + 0.476$	Fillion and Morsi [208]	

^a C denotes carbon; the first number, *e.g.* 18, represents the total carbon number of the fatty acids; the second number, *e.g.* 3, represents the total number of double bonds. ^b Weight percentage determined by GC, range from different batches of purchased oil.

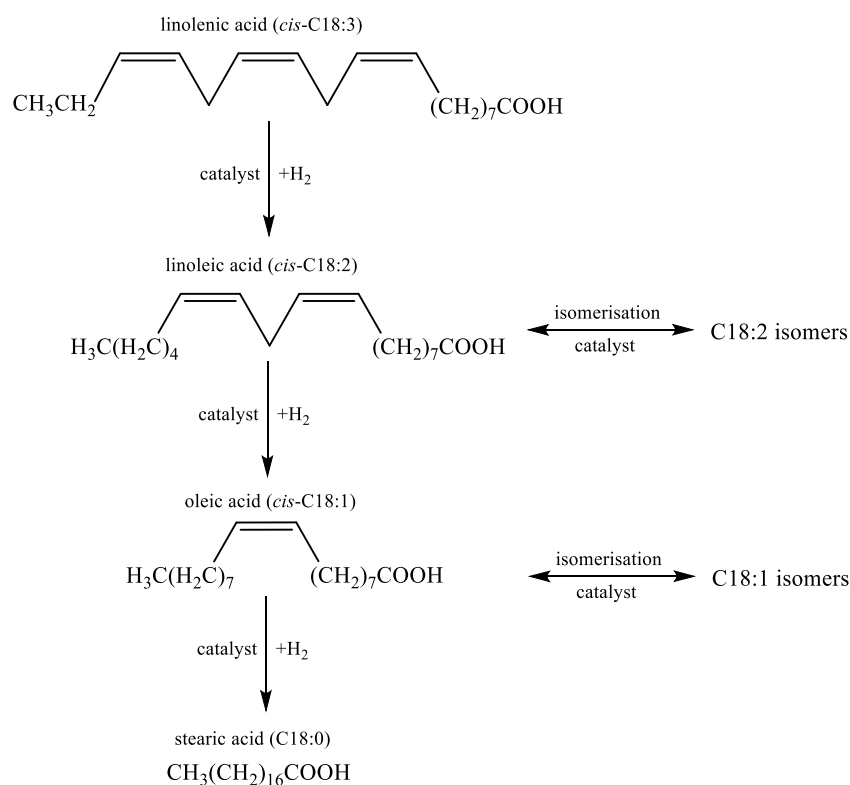


Figure 4.4 Simplified soybean oil hydrogenation and isomerisation network in the presence of solid catalyst.

A simplified reaction network of soybean oil hydrogenation is shown in Figure 4.4. For an agitated three-phase catalytic reactor, it is essential to operate the reaction under conditions such that the mass transfer and other complex effects (*e.g.* hydrodynamic resistances) are absent. For this purpose, in §4.3.1 the conventional inorganic catalyst 5wt%Pd/ Al_2O_3 was firstly employed in soybean oil hydrogenation to fully evaluate the mass transfer limitations in the present Baskerville autoclave reactor and achieve the minimisation by altering reaction operating conditions based on the engineering aspects (§4.3.1.1). This was followed by a kinetic study of soybean oil hydrogenation and the estimation of activation energy in the present reaction system (§4.3.1.2). Thereafter, §4.3.2 presents the evaluation of bio-Pd catalyst in soybean oil hydrogenation under the set of reaction conditions optimised using the inorganic supported catalyst. The catalytic performance of 5wt%Pd/*E. coli* was compared with that of conventional 5wt%Pd/ Al_2O_3 under identical operating conditions (§4.3.2.1), followed by the examination of the thermal stability of 5wt%Pd/*E. coli* by changing the

reaction temperature (§4.3.2.2). A different biomass strain (*Desulfovibrio desulfuricans*) was also used as the support of bio-Pd to investigate the effect of bacterial strain on the catalytic performance in soybean oil hydrogenation (§4.3.2.3). In addition, the reduction of Pd(II) to Pd(0) upon *E. coli* cells during bio-Pd/*E. coli* preparation was proceeded using two different pathways, namely H₂-reduction and formate-reduction, and its effect on the catalytic activity in soybean oil hydrogenation was also investigated (§4.3.2.4).

A control experiment was firstly conducted using dry biomass of *E. coli* in soybean oil hydrogenation and no substrates were converted. The performance of the palladium catalysts under different conditions was assessed in terms of conversion (of *cis*-C18:3, *cis*-C18:2) and product formation at the same conversion. The conversion is defined as the fraction of the *cis*-C18:*i* (*i*=2, 3) that has been consumed with respect to the original amount after the corresponding reaction time as follows:

$$cis\text{-C18:}i \text{ conversion \%} = \frac{[cis\text{-C18:}i]_0 - [cis\text{-C18:}i]_t}{[cis\text{-C18:}i]_0} \times 100\% \quad i=2, 3 \quad 4-7$$

where $[cis\text{-C18:}i]_0$ and $[cis\text{-C18:}i]_t$ correspond to concentrations at initial time ($t=0$) and subsequent time (t) respectively.

4.3.1 Conventional Catalyst 5wt%Pd/Al₂O₃

The palladium loading in the soybean oil was maintained at 0.05 mg(Pd).ml(oil)⁻¹ for all the soybean oil hydrogenation experiments, unless otherwise stated. Results are all presented from at least triplicate experiments as mean ± standard error of mean, unless otherwise stated. Error bars are within the dimensions of the symbols if not shown. Each catalyst was sampled from the same preparation, unless otherwise stated. Figure 4.5 depicts a typical time course of fatty acid concentration profiles using 5wt%Pd/Al₂O₃ under 5 bar of hydrogen at temperature of 125 °C with a stirring speed of 800 rpm. At the beginning of the reaction, it is thought that

the catalyst surface is saturated with the *cis*-C18:3 and *cis*-C18:2 components ready for initial reaction, due to the strong multi-site adsorption *via* multiple C=C double bonds and the C=O bond of the carbonyl group [283]. Referring to Figure 4.5 the concentration of *cis*-C18:3 (~0.23 mol.l⁻¹ in the starting material) was completely depleted within 1.5 hours. Meanwhile the other major reactant *cis*-C18:2 (~1.77 mol.l⁻¹ in the starting material) showed a conversion of 96.80±1.31% after 2 hours, with a residual mass percent of 1.74±0.41 wt%.

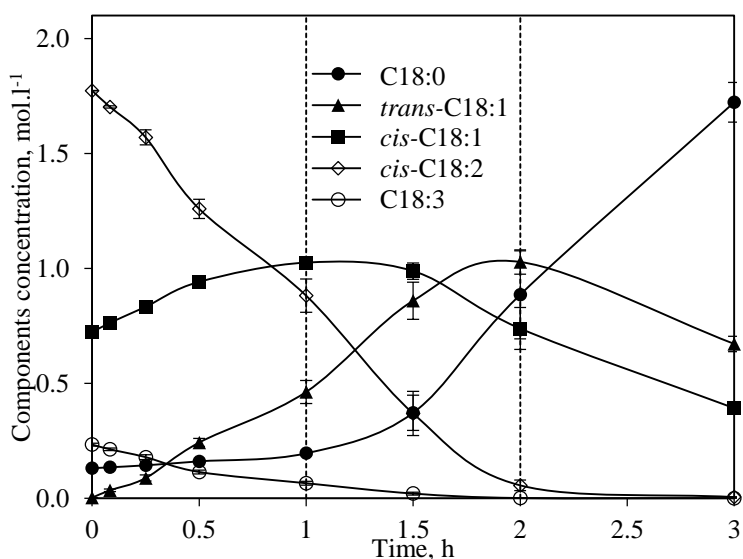


Figure 4.5 Example of the evolution of products distribution during the reaction time in soybean oil hydrogenation. Reaction conditions were: 150 mg of 5wt%Pd/Al₂O₃, 150 ml of soybean oil (solvent free), T= 125 °C, p_{H_2} = 5 bar, N= 800 rpm. Vertical dashed lines at time of 1 hour and 2 hours divide the profile into 3 time intervals, details refer to text.

The product formation with the course of the reaction time can be divided into 3 stages as demonstrated on Figure 4.5. i) Interval 1: 0~1 hours. During this period both *cis*-C18:1 and *trans*-C18:1 were formed from the beginning, indicating hydrogenation and isomerisation take place simultaneously. A gentle increasing rate was observed with *cis*-C18:1 (an increase from 0.72±0.00 mol.l⁻¹ to 1.02±0.02 mol.l⁻¹) while the formation of *trans*-C18:1 increased rapidly to 0.46±0.05 mol.l⁻¹ from almost zero initial concentration. According to the Horiuti-Polanyi mechanism [213] (as described in §2.4.1.2), the half-hydrogenated intermediate is firstly formed on the catalyst surface, and the free rotation of the half-hydrogenated

intermediate followed by hydrogen abstraction and desorption of the olefin results in *cis-trans* isomerisation. Hence, before the newly formed *cis*-C18:1 could be desorbed from the active site, it would be converted further to the higher thermochemical stable *trans*-C18:1 due to the steric hindrance [284]. The amount of terminal product C18:0 was maintained stably around the starting concentration ($0.13 \pm 0.00 \text{ mol.l}^{-1}$) showing a very minor increase by observing the almost flat trend line within the initial 1 hour. ii) Interval 2: 1~2 hours. The amount of intermediate *cis*-C18:1 levelled off and decreased in this time period, suggesting its consumption had started to take place. Meanwhile the *trans*-C18:1 kept increasing at a stable rate. It was also observed that the formation of C18:0, most directly from the hydrogenation of C18:1, accelerated dramatically. Evidently, the considerable decrease of the polyenic fatty acids concentration in the mixture (after 2 hours a conversion of 100% for *cis*-C18:3 and $96.80 \pm 1.31\%$ for *cis*-C18:2) could have vacated some of the catalyst active sites and thus promoted the access for *cis*-C18:1 adsorption onto the catalyst surface. This would lead to the successive hydrogenation of *cis*-C18:1 giving C18:0 and isomerisation to *trans*-C18:1. The profiles observed with steep increase of *trans*-C18:1 between 1 and 2 hours reaction time indicate intensification or acceleration of the reaction *cis-trans* isomerisation of *cis*-C18:1 during the consumption of *cis*-C18:2. iii) Interval 3: 2~3 hours. Both *cis*-C18:1 and *trans*-C18:1 decreased as a result of their further hydrogenation to saturated C18:0, with only C18:0 mounting up steadily to a concentration of $1.72 \pm 0.27 \text{ mol.l}^{-1}$ (~53.4 wt% of the mixture) after 3 hours reaction time. From the above observations, the reaction path was elucidated as the stepwise hydrogenation of polyenoic fatty acids (C18:3 and C18:2) to monoenoic fatty acid (C18:1) followed by deposition and re-adsorption for monoene (C18:1) and further hydrogenation to saturated fatty acid (C18:0), while the *cis-trans* isomerisation occurs as a parallel reaction of the unsaturated components. The mole balance of the liquid substances was conserved during the course of the reaction.

As described above, this being a typical multiphase catalytic process involving hydrogen (gas), soybean oil (liquid) and catalyst (solid), hydrodynamic resistances and several transport limitations may occur due to the low solubility of hydrogen in the oil and the long carbon chains of reactant molecules in the liquid phase. These engineering challenges of mass transfer and mixing must be overcome for maximum product yield or selectivity, as addressed in the following section.

4.3.1.1 Mixing and Mass Transfer Investigation

In the present agitated Baskerville reactor, a minimum stirring speed for complete suspension of Pd/Al₂O₃ catalyst particles must be determined, so that proper operating conditions can be chosen and altered to minimise the intervention of mass transfer in order not to limit the hydrogenation rates. The mass-transfer in this study was divided into two categories: i) external mass transfer that first takes place from the bulk fluid phase to the external surface of the solid catalyst, which is frequently the rate limiting step in the hydrogenation of fatty acids, and ii) intra-particle diffusion of the reactants from the external catalyst surface into and through the pores within the pellet to an active site, on which the reaction occurs. The following section presents a systematic study to identify these mass transfer limitations with the aim to improve the mass-transfer process.

4.3.1.1.1 Particle Suspension

The minimum stirring speed (N_m) was predicted using a correlation proposed by Zwietering *et al.* [246] (Equation 2-1 in §2.5.2.1) to be 279.0 rpm in the present system, for a catalyst (5wt%Pd/Al₂O₃) loading of 0.115 g.100g(solution)⁻¹ at an operating temperature of 100 °C. Parameters for calculation are listed in Table 4.4, which involve geometries of the Baskerville autoclave reactor, properties of the catalyst and soybean oil under the working temperature.

Table 4.4 Parameters used for the calculation of the minimum stirring speed (N_m) in the case of solvent-free soybean oil hydrogenation over 5wt%Pd/Al₂O₃ in the Baskerville autoclave reactor.

Parameter	Value	Description
<i>System geometries</i>		
d_T	7.62 cm	reactor inside diameter
d_I	5.84 cm	stirrer diameter
β^a	2.85	constant
<i>Catalyst properties (5wt%Pd/Al₂O₃)</i>		
w'	0.115 g(catalyst).100g(solution) ⁻¹	percentage catalyst loading
d_p^b	4.5×10 ⁻³ cm	average diameter of catalyst particles
ρ_p^c	3.538 g.cm ⁻³	catalyst density
<i>Soybean oil properties^d</i>		
μ_L	0.0668 g.cm ⁻¹ .s ⁻¹	liquid viscosity
ρ_L	0.866 g.cm ⁻³	liquid density
<i>Others:</i>		
g	981 cm.s ⁻²	gravitational acceleration

^a estimated using Equation 2-2; ^b Johnson Matthey Type 335; ^c measured by Micromeritics Accupyc II 1340 Pycnometer; ^d estimated using correlations in Table 4.3 under the reaction temperature of 100 °C.

4.3.1.1.2 External Mass Transfer

In order for the hydrogen to take part in a heterogeneously catalysed hydrogenation reaction, it must diffuse through the gas phase followed by dissolving in the oil and then diffuse to the catalyst surface. All the diffusion rate equations in this section are derived based on the details in §2.5.2.2~2.5.2.3 in the Literature Review chapter.

Step 1: Hydrogen Diffusion in the Gas Phase

Hydrogen diffusion rate in the gas bubble is determined by gas film mass transfer coefficient k_g , interfacial area a , and pressure difference ($p_{H_2} - p_{H_{2i}}$), which can be expressed as:

$$r_{H_2} = k_g a (p_{H_2} - p_{H_{2i}}) \quad 4-8$$

while the diffusion resistance of hydrogen in gas phase can be neglected due to the constant pure hydrogen feed (0.5 MPa) and the negligible vapour pressure of the oil (in the range of

0.85~3.97 $\times 10^{-3}$ MPa based on the correlation in Table 4.3) at the temperatures of reaction in this study (50 °C~125 °C).

Step 2: Mass-Transfer in the Gas-Liquid Interface

The rate of dissolution of hydrogen is proportional to the volumetric gas-liquid mass-transfer coefficient k_{La} , and the difference between the hydrogen solubility and its actual concentration in the bulk liquid ($[H_2^*] - [H_2^l]$) at the prevailing temperature and pressure, which can be expressed as:

$$r_{H_2} = k_{La}([H_2^*] - [H_2^l]) \quad 4-9$$

where the solubility of hydrogen in soybean oil is proportional to the pressure inside of the autoclave, in accordance with Henry's law. The Henry's law coefficient is a function of temperature (T) and can be represented by an Arrhenius type expression. The above relationships have been incorporated in an expression reported by Fillion *et al.* [120] as:

$$[H_2^*] = 0.113 \exp\left(\frac{-5000}{RT}\right) p_{H_2} \quad 4-10$$

For the reactions under identical temperature and hydrogen pressure, hydrogen mass transfer rate in the gas-liquid interface is mainly determined by k_{La} . The volumetric liquid-side mass transfer coefficient k_{La} of hydrogen can be affected by various parameters [252,285,286], such as the dimensions of reactor equipment (*e.g.* impeller type and diameter), speed of agitation, and liquid/solid type. For example, in the hydrogenation of monoeneic fatty acid methyl ester over nickel-based catalysts, Jonker [203] reported a k_{La} of 1.8 s^{-1} in a reactor setup with baffles. In the set of hydrogenations of sunflower oil over a nickel catalyst with only a change of the stirring speed reported by Fernández *et al.* [249], k_{La} was 0.03 s^{-1} for the reaction at 700 rpm and 0.1 s^{-1} at 1416 rpm. It appears that agitation speed plays an important role on k_{La} for a specific type of reaction in a given reactor configuration. Hence a set of

experiments were conducted at varied stirring speeds (500 rpm, 800 rpm, 1000 rpm, and 1200 rpm; all above $N_m = 279.0$ rpm), to examine the effect of stirring speed upon mass transfer rate in practice. The other reaction conditions were maintained the same as: 150 mg of 5wt%Pd/Al₂O₃ in 150 ml of soybean oil (solvent free), $p_{H_2} = 5$ bar, and $T = 100$ °C for 5 hours.

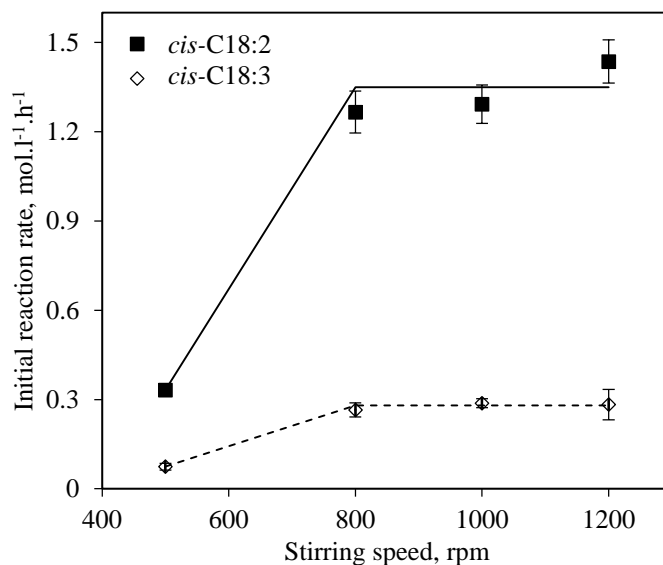


Figure 4.6 Evolution of the initial reaction rates with stirring speed (for both *cis*-C18:3 and *cis*-C18:2 at the initial 30 mins) in soybean oil hydrogenation. Reaction conditions were: 150 mg of 5wt%Pd/Al₂O₃ in 150 ml of soybean oil (solvent free) for 5 hours, $T = 100$ °C, and $p_{H_2} = 5$ bar.

Figure 4.6 shows the influence of agitation rate on the reaction performance, in which the x-axis denotes stirring speeds while the y-axis shows the corresponding initial reaction rates (at 30 mins) obtained for both *cis*-C18:3 and *cis*-C18:2. As clearly seen in the figure, the initial reaction rates (at 30 mins) were strongly dependent on the agitation speed within the range of 500~800 rpm, over which the rates increased from 0.07 ± 0.00 mol.l⁻¹.h⁻¹ to 0.26 ± 0.02 mol.l⁻¹.h⁻¹ for *cis*-C18:3 and 0.33 ± 0.01 mol.l⁻¹.h⁻¹ to 1.26 ± 0.07 mol.l⁻¹.h⁻¹ for *cis*-C18:2. While the later part of the graph ($N \geq 800$ rpm) shows the initial rates of both *cis*-C18:3 and *cis*-C18:2 to be independent of the stirring speed. As the lowest stirring speed of 500 rpm applied was greater than the calculated minimum speed for particle suspension (*i.e.* $> N_m = 279.0$ rpm), the catalyst particles were assumed to be dispersed uniformly in the reaction medium. However

the observed lower reaction rate indicates that a gas-liquid mass-transfer rate control regime occurred at a stirring speed of 500 rpm, *i.e.* the reaction rate was significantly affected by gas-liquid mass transfer. The strong influence of agitation speed from 500 rpm to 800 rpm implies the contribution of a sufficient stirring speed to a higher volumetric gas-liquid mass-transfer coefficient $k_L a$ (s^{-1}) of hydrogen, as suggested by Fernández *et al.* [249], thus a faster transfer rate of hydrogen across the gas-liquid interface occurred. More specifically, the liquid-side mass-transfer coefficient k_L ($m.s^{-1}$) is affected since increasing mixing speed increases the turbulence and surface renewal rate at the gas-liquid surface while decreases the liquid film thickness, correspondingly increasing k_L [208,287]. Also the volumetric gas-liquid interfacial area a (m^{-1}) could increase since a higher mixing speed introduces more gas into the slurry and breaks large gas bubbles into several small ones with larger specific surface area [287,288]. Considering the invariant reaction rates observed at the agitation conditions exceeding 800 rpm being within experimental error in Figure 4.6, it is verified by the agitation test that at a speed of 800 rpm the system was not under the gas-liquid mass-transfer rate control.

Regarding the effect of stirring speed on the product distribution, it is observed that at high *cis*-C18:2 conversion (>60%), stirring speed affected marginally the formation of the *trans*-C18:1 (Figure 4.7 *a*) and C18:0 (Figure 4.7 *b*). A slightly higher amount of *trans*-C18:1 was produced at a stirring speed of 500 rpm, a gas-liquid mass-transfer rate control regime, in which the lower hydrogen availability on catalyst surface may increase the possibility of *cis-trans* isomerisation. It is also likely that a low agitation speed slowed down the transport of product away from the catalyst surface (*i.e.* the retention time of the half-hydrogenated intermediate upon the catalyst), in turn promoting the isomerisation taking place on the same catalyst surface to form *trans*-C18:1. On the other hand, less saturated fatty acid C18:0 was formed at 500 rpm, which can also be explained by the limited hydrogen availability due to

the hydrogen mass-transfer limitation. When there were not gas-liquid limitations for the hydrogen molecule to reach at the metal (*i.e.* ≥ 800 rpm), an excess of gas was more likely to exist on the active site, and the fatty acid molecule would tend to saturate before the isomerisation.

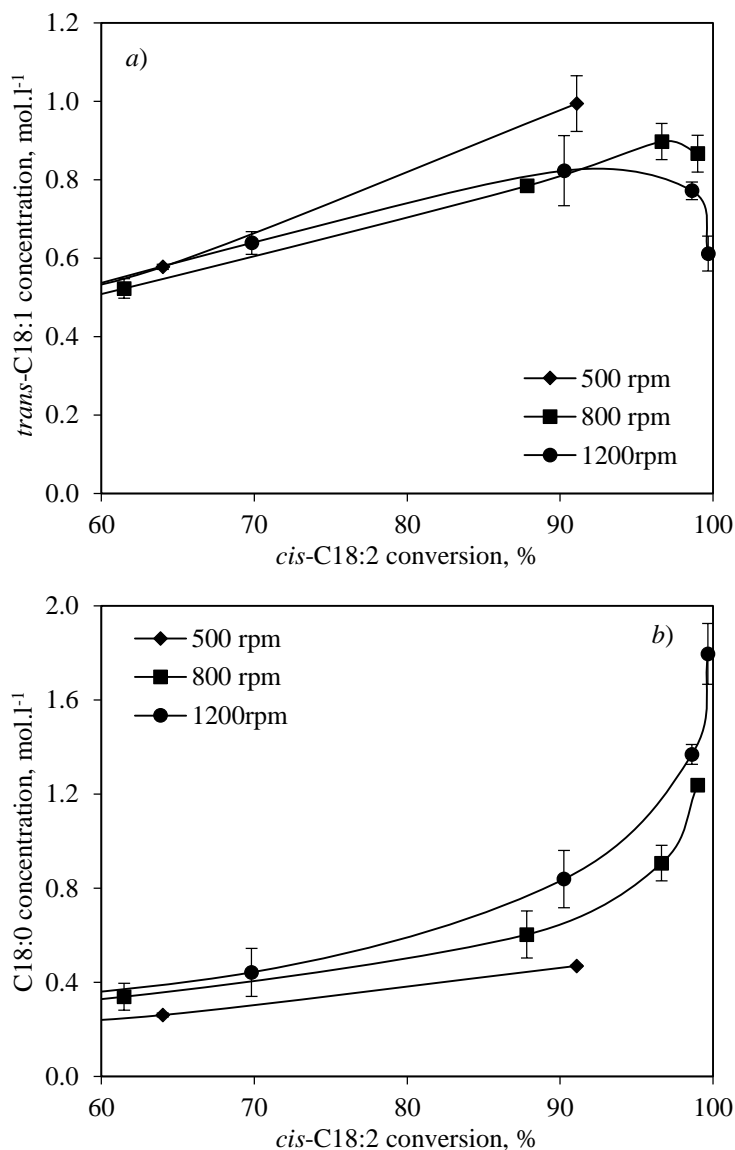


Figure 4.7 Comparison of the formation of a) *trans*-C18:1 and b) C18:0 at the same *cis*-C18:2 conversion under different stirring speeds. Reaction conditions were: 150 mg of 5wt%Pd/Al₂O₃, 150 ml of soybean oil (solvent free), $T = 100$ °C, $p_{H_2} = 5$ bar.

Thereafter, it was concluded that under the agitation conditions of 800 rpm and above, the gas-liquid mass transfer resistance in the present Baskerville autoclave was negligible. A

stirring speed of 800 rpm was consequently chosen as the stirring speed in all further hydrogenation experiments.

Step 3: Diffusive Transport of Hydrogen across Bulk

The resistance to the diffusion of hydrogen molecules in the oil can be neglected taking into account that near perfect mixing occurs due to the agitation and to bubbling of the gas [249].

Step 4: Mass Transfer in the Liquid-Solid Film

The agitation test is useful to check for the presence of interphase gradients both at the gas-liquid interphase and the liquid-solid interphase [289,290]; the resistance at the former interphase has satisfactorily reduced at a stirring speed of 800 rpm. However, the agitation test could be inadequate to evidence liquid-solid transport limitations, as stirring affects gas-liquid transport more than liquid-solid transport [291]. For example, in the study of 2-pentyne hydrogenation in a similar agitated slurry reactor by Bennett *et al.* [270], increasing the stirring speed from 445 rpm to 1100 rpm, the average gas-liquid mass-transfer coefficient k_L increased by a factor of 5.8, while the liquid-solid mass transfer coefficient k_s increased by a factor of only 1.85. The highest possible relative particle-liquid velocity favours faster mass transport at the liquid-solid interface; nevertheless the small catalyst particle tends to move together with the liquid in practice and thus the slip velocity of smaller particles is lower than larger ones [249]. Therefore, the increase of the agitation rate only causes the mixture to circulate faster, without increasing the relative velocity of the catalyst particle with respect to the liquid [249]. The 5wt%Pd/Al₂O₃ tested in this section was supplied by Johnson Matthey (Type 335), with an average size of 45 μm. In an attempt to identify the hydrogen mass transfer in the liquid-solid film, an additional test can be performed by varying the amount of catalyst m_c . As suggested by Ramachandran *et al.* [206] and Santacesaria *et al.* [13],

experimental results can be plotted classically by the reciprocal of the hydrogenation rate

$[H_2^l]/r_{H_2}$ versus the inverse of the catalyst mass $1/m$ using:

$$\frac{[H_2^l]}{r_{H_2}} = f\left(\frac{1}{m}\right) \quad 4-11$$

If a first-order reaction with respect to gaseous reactant occurs, the resulting plot from Equation 4-10 is expected to be linear, meanwhile revealing the comparative effects of the

gas absorption resistance through liquid film at gas-liquid interface (*intercept* = $\frac{1}{k_L a}$, s) and

the combined resistance to mass transfer through liquid film at liquid-solid interface and

resistance to intra-particle diffusion and reaction within catalyst particle (*slope* = $\frac{\rho_p d_p}{6k_s} + \frac{1}{\eta_c k_1}$

, kg.m⁻³.s) on the measured rate.

Adopting the determined optimal reaction conditions with agitation speed of 800 rpm, a series of experiments were conducted with the series of catalyst (5wt%Pd/Al₂O₃) loadings from 0.017, 0.025, 0.033 to 0.05 mg(Pd).ml(oil)⁻¹. In these experiments the temperature and pressure were maintained at 100 °C under 5 bar of hydrogen. At steady state, the rate of hydrogen mass transfer across the phase boundaries should be equal to the rate at which hydrogen is consumed in the catalyst particle [255,292]. Based on the discussion of Figure 4.5, at the early stage of the reaction (Interval 1: 0~1 hours), polyenic fatty acids (*cis*-C18:3 and *cis*-C18:2) are likely to occupy the catalyst active sites predominantly and undergo the hydrogen addition. Thereafter, it is reasonable to estimate the initial hydrogen uptake rate (r_{H_2} at 30 mins) as the sum of initial disappearance rates of *cis*-C18:3 and *cis*-C18:2. The concentration of hydrogen in the liquid-phase at the interface $[H_2^l]$, for the absence of gas-liquid mass transfer limitation, was approximated as being equal to the saturation value in soybean oil at the same temperature and pressure as the operating conditions $[H_2^*]$ (100 °C, 5

bar) by using Equation 4-9. Figure 4.8 *a* shows the resulting plot of $[H_2^*]/r_{H_2}$ versus $1/m$ in the present soybean oil hydrogenation system, giving a nonlinear relation. Extrapolating such data to obtain the values of k_{La} and k_s may lead to significant error [206]. In fact, the resulting pattern of $[H_2^*]/r_{H_2}$ versus $1/m$ in Figure 4.8 *a* indicates a fractional reaction order with respect to hydrogen concentration as suggested by Ramachandran *et al.* [206] (Figure 4.8 *b*). In the present specific soybean oil hydrogenation system, the detailed discussion on the reaction order with respect to the hydrogen is to follow based on the surface reaction mechanism (§4.3.1.2).

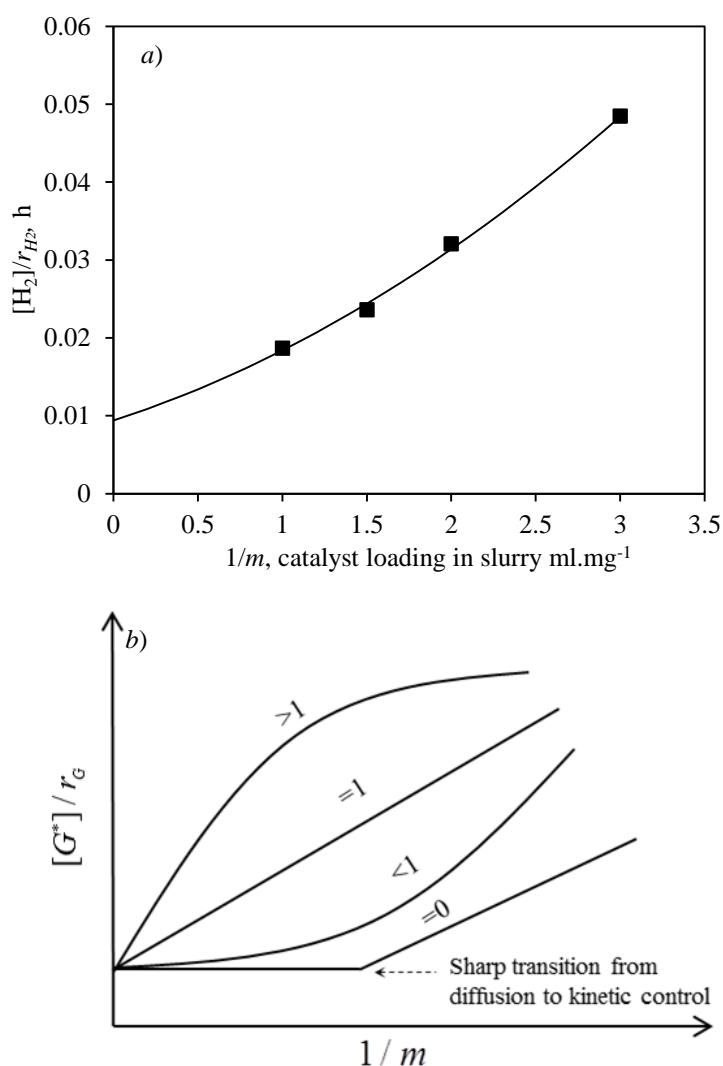


Figure 4.8 *a*) A plot of $[H_2^*]/r_{H_2}$ against $1/m$. Reaction conditions were: 5wt%Pd/ Al_2O_3 , 150 ml of soybean oil, $T=100^\circ\text{C}$, $N=800$ rpm, $p_{H_2}=5$ bar; *b*) An illustrative $[G^*]/r_G$ versus $1/m$ plot for different reaction orders (Taken from Ramachandran *et al.* [206]).

Thereafter for the evaluation of the coefficient of hydrogen mass transfer in the liquid-solid film k_s was estimated with, using the following expression proposed by Gutiérrez-Ortiz *et al.* [259]:

$$\left(\frac{k_s d_p}{D_{H_2}}\right)^2 = 16 + 4.84 \left(\frac{g d_p^3 (\rho_p - \rho_L)}{18 D_{H_2}}\right)^{2/3} \quad 4-12$$

Table 4.5 lists the corresponding parameters in Equation 4-12 for the calculation of k_s .

Table 4.5 Parameters, conditions, and references to determine the coefficient of hydrogen mass transfer in the liquid-solid film k_s .

	Variable	Value	Reference
<i>Catalyst (5wt%Pd/Al₂O₃)</i>			
mass of catalyst per unit volume of slurry	w	$1 \times 10^{-3} \text{ g.cm}^{-3}$	Experimental
mean particle diameter	d_p	$4.5 \times 10^{-3} \text{ cm}$	Johnson Matthey
density of catalyst	ρ_p^a	3.538 g.cm^{-3}	Experimental
<i>Hydrogen</i>			
diffusivity for H ₂ in soybean oil	D_{H_2}	$10.1 \times 10^{-5} \text{ cm}^2.\text{s}^{-1}$	Fillion and Morsi [208]
Henry's constant	H	$44.31 \times 10^9 \text{ pa.cm}^3.\text{mol}^{-1}$	Fillion and Morsi [208]
hydrogen concentration in soybean oil	$[H_2]^b$	$0.0113 \text{ kmol.m}^{-3}$	Fillion <i>et al.</i> [120]
<i>Soybean oil</i> ^c			
viscosity	μ_L	$0.0668 \text{ g.cm}^{-1}.\text{s}^{-1}$	Haighton <i>et al.</i> [281]
density	ρ_L	0.866 g.cm^{-3}	Bailey [282]
<i>Reaction conditions</i>			
operating temperature	T	373 K	Experimental
hydrogen pressure	P_{H_2}	$0.5 \times 10^6 \text{ pa}$	Experimental

^a Catalyst density was measured by Micromeritics Accupyc II 1340 Pycnometer; ^b the concentration of hydrogen in soybean oil was approximated as being equal to the saturation value at the operating conditions (100 °C, 0.5 Mpa); ^c properties of soybean oil were estimated using correlations in Table 4.3 under the reaction temperature of 373 K.

The value of liquid-solid mass transfer coefficient k_s estimated in the current reaction system at 100 °C was $9.32 \times 10^{-2} \text{ cm.s}^{-1}$. A criterion suggested by Ramachandran *et al.* [206] was used to test for the absence of liquid-solid mass transfer, which occurs if the following relationship is satisfied:

$$\alpha = \frac{R_{H_2} \rho_p d_p H}{6k_s w p_{H_2}} < 0.1 \quad 4-13$$

The overall rate of reaction R_{H_2} was obtained as the sum of the reaction rates of the *cis*-C18:3 and *cis*-C18:2 at the initial 30 mins. In the present reaction system, the value of α was then obtained as 0.8×10^{-3} ; therefore the reaction was not under liquid-solid mass transfer limitation.

4.3.1.1.3 Intra-Particle Diffusion

In obtaining kinetics data for a nonlinear system, it is preferable to ensure that an intra-particle gradient (caused by limitations in the reactant and products mass transfer within the catalyst) is absent.

Intra-particle Diffusion of Fatty Acids

The catalyst is uniformly immersed in the solvent-free soybean oil throughout the catalytic process, it is reasonable to assume that the catalyst particles are completely wetted and the pores filled with liquid. The concentrations of fatty acids are much greater compared with that of the dissolved hydrogen and vary very little from one position to another in the slurry, being virtually equal to the bulk concentration throughout. Thus the intra-particle diffusion of fatty acid molecules can be neglected.

Intra-particle Diffusion of Hydrogen

The determination of intra-particle mass transfer of hydrogen can usually be achieved experimentally by comparing the rate achieved with a large catalyst particle (in which there may be diffusion limitations) with the rate obtained using a fine size of catalyst particles [206,292,293]. For the given conventional 5wt%Pd/Al₂O₃ catalyst (Johnson Matthey) employed in this study, the average size of spherical catalyst particles is known as 45 μ m

with a distribution percentage that reaches 50%. The influence of intra-particle diffusion was then studied by the calculative approach as follows.

If the reaction rate expression is not known beforehand, a generalised criterion- the dimensionless Weisz-Prater modulus Φ [260,261] for the initial hydrogenation rate can be applied in order to evaluate the concentration gradient between the external surface and the inside of the pore structure:

$$\Phi = \frac{(-r_{H_2}) \rho_p d_p^2}{D_{H_2} [H_2^l]} \quad 4-14$$

The initial hydrogen uptake rate r_{H_2} , as aforementioned, equals the sum of the reaction rates of the *cis*-C18:3 and *cis*-C18:2 at the initial 30 mins. The corresponding parameters in Equation 4-14 were also listed in Table 4.5 for the calculation of Φ , which was obtained as 0.002. Usually, the absence of pore diffusion control for unknown kinetics is assumed when the values of $\Phi < 0.03 \sim 0.7$ [294], as found by calculation in this work.

Summarising the results, a surface reaction regime is assured for a stirring rate above 800 rpm, using 150 mg of 5wt% Pd/Al₂O₃ catalyst in 150 ml soybean oil under the temperature of 100 °C and hydrogen pressure of 5 bar.

4.3.1.2 Kinetics Model of the Surface Reaction

In the absence of diffusion limitations, the intrinsic reaction mechanism of soybean oil hydrogenation in the present system was investigated.

4.3.1.2.1 Effect of Hydrogen Pressure

Increasing the pressure to enhance the hydrogen dissolution (Equation 4-9) could increase the reaction rate and conversion. Thus in this section a range of pressures from 2 to 5 bar were investigated to understand their effect on the reaction performance. Other reaction conditions

were kept constant: 150 mg of 5wt%Pd/Al₂O₃ in 150 ml of soybean oil (solvent free), $T= 100$ °C, and $N= 800$ rpm.

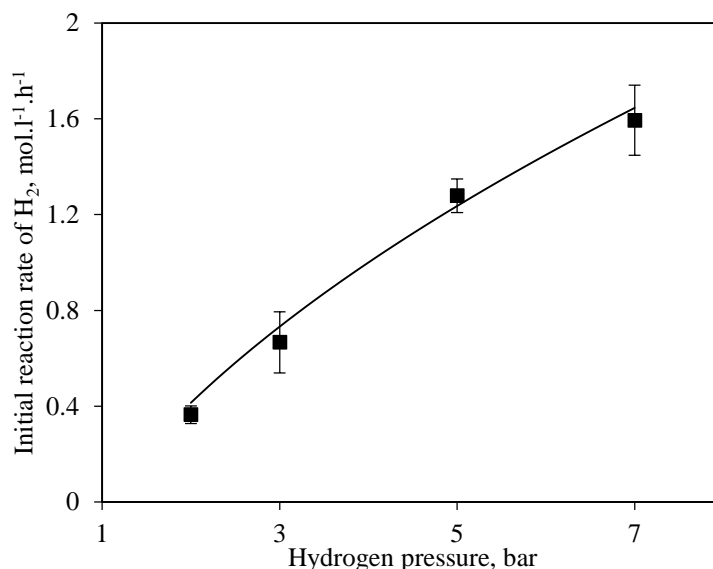


Figure 4.9 Effect of hydrogen pressure on initial reaction rate of hydrogen in soybean oil hydrogenation. Reaction conditions were: 150 mg of 5wt%Pd/Al₂O₃, 150 ml of soybean oil, $T= 100$ °C, $N= 800$ rpm.

Figure 4.9 displays the dependence of the initial reaction rate of hydrogen (r_{H_2}) on the operating pressure, in which r_{H_2} was obtained as the sum of initial hydrogenation rates of *cis*-C18:3 and *cis*-C18:2 at the initial 30 mins. A nonlinear dependence of rate on H₂ pressure was observed, indicating a fractional order-dependence with respect to H₂. This is consistent with the finding in Figure 4.8 *a* that a fractional order in hydrogen concentration suggested by the plot of $[H_2^*]/r_{H_2}$ versus $1/m$ for 5wt%Pd/Al₂O₃. However, inconsistent findings were reported in the literature in terms of the hydrogen reaction order. For example, a reaction order in hydrogen varying from 0.24 at 413 K to 0.54 at 473 K in rapeseed oil hydrogenation was reported by Bern *et al.* [295]; a half-order with respect to hydrogen was interpreted in the hydrogenation of butynediol in a batch slurry reaction by Chaudhari [293]; while the hydrogen reaction order was proposed to be zero in the report of the partial hydrogenation of a rapeseed oil in the presence of a supported palladium catalyst by Santacesaria *et al.* [13]. In this study, findings from effects of catalyst amount and hydrogen pressure on soybean oil

hydrogenation over 5wt%Pd/ Al_2O_3 suggested that a fractional order with regard to the hydrogen concentration may be assumed. However, given the errors in Figure 4.9 and the fact that the triplicate experiments were performed on one catalyst sample only, further tests are required for determining the hydrogen reaction order.

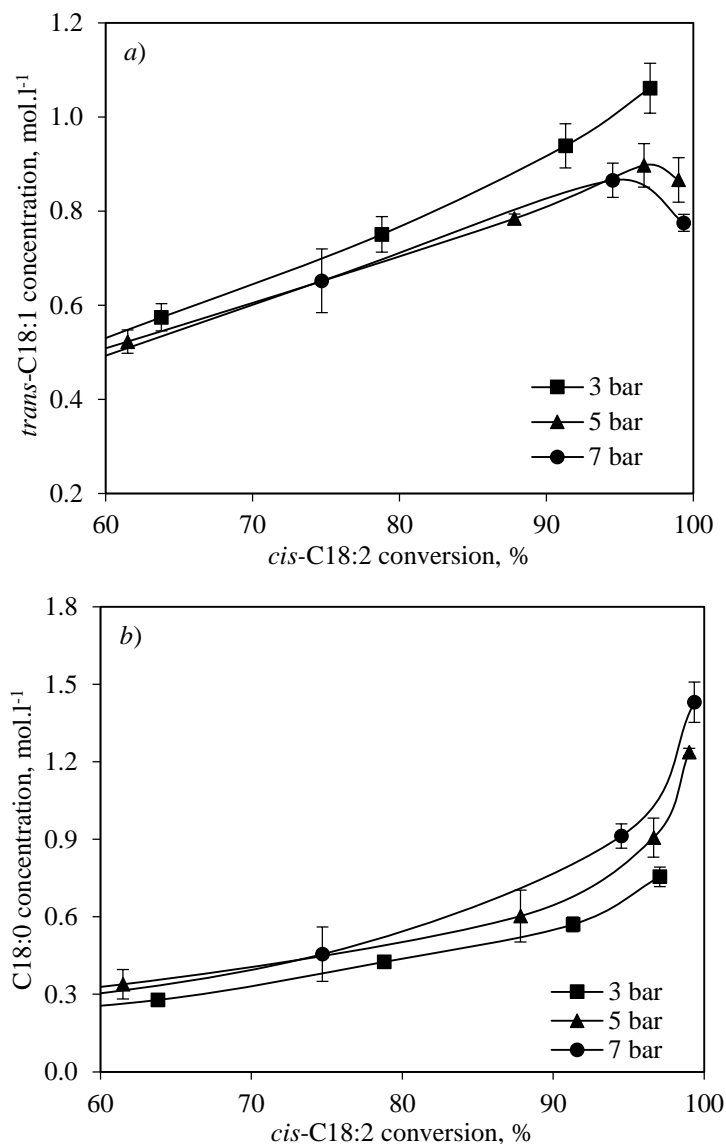


Figure 4.10 Comparison of the formation of a) *trans*-C18:1 and b) C18:0 at the same *cis*-C18:2 conversion under different hydrogen pressures. Reaction conditions were: 150 mg of 5wt%Pd/ Al_2O_3 , 150 ml of soybean oil, $T=100\text{ }^{\circ}\text{C}$, $N=800\text{ rpm}$.

The influence of hydrogen pressure on the product formation was also evaluated. Figure 4.10 a shows the concentration of side product *trans*-C18:1 as a function of the *cis*-C18:2 conversion, indicating that a slightly higher amount of *trans*-isomer was produced at lower

pressure of 3 bar, whereas very close behaviour was observed for 5 bar and 7 bar. This may suggest that low concentration of dissolved molecular hydrogen in the bulk liquid at low operating pressure promoted isomerisation on the catalyst surface, in preference to hydrogenation. A lower availability of hydrogen on the catalyst site also showed a lower production of saturated fatty acid (C18:0) in the case of 3 bar pressure (Figure 4.10 *b*). It appeared to be that the hydrogen concentration influences the reaction selectivity of hydrogenation versus isomerisation, a low hydrogen concentration favours the *cis-trans* isomerisation relative to the hydrogenation whilst increasing the hydrogen concentration on the catalyst surface by higher hydrogen pressure leads to the over-hydrogenation (saturation reaction) at the expense of the isomerisation reaction. Furthermore it is suggested that hydrogen is needed in isomerisation, which stops in the absence of hydrogen [120,296,297]. In the selective hydrogenation of fatty acid methyl esters of sunflower oil (FAME), Pérez-Cadenas *et al.* [296] found the isomerisation rate was weakly dependent on the hydrogen pressure although hydrogen was not consumed. The effect of hydrogen concentration on the reversible *cis-trans* formation in the soybean oil hydrogenation was reported to give different hydrogen orders, 0.88 ± 0.01 for *cis*-isomer to react (forward) and 1.56 ± 0.03 for *trans*-isomer to react (backward) respectively [120]. Another study by Dijkstra [297] on the isomerisation of the mono-unsaturated fatty acid suggested a half an order isomerisation in hydrogen.

Based on the above results, 5 bar of hydrogen pressure was chosen as a compromise between achieving an acceptable reaction rate and less formation of C18:0 for the following study. The *cis-trans* isomerisation mechanism in the present reaction system is studied.

4.3.1.2.2 Kinetic models for Soybean Oil Hydrogenation

In this section, the intrinsic mechanism of soybean oil hydrogenation using 5wt%Pd/Al₂O₃ was fully investigated in the present Baskerville autoclave reactor with the set of operating

conditions (150 mg of 5wt%Pd/Al₂O₃ in 150 ml of soybean oil, $T= 100\text{ }^{\circ}\text{C}$, $p_{H_2} = 5\text{ bar}$, and $N= 800\text{ rpm}$), under which the mass transfer limitations can be ignored. A well-accepted simple mechanistic kinetic Model 1 (Figure 4.11), proposed in 1949 by Bailey [298], was firstly applied as a preliminary model to identify the adsorption coefficients of the fatty acids upon the palladium active site. In Model 1, both *cis*- and *trans*-isomers with the same numbers of double bonds are combined or lumped into groups. On the basis of Model 1, a novel comprehensive Model 2 (Figure 4.13) was subsequently proposed to describe the soybean oil hydrogenation process involving *cis-trans* isomerisation and hydrogenation. Rate equations of both models were derived and fitted to the obtained experimental data. This section addresses the discussion on the model fitting with the details of equation derivation procedures referring to Appendix 8.1.28.1.2.

Model 1

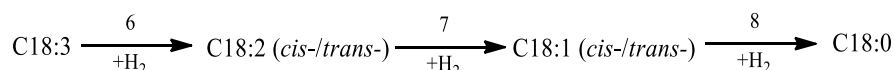


Figure 4.11 The reaction scheme of soybean oil hydrogenation based on Model 1 [298]. Reaction step numbers shown maintain consistent with those in the kinetic study in Appendix 8.1.2.

A Langmuir-Hinshelwood based adsorption kinetic relation was used to establish partial differential equations (Equations 4-15 ~ 4-18 in Table 4.6) of the fatty acids in Model 1.

K_i ($i=1, 2, 3$), is the equilibrium adsorption constant of the fatty acid. A ratio of 3:2:1 for $K_3:K_2:K_1$, corresponding to the adsorption probabilities of trienic (C18:3), dienic (C18:2), monoenic (C18:1) fatty acids on the palladium surface respectively, was proposed by Santacesaria *et al.* [13]. k denotes the rate constant of the double bond hydrogenation which was assumed to be independent of the degree of saturation [203]. To solve for parameters K_i and k in Model 1, the objective function F' (Equation 4-6, $i= \text{C18:3, C18:2, C18:1}$, and C18:0 ; $j= 1, 2, 3\dots$) was minimised.

Table 4.6 Partial differential equations in two kinetics models for hydrogenation of soybean oil.

Equations for corresponding components in soybean oil hydrogenation kinetics models ^a	Equation number
<i>Model 1</i>	
$\frac{\partial C_{18:3}}{\partial t} = -mkK_3[C_{18:3}]\theta_*\theta_H$	4-15
$\frac{\partial C_{18:2}}{\partial t} = mk(K_3[C_{18:3}] - K_2[C_{18:2}])\theta_*\theta_H$	4-16
$\frac{\partial C_{18:1}}{\partial t} = mk(K_2[C_{18:2}]\theta_H - K_1[C_{18:1}]\theta_H^2)\theta_*$	4-17
$\frac{\partial C_{18:0}}{\partial t} = mkK_1[C_{18:1}]\theta_*\theta_H^2$	4-18
<i>Model 2</i>	
$\frac{\partial C_{18:3}}{\partial t} = -mkK_3[cis-C_{18:3}]\theta_*\theta_H$	4-19
$\frac{\partial cis-C_{18:2}}{\partial t} = m\left\{(K_3[cis-C_{18:3}] - K_2[cis-C_{18:2}])k\theta_H - (k_i[cis-C_{18:2}] - k_{-i}[trans-C_{18:2}])K_2\theta_H^\gamma\right\}\theta_*$	4-20
$\frac{\partial trans-C_{18:2}}{\partial t} = mK_2\left\{(k_i[cis-C_{18:2}] - k_{-i}[trans-C_{18:2}])K_2\theta_H^\gamma - k[trans-C_{18:2}]\theta_H\right\}\theta_*$	4-21
$\frac{\partial cis-C_{18:1}}{\partial t} = mkK_2([cis-C_{18:2}] + [trans-C_{18:2}])\theta_*\theta_H - mK_1\left\{k[cis-C_{18:1}]\theta_H^2 + (k_i[cis-C_{18:1}] - k_{-i}[trans-C_{18:1}])\theta_H^\delta\right\}\theta_*$	4-22
$\frac{\partial trans-C_{18:1}}{\partial t} = mK_1\left\{(k_i[cis-C_{18:1}] - k_{-i}[trans-C_{18:1}])\theta_H^\delta - k[trans-C_{18:1}]\theta_H^2\right\}K_1\theta_*$	4-23
$\frac{\partial C_{18:0}}{\partial t} = mkK_1([cis-C_{18:1}] + [trans-C_{18:1}])\theta_*\theta_H^2$	4-24

^a In all equations: hydrogen adsorbed site fraction $\theta_H = \frac{\sqrt{K_H[H_2]}}{1 + \sqrt{K_H[H_2]}}$, vacant active site fraction $\theta_* = \frac{1}{1 + K_3[C_{18:3}] + K_2[C_{18:2}] + K_1[C_{18:1}] + K_0[C_{18:0}]}$

All model parameters were simultaneously estimated using a Solver function of MS Excel software. A constraint was imposed that the coefficients must be greater than or equal to zero. The experimental and predicted fatty acid compositions are displayed in Figure 4.12. It is clear that the Model 1 predicted the experimental concentration data points closely as a function of the reaction times and the trends of trienic (C18:3), dienic (C18:2), monoenic (C18:1) and saturated (C18:0) fatty acids distribution were also closely represented by the model. The values of optimised parameters by regression are shown in Table 4.7. It is noted that the equilibrium adsorption constant of the saturated product C18:0 was predicted as $K_0=0$, indicating that the saturation product moves away from the catalyst surface since the reaction is highly exothermic [297].

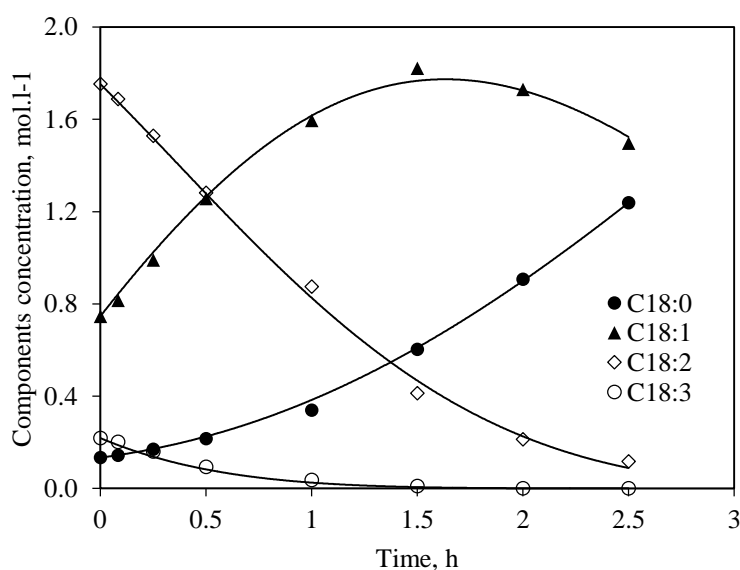


Figure 4.12 Experimental (scattered symbols) and predicted (solid lines) fatty acid composition profiles using Equations 4-15 ~ 4.18 for Model 1. Reaction conditions were: 150 mg of 5wt%Pd/Al₂O₃, 150 ml of soybean oil (solvent free), $T= 100\text{ }^{\circ}\text{C}$, $P_{H_2} = 5\text{ bar}$, $N= 800\text{ rpm}$.

Table 4.7 Values of fitted parameter using Equations 4-14 ~ 4.17 for Model 1.

Adsorption constant, l.mol ⁻¹				Rate constant, mol.g ⁻¹ .h ⁻¹	
C18:3	C18:2	C18:1	C18:0	H ₂	
K_3	K_2	K_1	K_0	K_H	k
5.51×10^6	3.68×10^6	1.84×10^6	0	54.73	4.17

Although the above Model 1 is able to represent hydrogenation rates adequately as shown in Figure 4.12, it neglects isomerisation by lumping isomers of the same chemical formula as one product. While in addition to the hydrogenation mechanism on the Pd surface site, the *cis-trans* isomerisation should also be taken into the account as the aim of this study since *cis*-isomers are of primary importance for the quality of the final product and *trans*-isomers are undesirable. Hence a more complete kinetic Model 2 where hydrogenation reactions are considered together with *cis-trans* isomerisation in a complex reaction scheme was proposed to better describe the soybean oil hydrogenation process.

Model 2

In this Model 2, the *cis-trans* isomerisation is considered following the well-known Horiuti-Polanyi mechanism [213]. Figure 4.13 describes the reaction scheme of soybean oil hydrogenation based on Model 2.

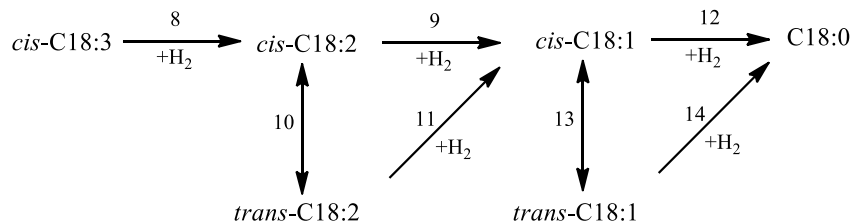


Figure 4.13 The reaction scheme of soybean oil hydrogenation based on Model 2. Reaction step numbers shown maintain consistent with those in the kinetic study in Appendix 8.1.2.

Likewise, the Langmuir-Hinshelwood-Hougen-Watson (LHHW)-based kinetics were applied in order to obtain the intrinsic rate equations. The mass balance for each component is given by the differential equations listed in in Table 4.6 as Equations 4-19 ~ 4-24.

The hydrogen orders for the isomerisation reactions are assumed to be different, presented as γ for *cis*-isomer to react (forwards) and δ for *trans*-isomer to react (backwards). Equations 4-19 ~ 4-24 were applied to fit to the experimental data. The equilibrium adsorption coefficients of the fatty acids K_i ($i=0, 1, 2, 3$) and the rate constant k obtained in Model 1

were used as the initial values in Model 2 to accelerate the parameter estimation routine. All the parameters were simultaneously optimised in the same way as for Model 1 using the Solver function of MS Excel software. As is shown in Figure 4.14, Model 2 is able to reproduce accurately the evolution of each component in the course of reaction time, including the concentration changes of *trans*-C18:1. Meanwhile, Table 4.8 summarises the values of optimised parameters for Model 2 by regression.

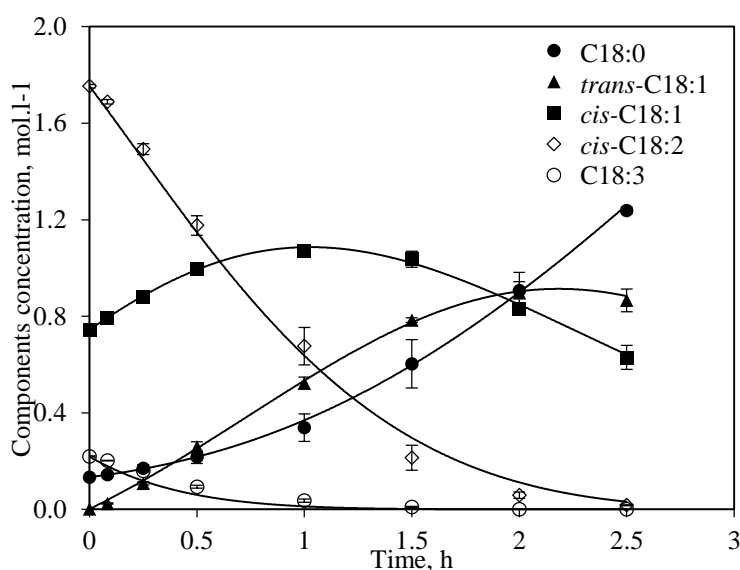


Figure 4.14 Experimental (scattered symbols) and predicted (solid lines) fatty acid composition profiles using Equations 4-18 ~ 4-23 for Model 2. Reaction conditions were: 150 mg of 5wt%Pd/Al₂O₃, 150 ml of soybean oil (solvent free), $T = 100\text{ }^{\circ}\text{C}$, $p_{\text{H}_2} = 5\text{ bar}$, $N = 800\text{ rpm}$.

Table 4.8 Fitted parameter values using Equations 4-18 ~ 4-23 for Model 2.

Adsorption constant, l.mol ⁻¹					Rate constant, mol.g ⁻¹ .h ⁻¹			Hydrogen order	
C18:3	C18:2	C18:1	C18:0	H ₂	k	k_i	k_{-i}	γ	δ
K_3	K_2	K_1	K_0	K_H	k	k_i	k_{-i}	γ	δ
5.51×10^6	3.68×10^6	1.84×10^6	0	42.66	4.08	3.09	1.68	2.24	0.11

From the Model 2, the rate constants of the reversible *cis-trans* isomerisation under current reaction conditions (150 mg of 5wt%Pd/Al₂O₃, 150 ml of soybean oil, $T = 100\text{ }^{\circ}\text{C}$; $p_{\text{H}_2} = 5\text{ bar}$; $N = 800\text{ rpm}$) were predicted to be 3.09 mol.g⁻¹.h⁻¹ for *cis*-isomer to react (forwards) and 1.68 mol.g⁻¹.h⁻¹ for *trans*-isomer to react (backwards) respectively, which were both lower than the rate constant of the hydrogenation of carbon-carbon double bond (C=C), indicating a

slower rate of isomerisation than that of hydrogenation. The hydrogen orders in the present reaction system were found as 2.24 for *cis*-isomer to react and 0.11 for *trans*-isomer to react, suggesting a hydrogen-dependent *cis-trans* isomerisation mechanism.

In summary, for the analysis of the experimental data collected at reaction times both of the resulting mathematical models are able to predict satisfactorily the concentrations of each species during the course of the selective hydrogenation of soybean oil in the current reaction system.

4.3.1.2.3 Effect of Temperature and Activation Energy

As explained by collision theory, conducting a reaction at a higher temperature delivers more energy into the system, and thus more of the colliding particles will have the necessary activation energy resulting in more successful collisions through breaking the pre-existing bonds between reactants and forming in new bonds. In order to obtain the activation energy in this reaction system, a series of reactions was carried out using 150 mg of 5wt%Pd/Al₂O₃ in 150 ml of soybean oil, under a constant hydrogen pressure of 5 bar with a stirring speed of 800 rpm at temperatures ranging from 50 °C, 75 °C, 100 °C to 125 °C.

The temperature dependence of the reaction rate constants obeys the Arrhenius-type equation as:

$$\ln(k) = \ln(A) - \frac{E_a}{R} \left(\frac{1}{T} \right) \quad 4-25$$

where k = reaction rate coefficient (mol.m⁻³.s⁻¹), A = pre-exponential factor, E_a = activation energy (kJ.mol⁻¹), R = gas constant (8.314 J.K⁻¹.mol⁻¹), and T = absolute temperature (K).

According to Equation 4-25, when $\ln(k)$ is plotted against $1/T$, the value of the intercept will correspond to $\ln(A)$, and the gradient of the line will be equal to $-E_a/R$, from which E_a can be easily estimated. Figure 4.15 shows the resulting Arrhenius plot for soybean oil

hydrogenation over 5wt%Pd/Al₂O₃ in this study, and the activation energy in the present reaction system was obtained as 37.8 kJ.mol⁻¹. This was lower than the activation energy (75.5 kJ.mol⁻¹) reported by Fillion *et al.* [120] in soybean oil hydrogenation over a Ni/Al₂O₃ catalyst, which could be attributed to the difference in the nature of catalyst. Similarly, Belkacemi and Hamoudi [299] also reported that reaction using the palladium catalyst gave a lower activation energy than that using the nickel catalyst, which were 38.6 kJ.mol⁻¹ for the palladium catalyst, 48.3 kJ.mol⁻¹ for the nickel catalyst in sunflower hydrogenation and 40.1 kJ.mol⁻¹ for the palladium catalyst, 73.7 kJ.mol⁻¹ for the nickel catalyst in canola oil hydrogenation.

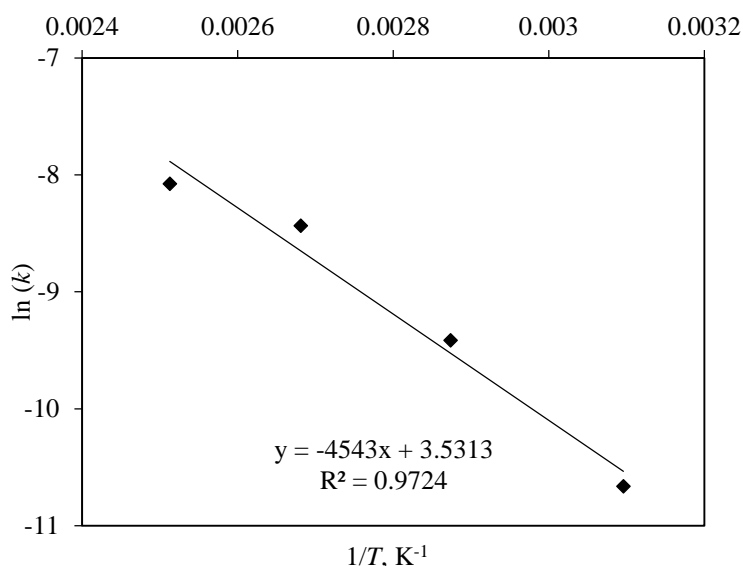


Figure 4.15 Arrhenius plot of $\ln(k)$ versus $1/T$ showing temperature dependence of soybean oil hydrogenation over a 5wt%Pd/Al₂O₃ catalyst. Reaction conditions were: 150 mg of 5wt%Pd/Al₂O₃, 150 ml of soybean oil (solvent free), $p_{H_2} = 5$ bar, $N = 800$ rpm.

As to the temperature effect on the product formation, Figure 4.16 shows that high temperature slightly enhanced the formation of fatty acid *trans*-isomers towards the end of the reaction (*cis*-C18:2 conversion > 50%), indicating a negative effect on the *trans*-C18:1 formation from the temperature increase. Deliy *et al.* [283] suggested this effect was related to reduction of concentration of hydride modes on the catalyst surface that led to the growth of contribution of isomerisation.

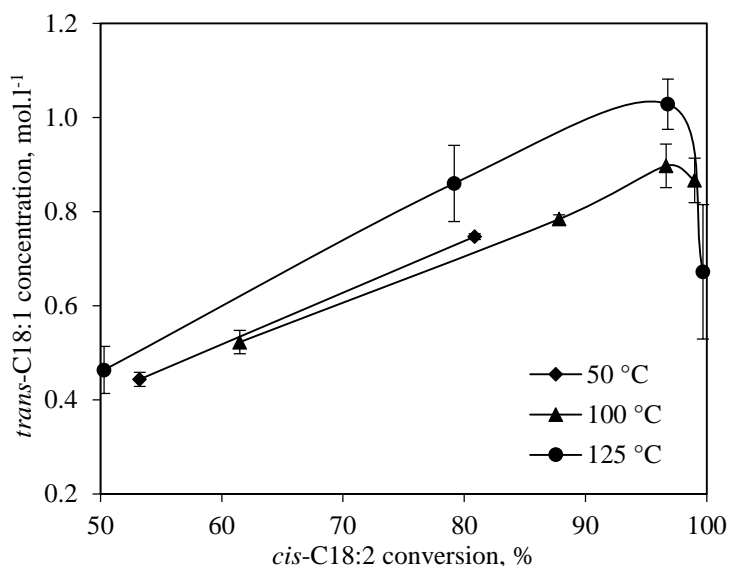


Figure 4.16 Formation of *trans*-C18:1 versus *cis*-C18:2 conversion in soybean oil hydrogenation using 5wt%Pd/Al₂O₃ under different reaction temperatures. Reaction conditions were: 150 mg of 5wt%Pd/Al₂O₃, 150 ml of soybean oil (solvent free), $p_{H_2} = 5$ bar, $N = 800$ rpm.

After the delineation of mass transfer and reaction mechanisms using conventional Pd/Al₂O₃, the following section reports the catalytic testing of bio-Pd catalysts in the hydrogenation of soybean oil.

4.3.2 Bio-Pd Catalyst

For the purpose of comparing the catalytic performance of the bio-Pd with that of Pd/Al₂O₃, all the reactions were conducted in the same system with identical loading of 0.05 mg(Pd).ml(oil)⁻¹ under the set of optimised conditions ($T = 100$ °C, $p_{H_2} = 5$ bar, and $N = 800$ rpm). The 5wt%Pd/*E. coli* catalyst reported in §4.3.2.1 and §4.3.2.2 was manufactured following the specific procedure described in §3.3 and sampled from two separate preparations; the 5wt%Pd/*D. desulfuricans* catalyst (one preparation) reported in §4.3.2.3 was provided by Dr K. Deplanche from the School of Biosciences, University of Birmingham; and 5wt%Pd/*E. coli* catalysts prepared by H₂-reduction and formate-reduction (one preparation) in §4.3.2.4 were provided by Dr I. Mikheenko from the School of Biosciences, University of Birmingham.

4.3.2.1 Comparison of Bio-Pd/*E. coli* with Pd/ Al_2O_3

The concentration profile of each component as a function of reaction time using 5wt%Pd/*E. coli* was displayed in Figure 4.17, showing the same product evolution but a much slower reaction rate as compared to the case of conventional catalyst 5wt%Pd/ Al_2O_3 (Figure 4.5). After 5 hours' reaction time a residual *cis*-C18:2 concentration of $0.97\pm 0.1 \text{ mol.l}^{-1}$ was retained (conversion of $45.52\pm 5.61 \%$), in contrast a complete consumption within 2.5 hours occurred by using 5wt%Pd/ Al_2O_3 under identical operating conditions in Figure 4.5.

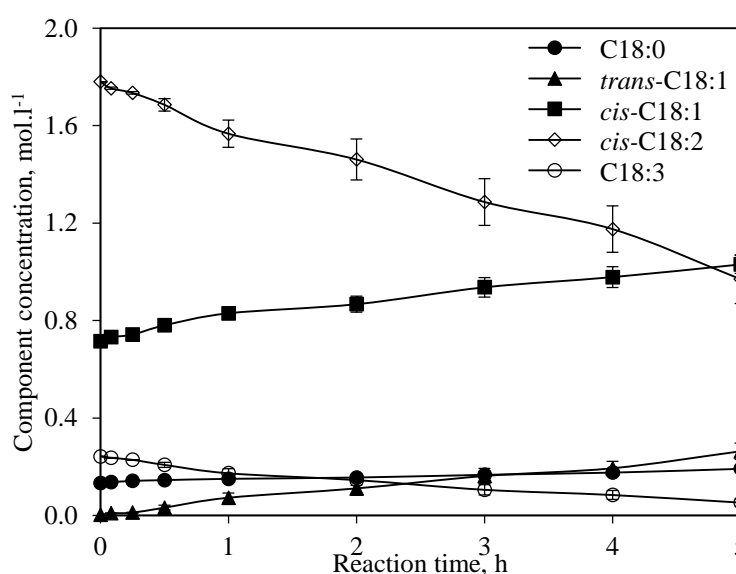


Figure 4.17 Concentration profiles as the function of reaction time in soybean oil hydrogenation using 5wt%Pd/*E. coli*. Reaction conditions were: 150 mg of 5wt%Pd/*E. coli*, 150 ml of soybean oil (solvent free), $T=100 \text{ }^\circ\text{C}$, $p_{H_2} = 5 \text{ bar}$, $N=800 \text{ rpm}$.

Table 4.9 A comparison of the component distribution in soybean oil hydrogenations using 5wt%Pd/*E. coli* and 5wt%Pd/ Al_2O_3 , at the reaction time when the highest amount of preferable product *cis*-C18:1 was produced (~5 hours for bio-Pd/*E. coli* and ~1 hour for Pd/ Al_2O_3). Reaction conditions were: 150 mg of 5 wt%Pd catalysts, 150 ml of soybean oil (solvent free), $T=100 \text{ }^\circ\text{C}$, $p_{H_2} = 5 \text{ bar}$, $N=800 \text{ rpm}$.

Products	Component concentration, mol.l^{-1}	
	5wt%Pd/ <i>E. coli</i>	5wt%Pd/ Al_2O_3
<i>cis</i> -C18:1	1.03 ± 0.04 (at ~5 hours)	1.07 ± 0.02 (at ~1 hour)
<i>trans</i> -C18:1	0.26 ± 0.03	0.52 ± 0.02
C18:0	0.19 ± 0.00	0.34 ± 0.06
<i>Reactants</i>		
<i>cis</i> -C18:3	0.05 ± 0.02 (78.36 \pm 6.10% conv.)	0.04 ± 0.01 (83.15 \pm 3.39% conv.)
<i>cis</i> -C18:2	0.97 ± 0.10 (45.52 \pm 5.61% conv.)	0.68 ± 0.08 (61.49 \pm 4.28% conv.)

A comparison of the product distribution between the bio-Pd/*E. coli* and Pd/ Al_2O_3 is shown in Table 4.9, at the reaction time when the highest amount of preferable product *cis*-C18:1 was produced. After 5 hours' reaction time over 5wt%Pd/*E. coli*, *cis*-C18:1 production accumulated to the highest concentration of $1.03 \pm 0.04 \text{ mol.l}^{-1}$. In the reaction over 5wt%Pd/ Al_2O_3 , a maximum yield of *cis*-C18:1 was $1.07 \pm 0.02 \text{ mol.l}^{-1}$ at ~1 hour, after which *cis*-C18:1 was consumed since the *cis-trans* isomerisation and further saturation of *cis*-C18:1 became dominant. Despite the slower reaction using bio-Pd/*E. coli*, with the same amount of *cis*-C18:1 produced, bio-Pd/*E. coli* produced a 50% less production of *trans*-C18:1 than Pd/ Al_2O_3 , which were $0.26 \pm 0.03 \text{ mol.l}^{-1}$ and $0.52 \pm 0.02 \text{ mol.l}^{-1}$ respectively. As to the saturated fatty acid C18:0 (another unwanted by-product), a lower concentration was also obtained in the case of bio-Pd/*E. coli* than that in the case of Pd/ Al_2O_3 , which were $0.19 \pm 0.00 \text{ mol.l}^{-1}$ and $0.34 \pm 0.06 \text{ mol.l}^{-1}$ respectively. Comparing the product formation at the same *cis*-C18:2 conversion (Figure 4.18 a), bio-catalyst again exhibited the advantage of less production of *trans*-C18:1 meanwhile maintaining the same amount of *cis*-C18:1 at the corresponding *cis*-C18:2 conversion. For instance, when a similar amount of *cis*-C18:2 was converted (~33%, as marked by the vertical dashed line on Figure 4.18 a), 5wt%Pd/*E. coli* produced ~24% less of *trans*-C18:1 than 5wt%Pd/ Al_2O_3 . A less or similar amount of saturated C18:0 was produced in the case of 5wt%Pd/*E. coli* as compared to 5wt%Pd/ Al_2O_3 catalyst at the same *cis*-C18:2 conversion (Figure 4.18 b). It is apparent from both Figure 4.18 a and b that the higher activity of the Pd/ Al_2O_3 catalyst contributed to the formation of *trans*-isomer and the saturated C18:0 at the expense of *cis*-C18:1 at high conversion. In other words, the conventional Pd/ Al_2O_3 catalyst presented a comparative lack of chemoselectivity and lack of control over the level of hydrogenation taking place (*i.e.* over hydrogenation). In contrast 5wt%Pd/*E. coli* appeared to have the capability of maintaining the production of *cis*-

C18:1 and at the same time suppressing the formation of unwanted *trans*-C18:1 and C18:0, although a lower level of hydrogenation was achieved.

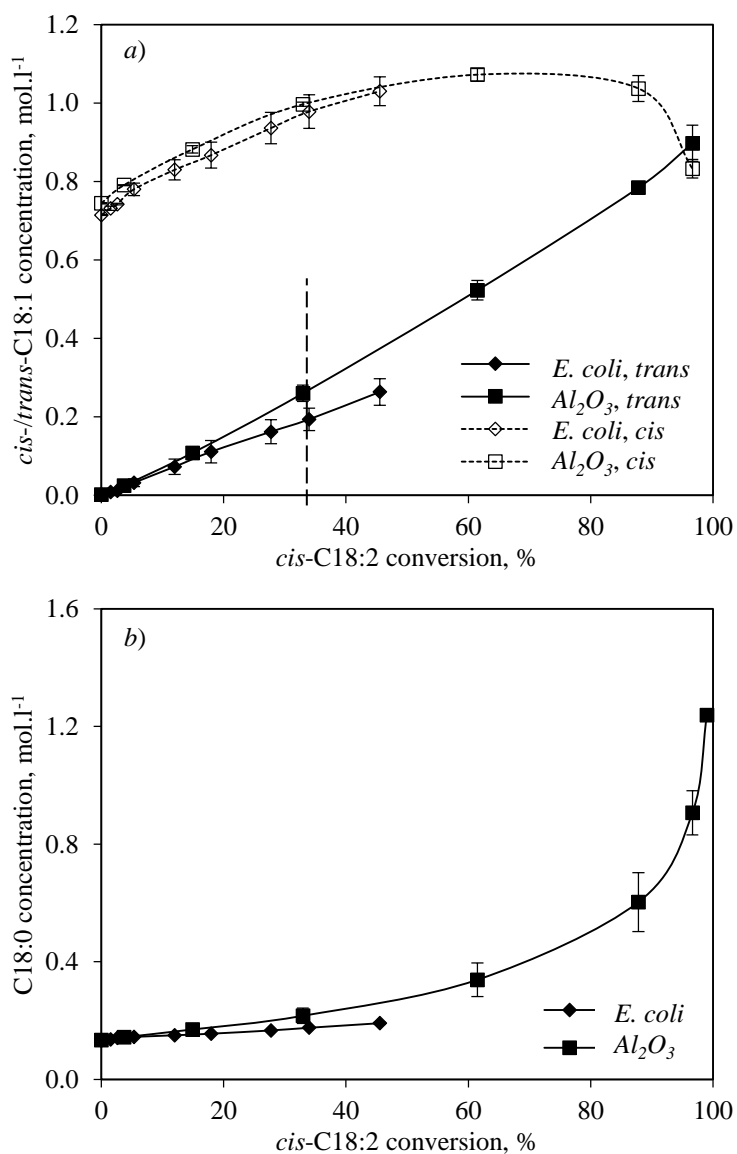


Figure 4.18 Comparison of the formation of a) *cis*-/*trans*-C18:1 and b) C18:0 at the same *cis*-C18:2 conversion by using different Pd catalysts. Reaction conditions were: 150 mg of 5 wt%Pd catalysts, 150 ml of soybean oil (solvent free), $T=100\text{ }^{\circ}\text{C}$, $p_{H_2}=5\text{ bar}$, $N=800\text{ rpm}$.

It was suggested [300] that the hydrogenation of unsaturated fatty acids is sensitive to the shape, geometry, and size of the metal crystallites deposited on the support. Similar to the observation of a less production of *trans*-pentene using bio-Pd/*E. coli* in §4.2, a lower yield of *trans*-C18:1 in soybean oil hydrogenation over 5wt%Pd/*E. coli* can also be attributed to its smaller average size of Pd particles as compared to 5wt%Pd/*Al*₂*O*₃, which are 4.31 nm and

12.77 nm respectively (details to be presented in §6.4). Therefore owing to the advantage of forming small Pd particles, catalyst manufactured by using *E. coli* as support is a better compromise between the activity and capacity to produce *trans*-C18:1 and C18:0 than conventional Pd/Al₂O₃, which justifies the further examination of the biomaterial.

4.3.2.2 Thermal Stability of Bio-Pd/*E. coli* in Hydrogenation

As has been addressed earlier in Literature Review (§2.3.4) that, one limitation for the use of bio-catalyst would be its thermal stability, especially when it is used in advanced synthetic organic chemistry which is often performed at high temperature [47]. In order to verify the stability of bio-Pd catalyst in soybean oil hydrogenation, this section investigates the catalytic performance 5wt%bio-Pd/*E. coli* at an operating temperature of 150 °C. The rest of the reaction conditions were retained the same as: 150 mg 5wt%Pd/*E. coli*, 150 ml of soybean oil (solvent free), $p_{H_2} = 5$ bar, and $N = 800$ rpm.

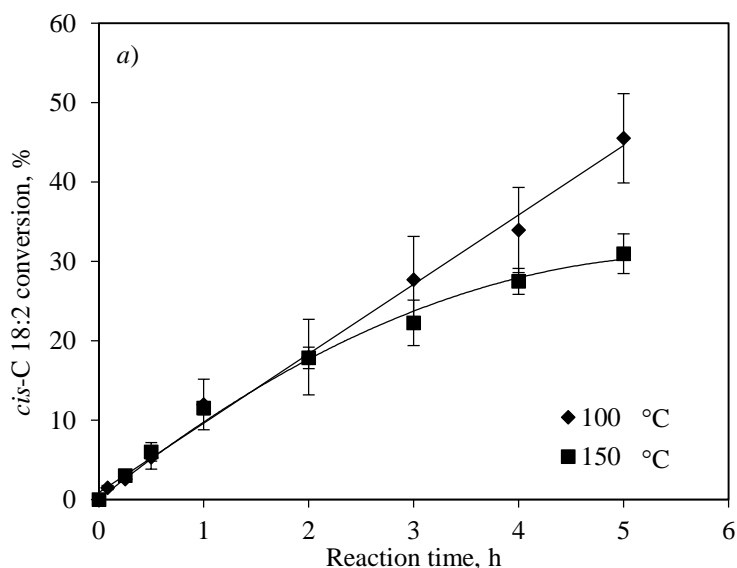


Figure 4.19 a) Comparisons of *cis*-C18:2 conversion versus reaction time in soybean oil hydrogenation using 5wt%Pd/*E. coli* at different reaction temperatures. Other reaction conditions were: 150 mg of 5wt%Pd/*E. coli*, 150 ml of soybean oil (solvent free), $T = 100$ °C, $p_{H_2} = 5$ bar, $N = 800$ rpm.

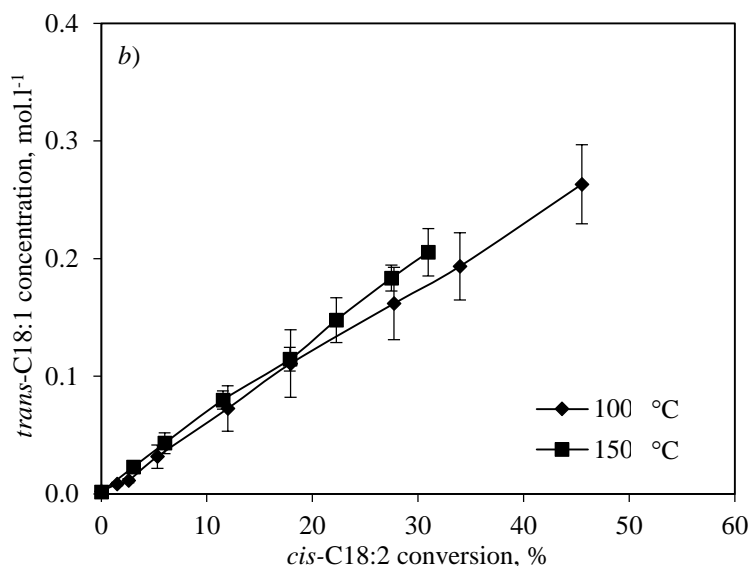


Figure 4.19 *continued*. b) Comparisons of *trans*-C18:1 formation in soybean oil hydrogenation using 5wt%Pd/*E. coli* at different reaction temperatures. Other reaction conditions were: 150 mg of 5wt%Pd/*E. coli*, 150 ml of soybean oil (solvent free), $T = 100\text{ }^{\circ}\text{C}$, $p_{\text{H}_2} = 5\text{ bar}$, $N = 800\text{ rpm}$.

Figure 4.19 *a* gives the comparison of *cis*-C18:2 conversion profiles under two different operating temperatures. In the case of $100\text{ }^{\circ}\text{C}$, *cis*-C18:2 conversion maintained a stable rate throughout the reaction. A higher energy input by raising reaction temperature from $100\text{ }^{\circ}\text{C}$ to $150\text{ }^{\circ}\text{C}$ did not practically affect the rate of *cis*-C18:2 hydrogenation from the beginning. Very close *cis*-C18:2 conversions were obtained at both temperatures from the beginning up to 2 hours reaction time, which may imply a potential catalytic activity loss of the 5wt%Pd/*E. coli*. During the following 3 hours' reaction time, *cis*-C18:2 conversion under $150\text{ }^{\circ}\text{C}$ developed at an obviously slower rate as compared to that under $100\text{ }^{\circ}\text{C}$, which further indicates that the deactivation of 5wt%Pd/*E. coli* may occur under $150\text{ }^{\circ}\text{C}$. As to the product formation, the higher temperature ($150\text{ }^{\circ}\text{C}$) did not affect the formation of *trans*-C18:1 in the present reaction system (Figure 4.19 *b*). A further investigation on the thermal stability of bio-catalyst by using a characterisation technology (Thermogravimetric Analysis) is to be presented in §6.2.

4.3.2.3 Comparison of Bio-Pd/*E. coli* with Bio-Pd/*D. desulfuricans*

A wide range of bacteria strains are able to deposit Pd nanoparticles for applications as bio-catalysts. For the purpose of studying the effect of bacterial support on the catalytic activity in the partial hydrogenation of soybean oil, another bio-Pd catalyst supported on a different bacterial strain *D. desulfuricans* (Gram-negative) was selected and tested. It has been previously reported that 5wt%Pd/*D. desulfuricans* was catalytically active in the hydrogenation of itaconic acid [48] and 2-pentyne [24]. Another early study by Deplanche [23] highlighted homogeneous coverage of small (5~10 nm) Pd nanoparticles on the cell surface of both *E. coli* and *D. desulfuricans* cells at the same loading of 5 wt%Pd, with a similar activity in the Heck reaction obtained [23]. In addition, Macaskie *et al.* [301] reported at a high loading of 25 wt%Pd to biomass, small Pd particles were confirmed on *D. desulfuricans* while fewer, larger ones were visible on *E. coli* via Electron Microscopy; this led to 25wt%Pd/*D. desulfuricans* being the better catalyst in the reduction of Cr(VI) and in the hydrogenation of polychlorinated biphenyls than 25wt%Pd/*E. coli*. Therefore it is possible that although both *D. desulfuricans* and *E. coli* belong to the Gram-negative bacterial type, palladium may be deposited by different mechanisms involving different enzymes and/or biochemical support matrices. In this section, a comparison of catalytic performance was made between 5wt%Pd/*E. coli* and 5wt%Pd/*D. desulfuricans* in soybean oil hydrogenation under the same reaction conditions ($T= 100\text{ }^{\circ}\text{C}$, $p_{\text{H}_2} = 5\text{ bar}$, and $N= 800\text{ rpm}$).

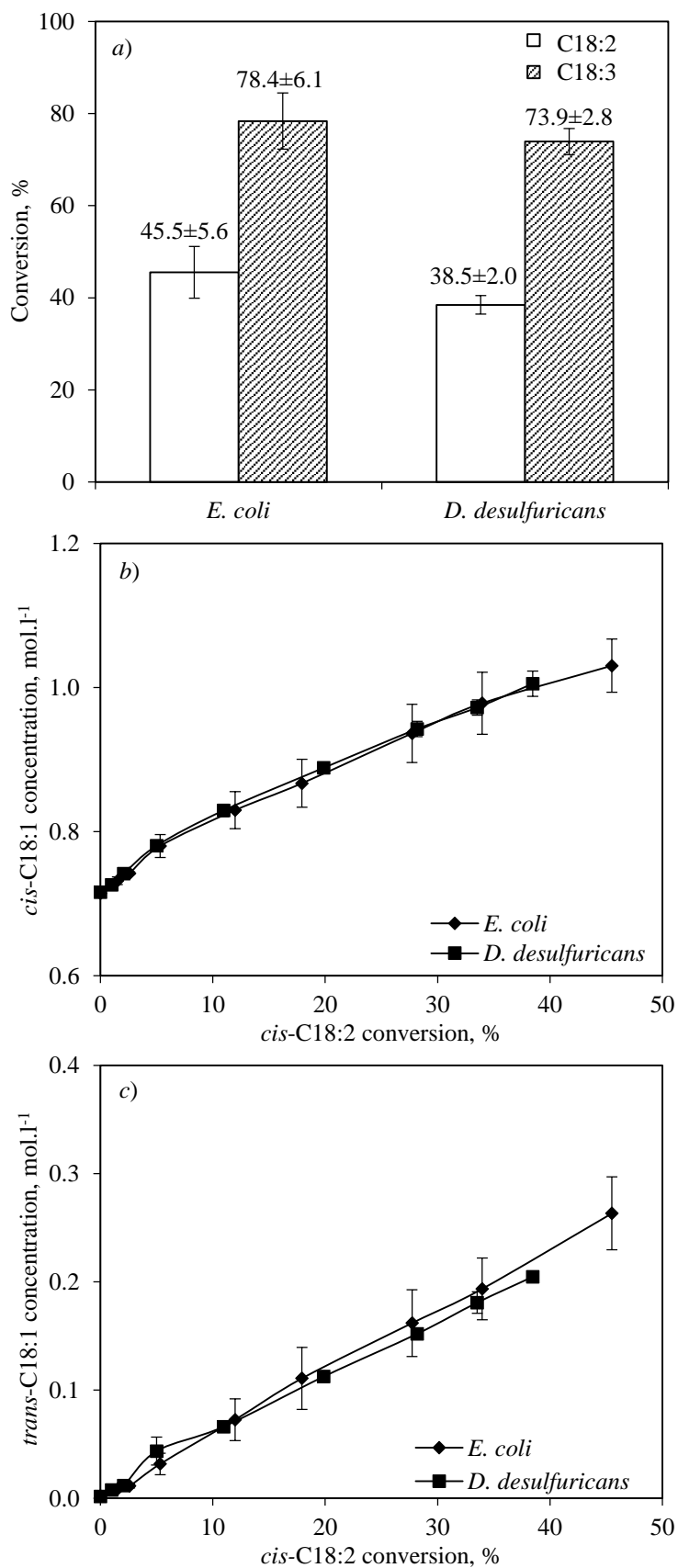


Figure 4.20 Comparison of *a)* the reactant conversion after 5 hours; comparison of the formation of *b)* *cis*-C18:1 and *c)* *trans*-C18:1 at the same *cis*-C18:2 conversion in soybean oil hydrogenation using bio-Pd/*E. coli* and bio-Pd/*D. desulfuricans*. Reaction conditions were: 150 mg of 5 wt% bio-Pd, 150 ml of soybean oil (solvent free), $T = 100\text{ }^{\circ}\text{C}$, $p_{\text{H}_2} = 5\text{ bar}$, $N = 800\text{ rpm}$.

As shown in Figure 4.20 a, 5wt%Pd/*E. coli* gave similar conversions (or within error) of both *cis*-C18:3 and *cis*-C18:2 after 5 hours than 5wt%Pd/*D. desulfuricans*, suggesting a similar activity of these two bio-Pd catalysts in the present soybean oil hydrogenation. In terms of the formation of desired *cis*-C18:1, almost the same amount was produced at the comparable *cis*-C18:2 conversion in both cases (Figure 4.20 b). Likewise, no difference was observed in the case of *trans*-C18:1 formation (Figure 4.20 c). It was discussed earlier in §4.3.2.1 that, 5wt%Pd/*E. coli* produced comparable amount of *cis*-C18:1 and less amount of *trans*-C18:1 than conventional 5wt%Pd/ Al_2O_3 , suggesting a better selectivity towards *cis*-isomer by using bio-Pd/*E. coli*. The maintained same levels of both *cis*-isomer formation and *trans*-isomer formation by using 5wt%Pd/*E. coli* and 5wt%Pd/*D. desulfuricans* (Figure 4.20 b and c) reveal the advantage of this type of biogenically produced palladium catalyst.

Based on the above catalytic performance in soybean oil hydrogenation, a significant advantage could not be shown, overall, in the use of another bio-Pd catalyst. However, *E. coli* (facultative anaerobe) was suggested to be a potentially useful alternative to sulfate-reducing bacteria *D. desulfuricans* (anaerobic) since *E. coli* can be pre-grown aerobically to high density at scale and does not produce H_2S (a catalyst poison) [301]. Hence, as concluded by Deplanche *et al.* [31] the choice between using *E. coli* and *D. desulfuricans* for manufacturing bio-Pd is governed by ease of biomass growth and economic considerations which are considered in Appendix 8.2.

4.3.2.4 Comparison of H_2 -Reduction with Formate-Reduction for bio-Pd/*E. coli*

Since Pd(0) catalyses the decomposition of formate $MCOOH$ into H_2 and CO_2 via the generation of the highly active $H\cdot$ within the crystal structure of the Pd(0), it is possible that bio-Pd reduced from formate may show a better catalytic activity than one made from H_2 . In this section, two types of bio-Pd/*E. coli* catalysts were prepared by applying two reduction methods during the palladisation of cells, denoted as H_2 -reduced and formate-reduced. Here,

E. coli cells were harvested from a 4-litre fermentation bioreactor after 3 weeks of hydrogen production (for another study) [262]. The harvested cells were transferred into an anaerobic respiratory medium (NB no. 2 with 0.4% sodium fumarate (wt/vol) and 0.5% glycerol (vol/vol)) and left overnight at 30 °C to activate cells before palladisation as described in §3.3.1. The catalytic activities of these two resulting 5wt% bio-Pd catalysts were tested in soybean oil hydrogenation for 5 hours under the conditions: 150 mg of 5wt%Pd/*E. coli* catalyst; 150 ml of soybean oil, $T= 100\text{ }^{\circ}\text{C}$, $p_{H_2} = 5\text{ bar}$, and $N= 800\text{ rpm}$.

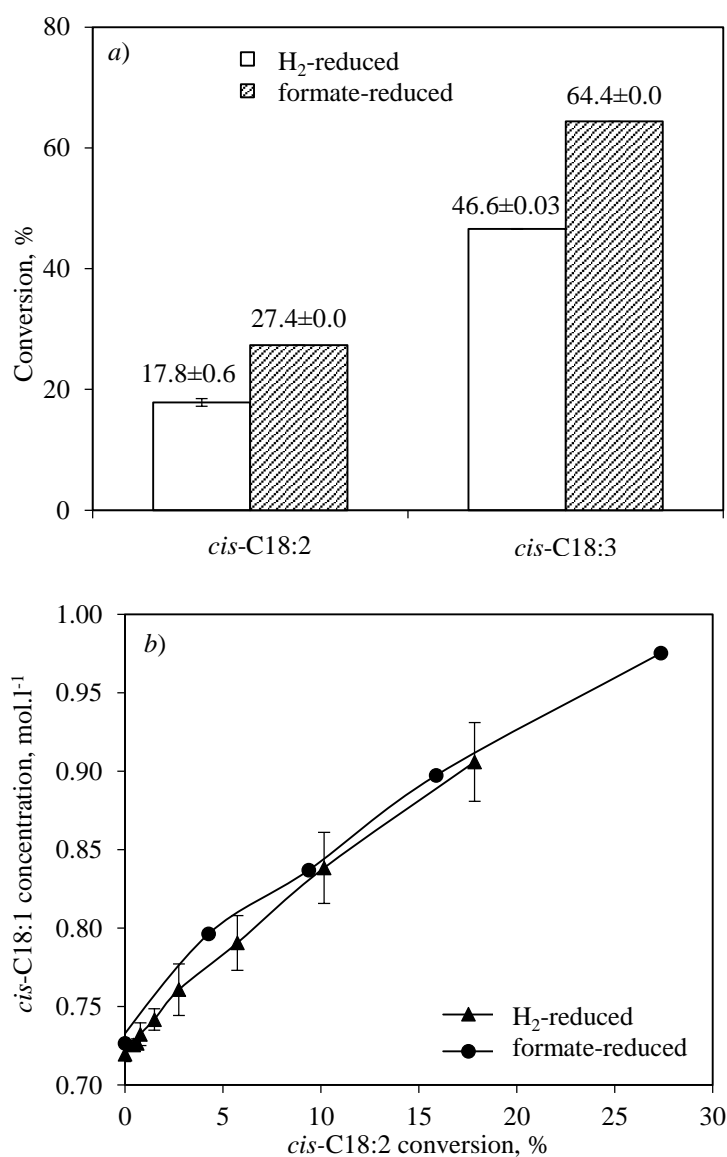


Figure 4.21 a) Comparisons of *cis*-C18:2 conversion and *cis*-C18:3 conversion after 5 hours in soybean oil hydrogenation using 5wt%Pd/*E. coli* prepared by different reduction methods; b) the formation of *cis*-C18:1 as a function of *cis*-C18:2 conversion. Reaction conditions were: 150 mg of 5wt%Pd/*E. coli*, 150 ml of soybean oil (solvent free), $T= 100\text{ }^{\circ}\text{C}$, $p_{H_2} = 5\text{ bar}$, $N= 800\text{ rpm}$.

Figure 4.21 *a* compares conversions of *cis*-C18:3 and *cis*-C18:2 after 5 hours in soybean oil hydrogenation, showing an improvement by ~30% for formate-reduced 5wt%Pd/*E. coli* than H₂-reduced 5wt%Pd/*E. coli*. In terms of the formation of *cis*-C18:1 when the same *cis*-C18:2 was converted (Figure 4.22 *b*), the same behaviour was obtained for both formate-reduced and H₂-reduced bio-Pd/*E. coli*.

4.4 Conclusions

In this chapter, a set of palladium catalysts, including both conventional Pd/Al₂O₃ and biomass supported bio-Pd, were investigated in two industrially important hydrogenations of 2-pentyne and soybean oil.

In 2-pentyne hydrogenation under identical operating conditions ($T = 40\text{ }^{\circ}\text{C}$, $p_{\text{H}_2} = 2\text{ bar}$, $N = 1000\text{ rpm}$, with isopropanol as a solvent), 5wt%Pd/*E. coli* showed similar activity meanwhile a higher production of *cis*-2-pentene in comparison with 5wt%Pd/Al₂O₃.

In the case of the more complicated solvent-free hydrogenation of soybean oil, the mass transfer and reaction mechanism was studied in detail by applying a set of operating conditions using 5wt%Pd/Al₂O₃. Under the reaction conditions of $T = 100\text{ }^{\circ}\text{C}$, $p_{\text{H}_2} = 5\text{ bar}$, and $N = 800\text{ rpm}$, the reaction system was confirmed in the absence of diffusion limitation. Two kinetic models were successfully established to fit the concentration profiles of the experimental data. The hydrogenation of soybean oil was found to be of half-order in the concentration of hydrogen, with the activation energy being $37.8\text{ kJ}\cdot\text{mol}^{-1}$ over the 5 wt% Pd/Al₂O₃ catalyst. Palladium bioinorganic catalyst manufactured using *E. coli* was then tested under the selected reaction conditions (150 mg of 5wt%Pd/*E. coli*, 150 ml of soybean oil, $T = 100\text{ }^{\circ}\text{C}$, $p_{\text{H}_2} = 5\text{ bar}$, $N = 800\text{ rpm}$) and its performance was compared with that of conventional 5wt%Pd/Al₂O₃ in terms of reactive activity and product formation. Bio-Pd/*E.*

coli showed a lower *cis*-C18:2 conversion than the corresponding conventional Pd/Al₂O₃. However the former catalyst showed an advantage of reducing the *cis-trans* isomerisation and complete hydrogenation to the unsaturated double bond on its active sites. A key finding was that by using formate as the electron donor for reduction of Pd(II) as compared to hydrogen, the conversion rates of both *cis*-C18:3 and *cis*-C18:2 in soybean oil were increased by ~30%.

Chapter 5

Aerobic Oxidation Using Bio-AuPd Catalyst

5.1 Chapter Overview

This chapter presents an investigation of biomass-supported AuPd bimetallic catalyst (bio-AuPd) for the aerobic oxidation of a range of alcohols. The work was motivated by promising initial studies of Deplanche *et al.* [170], who preliminarily found a positive synergistic effect between gold and palladium for bacteria-supported catalysts in benzyl alcohol oxidation using oxygen. Their work reported an increased catalyst activity and selectivity towards benzaldehyde over bio-AuPd when compared to bio-Pd and bio-Au individually.

This chapter further reports the in-depth evaluation of bio-AuPd catalysts in the solvent-free oxidation of various alcohols under compressed air (instead of pure oxygen) in a 100 ml Parr autoclave reactor (as described in §3.4.1). A range of alcohols were selected as oxidation substrates, with specific focus on benzyl alcohol (§5.2) as an aromatic alcohol. The first part of the work (§5.2.1) describes a number of modifications made to the original reactor and the optimisation of the reaction conditions based on the engineering aspects; the activation energy in the present solvent-free oxidation of benzyl alcohol over a 2.5wt% Au2.5wt% Pd/*E. coli* catalyst was estimated. A further aim of this study was to improve the catalytic performance of bio-AuPd in benzyl alcohol oxidation by altering the catalyst formulation (§5.2.2), such as the biomass strain, total AuPd metal loading, and Au: Pd metal ratio. Besides, different alcohols may present varied resistance to oxidation and therefore the study was extended to cover a range of different types of alcohols (§5.3).

Finally conclusions were drawn in §5.4 to summarise the catalytic performance of bio-AuPd, as a novel heterogeneous catalyst, in the aerobic oxidation of alcohols in the absence of solvent.

5.2 Oxidation of Benzyl Alcohol

For the oxidation reaction of benzyl alcohol, a comprehensive reaction network by which a number of products can be formed is depicted in Figure 5.1. Mechanistically, the oxidation of benzyl alcohol proceeds through a first oxidation step (denoted as R₁ in Scheme 1) to form benzaldehyde, the desired product in this study, and through a second oxidation of aldehyde step (R₂) to produce benzoic acid. Meanwhile other side reactions (denoted as SR_i) accompany the main reaction. One pathway is a condensation reaction between the generated aldehyde and the initial alcohol (SR₁ in Scheme 1). This generates a hemiacetal, which is a generally unstable compound. This hemiacetal could either be subsequently oxidised (SR₁₁) to the corresponding ester or, following a successive condensation (SR₁₂) with a further molecule of alcohol leading to the formation of the corresponding benzaldehyde dibenzyl acetal (BDDBA). In addition, there is also the possibility of disproportionation of two molecules of benzyl alcohol (SR₂ in Scheme 2) leading to equimolar amounts of toluene and benzaldehyde. Table 5.1 gives some properties of the major components presenting in the reaction system.

A control experiment was firstly conducted using dry biomass of *E. coli* in benzyl alcohol oxidation and no benzyl alcohol was converted. The catalytic activity of the bimetallic bio-AuPd catalyst was evaluated by estimating the conversion of benzyl alcohol, selectivity to desired product benzaldehyde, and turnover frequency (TOF, the converted moles of substrate per molar total metal in unit time), as calculated from the following equations:

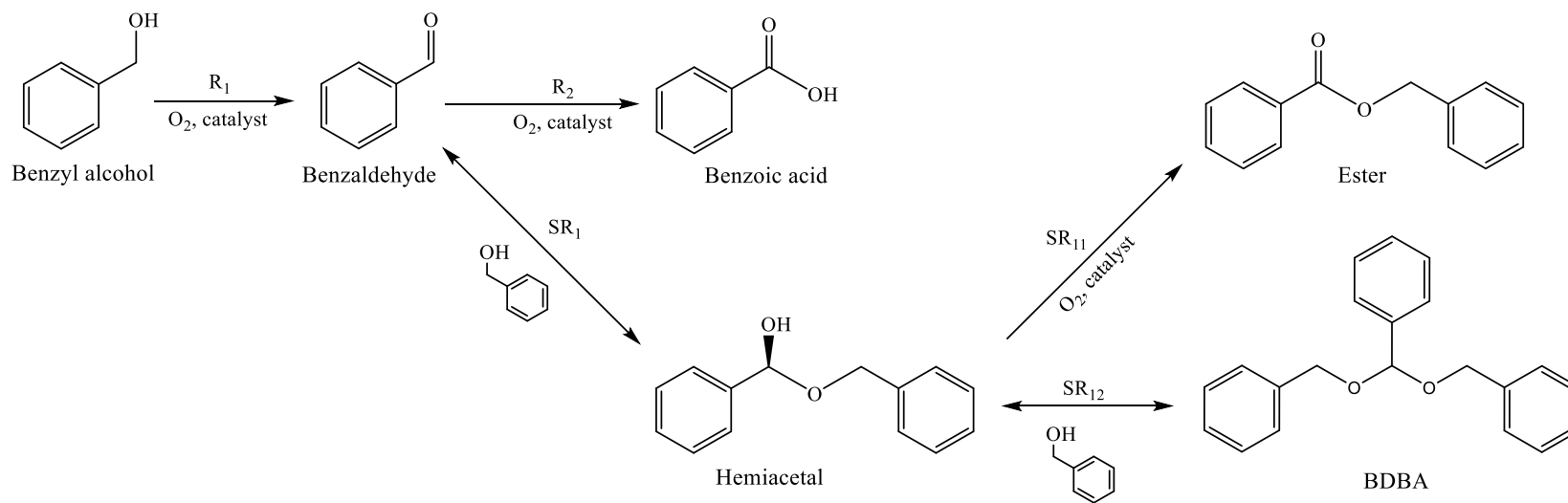
$$\text{alcohol conversion \%} = \frac{[\text{alcohol}]_0 - [\text{alcohol}]_t}{[\text{alcohol}]_0} \times 100\% \quad 5-1$$

$$\text{product selectivity \%} = \frac{[\text{target product}]_t}{[\text{all product}]_t} \times 100\% \quad 5-2$$

$$\text{TOF} = \frac{\text{moles of substrate converted}}{\text{moles of metal} \times \text{time}} \quad 5-3$$

where $[\text{alcohol}]_0$ and $[\text{alcohol}]_t$ correspond to concentrations at initial time ($t=0$) and subsequent time (t) respectively, the same rule applies to the selectivity calculation. TOF was measured after first 0.5 hour of reaction. Results are all presented from at least triplicate experiments as mean \pm standard error of mean, unless otherwise stated. Error bars are within the dimensions of the symbols if not shown. Each bio-AuPd catalyst sampled from the same preparation, unless otherwise stated.

Scheme 1



Scheme 2

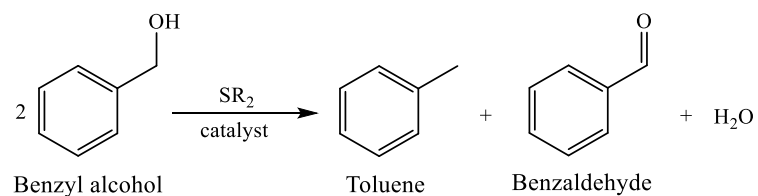


Figure 5.1 Reaction schemes of aerobic benzyl alcohol oxidation [302,303].

Table 5.1 Properties of the major components presenting in benzyl alcohol oxidation.

Component	Formula	Molar mass, g.mol ⁻¹	Boiling point, °C	Physical appearance
benzyl alcohol	C ₇ H ₈ O	108.14	205.3	clear, colourless liquid
benzaldehyde	C ₇ H ₆ O	106.12	178.1	colourless or yellowish liquid, strongly refractive
benzoic acid	C ₇ H ₆ O ₂	122.12	249.2	white, needle-like crystals
benzyl benzoate	C ₁₄ H ₁₂ O ₂	212.24	323	clear, colourless liquid
toluene	C ₇ H ₈	92.14	110.6	colourless liquid
BDDBA	C ₂₁ H ₂₀ O ₂	304.38	531.3	* Information not available.

5.2.1 Experimental Condition Optimisation

Initially the solvent-free benzyl alcohol oxidation was conducted using compressed air in a Parr autoclave with its original configuration of sample ports, sparging *etc.*, in a dead-end mode (§5.2.1.1). Based on the results it was found that the reactor configuration caused some drawbacks for the reaction and therefore a number of modifications to the set up were made in subsequent experiments (§5.2.1.2). The effect of the pre-reduction to the ‘as-received’ bio-AuPd was then investigated to verify whether the catalyst retained its original activity (§5.2.1.3). A mass transfer study was carried out to determine the resistances that occur in the modified reactor configuration (§5.2.1.4). After studies to minimise the mass-transfer limitation, the activation energy of the benzyl alcohol oxidation over the bio-AuPd catalyst in this particular system was estimated (§5.2.1.5).

5.2.1.1 Dead-End Reaction under Compressed Air

In a dead-end operation mode, solvent-free benzyl alcohol oxidation was carried out by keeping the inlet of reactant gas (compressed air) open. The pressure is maintained at a constant value and gas flows into the reactor to replace the equivalent amount consumed in the reaction (the standard operating procedure refers to §3.4.2). The reaction conditions were: 25 mg of 2.5wt% Au2.5wt% Pd/*E. coli*, 40 ml of benzyl alcohol, $T = 110\text{ }^{\circ}\text{C}$, $p_{air} = 5\text{ bar}$, and $N = 1200\text{ rpm}$.

Figure 5.2 (stage 1, 0~2.5 hours) shows the benzyl alcohol oxidation profile as a function of the reaction time. In the initial 15 mins, benzyl alcohol was consumed steadily with time, giving a consumption rate of $0.20 \pm 0.00\text{ mol.l}^{-1}.\text{h}^{-1}$ at 15 mins. Thereafter the rate of benzyl alcohol disappearance gradually slowed down and was observed to follow an overall non-linear function of benzyl alcohol concentration versus time in stage 1. At the end of stage 1 (2.5 hours), the alcohol consumption rate decreased considerably by 85% to $0.03 \pm 0.00\text{ mol.l}^{-1}.$

$^1\text{h}^{-1}$ with the majority of the benzyl alcohol still residual in the system (96.8 ± 0.1 wt% of the mixture, conversion of $3.15\pm 0.08\%$). The major products detected were principally benzaldehyde (1.63 ± 0.03 wt%), BDBA (1.29 ± 0.02 wt%), and traces of benzyl benzoate (0.02 ± 0.00 wt%) with no detection of benzoic acid. Furthermore, it was observed that the formation rate of benzaldehyde, which was produced through the reaction pathway with oxygen participating (R_1 in Scheme 1, Figure 5.1), levelled off with the reaction time. This trend, in contrast, was less obvious in the case of BDBA (product of the formed benzaldehyde consecutively reacting with two benzyl alcohol molecules) which kept growing at a relatively steady rate. It is likely, based on the above observation, that the availability of oxygen plays a role in the present reaction system. It has been reported [66,71,231,232] that the reaction rate of benzyl alcohol oxidation over AuPd bimetallics is zero-order in oxygen in a pressure range 100~3000 kPa. However the observed levelling-off of the alcohol consumption rate in Figure 5.2 (under a still alcohol-rich environment) goes against the behaviour of a zero-order reaction with respect to oxygen, suggesting that the reaction under the given conditions may be limited by the oxygen availability from the air in the dead-space of the semi-batch reactor. The use of compressed air rather than pure oxygen could have led to an inconsistent partial pressure of oxygen inside the vessel, as oxygen from the air was consumed by the bulk liquid to leave gas in the headspace richer in nitrogen. Assuming that as the reaction proceeded and oxygen in air is consumed, this leads to a decrease in overall pressure and a supplement of the same volume of air from the cylinder, of which only ~20 vol% is oxygen. Successively, oxygen from the headspace of the vessel would become depleted and the main residual gas inside of the reactor becomes predominantly inert nitrogen. Oxygen partial pressure decreases as a function of the reaction time, accordingly the dissolved oxygen concentration decreases in the bulk liquid, thus reaction is expected to slow down.

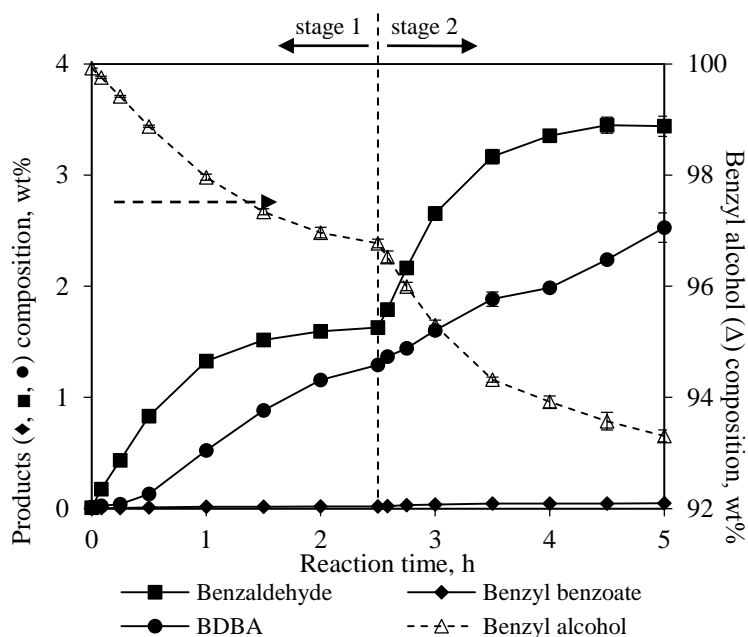


Figure 5.2 Concentration profiles from the benzyl alcohol oxidation in the original Parr autoclave reactor (dead-end mode). Reaction conditions were: 25 mg 2.5wt% Au/2.5wt% Pd/*E. coli*, 40 ml benzyl alcohol, $T=110\text{ }^{\circ}\text{C}$, $p_{air}=5\text{ bar}$, $N=1200\text{ rpm}$. The reaction profile was divided into two stages at the reaction time of 2.5 hours (marked as stage 1 and stage 2, details see text).

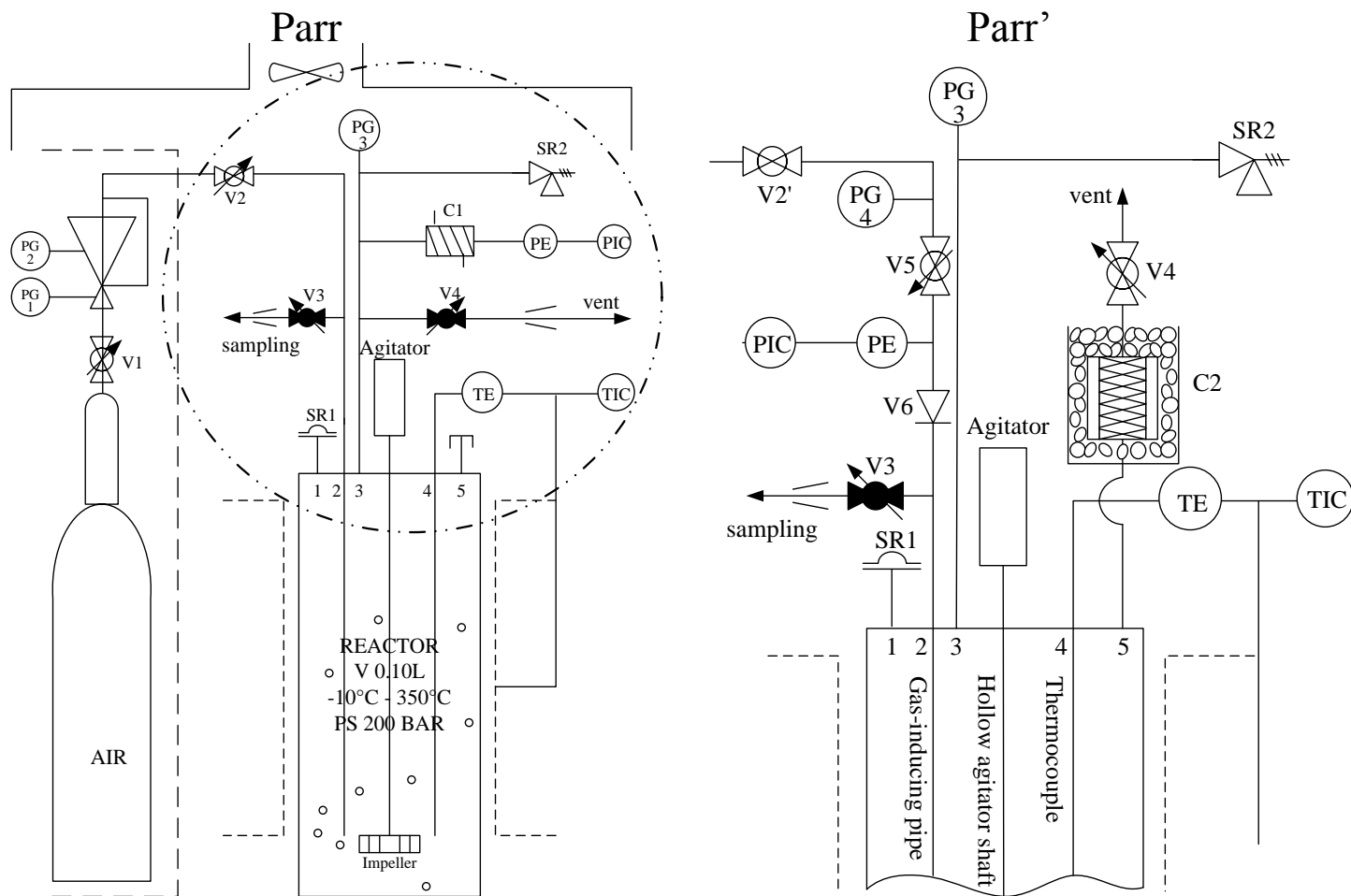
The above assumption was verified by the reaction profile of stage 2 shown in Figure 5.2. After 2.5 hours' dead-end reaction in stage 1, the remaining gas in the vessel was manually released by carefully opening gas release valve V4 (Figure 3.3 in §3.4.1) followed by an immediate replenishment of fresh compressed air to the same pressure of 5 bar. Correspondingly on the benzyl alcohol concentration plot, a second stage of accelerated consumption rate at the subsequent 15 mins was observed while the same non-linear trend was replicated in the following 3 hours' dead-end reaction. Likewise, the levelling-off of benzaldehyde formation and steady growth of BDBA were observed as the case in Stage 1. Besides, benzyl benzoate remained in a small amount with no detection of benzoic acid at the end of the Stage 2.

5.2.1.2 Parr Autoclave Modification

The ability to perform oxidation reactions in air, as an inexpensive and environmentally acceptable reagent, could be attractive for future industrial applications. The findings reported in §5.2.1.1 concerning the slowing down of reaction rate demonstrated that the

depletion of oxygen in the dead-end experimental system affected the oxygen availability which in turn limited the overall reaction performance. As ultimately the quantity of interest is the benzyl alcohol conversion with the reaction time, a modification to the reaction system was carried out to provide the system with a continuous feed of fresh air thus to maintain the oxygen partial pressure with the aim to increase the overall conversion of benzyl alcohol. Attempts were therefore made to change the operating procedure or physical set up of the autoclave reactor in order to achieve this constant through flow. The initial attempt was done by opening the gas release valve V4, creating a steady air flow, of which the flow rate through the outlet was measured by an air rotameter ($200 \text{ ml}\cdot\text{min}^{-1}$, 1 atm), meanwhile a constant pressure (5 bar) inside the vessel was maintained and monitored by a pressure sensor. Due to the 'open' system and considering the volatility of the components (Table 5.1), the overall mass balance was taken into account by weighing the material added into the vessel before and after the reaction. Thereafter the subsequent reactions in this 'open' system showed a continuing consumption of benzyl alcohol as a function of time, the conversion of which at 2 hours was increased by a factor of three in comparison with that in the dead-end system. However a record of overall mass balance indicated a significant 17.5% total mass lost at the end of the reaction (7 hours). This was thought to be due to excessive evaporation of reactants when using a through flow of air.

In order to deal with this problem, a further modification was set up to establish a more reliable reaction system (Figure 5.3, Parr and Parr' denote the reactors before and after modification). A double helix stainless steel condenser coupled with a sufficient water-ice cooling bath (C2 in Parr') was designed and fixed in the gas outlet line, prior to the gas outlet valve V4. At the same time in the gas inlet line, a Hoke metering needle valve (V5 in Parr') was installed to precisely adjust the gas inlet flow rate (calculation refers to Appendix 8.3), with the pressure gauge PG4 and the pressure sensor PE installed before and after the



Valves:	Gauges:	Others
V2' gas inlet control valve	PG1, PG2, PG3 mechanical pressure gauges	SR1 relief valve (set at 40 bar)
V3 sampling valve	Indicators:	SR2 safety rupture disc (set at 70 bar)
V4 gas release valve	TE, TIC temperature sensor, temperature indicator	C1 original built-in condenser
V5 metering valve	PE, PIC pressure sensor, pressure indicator	C2 designed double helix stainless condenser with a water-ice cooling bath
V6 inlet non-return valve		

Figure 5.3 Schematic profiles of oxidation reactor (Parr- original reactor, Parr'- reactor after modification). The working area was circled as shown in the left Parr and details of modification were magnified as the right Parr'. Symbols in Parr' are denoted, symbol description in Parr refers to Figure 3.3 in §3.4.1

metering valve V5 for monitoring the pressure drop. In addition, some other modifications were made to improve the reactor performance, namely: the original needle valve V2 (in Parr, Figure 5.3) in the gas supply line for gas control was replaced by an on-off valve V2' (in Parr'), for the purpose of a quick and efficient isolation between both pressurised gas cylinder and reactor (in case gas trapping happened for instance); a non-return valve V6 (in Parr') was added immediately after the pressure sensor PE to avoid a reflux from the reactor when taking liquid samples, causing the damage to the pressure sensor PE.

Figure 5.4 shows the benzyl alcohol concentration profiles in both the original Parr and modified Parr' reactors, from which an improvement in the benzyl alcohol consumption rate in the flow-through system is observed as compared to that in the dead-end system. Benzyl alcohol in the flow-through system, Parr', was consumed continuously with the reaction time owing to the constant fresh air flow. More importantly, although the modified reactor is a flow-through system, the measured loss of total material after 7 hours was significantly reduced to 1.19% when a condenser with efficient cooling bath (C2 in Parr', Figure 5.3) was fitted, compared with the 17.5% loss in the flow-through system without condenser.

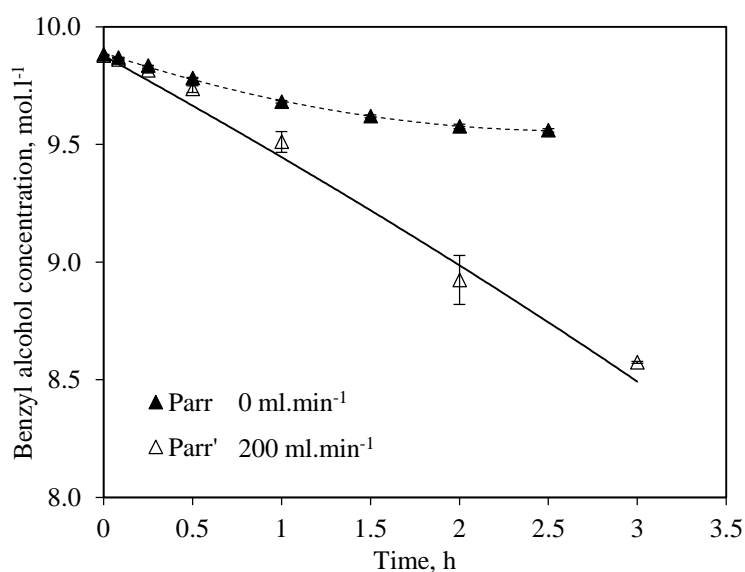


Figure 5.4 Profiles of benzyl alcohol concentration versus reaction time in the original reactor (Parr) and the modified reactor (Parr'). Reaction conditions were: 25 mg 2.5wt%Au2.5wt%Pd/*E. coli*, 40 ml benzyl alcohol, $T = 110\text{ }^{\circ}\text{C}$, $p_{air} = 5\text{ bar}$, $N = 1200\text{ rpm}$.

In terms of the product formation in the modified configuration Parr', the majority of the products based on the aforementioned reaction schemes in Figure 5.1 were identified. In Figure 5.5 *a*, the concentration profile of the desired benzaldehyde kept increasing with time and achieved 31.00 ± 0.35 wt% (3.50 ± 0.04 mol.l⁻¹) after 7 hours. Other products like toluene, benzoic acid and benzyl benzoate also kept increasing, but were retained in minor amounts, the estimated concentrations of these being less than 3 wt% of the total mixture. Another major by-product in this reaction system was benzaldehyde dibenzyl acetal (BDBA). As described in Scheme 1 (SR₁₂ Figure 5.1), BDBA was formed by one molecule of aldehyde successively reacting with two molecules of alcohol, which was reported as a reversible oxidative degradation of benzyl alcohol [304,305]. The monitored concentration of BDBA increased in the time period of 0~5 hours (reaching a maximum 5.80 ± 0.17 wt%), at a lower rate than that of benzaldehyde but faster than those of toluene, acid and benzyl benzoate. The decrease of the BDBA concentration after 5 hours reaction time indicates that the BDBA was being converted to other products. It is well accepted that acetals are stable to neutral and basic reaction conditions but susceptible to hydrolysis in the presence of acid which, in this study, could have been catalysed by benzoic acid starting to form. The reversible reaction of BDBA led to other products, including benzaldehyde [231,302]. This, as a result, led to an increase of the final selectivity towards benzaldehyde. The reversible relation between benzaldehyde and BDBA was confirmed by the mirror trends in Figure 5.5 *b* in terms of selectivity. In other words the formation of BDBA in the early stage caused an initial decrease of selectivity to aldehyde (from $75.9 \pm 2.5\%$ to $61.5 \pm 0.1\%$), which was observed to recover once BDBA started to be hydrolysed.

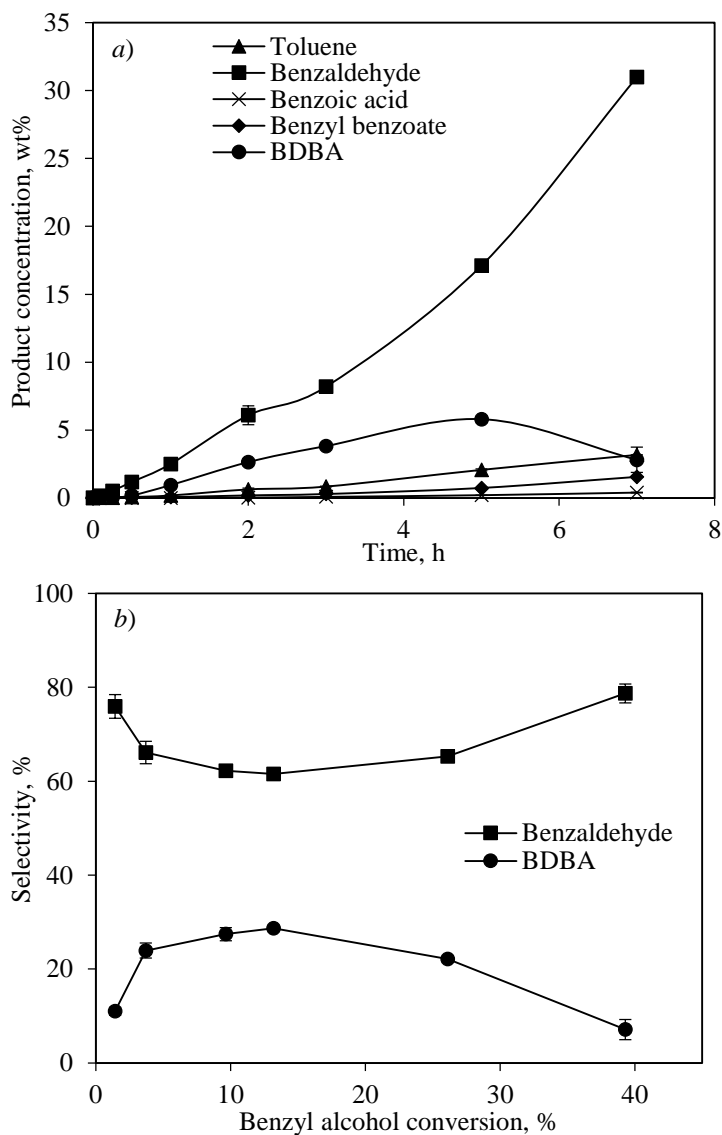


Figure 5.5 a) Product profiles as a function of reaction time in benzyl alcohol oxidation; b) Selectivities to different products versus benzyl alcohol conversion. Reaction conditions were: 25 mg 2.5wt% Au2.5wt% Pd/*E. coli*, 40 ml benzyl alcohol, $T = 110\text{ }^{\circ}\text{C}$, $p_{air} = 5\text{ bar}$, $N = 1200\text{ rpm}$.

A further comparison of product formation was made between the reactor before (Parr) and after (Parr') modification during the first 2 hours reaction time (Figure 5.6), the only reaction condition difference being the air flow of $0\text{ ml}\cdot\text{min}^{-1}$ for Parr and $200\text{ ml}\cdot\text{min}^{-1}$ for Parr' respectively.

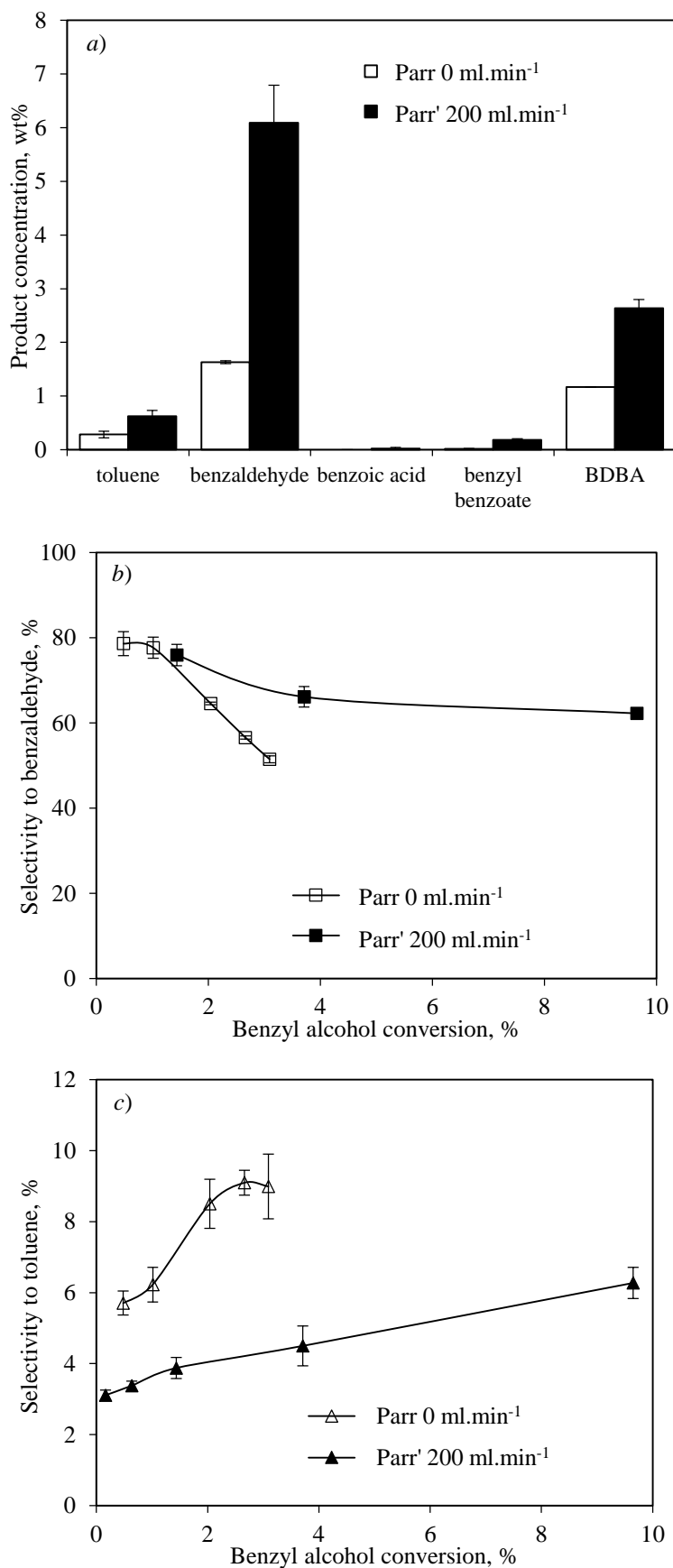


Figure 5.6 Comparison of results from the original reactor (Parr) and the modified reactor (Parr') based on *a*) product distributions at 2 hours; *b*) benzaldehyde selectivity versus benzyl alcohol conversion; *c*) toluene selectivity versus benzyl alcohol conversion.

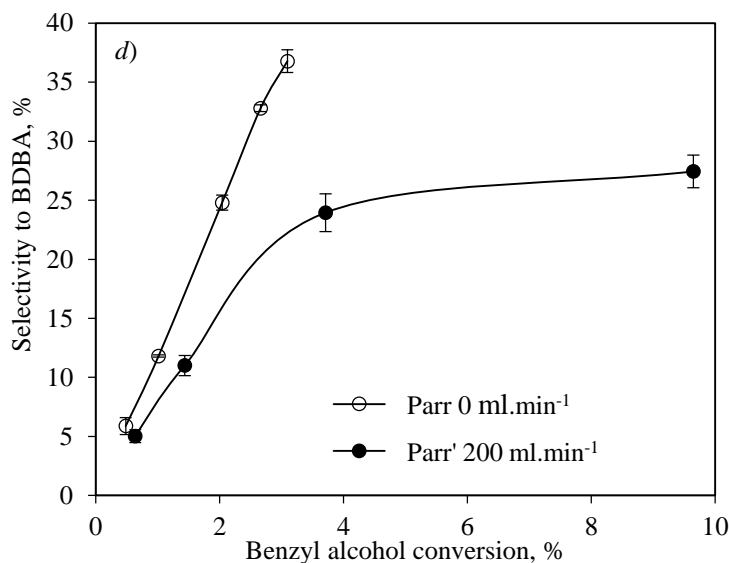


Figure 5.6 *continued*. *d*) Comparison of BDDBA selectivity versus benzyl alcohol conversion in the original reactor (Parr) and the modified reactor (Parr'). Reaction conditions were: 25 mg 2.5wt% Au2.5wt%Pd/*E. coli*, 40 ml benzyl alcohol, $T = 110\text{ }^{\circ}\text{C}$, $p_{air} = 5\text{ bar}$, $N = 1200\text{ rpm}$.

As shown in Figure 5.6 *a*, a considerable improvement in the formation of each product was obtained after reactor modification due to the higher alcohol conversion contributed by the constant air feeding (an improved the oxygen availability). Meanwhile in terms of the desired product benzaldehyde (Figure 5.6 *b*), a higher selectivity was obtained in Parr' than in Parr when the same amount of benzyl alcohol was converted, suggesting conditions that maximised the availability of oxygen on the catalyst surface favour the synthesis of benzaldehyde. In contrast the selectivities to the rest of the by-products (toluene in Figure 5.6 *c* and BDDBA in Figure 5.6 *d*), were higher in the original Parr reactor than in the modified Parr' reactor. As was previously verified, the availability of oxygen in the dead-end Parr reactor reduced with the reaction time, thus the reaction pathway was then thought to alter towards the side reactions which do not involve oxygen. This could lead either towards the condensation between alcohol and aldehyde to form BDDBA (SR₁ in Scheme 1, Figure 5.1) or disproportionation of alcohol to produce toluene (SR₂ in Scheme 2, Figure 5.1), which can explain the observed higher selectivity towards both toluene and BDDBA. Furthermore for the reaction in original Parr (0 ml.min⁻¹), benzoic acid was not detected, in the absence of which

BDBA is rather stable and not susceptible to hydrolysis. As a result, the BDBA selectivity was further enhanced with a steep increase in rate (Figure 5.6 *d*), corresponding to a fast decrease of benzaldehyde selectivity in Figure 5.6 *b*).

On the basis of the above investigation, the following oxidation reactions were all operated in the modified flow-through reaction system, Parr’.

5.2.1.3 Stability Investigation of Bio-AuPd Catalyst

The ‘as-received’ bio-AuPd catalyst (provided by Dr K. Deplanche, School of Biosciences, University of Birmingham) was kept in a sealed glass vial under normal atmospheric environment, and was air-stored for over one year. Catalyst after long-term storage may be covered with impurities such as moisture or adsorbed oxygen or become otherwise oxidised [65], for example Mallat *et al.* [111] reported that a noble metal catalyst stored in air has a potential close to its oxygen rest potential. Similarly, in a related study of benzyl alcohol oxidation using inorganic AuPd catalyst by a previous group member Mounzer [79], the ‘as-received’ AuPd/TiO₂ was found to be in an oxidised state which, as a result of the poor availability of active sites, gave a rather low alcohol conversion (less than 20% after 5 hours) while catalyst in a predominantly reduced state considerably increased the conversion, by more than three-fold to nearly 60% [79].

In order to check whether the catalytic activity of the ‘as-received’ bio-catalyst becomes aged during long-term storage, a portion of the sample of bio-AuPd/*E. coli* catalyst was taken and pre-reduced *ex-situ* under hydrogen (details refer to §3.4.2). Both the *ex-situ* reduced and untreated bio-AuPd catalysts were then tested for the oxidation of benzyl alcohol under identical conditions: 7 mg of 2.5wt%Au2.5wt%Pd/*E. coli*, 40 ml of benzyl alcohol, $T= 100$ °C, $p_{air}= 5$ bar, $F_{air}= 100$ ml.min⁻¹, and $N= 1200$ rpm. After 7 hours reaction time bio-AuPd/*E. coli* ‘as-received’ and ‘pre-reduced’ showed very similar catalytic behaviours,

giving an average benzyl alcohol conversion of $3.15 \pm 0.12\%$ with similar product selectivities (Table 5.2). This indicates that the long-term storage of ‘as-received’ 2.5wt% Au 2.5wt% Pd/*E. coli* catalyst under normal atmosphere environment did not bring affect to its catalytic activity.

Table 5.2 Comparison of the product selectivities in benzyl alcohol oxidation over ‘as-received’ and ‘pre-reduced’ 2.5wt% Au 2.5wt% Pd/*E. coli*. Reaction conditions were: 7 mg of 2.5wt% Au 2.5wt% Pd/*E. coli*, 40 ml of benzyl alcohol, $T = 100\text{ }^{\circ}\text{C}$, $p_{air} = 5\text{ bar}$, $F_{air} = 100\text{ ml}\cdot\text{min}^{-1}$, $N = 1200\text{ rpm}$; reaction time = 7 hours. Benzoic acid was not included for it was not detected in the products under the given conditions.

Catalyst status	Product selectivities, %				
	toluene	benzyl aldehyde	benzoic acid	benzyl benzoate	BDBA
‘as-received’	3.01 ± 0.16	50.55 ± 0.93	0.00 ± 0.00	3.64 ± 0.03	42.31 ± 0.60
‘pre-reduced’	2.79 ± 0.06	46.86 ± 0.25	0.00 ± 0.00	3.68 ± 0.00	46.28 ± 0.08

Another factor that must be considered for the heterogeneous catalysts operating in a three-phase system is the possibility that active metals (palladium and gold herein) can leach into the reaction mixture, leading to catalyst deactivation, or to the formation of an active homogeneous catalyst. Therefore, the final reaction solutions were centrifuged (7000 rpm, 4 °C, 10 min) and the supernatants were analysed by atomic absorption spectroscopy to determine if the metal was leached (see assays of Pd(II) and Au (III) in §3.3.3). Negligible metals constituting the active phase were detected in the supernatants (<0.01 wt% of Au(III) and 0.28 wt% of Pd(II)). These results imply that bio-AuPd catalyst was well maintained in an active condition under the normal storage, as air-dried, ground material.

5.2.1.4 Mixing and Mass Transfer

In this section, investigations of hydrodynamics and mass transfer resistances in the present agitated slurry reactor are reported. First of all, an approximate value of the minimum agitation speed (N_m) required for a complete catalyst particle suspension (*i.e.* 2.5wt% Au 2.5wt% Pd/*E. coli* in benzyl alcohol) was calculated as 293.7 rpm using a correlation proposed by Zwietering *et al.* [246] (Equation 2-1 in §2.5.2.1). The parameters for

the calculation involve geometries of the Parr autoclave reactor, properties of the catalyst and benzyl alcohol (Table 5.3). A stirring speed of 1200 rpm was employed in all the oxidation reactions, the highest possible value with the Parr autoclave reactor used and far above the calculated value of N_m , thus perfect mixing was assumed to occur. All the oxidation reactions in this chapter were then stirred at this speed.

Table 5.3 Parameters used for the calculation of the minimum stirring speed (N_m) in the case of solvent-free benzyl alcohol oxidation over a 2.5wt% Au2.5wt%Pd/*E. coli* catalyst in Parr autoclave reactor.

Parameter	Value	Description
<i>System geometries</i>		
d_T	3.30 cm	reactor inside diameter
d_I	2.06 cm	stirrer diameter
β^a	3.74	constant
<i>Catalyst properties (2.5wt% Au2.5wt%Pd/<i>E. coli</i>)</i>		
w'	0.017 g(catalyst).100g(solution) ⁻¹	percentage catalyst loading
d_p^b	6.3×10^{-3} cm	mean diameter of catalyst particles
ρ_p^c	1.4952 g.cm ⁻³	catalyst density
<i>Benzyl alcohol properties^d</i>		
μ_L	0.05474 g.cm ⁻¹ .s ⁻¹	liquid viscosity
ρ_L	1.044 g.cm ⁻³	liquid density
<i>Others</i>		
g	981 cm.s ⁻²	gravitational acceleration

^a estimated using Equation 2-2; ^b approximated by sieve; ^c measured by Micromeritics Accucyc II 1340 Pycnometer; ^d values at 298 K.

In terms of the mass transport resistances, if as here the catalyst is immersed in solvent-free benzyl alcohol, the intra-particle diffusion of liquid substrate molecules can be neglected. This is a valid assumption, since the liquid concentrations are always much higher than the oxygen concentration and vary very little from one position to another in the slurry, being virtually equal to the bulk concentration throughout. For the evaluation of oxygen transport in the current system, it is not practicable in this study to predict the oxygen reaction rate r_{O_2} during the course of the reaction based on two reasons: i) No suitable device was available to determine the solubility of oxygen during the course of the reaction thus the oxygen mass

balance in transfer and reaction step cannot be established properly; ii) The overall complex reaction pathways whereupon oxygen participates in several different reactions (*i.e.* R_1 , R_2 and SR_{11} in Figure 5.1), and the corresponding products (*i.e.* benzaldehyde, benzoic acid, ester and BDBA) also react further in other side reactions (*i.e.* SR_{12} and SR_2). Therefore neither the alcohol consumption rate nor the aldehyde generation rate is reliable to predict the reaction rate of oxygen during the course of the reaction. However, since low benzyl alcohol conversion was usually observed in the initial half an hour, the estimation of initial oxygen reaction rate based on benzyl alcohol reaction rate is still acceptable.

Given the intrinsically zero-order kinetics with respect to oxygen in the benzyl alcohol oxidation over AuPd bimetallic catalyst [66,71,231,232], the rate is suggested to be independent of the concentration of oxygen as long as the concentration is finite everywhere inside the catalyst [306,307]. However a concept of oxygen critical concentration must be introduced (§5.2.1.4.1) as proposed by Chaudhari *et al.* [306] for zero-order reactions with respect to the gas-phase reactant in a catalytic slurry reactor. Furthermore, due to the application of the dilute gas reactant, special care needs to be taken to maintain the oxygen partial pressure inside the autoclave, which may be influenced by air flow rate (§5.2.1.4.2) and catalyst concentration (§5.2.1.4.3).

5.2.1.4.1 Critical Concentration of Oxygen in Benzyl Alcohol Oxidation

Based on the Henry's law, the amount of a given gas that dissolves in a given type and volume of liquid at a constant temperature, is directly proportional to the partial pressure of gas in equilibrium with the liquid. Chaudhari *et al.* [306] suggested for zero-order reactions with respect to the gas-phase reactant (G) in a catalytic slurry reactor, a critical concentration of G at catalyst surface $[G^s]_{crit}$, corresponding to a $[G^l]_{crit}$ in bulk liquid and a $p_{G,crit}$ in the gas phase, exists for given operating conditions. Below this value, the reaction rate becomes a function of concentration and beyond the critical value any further increase in concentration

will not improve the rate. Accordingly, in benzyl alcohol oxidation, if $[O_2^s] > [O_2^s]_{crit}$ (correspondingly, $[O_2^l] > [O_2^l]_{crit}$ and $p_{O_2} > p_{O_2,crit}$), the concentration of oxygen does not become zero at any point within the catalyst and rate of reaction is independent of concentration and mass transfer rates. When $[O_2^s] < [O_2^s]_{crit}$, the concentration of oxygen may drop to zero at some radius λ within the catalyst (Figure 2.9 in §2.5.2.2). Then only the zone λ to R in the catalyst is effective for reaction. In the region 0 to λ , no reaction can take place because of oxygen starvation. The overall rate of reaction would then be less than that for a purely kinetically controlled case and would also be affected by mass transfer parameters.

In this study, the benzyl alcohol oxidation operated in the dead-end mode was observed to suffer from the reaction slowing down over the course of the experiment (Parr, §5.2.1.1). From the above considerations it can be deduced that the plateau in Figure 5.2 started when the dissolved oxygen concentration dropped below the critical concentration, which may result from the decreasing of oxygen partial pressure caused by the depletion of oxygen in the gas phase. This experiment in dead-end mode may be considered as an extreme case of oxidation under a stagnant air flow rate (*i.e.* $\sim 0 \text{ ml}\cdot\text{min}^{-1}$), with the effect being less severe in the flow-through experiment in the modified Parr' operation (§5.2.1.2). It appeared that an air flow of $200 \text{ ml}\cdot\text{min}^{-1}$ contributed to maintain a higher oxygen partial pressure (leading to a higher dissolved oxygen concentration) thus promoted higher rate of oxidation of benzyl alcohol. Thereafter a series of reactions were carried out in order to study the effect of air flow rate on the oxygen partial pressure in the current system.

5.2.1.4.2 Effect of Air Flow Rate on the Oxygen Partial Pressure

Experiments were conducted by changing the air flow rate from $100 \text{ ml}\cdot\text{min}^{-1}$, $200 \text{ ml}\cdot\text{min}^{-1}$ to $350 \text{ ml}\cdot\text{min}^{-1}$, with the other reaction conditions maintained as: 7 mg of 2.5wt% Au2.5wt% Pd/*E. coli*, 40 ml of solvent-free benzyl alcohol, $p_{air} = 5 \text{ bar}$, $T = 100 \text{ }^\circ\text{C}$, and

$N= 1200$ rpm. The reactor contents were weighed before and after reaction and percentage loss of material was calculated for each reaction.

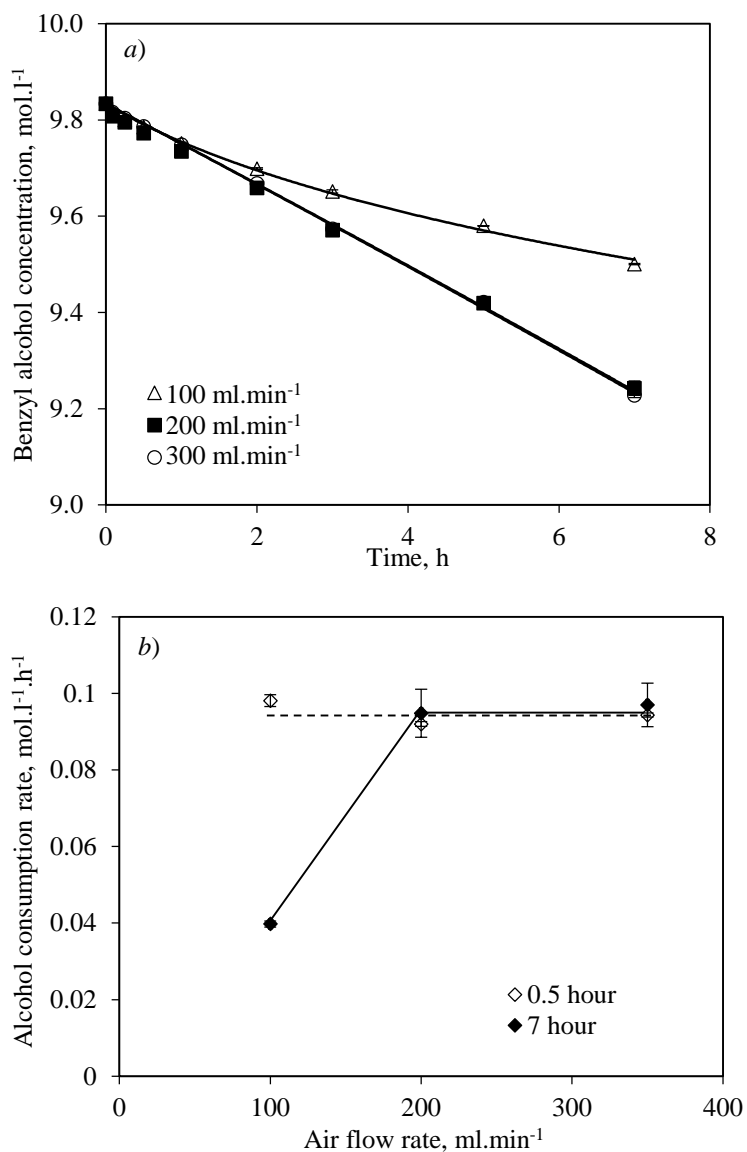


Figure 5.7 a) Benzyl alcohol concentration profiles under different flow rates (symbols of 200 ml.min⁻¹ and 350 ml.min⁻¹ are overlapped on the plot); b) Effect of the air flow rate on the benzyl alcohol consumption rate. Reaction conditions were: 7 mg 2.5wt% Au2.5wt% Pd/*E. coli*, 40 ml solvent-free benzyl alcohol, $T= 100$ °C, $p_{air}= 5$ bar, $N= 1200$ rpm.

Figure 5.7 a shows the evolution of benzyl alcohol concentration during the course of reaction under different flow rates. It was observed that alcohol consumption rate under 100 ml.min⁻¹ air flow was slower than the rates under the other two flow rates (200 and 350 ml.min⁻¹), which were almost the same. Figure 5.7 b displays the alcohol consumption rates at different reaction times. Similar initial alcohol consumption rates at 0.5 h were observed

under all flowrates of air ($0.096 \pm 0.002 \text{ mol.l}^{-1}.\text{h}^{-1}$ under 100 ml.min^{-1} , $0.093 \pm 0.001 \text{ mol.l}^{-1}.\text{h}^{-1}$ under 200 ml.min^{-1} and $0.095 \pm 0.001 \text{ mol.l}^{-1}.\text{h}^{-1}$ under 350 ml.min^{-1}). After 7 hours reaction time, the reactions under 200 ml.min^{-1} and 350 ml.min^{-1} air consistently maintained almost the same rates as the initial values. However, at the lowest air flow rate of 100 ml.min^{-1} the rate dropped considerably to $0.041 \pm 0.001 \text{ mol.l}^{-1}.\text{h}^{-1}$, suggesting oxygen being the limiting reactant. In other words, benzyl alcohol oxidation under an air flow rate of 100 ml.min^{-1} became oxygen mass transfer controlled at the reaction time of 7 hour as compared to the reactions under 200 ml.min^{-1} and 350 ml.min^{-1} . It was thought that the air flow rate was likely to play a role on the oxygen partial pressure (the equilibrium oxygen concentration in solution) in the system under the given conditions.

A plot in Figure 5.8 can be envisaged to illustrate the changing of oxygen partial pressure versus time at different air flowrates in the modified ‘open-end’ autoclave reactor (Parr’); it must be stated here that the lines in the graph only demonstrate a general trend rather than any actual physical recording. Initially, reactions all started with the same initial oxygen partial pressure for identical air pressure (5 bar) applied. The similar benzyl alcohol consumption rates in the early time period (~ 1 hour, Figure 5.7 a) under all three flows rates implies initial value of oxygen partial pressure $p_{O_2, \text{initial}}$ was above the critical value $p_{O_2, \text{crit}}$. For the use of dilute gas reactant in benzyl alcohol oxidation, oxygen partial pressure in the gas phase is thought to decrease with the reaction time in each case, the rate of which varies with the air flow rate. In the case of dead-end operation (Parr, dashed trend line in Figure 5.8) oxygen partial pressure was expected to drop to the critical value at the fastest rate within the time period of t_0 . When applying an air flow rate, the time for oxygen partial pressure decreasing from $p_{O_2, \text{initial}}$ to $p_{O_2, \text{crit}}$ was prolonged to t_i ($t_i > t_0$; $i=1, 2, \text{ and } 3$ for $100, 200, \text{ and } 350 \text{ ml.min}^{-1}$ respectively as shown in Figure 5.8). During the time period of $0 \sim t_i$ ($i=0, 1, 2, \text{ and } 3$), oxygen partial pressure was above $p_{O_2, \text{crit}}$, the reaction was expected to be

independent of the oxygen concentration. When oxygen partial pressure reduced below $p_{O_2, \text{crit}}$ (after t_i), an oxygen mass-transfer-controlled regime would occur; in the case of 100 ml.min⁻¹, t_1 appeared to be ~1 hour. In contrast, the observed invariant and stable benzyl alcohol consumption rates under both 200 ml.min⁻¹ and 350 ml.min⁻¹ within the 7 hours' reaction time (Figure 5.7) implies that both t_2 and t_3 were beyond the reaction end time of 7 hour (the reaction time for each benzyl alcohol oxidation test, indicated as the vertical dashed line in Figure 5.8), and reactions were in a kinetic control regime in dependent of mass transfer rates.

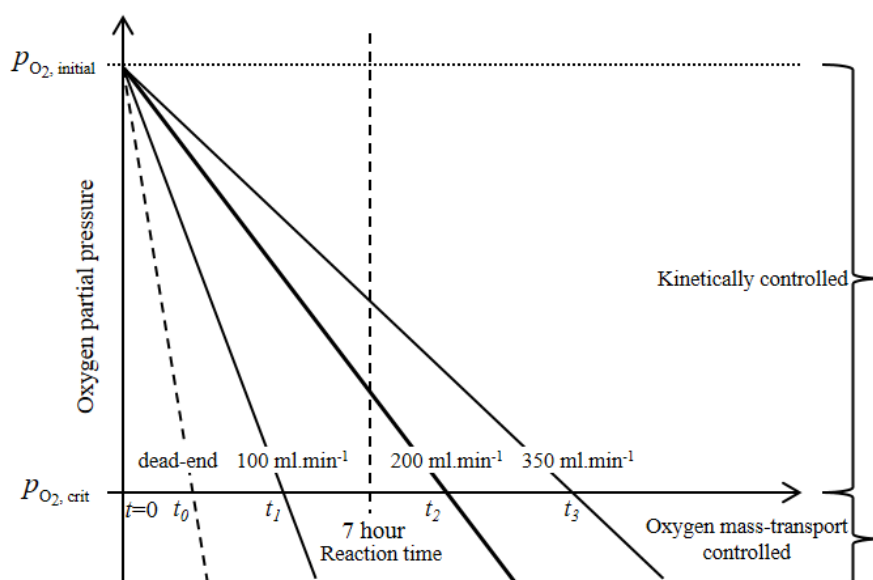


Figure 5.8 An illustration on the oxygen partial pressure changing with reaction time under different air flow rates in the modified autoclave reactor. The pointed out 7 hour is the total reaction time in this study. Reaction conditions: 7 mg of 2.5wt% Au2.5wt%Pd/*E. coli*, 40 ml of benzyl alcohol, $T= 100\text{ }^{\circ}\text{C}$, $p_{\text{air}}= 5\text{ bar}$, $N= 1200\text{ rpm}$. The straight lines are only for the general trends; they do not represent any experimental meanings.

In terms of product formation, similar product distributions were observed at flow rates of 200 and 350 ml.min⁻¹. Both benzaldehyde and BDBA were detected as the major products, giving yields of $2.90\pm 0.03\text{ wt}\%$ for aldehyde and $3.25\pm 0.12\text{ wt}\%$ for BDBA at a flow rate of 200 ml.min⁻¹ after 7 hours. The even higher production of BDBA than the target product benzaldehyde resulted in the low aldehyde selectivity being 40%~50%. Only a minor amount

of toluene (0.15 ± 0.01 wt%) and benzyl benzoate (0.20 ± 0.00 wt%) were formed as by-products, and no benzoic acid was detected in the present system.

The catalytic performance of bioinorganic 2.5wt% Au2.5wt% Pd/*E. coli* in this study was compared with the chemical 2.5wt% Au2.5wt% Pd/ TiO_2 reported by Enache *et al.* [231] in a very similar system. The main difference between the reaction conditions in these two studies were the support of catalyst and the purity of gas reactant employed, being *E. coli*, air in this work and TiO_2 , oxygen in Enache's work respectively. The turnover frequency (TOF) for the oxidation by bio-AuPd catalyst was estimated as an average of 1423 ± 20 turnovers per hour under the air flow rates above $200\text{ ml}\cdot\text{min}^{-1}$. This was approximately one quarter of the TOF reported by Enache *et al.* [231] with the use of AuPd/ TiO_2 under 1 bar of pure oxygen at the same temperature (6190 hr^{-1}). The difference in TOF can be ascribed to the activity of the catalyst itself, for example the nature of support and the metal (Au and Pd) configuration. In terms of the configuration of the gold and palladium on *E. coli*, it was shown in a relevant work to his work that the nanocrystals were made up of an Au-rich core with a Pd-rich shell [161], which is in agreement with the case of AuPd/ TiO_2 in Enache's work. On the other hand inorganic catalyst support like titanium dioxides for precious metal catalysts have gained interest due to the high surface area [308]; while the biomass employed in this study possesses completely different physical properties and chemical compositions (§2.3.1). For the catalytic tests of 2.5wt% Au2.5wt% Pd/*E. coli* reported here, due to some inaccessible intracellular located metal particles (see later the characterisation work in §6.3.2), the actual amount of the active metal exposed at the outer membrane of the cell for reaction to take place is less than the total palladium loading, which can explain the obtained lower TOF.

Although an increased air flow rate was found to improve oxygen availability in the present benzyl alcohol oxidation system, it could also lead to increased loss by evaporation of some

low boiling point components (*e.g.* toluene or benzaldehyde). Thus, 200 ml.min⁻¹ of air flow was chosen as optimum operating flow rate in the following study.

5.2.1.4.3 Effect of Catalyst Concentration on the Oxygen Partial Pressure

In this section benzyl alcohol oxidation was carried out by varying the mass (m_c) of 2.5wt% Au2.5wt% Pd/*E. coli* (7 mg, 14 mg, 25 mg, 70 mg and 100 mg) under the same reaction conditions (40 ml of benzyl alcohol, p_{air} = 5 bar, F_{air} = 200 ml.min⁻¹, T = 110 °C, and N = 1200 rpm). Performing reactions with different catalyst masses can be used to deduce information about the upper-use amount of catalyst in current reaction system without mass transfer resistances.

Intuitively, increasing the mass of catalyst would lead to the promotion of the overall reaction performance, as more active sites per volume of slurry are available for reactant molecules to adsorb upon for the subsequent reaction. As shown in Figure 5.9 *a*, a proportionate increase in the observed initial rate of benzyl alcohol disappearance (estimated up to 30 mins) was found by increasing the catalyst amount. This indicates a linear dependence of the rate on the weight of catalyst and hence on the number of catalytic sites. Similar conclusions were reported in the aerobic oxidation of benzyl alcohol over Ru/ Al_2O_3 by Yamaguchi and Mizuno [241] and AuPd/ TiO_2 by Meenakshisundaram *et al.* [66].

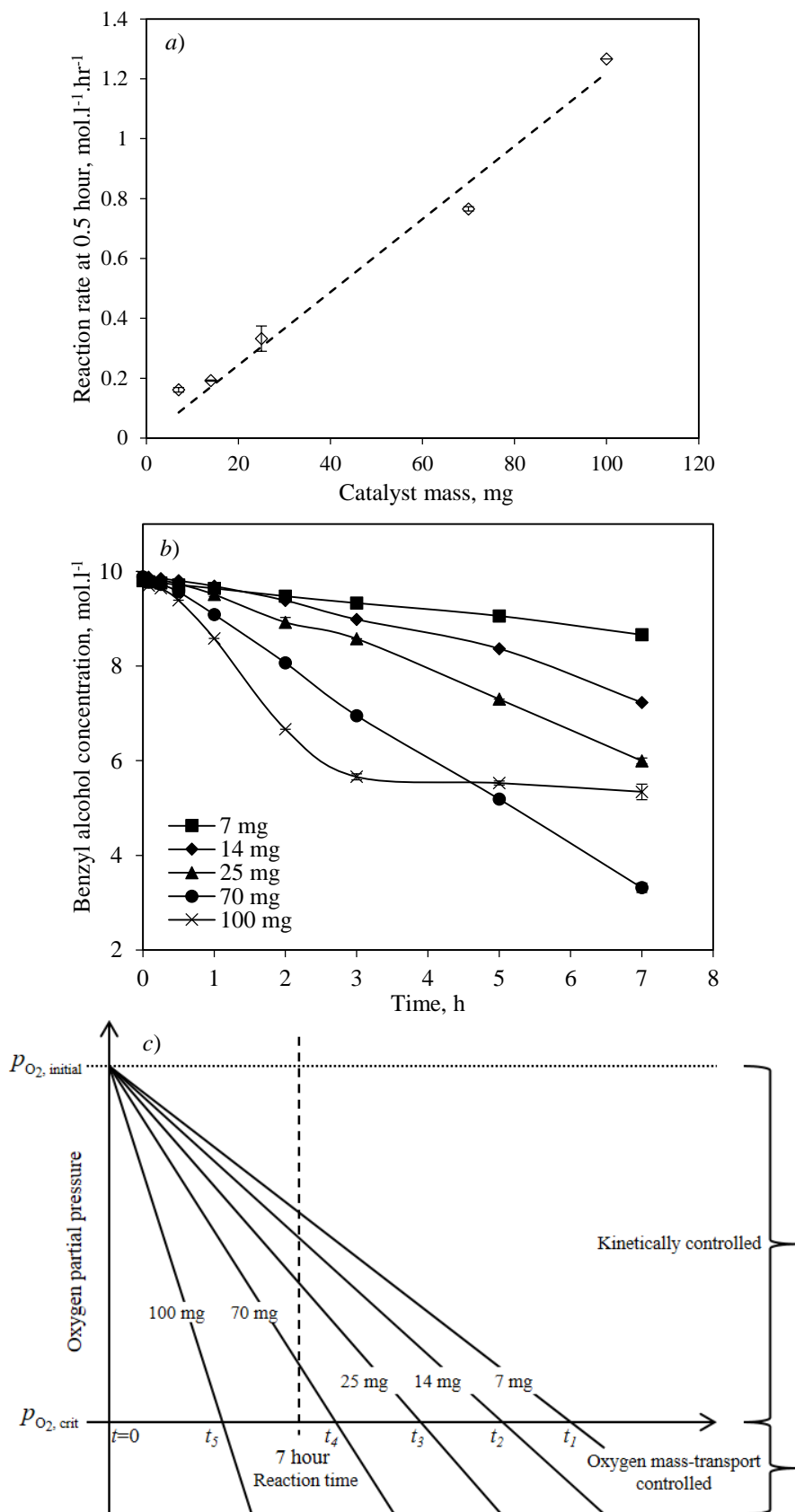


Figure 5.9 a) Evolution of the initial benzyl alcohol reaction rate by changing the catalyst loading of bio-AuPd in benzyl alcohol oxidation; b) Benzyl alcohol concentration profiles using different masses of bio-AuPd; c) A demonstration on the partial pressure changing with the reaction time when using different masses of bio-AuPd in the modified autoclave. Reaction conditions: use of 2.5wt% Au/2.5wt% Pd/*E. coli* catalyst in 40 ml benzyl alcohol, $T = 110\text{ }^{\circ}\text{C}$, $p_{air} = 5\text{ bar}$, $F_{air} = 200\text{ ml}\cdot\text{min}^{-1}$, $N = 1200\text{ rpm}$.

Figure 5.9 *b* shows the benzyl alcohol concentration profiles as a function of reaction time using different catalyst masses. It was noted that the highest catalyst loading of 100 mg displayed the fastest initial benzyl alcohol consumption rate (Figure 5.9 *a*) but the conversion rate decelerated and levelled off after 3 hours at $\sim 42.72 \pm 0.64\%$ of benzyl alcohol conversion. The benzyl alcohol concentration curves for the bio-AuPd masses of 70 mg and 100 mg were observed to cross over each other, with eventually higher conversion being attained for 70 mg ($67.87 \pm 1.00\%$) than that of 100 mg ($48.28 \pm 1.66\%$) after 7 hours. It is considered that due to the increased number of active surface sites per unit mass of slurry, the accelerated consumption rate of oxygen would speed up the decreasing rate of oxygen partial pressure. As illustrated in Figure 5.9 *c*, at the 100 mg loading of bio-AuPd/*E. coli*, the time (t_5) for oxygen partial pressure to decrease from the initial value ($p_{O_2, \text{initial}}$) to the critical value ($p_{O_2, \text{crit}}$) occurred before 7 hour, as a result the benzyl alcohol oxidation after t_5 (*i.e.* ~ 3 hours) was again limited by oxygen mass transfer.

From the above considerations it is suggested that in the Parr' system under the tested reaction conditions, the catalyst amount should be below 100 mg to ensure the reaction being predominantly in the kinetic regime.

5.2.1.5 Effect of Temperature and Activation Energy

The following work reports the estimation of the activation energy in current reaction system by performing the benzyl alcohol oxidation under a range of temperatures from 100 °C, 110 °C, 120 °C to 140 °C. The rest of the reaction conditions were: 7 mg of 2.5wt% Au2.5wt%Pd/*E. coli*, 40 ml of benzyl alcohol, $p_{\text{air}} = 5$ bar, $F_{\text{air}} = 200$ ml.min⁻¹, and $N = 1200$ rpm.

Firstly, the effect of reaction temperature upon rate is observed in the alcohol concentration profile as a function of reaction time in Figure 5.10 *a*. Considerable improvement in the final

conversion of benzyl alcohol was obtained at the end of the reaction at higher temperatures. As shown in Table 5.4, the corresponding TOF increased significantly with the temperature. While comparing with the work reported in the literature (Table 5.4), the TOF in this study was still lower at the corresponding reaction temperature, which has been discussed above in §5.2.1.4.

Table 5.4 Comparison of the reaction conditions and the catalytic activity in benzyl alcohol oxidation in this study with those in literature. Catalyst loadings were consistent as $2.1 \times 10^{-5} \text{mol.l}^{-1}$ for Au and $3.9 \times 10^{-5} \text{mol.l}^{-1}$ for Pd. The air flow rate of ml.min^{-1} was an optimised flow rate. TOF was measured after first 0.5 hour of reaction. Benzyl alcohol conversion was determined after 7 hours in this study.

Catalyst		Reaction conditions			TOF hr^{-1}	Conversion %	Activation energy kJ.mol^{-1}	Reference
Metal loading	Support	T k	P bar	Flow ml.min^{-1}				
2.5wt% Au 2.5wt% Pd	<i>E. coli</i>	373	5, air	200	1383	6.0±0.2	71.8	This study
		383	5, air	200	2881	11.7±0.5		
		393	5, air	200	4337	22.0±0.6		
	TiO ₂	413	5, air	200	16818	50.4±0.1		
		373	1, O ₂	NA	6190	NG		Enache <i>et al.</i> [65]
		383	1, O ₂	NA	14270	NG	45.8	
393	1, O ₂	NA	26400	NG				

NA: not applicable; NG: not given.

The influence of temperature on the rates of chemical reactions is described by the Arrhenius equation as follows:

$$\ln(k) = \ln(A) - \frac{E_a}{R} \left(\frac{1}{T} \right) \quad 5-4$$

where k = reaction rate coefficient ($\text{mol.m}^{-3}.\text{s}^{-1}$), A = pre-exponential factor, E_a = activation energy (kJ.mol^{-1}), R = gas constant ($8.314 \text{J.K}^{-1}.\text{mol}^{-1}$), and T = absolute temperature (K).

The reaction rates (over 30 mins) at different temperatures were calculated from the slope of the concentration-time lines in Figure 5.10 *a* and these rates were used to construct an Arrhenius plot of $\ln(k)$ versus $1/T$. The resulting Arrhenius plot based on this system is displayed in Figure 5.10 *b*, from which the activation energy was estimated as 71.8kJ.mol^{-1}

for benzyl alcohol oxidation over the 2.5wt% Au2.5wt% Pd/*E. coli* under 5 bar of air. In comparison with the lower activation energy reported by Enache *et al.* [231], 45.8 kJ.mol⁻¹ in Table 5.4, the higher activation energy in this study indicates the reaction is kinetically limited. By contrast, a low value of activation energy is related to mass transfer effects masking the true activation energy.

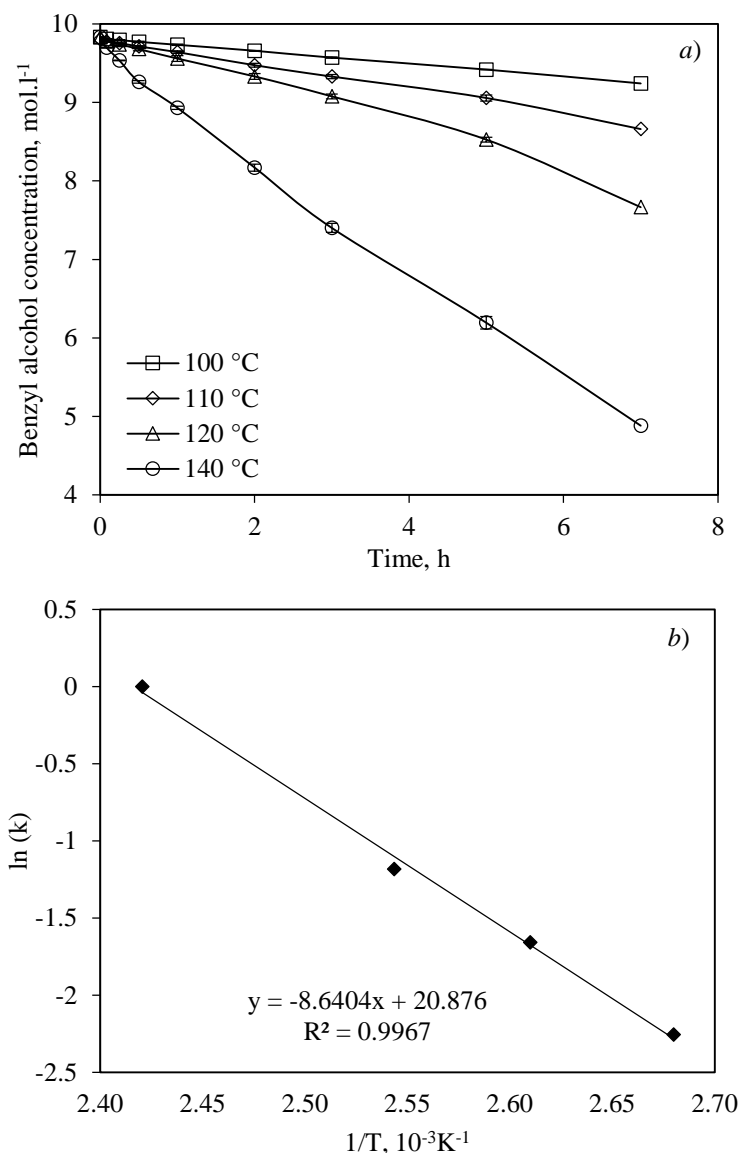


Figure 5.10 a) Benzyl alcohol concentration profiles under different reaction temperatures; b) Arrhenius plot of ln(k) versus 1/T showing temperature dependence of benzyl alcohol oxidation over a 2.5wt% Au2.5wt% Pd/*E. coli* catalyst. Reaction conditions: 7 mg of 2.5wt% Au2.5wt% Pd/*E. coli*, 40 ml of benzyl alcohol, p_{air} = 5 bar, F_{air} = 200 ml.min⁻¹, N = 1200 rpm.

The effect of reaction temperature on the product distribution was also investigated. At all temperatures studied, benzaldehyde was maintained as the major product with minor amounts

of consecutive products such as benzoic acid and benzyl benzoate, as shown in the product concentration profiles in Figure 5.11 *a* for 110 °C and *b* for 140 °C. At a reaction temperature of 110 °C, less than $11.7\pm 0.5\%$ of benzyl alcohol conversion was obtained after 7 hours, producing 6.6 ± 0.5 wt% of benzaldehyde and 4.5 ± 0.3 wt% of BDBA as the major products. It was also noted that high temperature (140 °C) considerably increased the yield of toluene, reaching a concentration of 13.2 ± 0.4 wt% after 7 hours. In terms of the selectivity to toluene displayed in Figure 5.11 *c*, it was observed that raising the reaction temperature dramatically increased the selectivity to this by-product at the same benzyl alcohol conversion. As described in reaction scheme 2 (Figure 5.1), toluene can be formed by the disproportionation of benzyl alcohol in the absence of oxygen. Li *et al.* [303] also concluded that this reaction is favoured by high temperature and low partial pressure of O₂. Therefore at the higher temperature of 140 °C, a reduced concentration of dissolved oxygen leads to increased toluene formation. Meanwhile with the finding of higher toluene formation in the original reactor (Parr) than that in the reactor after modification (Parr'), it is evident that the availability of dissolved O₂ in the solution has the key influence upon the toluene formation.

Considering the formation of other side products, for the concentration profile at a relatively low temperature of 110 °C in Figure 5.11 *a*, the concentration of generated BDBA was only slightly lower than that of target product of benzyl aldehyde. However the BDBA production varied significantly with the temperature (100 °C, 110 °C and 120 °C in Figure 5.11 *d*). When the temperature was increased to 140 °C, an increase of BDBA concentration to a maximum (4.4 ± 0.1 wt% after 2 hours) followed by its decrease (0.9 ± 0.3 wt% after 7 hours) was observed. As shown in Figure 5.11 *e*, benzoic acid started to form at a considerable rate under more severe conditions (*i.e.* temperature of 140 °C); a significant promotion of acid production was observed when increasing the temperature from 120 °C to 140 °C. The accelerated formation of acid in the reaction at 140 °C led to the decomposition of BDBA.

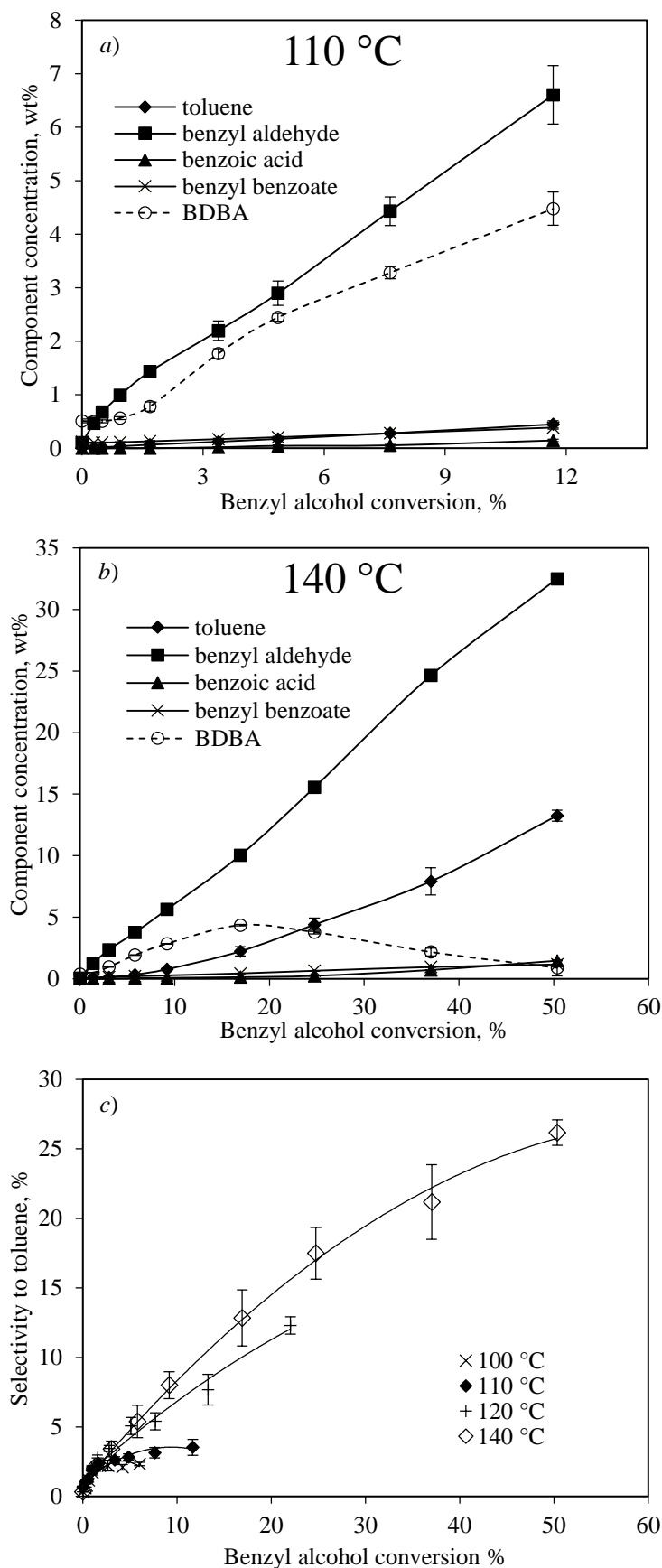


Figure 5.11 Product concentration as a function of benzyl alcohol conversion at temperature of a) 110 °C and b) 140 °C; c) Comparison of selectivity to toluene under different reaction temperatures. Reaction conditions: 7 mg 2.5wt% Au2.5wt% Pd/*E. coli*, 40 ml benzyl alcohol, $p_{air}=5$ bar, $F_{air}=200$ ml.min⁻¹, $N=1200$ rpm.

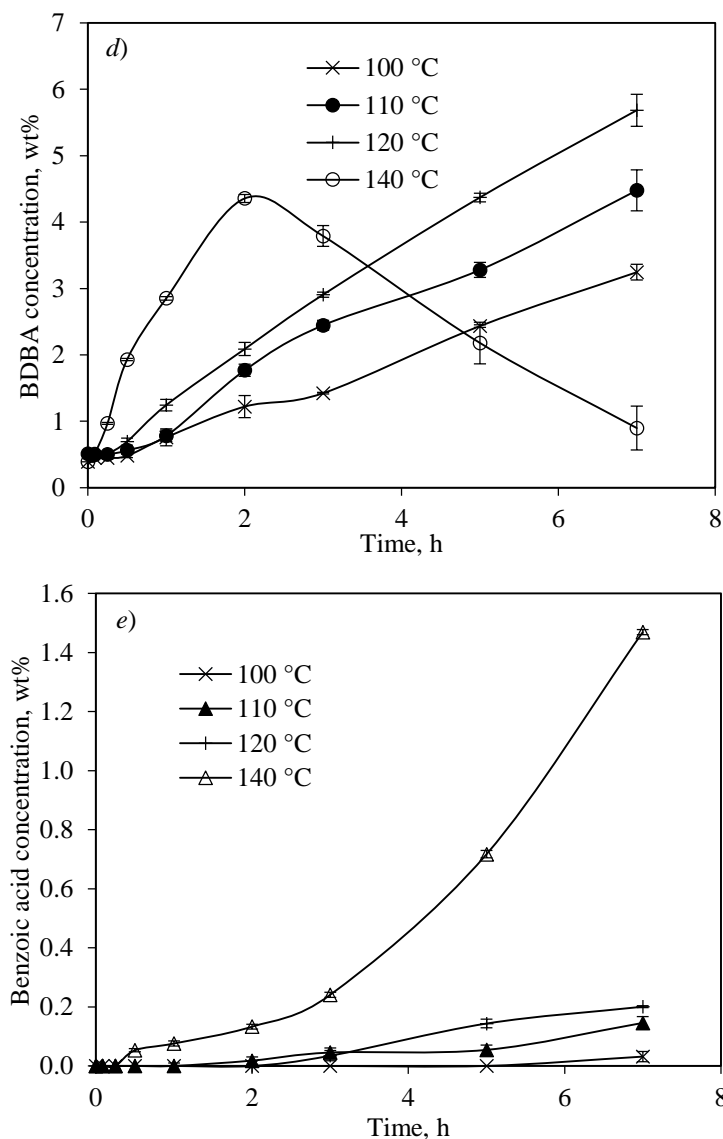


Figure 5.11 *continued*. Comparison of d) BDBA formation and e) benzoic acid formation under different reaction temperatures. Reaction conditions were: 7 mg 2.5wt% Au2.5wt%Pd/*E. coli*, 40 ml benzyl alcohol, $p_{air}=5$ bar, $F_{air}=200$ ml.min⁻¹, $N=1200$ rpm.

In summary, the activation energy of benzyl alcohol oxidation over the 2.5wt% Au2.5wt% Pd/*E. coli* catalyst in the present system was found to be 71.8 kJ.mol⁻¹. Although much higher benzyl alcohol conversion and less BDBA were obtained under high temperature, a substantial level of toluene was formed as by-product under oxygen limited conditions due to the lower oxygen solubility at the raised temperatures. Therefore, a trade-off exists between reaction rate and by-product selectivity in current benzyl alcohol oxidation

system, an intermediate temperature of 110 °C was finally selected as the optimum temperature for the following reactions.

5.2.2 Bio-AuPd Catalyst Formulation

For bimetallic catalyst bio-AuPd, the catalytic performance can be affected by the catalyst formulation, *e.g.* the biomass strain, total metal loading, and metal ratio (Au:Pd). The first objective of this study is to compare the biofabrication of AuPd catalyst by four different biomass strains which may deposit active metal by different mechanisms, the influence of the supporting biological matrix on the catalytic specificity of the resulting bio-AuPd is discussed (§5.2.2.1). The optimal type of bacterial strain was then selected based on the catalytic performance of its bio-AuPd in benzyl alcohol oxidation, and this strain was tested in the following work by adjusting the total metal loading at the same metal ratio (§5.2.2.2) and metal ratio at the same total metal loading (§5.2.2.3) to optimise the AuPd loading.

5.2.2.1 Effect of Biomass Strain

As introduced in §2.3, different bacterial strains possess different metal ion sorption and reduction abilities, which would affect the final patterning and size distribution of the cell-bound metal nanoparticles and hence potentially the catalytic activity of the resulting bio-catalysts. In addition to Gram-negative *E. coli* (-) being the focus throughout this study, this section investigates the catalytic activities of bio-AuPd nanoparticles on Gram-negative *R. sphaeroides* (-), Gram-positive *A. oxydans* (+), and Gram-positive *M. luteus* (+) in benzyl alcohol oxidation. These strains were selected for their known high metal tolerance and/or hydrogenase activity; some characters of these strains were listed earlier in Table 2.7. In each bio-AuPd preparation the metal loading was set identically as 2.5wt%Au2.5wt%Pd for the purpose of comparison. The optimal benzyl alcohol oxidation conditions determined from the

previously reported work (§5.2.1), were applied as: 7 mg of bio-2.5wt% Au2.5wt%Pd, 40 ml of benzyl alcohol, $p_{air}=5$ bar, $F_{air}=200$ ml.min⁻¹, $N=1200$ rpm, and $T=110$ °C.

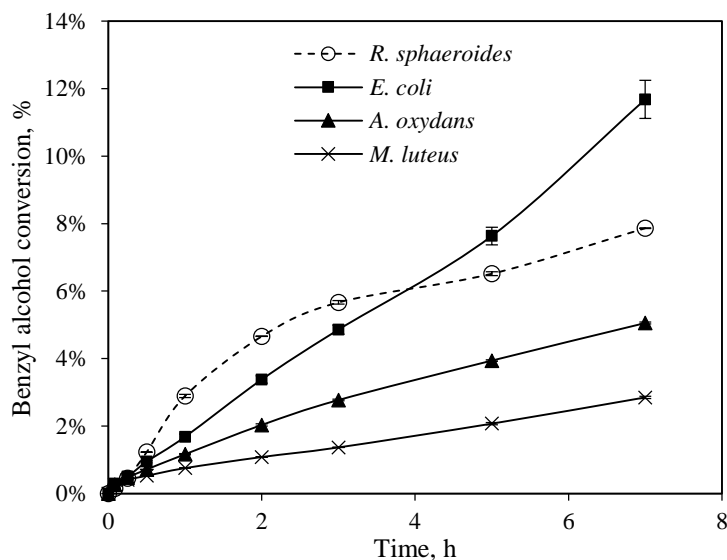


Figure 5.12 Benzyl alcohol conversion profiles using bio-AuPd catalysts supported on different strains of bacteria. Reaction conditions: 7 mg bio-2.5wt% Au2.5wt%Pd catalysts, 40 ml benzyl alcohol (solvent free), $T=110$ °C, $p_{air}=5$ bar, $F_{air}=200$ ml.min⁻¹, and $N=1200$ rpm.

Figure 5.12 shows the benzyl alcohol conversion profiles as a function of reaction time, from which the specificity of the above four bio-AuPd preparations in terms of the resulting catalytic behaviours can be observed. The Gram-negative bacteria (*R. sphaeroides* and *E. coli*) prepared bio-AuPd catalysts showed significantly higher catalytic activity than Gram-positive (*A. oxydans* and *M. luteus*) supported ones. An analogous finding was reported in the case of bio-Pd in Cr(VI) reduction [23], in which bio-Pd catalysts manufactured from Gram-negative bacteria gave better conversion to the ones from Gram-positive bacteria. In the present benzyl alcohol oxidation, bio-AuPd/*M. luteus* gave the lowest benzyl alcohol conversion, which was only ~2.8% after 7 hours. A slightly better performance was achieved by using bio-AuPd/*A. oxydans*, showing a final ~5.0% of benzyl alcohol conversion. The highest benzyl alcohol conversion after 7 hours was observed in the case of bio-AuPd/*E. coli*, achieving $11.7\pm 0.5\%$ at a steady benzyl alcohol consumption rate of ~ 0.16 mol.l⁻¹.hr⁻¹. As to the other Gram-negative biomass supported catalyst bio-AuPd/*R. sphaeroides*, a much higher

alcohol conversion than that over bio-AuPd/*E. coli* was observed during the initial 2 hours, after which the reaction rate gradually tailed off and the conversion curves crossed over as shown in Figure 5.12. By the end of the reaction (7 hours), benzyl alcohol conversion using bio-AuPd/*R. sphaeroides* was 32.5% lower than that using bio-AuPd/*E. coli*. Nonetheless the reason for the conversion tailing-off in Figure 5.12 when using 7 mg of bio-AuPd/*R. sphaeroides* has to be distinguished from the early case over 100 mg of bio-AuPd/*E. coli* in §5.2.1.4.3, in which it was concluded that reaction became oxygen-limited after ~3 hours (conversions of $42.7 \pm 0.6\%$ after 3 hours and $45.9 \pm 1.0\%$ after 7 hours). This reason is less likely to occur for the reaction using 7 mg of bio-AuPd/*R. sphaeroides*, where a much slower reaction was observed with the alcohol conversions of only $5.6 \pm 0.1\%$ after 3 hours and $7.9 \pm 0.1\%$ after 7 hours. Therefore it is unlikely that oxygen transfer limitation caused the reduction of reaction rate in the latter stage (3 hour onwards) in the reaction system over bio-AuPd/*R. sphaeroides*. In fact the performance could be explained by the weak thermal stability of this strain of bacterium as the later comparison of thermogravimetric analysis (TGA) analysis of bio-AuPd/*R. sphaeroides* and bio-AuPd/*E. coli* in Figure 6.2 in §6.2. The mass loss profile as a function of the temperature suggested that the catalyst started to decompose considerably at temperatures ~125 °C in the case of bio-AuPd/*R. sphaeroides*, while 2.5wt% Au2.5wt% Pd/*E. coli* was stable up to ~175 °C (details to see in §6.2). Thus in the operating reaction temperature of 110 °C for continuous 7 hours, the bio-AuPd/*R. sphaeroides* catalyst may gradually undergo deactivation with time due to its weak resistance towards heating, which may even be accelerated by the attrition caused by the high-speed mechanical stirring. As a result, the tailing of benzyl alcohol conversion after around 3 hours was observed in Figure 5.12. However, it must be stressed that these tests were made (in triplicate) using single catalyst preparation and that these data require verification using second, independent preparation.

Examination of the catalysts supported upon different bacterial strains reveals the strain-specific size of AuPd nanoparticles (NPs) in the backscattered-SEM (BSE) images reported in Figure 6.5 *b~d* (in §6.3.1). It is worth stating here in brief that at the same loading of 2.5wt% Au2.5wt%Pd, the BSE images display spherical-shaped *M. luteus* (+) with the poorly dispersed large metal clusters (~100 nm), which is similar to the case of rod-shaped *A. oxydans* (+). In contrast, the metal particles are relatively evenly deposited on the rod-shaped bacteria *E. coli* (-) meanwhile showing smaller metal particles. In accordance with the individual catalytic performance in the benzyl alcohol oxidation, it is suggested that the reaction is sensitive to the size of the active component. It is much likely that the larger clusters induced smaller surface area, as a result less active sites for reaction to take place.

In terms of product formation, bio-AuPd/*A. oxydans*, the more active bio-AuPd within the two Gram-positive bacteria-supported catalysts, showed the lowest selectivity to the desired product benzylaldehyde (Figure 5.13 *a*) accompanied by the highest selectivity to BDBA (Figure 5.13 *b*) and toluene (Figure 5.13 *c*). Bio-AuPd/*E. coli* maintained the highest benzaldehyde selectivity at higher alcohol conversion in the later stage. Although bio-AuPd/*R. sphaeroides* produced the least toluene, it gave the highest selectivities towards both benzoic acid (Figure 5.13 *d*) and benzyl benzoate (Figure 5.13 *e*).

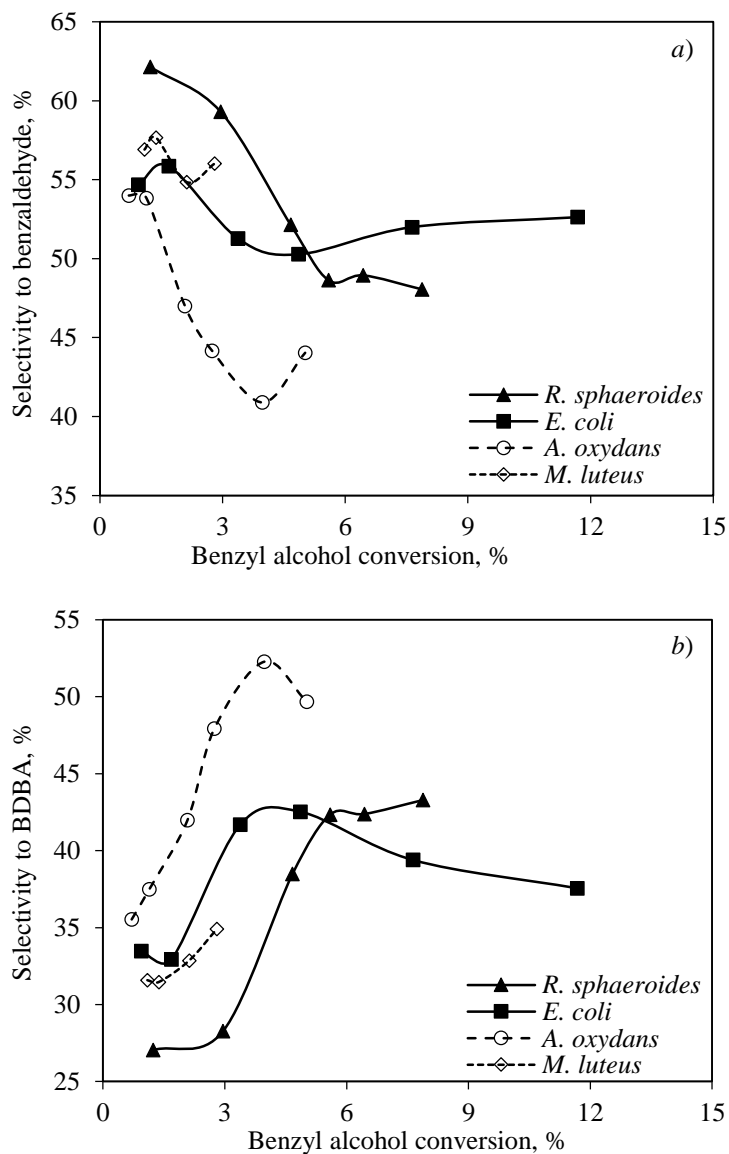


Figure 5.13 Profiles of selectivity to a) benzaldehyde and b) BDBA as a function of benzyl alcohol conversion in the reactions using bio-AuPd catalysts supported on different strains of bacteria. Reaction conditions: 7 mg bio-2.5wt% Au2.5wt%Pd, 40 ml benzyl alcohol (solvent free), $p_{air} = 5$ bar, $F_{air} = 200$ ml.min⁻¹, $N = 1200$ rpm.

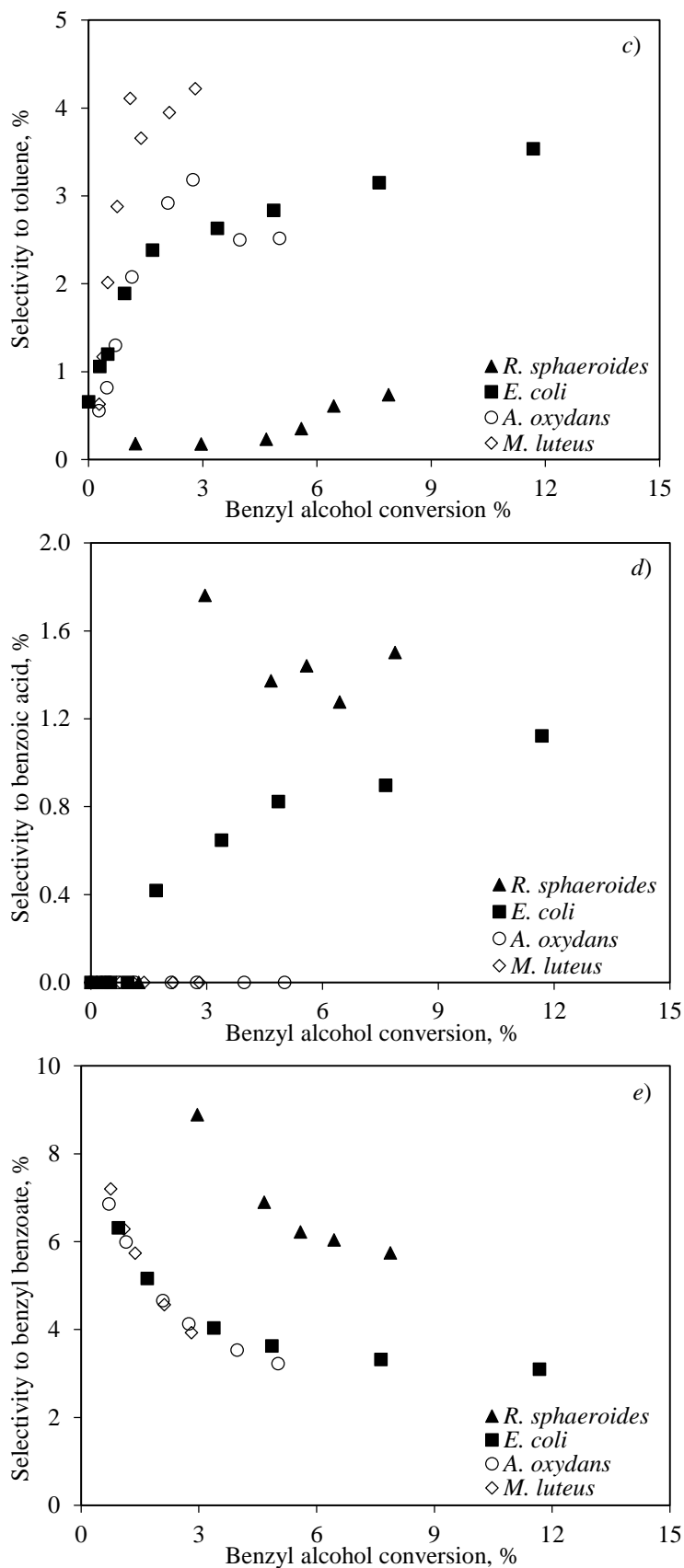


Figure 5.13 *continued*. Profiles of selectivity to c) toluene, d) benzoic acid, and e) benzyl benzoate as a function of benzyl alcohol conversion in the reactions using bio-AuPd catalysts supported on different strains of bacteria. Reaction conditions: 7 mg bio-2.5wt% Au2.5wt% Pd, 40 ml benzyl alcohol (solvent free), $p_{air} = 5$ bar, $F_{air} = 200$ ml.min⁻¹, $N = 1200$ rpm.

In summary, bio-AuPd catalysts on Gram-positive bacteria (*A. oxydans* and *M. luteus*) gave lower catalytic activities in benzyl alcohol oxidation as compared those on Gram-negative bacteria (*R. sphaeroides* and *E. coli*), which was attributed to the larger and unevenly distributed metal particles in the former. A critical role of the biological support matrix in the preparation of catalytically active AuPd nanoparticles is suggested. Among the four catalysts, bio-AuPd/*E. coli* showed superior catalytic performance in benzyl alcohol oxidation. The alcohol was consumed steadily with a higher selectivity to benzaldehyde in comparison with the rest of the bio-AuPd catalysts. Hence *E. coli* bacterium was selected as the catalyst support for the subsequent studies.

5.2.2.2 Effect of Total Metal Loading

In this section, the preparation and testing of bio-AuPd catalyst on *E. coli* with different total metal loadings at a constant Au:Pd ratio as 1:1 by weight (Table 5.5) is reported. In each benzyl alcohol oxidation reaction, the catalyst mass was adjusted to keep the same mole ratio of substrate/total metal. At the lower total loadings (*i.e.* 0.5wt% Au0.5wt%Pd, 1wt% Au1wt%Pd, and 2.5wt% Au2.5wt%Pd), comparisons were made at an alcohol/AuPd mole ratio of 152,000 which requires 7 mg mass of 2.5wt% Au2.5wt%Pd/*E. coli*. However a mass of 0.7 mg catalyst required for the highest loading of 25wt% Au25wt%Pd/*E. coli* to maintain the above ratio is difficult to precisely weigh out in practice. Thus a lower alcohol/AuPd molar ratio of 15,200 was applied in another separate comparison between 25wt% Au25wt%Pd/*E. coli* and 2.5wt% Pd2.5wt% Au/*E. coli*, corresponding to a catalyst mass of 7 mg and 70 mg respectively. Other reaction conditions were: 40 ml of benzyl alcohol, $T=110\text{ }^{\circ}\text{C}$, $p_{air}=5\text{ bar}$, $F_{air}=200\text{ ml}\cdot\text{min}^{-1}$, and $N=1200\text{ rpm}$.

Table 5.5 Details of catalyst amount used for catalytic activity comparison

Metal loading on <i>E. coli</i> , %		Mole ratio of substrate/total metal	
Au	Pd		
0.5	0.5	152,000	-
1	1	152,000	-
2.5	2.5	152,000	15,200
25	25	-	15,200

Figure 5.14 *a* shows the benzyl alcohol conversions using lower AuPd-loaded bio-catalysts (0.5wt% Au0.5wt%Pd, 1wt% Au1wt%Pd, 2.5wt% Au2.5wt%Pd), from which it was observed that the reaction rate improved with the increase of AuPd total loading. For similar reasons suggested in the discussion of the metal particle growth in bio-Pd/*E. coli* from 2 wt% to 5 wt% in §4.2, it is possible that at lower loading of AuPd, the eruption of metal particles on the cell surface was restricted. The gradual increase of the metal loading promotes the growth of particles to be exposed to the outer-surface of the cell wall, as a result providing more active sites available for reaction to take place. However with a further increase of AuPd loading from 2.5wt% Au2.5wt%Pd to 25wt% Au25wt%Pd, a considerable decrease of the reaction rate based on the benzyl alcohol conversion was observed (Figure 5.14 *b*). After 7 hours 66.5±1.0% of benzyl alcohol conversion was achieved by using 70 mg of 2.5wt% Au2.5wt%Pd/*E. coli*, revealing an increase of more than 2-folds of the conversion (~31.0%) when using 7 mg of 25wt% Au25wt%Pd/*E. coli*. This decrease in catalyst activity could be rationalised by the possibility that a higher catalyst loading contained larger clusters of metal, with poor dispersion of active metals providing limited accessible active sites for reaction. The AuPd particle growth corresponding to the increase of the metal loading was confirmed by observations recorded under examination by both SEM and TEM which is reported in §6.3.

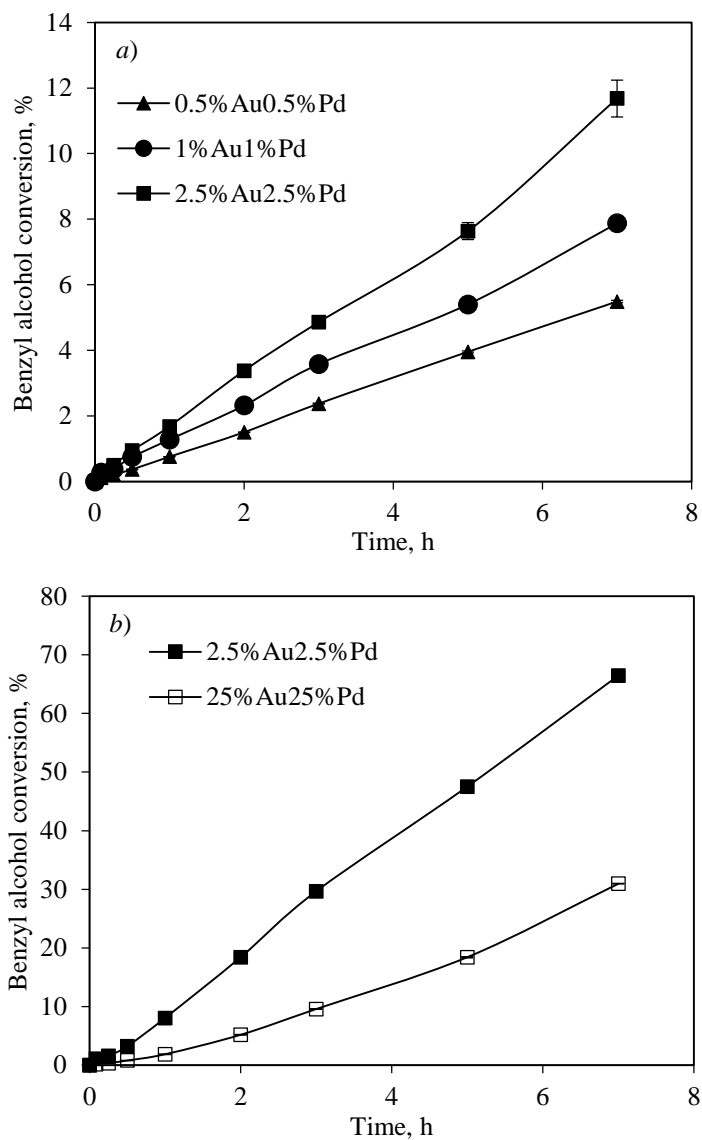


Figure 5.14 a) and b) Comparisons of benzyl alcohol conversions over bio-AuPd/*E. coli* catalysts with different total loadings. Reaction conditions were: 40 ml benzyl alcohol (solvent free), $p_{air} = 5$ bar, $F_{air} = 200$ ml.min⁻¹, $N = 1200$ rpm, and $T = 110$ °C.

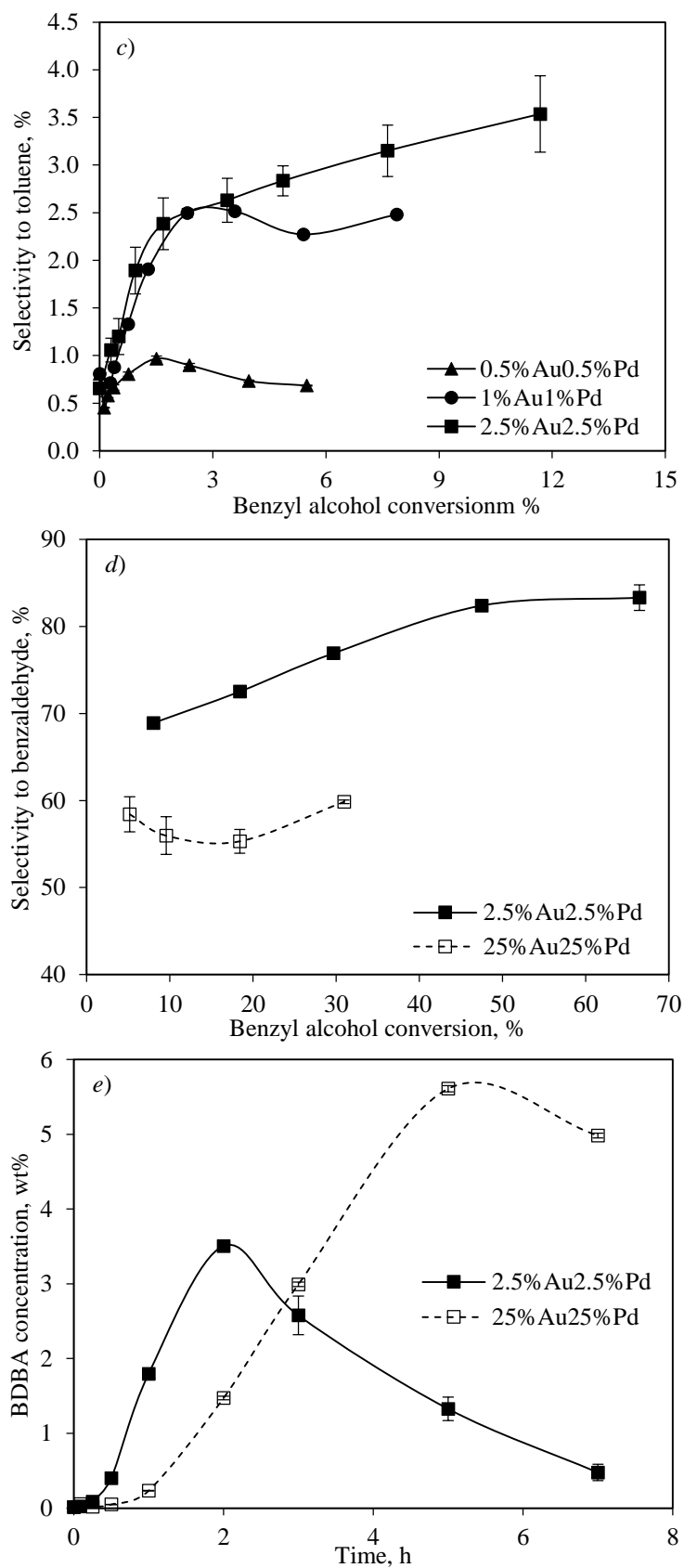


Figure 5.14 *continued*. c) Comparison of the selectivity to toluene over bio-AuPd/*E. coli* catalysts with loadings of 0.5wt% Au/0.5wt%Pd, 1wt% Au/1wt%Pd, and 2.5wt% Au/2.5wt%Pd; d) Comparisons of the selectivity to benzyl aldehyde and e) Comparisons of the selectivity to BDDBA formation using 2.5wt% Au/2.5wt%Pd/*E. coli* and 25wt% Au/25wt%Pd/*E. coli*. Reaction conditions were: 40 ml benzyl alcohol (solvent free), $p_{air} = 5$ bar, $F_{air} = 200$ ml.min⁻¹, $N = 1200$ rpm, $T = 110$ °C.

In terms of the product distribution at lower AuPd-loadings (0.5wt% Au0.5wt% Pd, 1wt% Au1wt% Pd, 2.5wt% Au2.5wt% Pd), similar selectivity towards benzaldehyde was obtained, giving an average aldehyde selectivity of ~51.3%. However, it is worthy of note that the selectivity to toluene changed considerably with these three total metal loadings (Figure 5.14 c). A very minor amount of toluene was formed over the lowest loading of 0.5wt% Au0.5wt% Pd on *E. coli*, with 0.7% of the selectivity at 5.5% benzyl alcohol conversion; however this number increased by 3.5-fold over 1wt% Au1wt% Pd/*E. coli* and 5-fold over bio-2.5wt% Au2.5wt% Pd/*E. coli* at a comparable level of benzyl alcohol conversion. Therefore it was concluded that the formation of toluene is sensitive to the increase of the exposed metal surface area. In addition, in the comparison between 2.5wt% Au2.5wt% Pd/*E. coli* and 25wt% Au25wt% Pd/*E. coli*, a much lower selectivity to the target product of benzaldehyde was observed for 25wt% Au25wt% Pd/*E. coli* than 2.5wt% Au2.5wt% Pd/*E. coli* (Figure 5.14 d), meanwhile a correspondingly higher formation of BDBA (Figure 5.14 e).

From the above discussion it is evident that AuPd total loading (equal weight ratio of Au: Pd) on the bacteria *E. coli* is an important factor influencing the performance of the catalysts due to the particle size of the AuPd alloy and its availability onto the bacteria surface. Increasing the metal loading from 0.5wt% Au0.5wt% Pd to 2.5wt% Au2.5wt% Pd provides more exposed active metal nanoparticles upon the cell surface which, as a result, appears to be associated with the improved catalytic performance. While catalyst with a very high loading of 25wt% Au25wt% Pd on *E. coli* is thought to have exhibited large metal clusters which gave a poor catalytic activity in benzyl alcohol oxidation (lower benzyl alcohol conversion and benzaldehyde selectivity). Under the current experimental conditions, among the examined four bio-AuPd/*E. coli* preparations with varied metal loadings, the 2.5wt% Au2.5wt% Pd on *E. coli* demonstrated a good dispersion of metal nanoparticles with the best catalytic activity.

5.2.2.3 Effect of Au:Pd Mass Ratio

After investigating the total AuPd loading on biomass *E. coli*, a study was carried out to examine the effect of the Au:Pd mass ratio. A range of bio-AuPd catalysts was then prepared with identical 5 wt% total AuPd weight loading, while different mass ratios of 1wt%Au4wt%Pd, 2.5wt%Au2.5wt%Pd and 4wt%Au1wt%Pd on *E. coli* were utilised for the different samples. The mass of catalyst was adjusted to maintain the same substrate/total metal mole ratio of 152,000. All the oxidation reactions were operated under the same conditions: 40 ml of benzyl alcohol, $T = 110\text{ }^{\circ}\text{C}$, $p_{air} = 5\text{ bar}$, $F_{air} = 200\text{ ml}\cdot\text{min}^{-1}$, and $N = 1200\text{ rpm}$.

Figure 5.15 *a* shows the order of catalytic activity as: 4wt%Au1wt%Pd < 1wt%Au4wt%Pd < 2.5wt%Au2.5wt%Pd. Under the same reaction conditions, 2.5wt%Au2.5wt%Pd/*E. coli* was found to retain its advantage in catalytic activity when compared with the other two bio-AuPd catalysts, showing a higher benzyl alcohol conversion. In another published work by Deplanche *et al.* [161], the Au-rich core with Pd-rich shell configuration was found to occur on AuPd/*E. coli* with equal Au:Pd mass ratio, more specifically the bimetallic biogenic particle was developed where surface-exposed Pd atoms decorate a core of Au atoms. Meanwhile, it is suggested that the active site for dissociative adsorption of the alcohol and β -hydride elimination (details refer to §2.4.2.2) is considered to be the reduced metal Pd(0) [103,230]. Au plays a role to isolate Pd sites within bimetallic systems [166] thus acting as a promoter to reduce the deactivation of Pd in oxidation reactions (details refer to §2.2.5.2). In addition, it is known that Au particles are easily grown to bigger sizes than Pd particles under the same conditions [153,309], which is confirmed in this study by the XRD analysis presented in §6.4.3. Thus at a higher content of Au in 4wt%Au1wt%Pd/*E. coli*, changes to the metal configuration may lead to the Pd active sites becoming covered by Au atoms, resulting in a decreased activity in the benzyl alcohol oxidation. The benzyl alcohol

conversion (after 7 hours) was obtained as $11.7\pm 0.5\%$ using $2.5\text{wt}\% \text{Au}2.5\text{wt}\% \text{Pd}/E. coli$, however only half of the conversion was achieved by the $4\text{wt}\% \text{Au}1\text{wt}\% \text{Pd}/E. coli$ giving $6.6\pm 0.1\%$ after 7 hours.

On the other hand, adjusting the Pd proportion from $2.5\text{wt}\% \text{Au}2.5\text{wt}\% \text{Pd}$ to $1\text{wt}\% \text{Au}4\text{wt}\% \text{Pd}$ also resulted in a reduction in the activity of the catalyst. After 7 hours, benzyl alcohol conversion using $1\text{wt}\% \text{Au}4\text{wt}\% \text{Pd}/E. coli$ reached to $10.3\pm 0.1\%$, which was about 88% of the conversion using $2.5\text{wt}\% \text{Au}2.5\text{wt}\% \text{Pd}/E. coli$. This finding implicates that the larger content of Pd sites, which are responsible to be the active sites for the oxidation, are not required to secure high catalytic performance. Prati *et al.* [71] suggested that the catalytic activity of supported bimetallic catalyst depends on the geometric effect and the electronic interactions between the two metals. In addition, all three bio-AuPd/*E. coli* presented similar selectivities towards benzaldehyde (Figure 5.15 *b*) and toluene (Figure 5.15 *c*).

Based on the above discussion, $2.5\text{wt}\% \text{Au}2.5\text{wt}\% \text{Pd}/E. coli$ was determined to be the optimal ratio for synergistic effect between Au and Pd in the present benzyl alcohol oxidation.

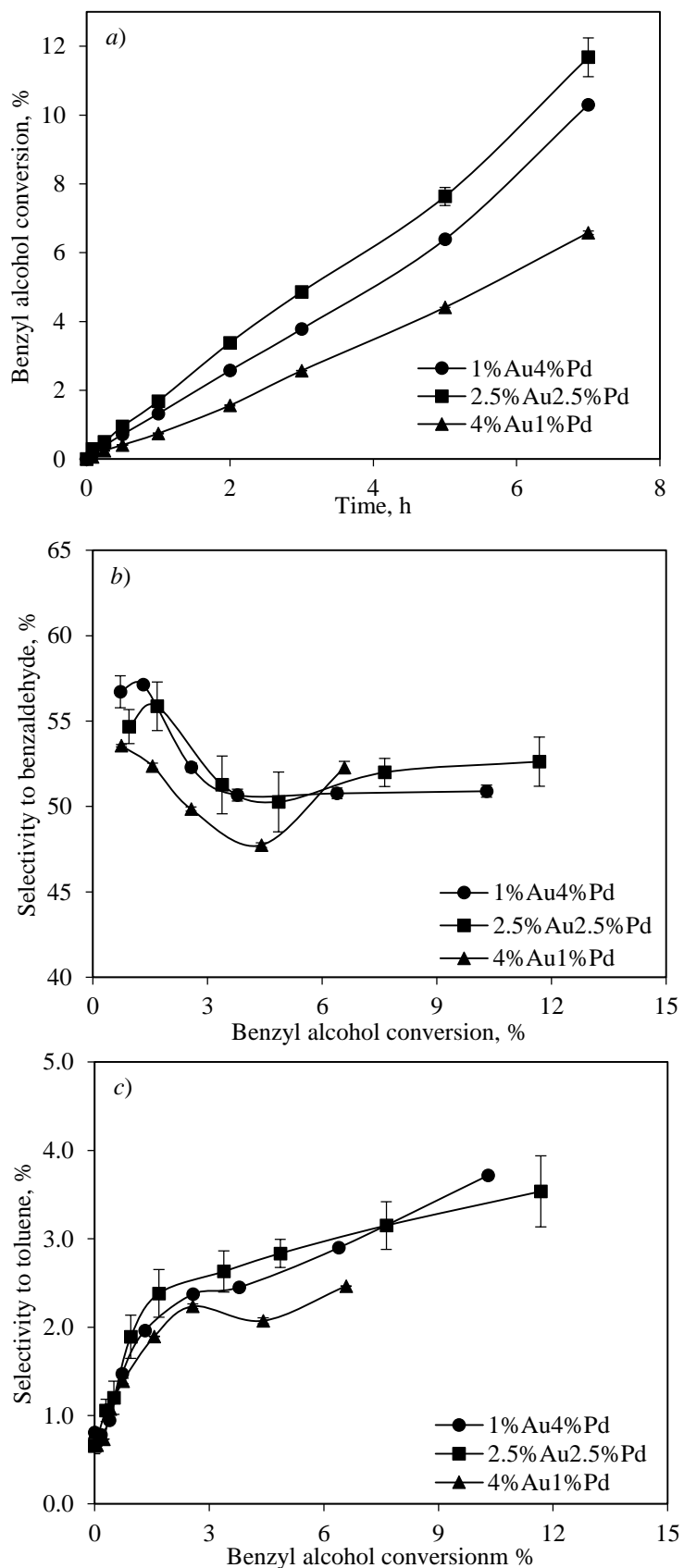


Figure 5.15 a) Benzyl alcohol conversion profiles, b) selectivity towards benzaldehyde, and c) selectivity to toluene over bio-AuPd catalyst prepared by different Au:Pd mass ratios. Reaction conditions: 40 ml of benzyl alcohol, $T = 110\text{ }^{\circ}\text{C}$, $p_{\text{air}} = 5\text{ bar}$, $F_{\text{air}} = 200\text{ ml}\cdot\text{min}^{-1}$, and $N = 1200\text{ rpm}$.

5.3 Oxidation of Other Alcohols

For a potential use in fine chemicals synthesis it is important that a catalyst preparation method is broad in scope, such that the catalysts are effective with a broad range of alcohols that often contain other functional groups. The catalytic activity of the optimised bio-AuPd (2.5wt% Au2.5wt% Pd/*E. coli*) was investigated with a range of other alcohols as oxidation substrates, including 1-phenylethanol (secondary, benzylic), 1-octanol (primary, straight chain), 2-octanol (secondary, straight chain) and 1,4-butanediol (diol, straight chain) as reported in this section. These substrates contrast with the earlier studies of benzyl alcohol as a model for aromatic activated alcohol (primary benzylic).

Table 5.6 Oxidation of different alcohols over 2.5wt% Au2.5wt% Pd/*E. coli*.

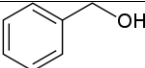
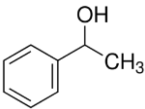
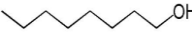
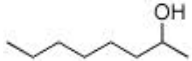
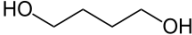
Substrate	Structure		Reaction condition				Conversion after 5 hours, %
			T °C	P bar	F ml.min ⁻¹	N rpm	
Benzyl alcohol		primary, benzylic	140	5, air	200	1200	35.8±0.8
1-phenylethanol		secondary, benzylic	160	5, air	200	1200	14.9±0.1
1-octanol		primary, straight chain	160	5, air	200	1200	65.5±1.1
2-octanol		secondary, straight chain	160	5, air	200	1200	19.8±0.1
1,4-butanediol		diol straight chain	160	5, air	200	1200	49.1±0.7

Table 5.6 summarises the alcohols examined over the 2.5wt% Au2.5wt% Pd/*E. coli* catalyst, along with the corresponding reaction conditions and the resulting reaction performance. The reaction temperatures were selected based on the reference to the work by Enache *et al.* [231]. As expected, different substrates exhibited quite different reactivities. Compared with the performance in benzyl alcohol oxidation, the bio-AuPd/*E. coli* showed a low activity in the reaction of secondary benzylic alcohol, 1-phenylethanol, with only 14.9±0.1% of the conversion being achieved after 5 hours under an even higher temperature of 160 °C. In

terms of the oxidation of alkanols, 2.5wt% Au2.5wt% Pd/*E. coli* demonstrated a total conversion of $65.5 \pm 1.1\%$ in 1-octanol oxidation after 5 hours, while much worse performance was achieved in 2-octanol showing only $19.8 \pm 0.1\%$ conversion. Thus, a general conclusion could be made that secondary alcohols are less reactive than the primary alcohols but this requires confirmation using additional bio-AuPd preparations. In addition, in the oxidation of 1,4-butanediol, a conversion of $49.1 \pm 0.7\%$ was obtained at the end of the reaction. The difference in the above observed catalytic performance using the same bioAuPd catalyst may be due to the interaction of the substrate with the active site.

5.4 Conclusions

In this chapter a reliable reaction system was designed for oxidation of alcohols using compressed air as a gas reactant in a solvent-free environment. This included modifying a reactor to allow for continuous air flow with condensation of volatile products. Reaction conditions were optimised in benzyl alcohol oxidation using bio-AuPd catalysts. Under the optimised reaction conditions (5 bar of air, $200 \text{ ml} \cdot \text{min}^{-1}$ of air flow rate, and a stirring speed of 1200 rpm), the activation energy of solvent-free oxidation of benzyl alcohol over 2.5wt% Au2.5wt% Pd/*E. coli* was evaluated as $71.8 \text{ kJ} \cdot \text{mol}^{-1}$.

In order to improve the catalytic performance of bio-catalysts, bio-AuPd/*E. coli* samples were manufactured using different biomass strains and with various total AuPd loading as well as Au: Pd mass ratio, of which the catalytic behaviours were investigated in benzyl alcohol oxidation. Bacterial strain of *E. coli* was demonstrated to be the best biomass strain to manufacture the AuPd bimetallic bioinorganic catalyst. From the investigation of total metal loading and Pd/Au weight ratio effects, bio-AuPd/*E. coli* with the Au: Pd mass ratio of 1:1 and metal AuPd loading content of 5 wt% showed to be the most active bio-catalyst in the

benzyl alcohol oxidation in this study. 2.5wt%Au2.5wt%Pd/*E. coli* also demonstrated certain catalytic activity in a range of other alcohols.

Chapter 6

Characterisation of Catalyst

6.1 Chapter Overview

This chapter presents the results and discussion focusing on the characteristic properties of bionanomaterials (bio-catalyst) by a range of characterisation techniques.

To investigate the thermal stability of the bio-catalyst manufactured using bacterial biomass from various strains as supports, ThermoGravimetric Analysis (TGA) was performed with results interpreted in §6.2. This was followed by examination of bio-catalysts under the electron microscope (§6.3). Surface morphologies were revealed by Scanning Electron Microscopy (SEM) and the deposited elemental components were confirmed by Backscattered-SEM (BSE) accompanied by Energy Dispersive X-ray spectroscopy (EDS). In addition, the metal deposition on different strains of bacteria was characterised by Transmission Electron Microscopy (TEM). For the estimation of metal particle size, three approaches were employed in this study (§6.4) based on CO chemisorption analysis, TEM imaging, and X-ray Diffraction (XRD) analysis.

Finally conclusions are drawn in §6.5 based on the properties of the bio-catalysts.

6.2 Thermal Stability of Bio-catalyst

The reaction results in both §4.3.2.2 (bio-Pd/*E. coli* in hydrogenation; 150 °C) and §5.2.2.1 (bio-AuPd/*R. sphaeroides* in oxidation; 110 °C) suggested that one consideration when using bio-catalysts is their thermal stability under the operating temperature due to the nature of biomass (see §2.3.1), particularly the polymeric organic material components which support the NPs. For example, the decomposition of carbohydrates in biomass was shown to occur at temperature between 200 °C and 270 °C [267]. The strain-specific composition, structure, and organisation of the components could account for the overall stability of the bacterial biomass during heating. This section covers TGA analysis on bio-Pd catalysts used for partial hydrogenations (5wt%Pd on *E. coli* and *D. desulfuricans*) and bio-AuPd catalysts used in aerobic oxidations (2.5wt%Au2.5wt%Pd on *E. coli*, *R. sphaeroides*, *A. oxydans*, and *M. luteus*). Triplicate TGA analyses were performed for each bio-catalyst, sampled from one single preparation, unless otherwise stated.

Typical weight loss curves as a function of the temperature ramp from 25 °C to 1000 °C at 10 °C/min from 5wt%Pd/*D. desulfuricans* and 5wt%Pd/*E. coli* catalyst samples are compared in Figure 6.1 *a*. It is noted here that the temperature region of interest for this study is between 25 °C and 375 °C (indicated by vertical solid lines in Figure 6.1), which was responsible for the decomposition of polymeric organic material and covered the highest-used reaction operating temperature in the present work (160 °C). Only a very small difference between the two TG curves of 5wt%Pd/*D. desulfuricans* and 5wt%Pd/*E. coli* was shown between 25 °C and 375 °C, suggesting similar thermal behaviours of these two biomaterials in this temperature range. Furthermore, the following conclusions can be drawn, relating to the decomposition observed: i) at temperature ~100 °C, the mass changes of the samples can be attributed to predominantly the evaporation of residual moisture attached to the surfaces of

the samples, being 3.42 wt% and 6.52 wt% for 5wt%Pd/*D. desulfuricans* and 5wt%Pd/*E. coli* respectively; ii) a second phase of minimal mass loss occurs between a temperature range of 100~175 °C (indicated by the dashed lines in Figure 6.1) for both bio-Pd catalysts, suggesting that these two catalysts are thermally stable within this temperature interval; iii) at a temperature exceeding 175 °C, catalyst mass decreases substantially in both samples, indicating the starting of decomposition of the biomass. It is therefore concluded that bio-catalyst samples of 5wt%Pd/*D. desulfuricans* and 5wt%Pd/*E. coli* can be used without decomposition at reaction temperatures up to 175 °C. A comparison was also made between two *E. coli* supported bio-catalysts, *i.e.* *E. coli* cells loaded with 5wt%Pd and 2.5wt%Au2.5wt%Pd, with the corresponding weight loss curves shown in Figure 6.1 *b*. In the temperature range of 25 °C~375 °C, 5wt%Pd/*E. coli* and 2.5wt%Au2.5wt%Pd/*E. coli* gave very close TG curves, indicating that a change of metal composition from 5wt%Pd to 2.5wt%Au2.5wt%Pd on the same strain of bacterial (*E. coli*) had almost no effect on the overall thermal behaviour of the resulting bio-catalysts in this temperature range.

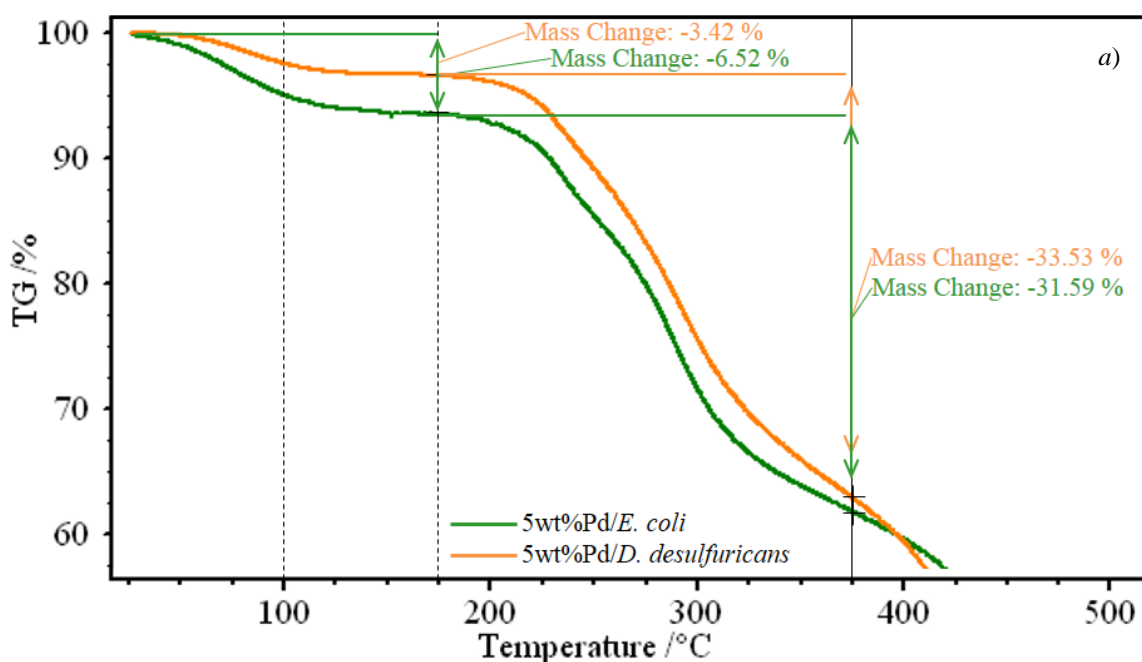


Figure 6.1 *a*) Weight loss curves for 5wt%Pd/*E. coli* and 5wt%Pd/*D. desulfuricans*. TGA was performed in air at a heating rate of 10 °C/min from 25 °C to 1000 °C.

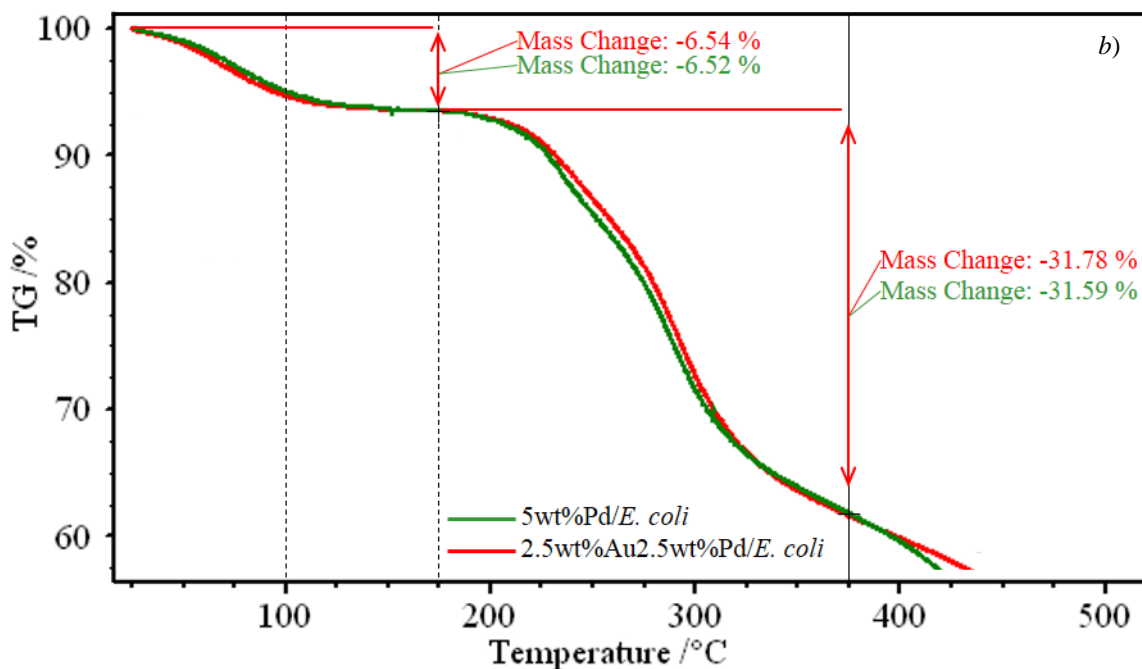


Figure 6.1 continued. b) Weight loss curves for 5wt%Pd/*E. coli* and 2.5wt%Au2.5wt%Pd/*E. coli*. TGA was performed in air at a heating rate of 10 °C/min from 25 °C to 1000 °C.

As to the four bio-2.5wt%Au2.5wt%Pd catalysts tested in benzyl alcohol oxidation (§5.2.2.1), the same TGA analysis was conducted with a comparison of the corresponding TG curves presented in Figure 6.2. As a common feature in terms of the thermal behaviour between these four bio-AuPd catalysts, after the initial moisture evolution (~100 °C), the major part of catalyst mass decreased in a multi-stage manner. The stepwise feature indicates the progressive decomposition of the various biomass components (*e.g.* polysaccharides, lipids, and protein [267]) in order of their individual thermal stability, which could be confirmed by subjecting each component fraction to TGA analysis under the same temperature program however this was not examined further in this study. In addition, it appears that different decomposition characteristics could exist between different types of bacterial biomass. Among the four bio-AuPd catalysts in Figure 6.2, bio-AuPd catalysts on *E. coli*, *A. oxydans*, and *M. luteus* showed small differences between 25~375 °C (indicated by solid line) with major differences at temperatures above 500 °C (indicated by the dashed line). However bio-AuPd/*R. sphaeroides* gives an anomalous TG curve from the other three

bio-AuPd catalysts in the temperature range of interest (25 °C~375 °C). Although polysaccharides, lipids, protein, and nucleotides are four fundamental types of components that occur in all forms of cells (§2.3.1), it was suggested [310] that the composition, chemical structure, and degree of polymerisation of the individual component all play roles in determining the overall thermal stability characteristics of biomass between different strains.

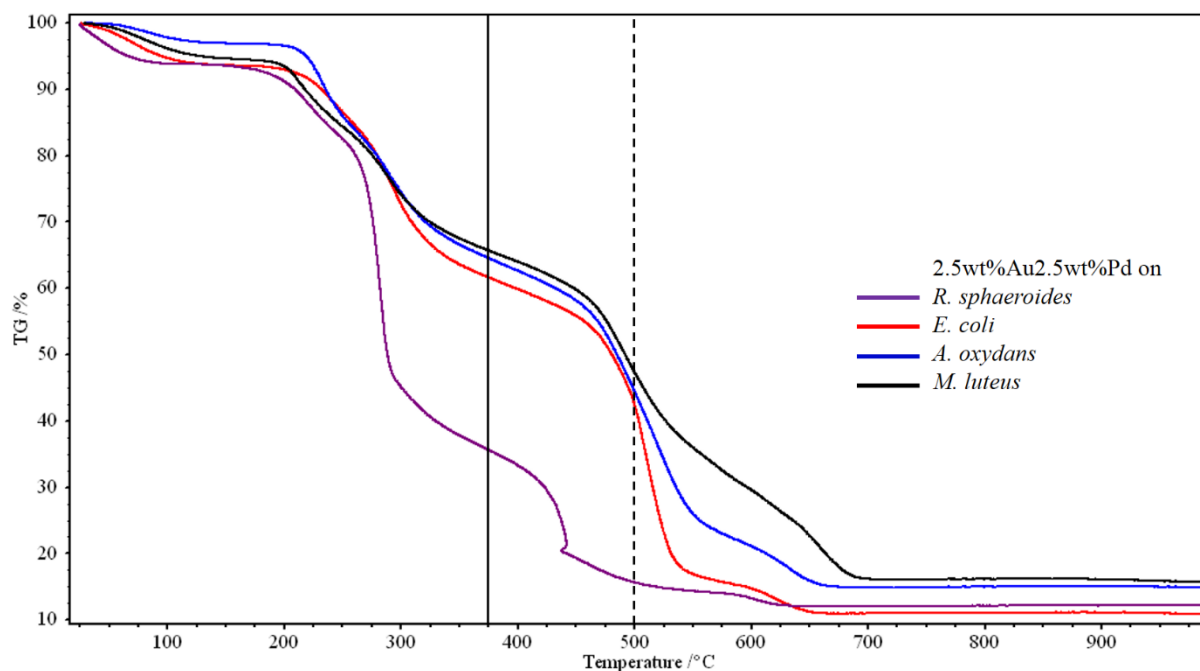


Figure 6.2 Weight loss curves for 2.5wt% Au2.5wt%Pd bio-catalysts supported on different strains of bacteria at heating rates of 10 °C/min from 25 °C to 1000 °C.

A higher conversion was observed in benzyl alcohol oxidation (at 110 °C) using 2.5wt% Au2.5wt%Pd/*R. sphaeroides* and 2.5wt% Au2.5wt%Pd/*E. coli* than the other two bio-AuPd catalysts, however early deactivation of bio-AuPd/*R. sphaeroides* occurred after ~3 hours (§5.2.2.1). Hence the TG curves from bio-AuPd on *E. coli* and *R. sphaeroides* as catalysts of higher activity were selected for further comparison, as shown in Figure 6.3 *a* and Figure 6.3 *b* respectively.

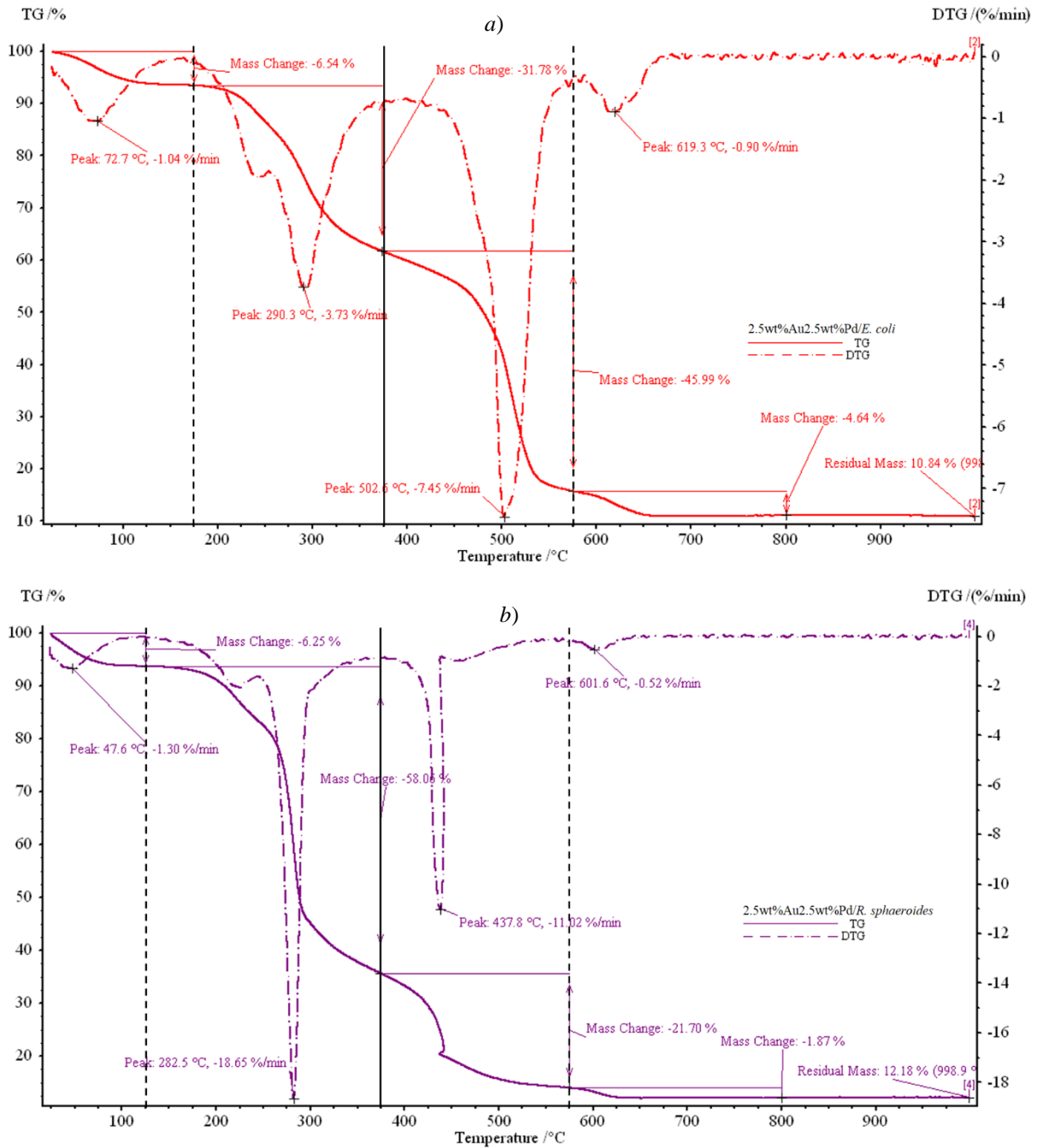


Figure 6.3 Detailed TGA analysis of a) 2.5wt% Au2.5wt% Pd/*E. coli*, and b) 2.5wt% Au2.5wt% Pd/*R. sphaeroides* at heating rates of 10 °C/min from 25 °C to 1000 °C.

The Differential TGA curves (DTG) are presented in Figure 6.3 as dashed curves with inverted peaks, providing the rate of mass loss ($\% \cdot \text{min}^{-1}$) versus temperature. The first DTG peak in Figure 6.3 a shows a similar rate with that in Figure 6.3 b ($-1.04 \% \cdot \text{min}^{-1}$ for bio-AuPd/*E. coli* and $-1.30 \% \cdot \text{min}^{-1}$ for bio-AuPd/*R. sphaeroides*), representing the loss of moisture in both cases. The onset of decomposition for bio-AuPd/*E. coli* is seen prominently

after ~ 175 °C, with a much lower temperature of ~ 125 °C in the case of bio-AuPd/*R. sphaeroides*. Thereafter, two extensive DTG peaks were obtained in both cases during the main decomposition period (25 °C \sim 575 °C, indicated) however each showing strain-specific features. The narrower and sharper peaks in Figure 6.3 *b* than Figure 6.3 *a* clearly indicate that the decomposition of organic components in bio-AuPd/*R. sphaeroides* occurred much faster than that in bio-AuPd/*E. coli*. The observed lower decomposition onset temperature (~ 125 °C) and the subsequent higher rate of mass loss of bio-AuPd/*R. sphaeroides* than those of bio-AuPd/*E. coli* could explain the thermal deactivation of the former catalyst in benzyl alcohol oxidation (at 110 °C, after ~ 3 hours). Although the oxidation reaction temperature of 110 °C was ~ 15 °C lower than the TGA determined upper-use temperature of bio-AuPd/*R. sphaeroides*, it was likely that its deactivation was accelerated by some other factors, *e.g.* the attrition caused by high-speed agitation.

6.3 Examination of Bio-Catalyst by Electron Microscopy

This section reports an investigation of the morphology of the bio-catalyst and metal particle deposition on the biomass under the electron microscope.

6.3.1 Surface Morphology and Element Confirmation (SEM/BSE-EDS)

The bio-catalyst material comprises black powder containing cells which are killed by the metallisation process; the dead bacteria act as a carbon-based support for metal nanoparticles, providing a similar function to conventional catalyst supports such as various forms of carbons, Al₂O₃ or TiO₂. Typical SEM surface images of the dry powder of bio-catalysts are given in Figure 6.4 *a* and *b*. It is observed that the ensembles of bacteria are overlapping each other, while showing the individual bacteria with well-maintained original shapes. The shape

of the cells varies depending on the strain of the bacteria, *e.g.* rod-shape for *E. coli* (Figure 6.4 *a*) while spherical-shape for *M. luteus* (Figure 6.4 *b*).

In general, the SEM analysis of the cells can hardly distinguish the presence of the metal depositions on the bacteria. With the detection of backscattered electrons, *e.g.* BSE image of *E. coli*-supported bio-catalyst in Figure 6.4 *c*, the presence of well-dispersed metal NPs is clearly evidenced by the bright dots. To identify the metal element, the acquired BSE image from the bio-catalyst was processed by EDS analysis, by which the identification of the palladium element in bio-Pd catalyst was confirmed, *e.g.* 25wt%Pd/*E. coli* in Figure 6.4 *d*. Similarly, for the bimetallic catalyst (bio-AuPd) used in the oxidation reaction, the existence of both palladium and gold elements were confirmed by the EDS spectrum from the corresponding BSE image of 25wt%Au25wt%Pd/*E. coli* (Figure 6.4 *e*). It is noted here that the above two high metal loaded bio-catalysts (25wt%Pd and 25wt%Au25wt%Pd) were selected as examples for the convenient observation of palladium and gold peaks from the EDS spectra, since the EDS method is relatively insensitive at low metal concentrations.

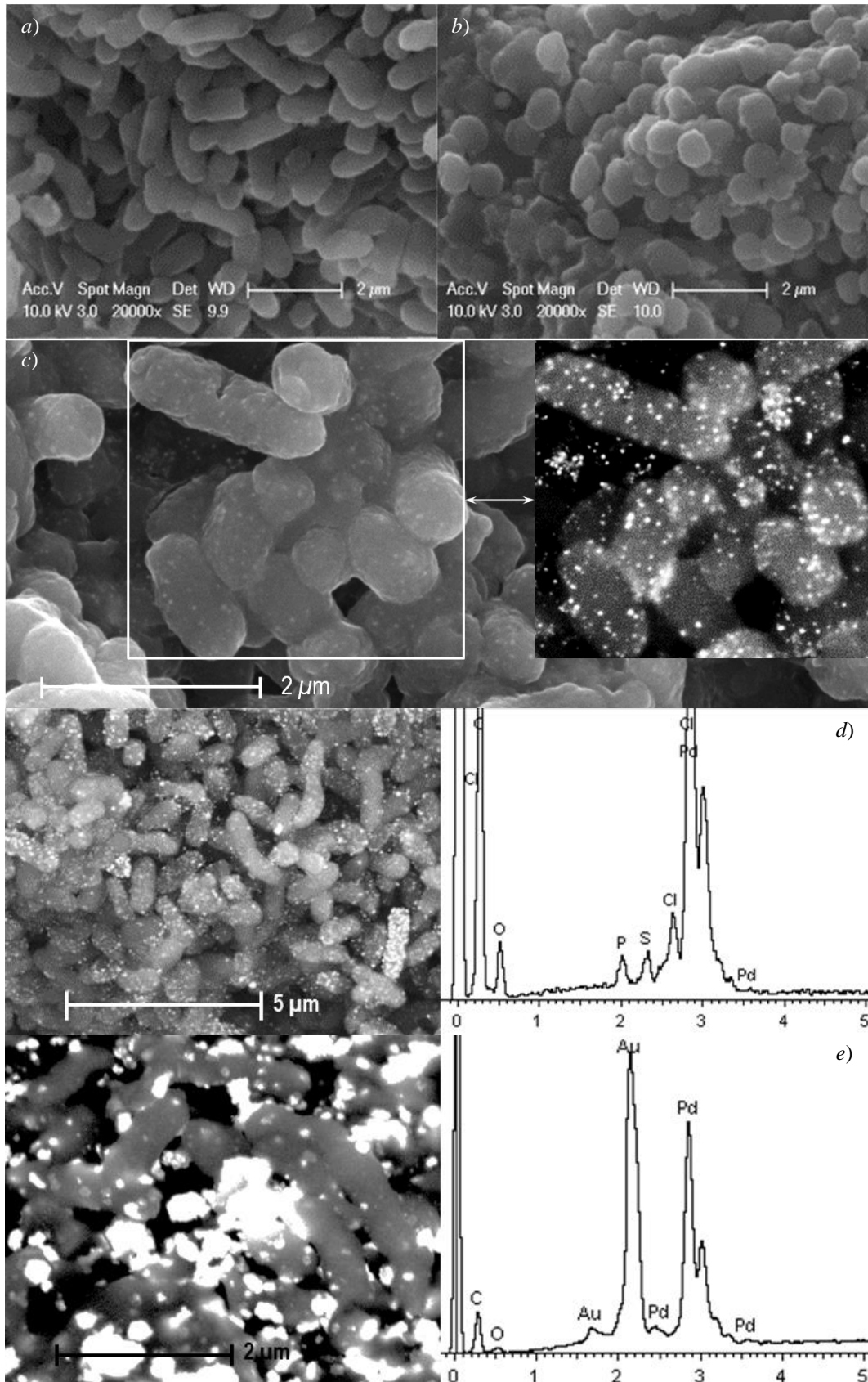


Figure 6.4 a) SEM image of *E. coli*-supported bio-catalyst powder, showing rod-shaped *E. coli* cells; b) SEM image of *M. luteus*-supported bio-catalyst powder, showing spherical-shaped *M. luteus* cells; c) SEM image of one *E. coli*-supported bio-catalyst powder, inset corresponding BSE image of the selected area; d) BSE image from dry powder of 25wt%Pd/*E. coli* catalyst with the corresponding EDS spectrum; and e) BSE image from dry powder of 25wt%Au/25wt%Pd/*E. coli* catalyst with the corresponding EDS spectrum.

In addition to the detection of metal types, a variation of the size of deposited metal particles can be observed in BSE images. Metal particles for 1wt% Au1wt%Pd/*E. coli* (Figure 6.5 a) are smaller than those in Figure 6.5 b for 2.5wt% Au2.5wt%Pd/*E. coli*, indicating the particle growth with the increase of AuPd loading as compared to the formation of additional metal-loaded sites. At an identical loading of 2.5wt% Au2.5wt%Pd, discriminations between the different strain-supported AuPd NPs can also be revealed by the BSE images from these samples. For example the 2.5wt% Au2.5wt%Pd preparations on *E. coli*, *M. luteus*, and *A. oxydans* in Figure 6.5 b~d clearly show strain-specific features of AuPd NPs.

As described in §3.3.2, the manufacturing procedure of bio-AuPd catalyst involves a sequential reduction of Pd(II) and Au(III) salts onto the biomass support with H₂ as electron donor. The resulting bio-Pd(0) NPs from the first step of palladisation on Gram-positive biomass were observed to be consistently larger than the ones on Gram-negative biomass [23,25]. Therefore it was deduced that the subsequent addition of Au(III) to bio-Pd(0), as the seed for the formation of Au NPs from the Au(III) solution to form bio-AuPd, would result in larger AuPd clusters on Gram-positive strains than on Gram-negative strains as is suggested in Figure 6.5 c and d. A study by Redwood *et al.* [176] suggested that the outer membrane of Gram-negative bacteria may help to tether and hold the Pd(0) NPs, thus could prevent the aggregation of small particles. If this is correct, Gram-positive strains, lacking an outer membrane, would not benefit from this and accordingly, they may possess fewer and larger metal clusters. Indeed, large electron bright aggregates were observed in Figure 6.5 c and d, the BSE images for 2.5wt% Au2.5wt%Pd on *M. luteus* (Gram-positive) and *A. oxydans* (Gram-positive). The particle distribution on a single *M. luteus* cell tended to be one very large metal cluster accompanied by very few scattered small particles. In the case of *A. oxydans*, metal particles tended to form either isolated large clusters (arrowed) or strips of ‘cloud’ (circled). The typical size range of the observed large AuPd particles in the image is

estimated as 100~200 nm on both *M. luteus* and *A. oxydans* (sizes indicated were measured using the Image J program). In contrast, the 2.5wt% Au2.5wt% Pd/*E. coli* in Figure 6.5 b) shows relatively evenly located metal particles with smaller sizes.

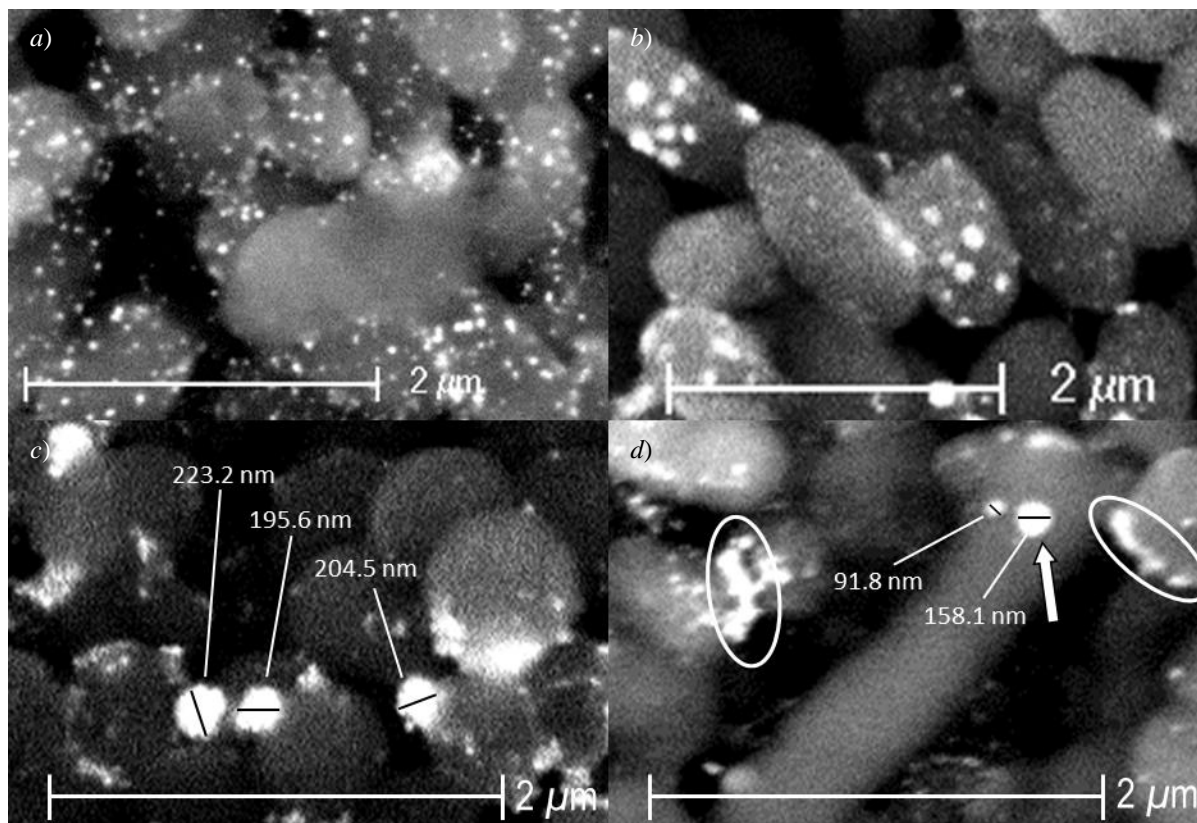


Figure 6.5 BSE images of bio-catalyst powders of a) 1wt% Au1wt% Pd/*E. coli*; b) 2.5wt% Au2.5wt% Pd/*E. coli*; c) 2.5wt% Au2.5wt% Pd/*M. luteus*; and d) 2.5wt% Au2.5wt% Pd/*A. oxydans*.

Comparing the images of Gram-negative and Gram-positive bacteria, it appears that the outer membrane layer which is only present upon the Gram-negative bacteria, may act as a support for the finely dispersed nanoparticles. However the above images do not give conclusive proof since the two cell types differ in other surface features also. Thus further examinations using ultra-thin sections of bio-catalyst were carried out.

6.3.2 Metal Deposition on the Bacteria (TEM)

Transmission Electron Microscopy (TEM) enables the visualisation of the cell-bound metals in cell sections. Figure 6.6 a shows a TEM image of an ultra-thin section of the native *E. coli* cell (Gram-negative) before metallisation, displaying an overall indistinct cell surface region

in the absence of osmium or uranium staining. The layers of the *E. coli* cell surface are denoted, following the direction of the arrow being the outer membrane (*o*), the inner (cytoplasmic) membrane (*i*), and the periplasmic space between these two membrane layers. Figure 6.6 *b* shows a TEM image of palladised *E. coli* cell section (5 wt%Pd), also not treated with any stain during the specimen preparation process. In contrast to the native cell section, some small discrete electron-opaque Pd(0) deposits (black dots indicated) were clearly observed, resolvable to individual particles. More specifically, most of the palladium nanoparticles (NPs) (arrowed) were held as discrete NPs beneath the outermost cell layers and bounded by the Gram-negative double membrane structure. The majority of NPs exhibited monodispersity (Figure 6.6 *c*, 5wt%Pd/*E. coli* from a separate preparation), although some large clusters were observed, apparently indicating agglomerations of smaller NPs in some cases (arrowed).

For bio-catalysts on Gram-negative bacteria, hydrogenases are believed to be responsible for the location of metal particles [177,181], *i.e.* hydrogenases supply electrons from the splitting of hydrogen to promote reduction of Pd(II) to Pd(0) and act as nucleation sites for the formation of Pd(0) NPs. For instance, Mikheenko *et al.* [181] investigated *Desulfovibrio fructosovorans* (Gram-negative) which has four hydrogenases (two periplasmic and two bound within the inner membrane), and found that removal by mutation of the major periplasmic hydrogenase resulted in relocation of the Pd(0) nanoparticles (NPs) from the periplasm to the inner cytoplasmic membrane. In addition, the size of bio-Pd NPs on Gram-negative bacteria has been reported at 3~5 nm [25] at a loading of 5 wt%. The observation that the larger metallic NPs appeared as clusters in some cases (Figure 6.6 *c*) suggests possibly more than one nucleation focus at a given cell surface location. It was suggested that the polymeric nature of the intertwined cell surface layers (see §2.3.1) could offer support to the growing palladium NPs and hold them as stable entities [21].

For the demonstration of metal particle deposition on Gram-positive bacteria, preparation of 5wt%(AuPd)/*M. luteus* was chosen as the example (Figure 6.6 *d* and *e*) since no 5 wt%Pd preparation on Gram-positive bacteria was available in this study. The TEM image in Figure 6.6 *d* shows two metallised *M. luteus* whole cells (specimen made by dropping the catalyst powder in water solution onto the TEM grids, no sectioning). It is illustrated that the cell surface was unevenly covered by a small amount of large palladium particles, meanwhile one over-sized Pd cluster (arrowed) was observed at the joint of the cell-chain suggesting an overall poor Pd distribution on this bacteria strain. When looking at the cell section of the bio-AuPd/*M. luteus* in Figure 6.6 *e*, one large metal cluster was exposed at the outer surface (arrowed) while several larger metal clusters are visible beneath the surface layers (arrowed). No obvious metal particles within the cell wall (a thick layer of peptidoglycan) can be seen in Figure 6.6 *e*. This may be in accordance with the hypothesis that a *M. luteus* cell (as Gram-positive bacterium) has no hydrogenases within its cell wall structure for metal particle nucleation. It is also likely that metal particles aggregate due to the surface layer of *M. luteus* lacking an outer membrane which may help to tether and hold separate the Pd(0) nanoparticles.

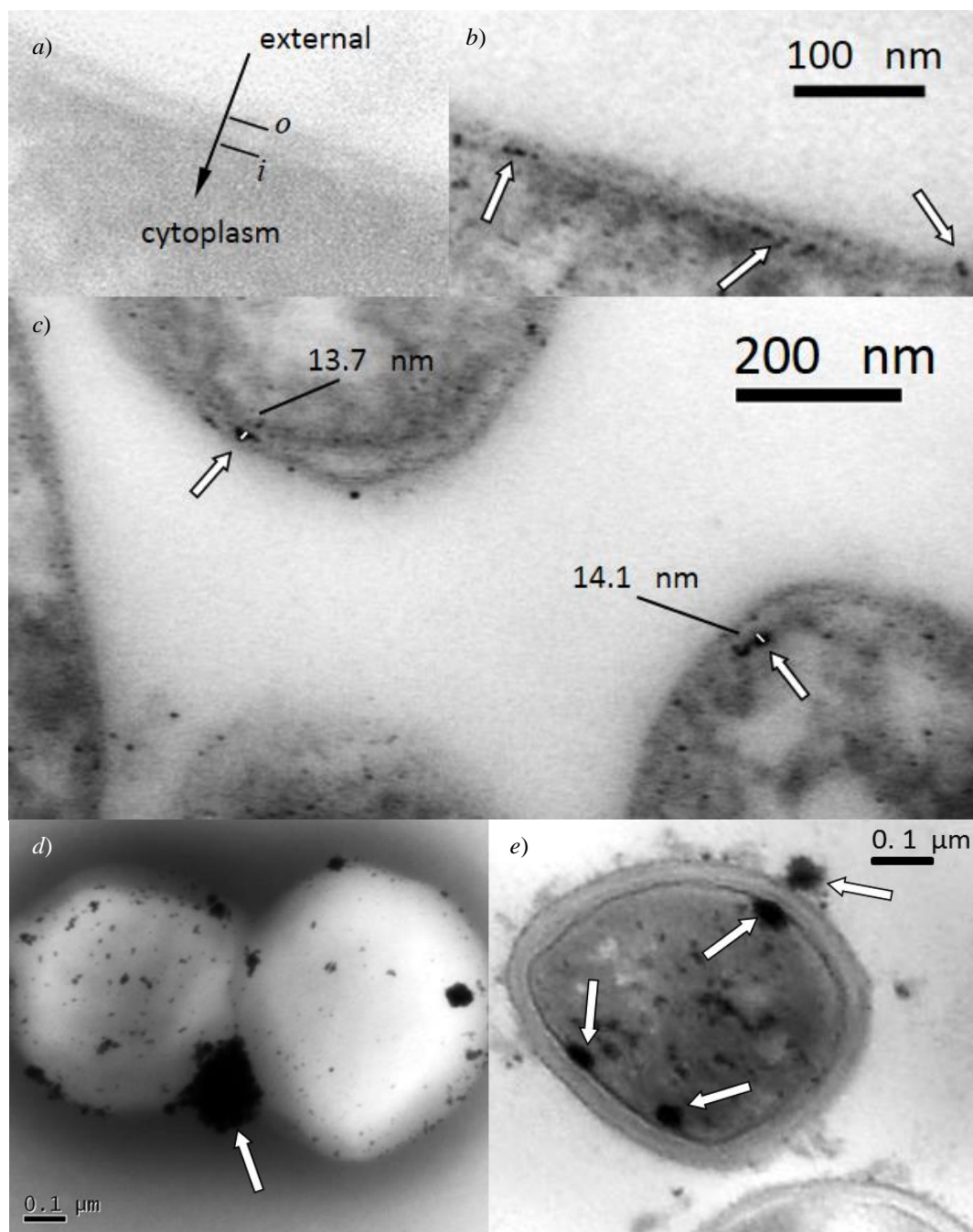


Figure 6.6 *a*) TEM image of an ultra-thin section of native *E. coli* cell (image courtesy of Dr I. Mikheenko), *o* indicates outer membrane and *i* indicates inner membrane; *b*) TEM image of an ultra-thin section of 5 wt% palladium loaded *E. coli* cells showing the cell wall structure after palladisation, sectioned specimen without osmium or uranyl acetate/lead citrate stain; *c*) TEM image of 5 wt% palladium loaded *E. coli* cells from another separate preparation, sectioned specimen without osmium or uranyl acetate/lead citrate stain; *d*) TEM image of *M. luteus* whole cells loaded with 2.5wt% Au/2.5wt% Pd, specimen prepared by dropping the catalyst powder in water solution onto the TEM grid; *e*) TEM image of 2.5wt% Au/2.5wt% Pd/*M. luteus* section (photo courtesy of Dr K. Deplanche). All sectioned specimens in this figure were made from freshly metallised cells.

For the purpose of observing the metal particle growth on Gram-negative bacteria, Figure 6.7 *a-d* display TEM images of bio-AuPd/*E. coli* catalysts (whole cells) with different loadings (0.5wt% Au/0.5% wtPd, 1wt% Au/1% wtPd, 2.5wt% Au/2.5% wtPd, and 25wt% Au/25% wtPd) for

comparison. These specimens were all prepared by dropping the bio-AuPd catalyst powders in water solution onto the TEM grids (no sectioning), thus images in Figure 6.7 represent the whole cells. For the lowest loading of 0.5wt% Au/0.5wt% Pd on *E. coli* (Figure 6.7 a), the inset image from a portion of the cell shows that metal NPs were located beneath the cell surface. The 1wt% Au/1wt% Pd/*E. coli* demonstrates some metal NPs occurrence beyond the cell surface but still in association with it (inset in Figure 6.7 b, arrowed). Further increasing the loading to 2.5wt% Au/2.5wt% Pd, particle eruption through the cell membrane becomes apparent (Figure 6.7 c, arrowed), providing more active metal NPs exposed upon the cell surface. It appears that upon increasing the loading, metal particles grow into larger metal clusters from the initial nuclei, causing the particles to protrude beyond the outer membrane thus becoming exposed at the surface. The preparation with a very high loading of 25wt% Au/25wt% Pd on *E. coli* resulted in excessive growth into very large metal clusters protruding beyond the cell (as shown in Figure 6.7 d). In this case increased loading does not lead to the formation of more particles but rather a number of larger particles causing a reduced overall active surface area.

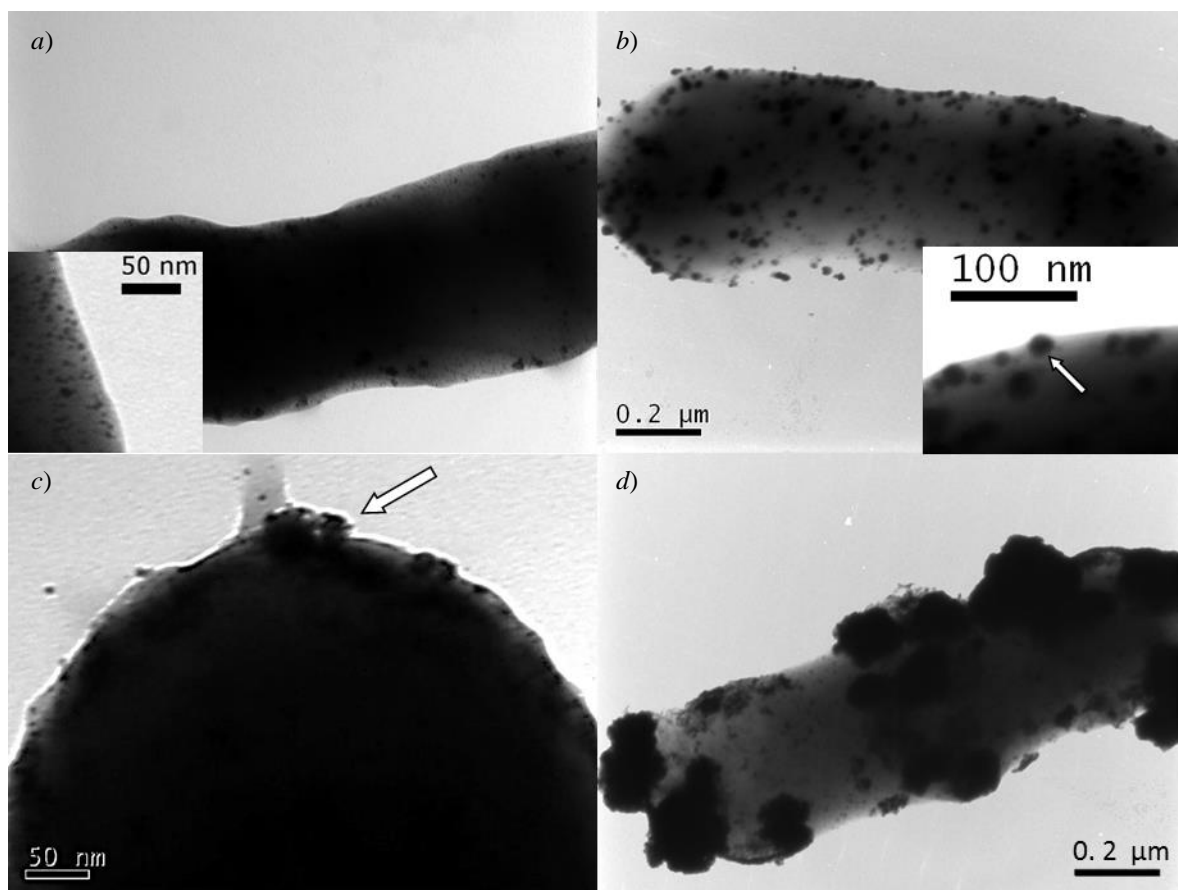


Figure 6.7 TEM images of whole cells (unsectioned) a) 0.5wt% Au/0.5wt% Pd/*E. coli*; b) 1wt% Au/1wt% Pd/*E. coli*; c) 2.5wt% Au/2.5wt% Pd/*E. coli*; and d) 25wt% Au/25wt% Pd/*E. coli*. Specimens prepared by dropping the catalyst powder in water solution onto the TEM grids.

Another consideration for characterising the bimetallic bio-AuPd catalyst is the determination of the metal configuration (*e.g.* AuPd randomly alloyed, or Au(core)-Pd(shell), or Au(shell)-Pd(core)), which could impact upon its catalytic activity in the chemical reaction. For example in solvent-free benzyl alcohol oxidation (§5.2.2), 2.5wt% Au/2.5wt% Pd/*E. coli* showed the best performance among all the different formulated bio-AuPd/*E. coli* catalysts (bio-1wt% Au/4wt% Pd and bio-4wt% Au/1wt% Pd in this study). However, this was not further investigated using electron microscopy. Previous work has shown [161] that the bimetallic NPs (Au:Pd mass ratio of 1:1) on *E. coli* have a Au(core)-Pd(shell) configuration.

6.4 Estimation of Particle Size

It is important to estimate the size of the active metal particle, since this is well known to influence the catalytic performance. Indeed, the change of reaction performance observed in

hydrogenation and oxidation while altering the formulation of either Pd or AuPd loading on bacterial biomass, implies the change of the resulting metal nanoparticle (NP) size. For this reason, this section presents three different methodologies for estimating the metal NP sizes, these being CO chemisorption analysis to determine active particle diameter, TEM imaging with image processing software to get average grain size, and XRD analysis to estimate crystallite size.

6.4.1 CO Pulse Chemisorption Analysis

A CO Pulse Chemisorption analysis was initially carried out using the conventional 5wt%Pd/Al₂O₃ catalyst following the procedure as described in §3.6.2. Figure 6.8 *a* shows the corresponding Thermal Conductivity Detector (TCD) response to successive and consistent in volume of carbon monoxide pulses. CO chemisorbs on palladium according to the stoichiometry (*F*) CO/Pd= 1.

The first peak (corresponding to the 7th injection of CO gas) in Figure 6.8 *a* appeared at ~25 mins, representing the concentration of unconsumed CO molecules from the 7th injection as the sorption sites approached saturation. This also indicates the initial 6 injections of CO gas were totally chemically reacted with each active site thus no change in TCD signal from the detector (0~24 mins in Figure 6.8 *a*) was recorded. After chemisorption was complete, each of the discretely injected gas volumes emerged from the sample tube unchanged thus the detected peaks were constant in area (> 28 mins in Figure 6.8 *a*). The programme terminated after 5 times recording of equal-sized TCD peaks (12 injections in total within 50 mins in Figure 6.8 *a*). The quantity of CO molecules chemisorbed was determined by subtracting the total amount of CO injected and the sum amount that did not react with the active sites of the sample as measured by the detector. The calculations were performed by the instrument software. Table 6.1 presents the parameters used for the evaluation of pulse chemisorption

data together with the repeatable characterisation results for the conventional 5 wt% Pd/Al₂O₃ catalyst.

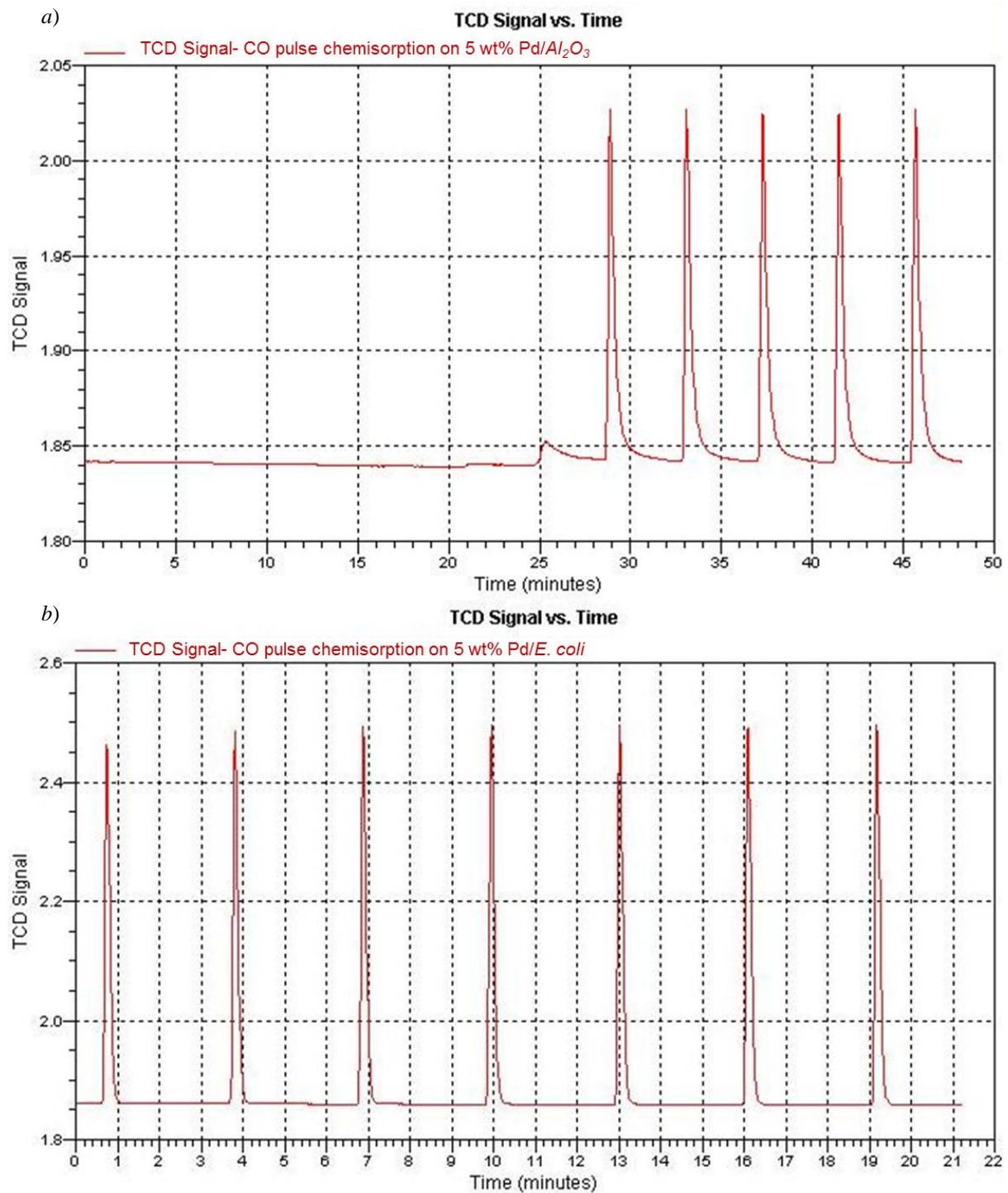


Figure 6.8 TCD signal versus time for a) 5wt%Pd/Al₂O₃, and b) 5wt%Pd/E. coli.

Table 6.1 Parameters for CO Pulse Chemisorption and the resulting data on 5wt%Pd/Al₂O₃ catalyst.

Element	% Sample atomic weight	Stoichiometric factor, F	Atomic cross-sectional area, A_c (nm ²)	Atomic weight (g.mol ⁻¹)	Density, ρ (g.cm ⁻³)
Palladium	5.0	1.0	0.0787	106.4	12.02

Sample weight	Active loop volume at 110.5 °C	Cumulative volume ^a	Metal dispersion	Metallic surface area		Active particle diameter
g	cm ³	cm ³ .g ⁻¹	%	m ² .g(sample) ⁻¹	m ² .g(metal) ⁻¹	nm
0.5249	0.38367	1.02953	9.7745	2.1173	43.5405	11.4633
0.5202	0.38368	0.80878	7.6786	1.7104	34.2080	14.5921
0.5291	0.38369	0.94255	8.9486	1.9933	39.8659	12.5212
0.5350	0.38420	0.92344	8.7672	1.9529	39.0576	12.7803
0.5408	0.38365	0.94372	8.9597	1.9958	39.9155	12.5056
Average±SEM ^b		0.93±0.03	8.82±0.30	1.95±0.06	39.32±1.34	12.77±0.45

^a measured at Standard Temperature Pressure (STP) conditions (273.13K and 760 mmHg). ^b SEM: Standard Error of the Mean.

Applying the same CO pulse chemisorption analysis to the 2wt%Pd/Al₂O₃ catalyst, an average active particle diameter of 8.63 nm was obtained, being smaller than the diameter of 12.77 nm for 5wt%Pd/Al₂O₃ catalyst. Meanwhile the metal dispersion at the former lower palladium loading was estimated to be higher (12.98% at 2wt%Pd/Al₂O₃) than that at the higher loading (8.82% at 5wt%Pd/Al₂O₃). Similarly, Babu *et al.* [311] characterised a series of alumina-supported Pd catalyst with metal loadings between 0.5 wt% and 5 wt% and reported that the catalysts with metal loadings up to 2 wt% demonstrated higher dispersion with homogeneous distribution of active species and predominance of metal-support interaction, while at a loading beyond 2 wt% bulk Pd particles may be formed due to the reduced interaction with the support. Based on the CO chemisorption results, the observed better activity of 2wt%Pd/Al₂O₃ than that of 5wt%Pd/Al₂O₃ in 2-pentyne hydrogenation (see Figure 4.3 in §4.2) under the same reaction conditions can be attributed to the smaller palladium diameter and higher metal dispersion of the former catalyst.

Bio-Pd catalysts (5 wt%Pd and 25 wt%Pd on both *E. coli* and *D. desulfuricans*) were also subjected to the same CO pulse chemisorption analysis. The diagram of TCD signal versus time is shown in Figure 6.8 *b* using a 5wt%Pd/*E. coli* catalyst as an example. The TCD peak appeared from the first injection of CO gas, and the analysis terminated after 6 times recording of equal-sized TCD peaks (7 injections in total within 20 mins in Figure 6.8 *b*). The size of the first peak was shown only slightly smaller than the following 6 equal-sized TCD peaks, indicating very small amount of CO gas was consumed by 5wt%Pd/*E. coli* catalyst throughout the analysis. The calculated results from the CO pulse chemisorption are summarised in Table 6.2. By CO chemisorption, much larger active particle diameters for the bio-catalysts were estimated (149.06 nm for Pd/*D. desulfuricans* and 64.51 nm for Pd/*E. coli*), than that for Pd/ Al_2O_3 (12.77 nm) at the equivalent 5 wt%Pd loading. For the bio-Pd/*D. desulfuricans*, previously published studies using magnetic measurements and extended X-ray Absorption Fine Structure (EXAFS) analysis reported the Pd particles on *D. desulfuricans* at 5 wt% loading to have diameters in the range of 2~5 nm [30], which is far smaller than the size of 149.06 nm by CO chemisorption in this study. Meanwhile a similar Pd particle diameter of 145.95 nm was determined by CO chemisorption in the case of 25wt%Pd/*D. desulfuricans*, which is in clear conflict with the Electron Microscopy which shows large particles at high but not low metal loadings.

The 5-fold larger Pd particle diameter on 5wt%Pd/*E. coli* than that on 5wt%Pd/ Al_2O_3 appears to be contradictory with the observed better catalytic activity by 5wt%Pd/*E. coli* than that by 5wt%Pd/ Al_2O_3 in the 2-pentyne hydrogenation (see Figure 4.3 in §4.2). On the other hand in the TEM image for 5wt%Pd/*E. coli* in Figure 6.6 *c*, where the nanoparticulate-palladium has been visually confirmed (1.0~2.0 μm length for *E. coli* cell), one typical large metal cluster was estimated to be 14.1 nm and only a rare cluster exceeding a size of 64.51 nm was observed. By the CO chemisorption method, the even smaller Pd particle diameter of

25wt%Pd/*E. coli* (47.80 nm) than that of 5wt%Pd/*E. coli* (64.51 nm) furthermore implies that CO chemisorption is not a reliable technology to determine the active metal particle size on biomass, due, probably, to its high content of iron and also trace amounts of copper, manganese and zinc, for example, as components of enzymes.

Table 6.2 Summary of the characterisation data on different catalysts using different technologies.

Support	Metal loading	Surface area ^a m ² .g(metal) ⁻¹	Metal dispersion ^a	Metal particle size, nm			
	Pd, wt%		%	<i>d</i> ₁ ^a	<i>d</i> ₂ ^b	<i>d</i> ₃ ^c	<i>d</i> ₄ ^d
<i>Al</i> ₂ <i>O</i> ₃	2.0	57.85	12.98	8.63	-	-	
	5.0	39.32	8.82	12.77	-	-	
<i>D. desulfuricans</i>	5.0	3.35	0.75	149.06	4.71	-	2~5 [30]
	25.0	3.42	0.77	145.95	-	-	
<i>E. coli</i>	5.0	7.74	1.74	64.51	4.31	4.12	
	25.0	10.44	2.34	47.80	-	28.74	

^a *d*₁: Active particle diameter measured by CO chemisorption. At least triplicate analyses were repeated for each catalyst. Each catalyst sample was from one single preparation; ^b *d*₂: Average metal grain size estimated by TEM measurements and image analysis software Image J (details to follow in §6.4.2); ^c *d*₃: Crystallite size estimated by XRD technique (details to follow in §6.4.26.4.3). ^d Particle size value obtained from the literature.

The reason for the big difference between the active particle diameter by CO chemisorption report and average grain size by TEM image observation can also be explained by the methodology that the former technology applies to calculate the active particle diameter. The equation calculating the active particle diameter has been introduced in §3.6.2 (Equation 3-2), which shows the sorptive particle diameter to be proportional to the reciprocal of the CO volume adsorbed (*V*_s, cm³ at STP). Given that most Pd particles were enclosed beneath the cell outer membrane (see discussion in §6.3.2) at a low loading such as 5wt%Pd/*E. coli*, the actual amount of the palladium metal exposed at the surface layer is much less than the initial formulated palladium loading causing CO uptake in pulse chemisorption to be reduced due to the fewer active sites available. As a result, the calculated active particle diameter tends to be overestimated. However it is not known to what extent the CO penetrated throughout the

biomass. Cellular reactions involving molecular O₂ are all intracellular, as are some reactions involving H₂ while plant cells fix CO₂. It must be assumed, therefore, that the biomass surface is not a barrier to gas transport and that CO was able to permeate freely.

6.4.2 TEM Method

Based on the results presented in §6.3.2, TEM images were then processed using appropriate software (Image J) with the aim to estimate the average metal grain size for the bio-catalysts. Figure 6.9 presents the TEM images used for particle acquisition and the corresponding particle size distribution plots of two bio-Pd catalysts (5 wt%Pd on *D. desulfuricans* and *E. coli*). It is noted here TEM images of 5wt%Pd/*D. desulfuricans* (Figure 6.9 a-1 and a-2) were acquired from sectioned specimens made using the corresponding dried catalyst powder (one single batch), while those of 5wt%Pd/*E. coli* (Figure 6.9 b-1~b-4) were from sectioned specimens made using freshly metallised *E. coli* cells (two separate preparations). Details of cell wall structure are not seen from the former preparation (Figure 6.9 a), which however is sufficient to observe the discrete palladium NPs around the perimeter of the *D. desulfuricans* cells. For each catalyst at least 100 individual metal particles around the cell surface were examined, the corresponding mean grain sizes of these two bio-Pd catalysts are listed in Table 6.2.

By applying the TEM method, the palladium particle size on *D. desulfuricans* (5 wt%) is estimated to be an average of 4.71 nm, which is in good agreement with the diameter range of 2~5 nm reported by Creamer *et al.* [30]. The metal particle size of 5wt%Pd/*E. coli* was comparable at 4.31 nm. The nanoparticle size distribution on *E. coli* was narrow, with the majority of NPs within the size range 3~5nm while the nanoparticles on *D. desulfuricans* were more broadly distributed between 3~7 nm.

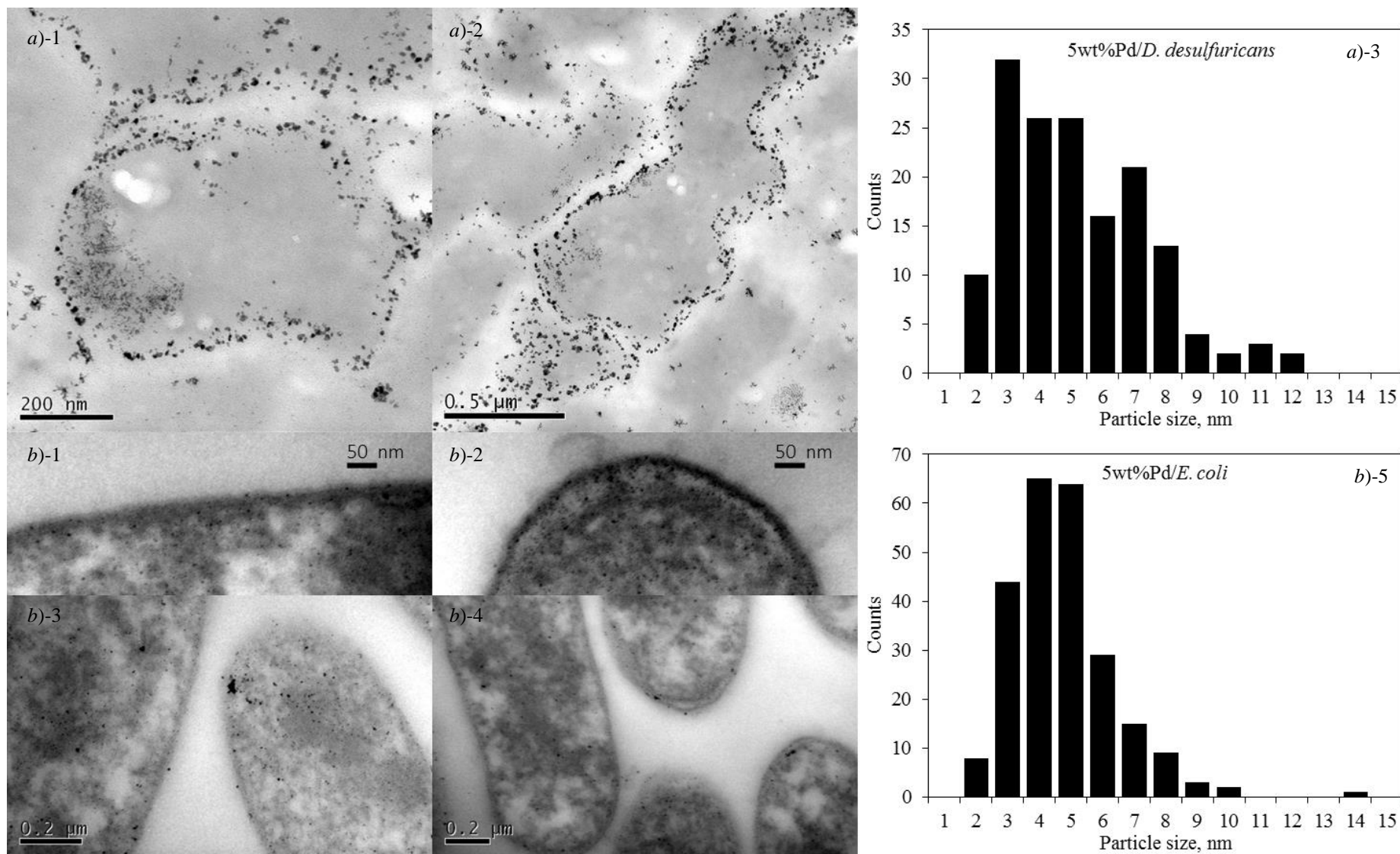


Figure 6.9 a) TEM images of ultra-thin sections made from the 5wt%Pd/*D. desulfuricans* catalyst powder, two images shown were used for the acquisition of particles representing two different areas from one single catalyst preparation, 155 surface particles were estimated with the inset particle size distribution; b) TEM images of ultra-thin sections made from two separate batches of freshly palladised 5wt%Pd/*E. coli* cells, sectioned specimen without osmium or uranyl acetate/lead citrate stain, four images shown represent four different areas, 240 surface particles were estimated with the inset particle size distribution.

6.4.3 X-ray Diffraction Technique

Firstly, the X-ray powder patterns of bio-Pd/*E. coli* catalysts with different palladium loadings (2 wt%Pd, 5 wt%Pd, and 25 wt%Pd) are shown in Figure 6.10 *a-c*, from which it was observed an enhancement of the peak signal in the order from 2 wt%Pd to 25 wt%Pd. No defined peaks were visible at a loading of 2 wt%Pd. When increasing the palladium loading to 5 wt%, broad peaks started to appear in the XRD pattern. At a palladium loading of 25 wt%, the XRD pattern showed intense sharp peaks matching the bulk Pd(0) found in the Crystallography Open Database (COD 96-900-8479) (indicated by the dashed lines). Since the peak width from XRD patterns varies inversely with crystallite size (*i.e.* as the crystallite size gets bigger, the peak gets sharper and narrower), Figure 6.10 *a-c* give a clear indication of particle growth from the palladium loading of 2wt%, 5wt% to 25wt%. The crystallite sizes of the cell-bound Pd(0) of 5 wt%Pd and 25 wt%Pd on *E. coli* cells were estimated using Scherrer's equation [269] to be 4.12 nm and 28.74nm. The former size is in a good agreement with the average particle size determined by the TEM method (Table 6.2).

Different bimetallic AuPd/*E. coli* catalysts (25wt%Au25wt%Pd, 2.5wt%Au2.5wt%Pd, 4wt%Au1wt%Pd, and 1wt%Au4wt%Pd) were also subjected to the same XRD analysis with X-ray diffraction patterns shown in Figure 6.10 *d-g*, in which the peaks representing gold were confirmed by matching those in the measured pattern with the bulk Au(0) found in the Crystallography Open Database (COD 96-900-8464) (indicated by the solid lines). The intensity of the peaks varied with the changes of the AuPd loading formulations, showing strong Au peaks accompanied by weak Pd peaks at a loading of 25wt%Au25wt%Pd, the main presences of the Au peaks being in the cases of 2.5wt%Au2.5wt%Pd and 4wt%Au1wt%Pd. Overall the broadest XRD peaks attributable to Au(0) were observed at a loading of 1wt%Au4wt%Pd.

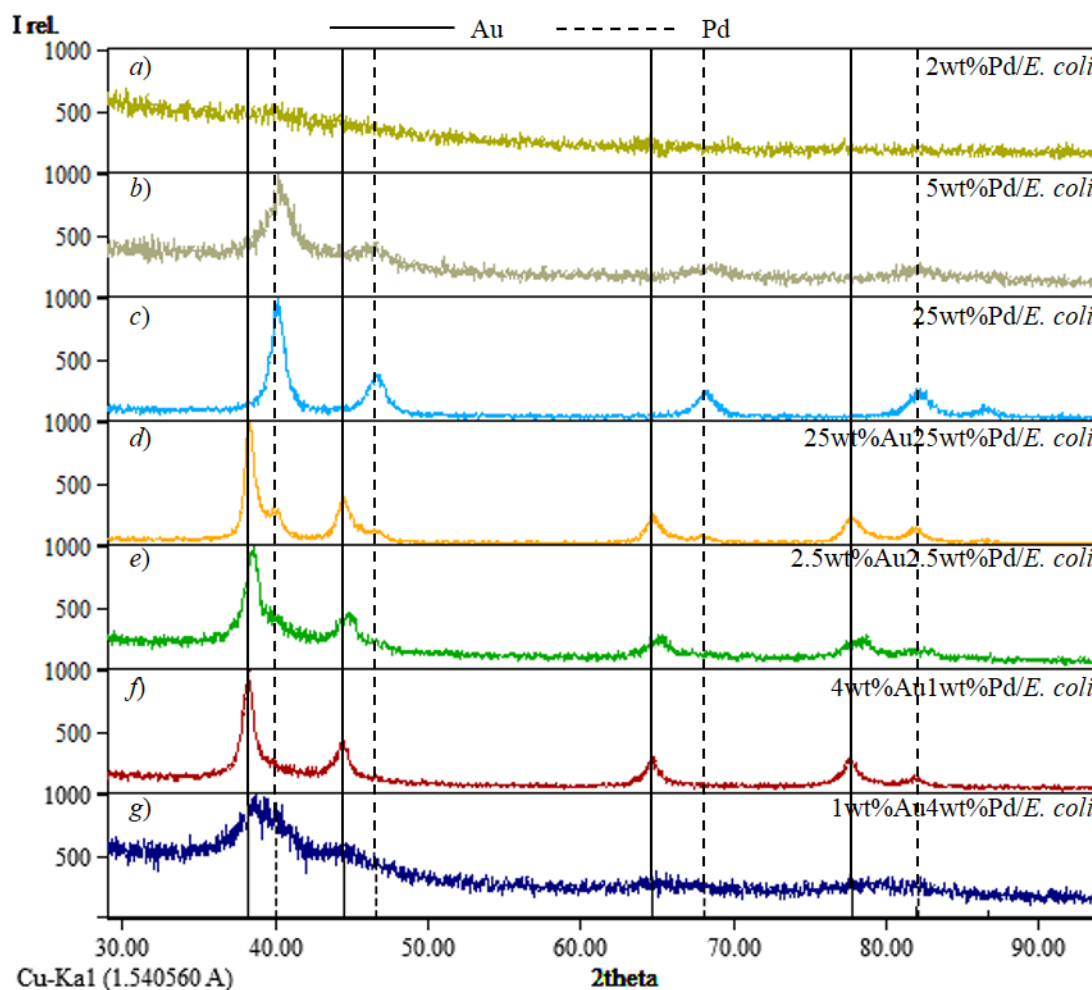


Figure 6.10 X-ray powder diffraction (XRD) analysis of monometallic Pd and bimetallic AuPd NPs formed by *E. coli*: a) 2wt%Pd/*E. coli*, b) 5wt%Pd/*E. coli*, c) 25wt%Pd/*E. coli*, d) 25wt%Au25wt%Pd/*E. coli*, e) 2.5wt%Au2.5wt%Pd/*E. coli*, f) 4wt%Au1wt%Pd/*E. coli*, and g) 1wt%Au4wt%Pd/*E. coli*. The pattern obtained experimentally matches the pattern found in the Crystallography Open Database (COD), COD-96-900-8479 for Pd(0) and COD-96-900-8464 for Au(0).

When comparing Figure 6.10 c with d, the loss of bulk Pd diffraction peaks was observed in the XRD spectrum after adding Au to 25wt%Pd/*E. coli* to form bimetallic 25wt%Au25wt%Pd/*E. coli* catalyst. This phenomenon was also observed in Figure 6.10 b for 5wt%Pd and Figure 6.10 g for 1wt%Au4wt%Pd, the disappearance of Pd peaks in the spectrum of the latter suggesting that just a small amount of Au (20% of the total metal mass) is sufficient to destroy the crystallinity of the Pd. The appearance of the intense Au peaks while weak Pd signals in the all bio-AuPd/*E. coli* preparations implies that most palladium in the bimetallic sample tended to form smaller particles than gold. This is explained by the migration of Pd from the pre-formed Pd(0) NPs and the subsequent formation of more

dispersed Pd atoms [161]. More specifically, the synthesis procedure involves a successive reduction of Pd(II) and Au(III) onto the bacteria cells, Pd(II) ions were firstly reduced enzymatically from a precursor using H₂ as an electron donor [177]. The resulting fine layer of Pd(0) seeds reduce the subsequent Au(III) to generate Pd(II) ions which then relocate around Au(0) NPs and are reduced to Pd(0) via H₂ on the Au-NP surface to produce a Au(core)-Pd(shell) configuration [161]. The above observation further suggests Au occupied the bulk sites with the absence of large, discrete Pd NPs in all cases.

6.5 Conclusions

In this chapter, characterisation work on the biomass-supported bio-Pd and bio-AuPd catalysts were presented and discussed. The ThermoGravimetric Analysis (TGA) revealed that different strains of bacteria could have unique thermal stability characteristics, by virtue of the specific proportion, structure or degree of polymerisation of the components within them. This is an important criterion to be considered for any catalytic application of biomass-supported catalyst in the reaction process design with respect to temperature. Within the strains examined in this study, *R. sphaeroides* gave a relatively lower level of thermal stability, and an upper temperature for utilisation is around 125 °C, beyond which the material will begin to degrade. The other bio-catalysts involved in the present catalytic testing show broadly similar thermal stabilities up to 175 °C. Given that some extra factors may accelerate the damage to bio-catalysts during application, such as the potential attrition caused by stirring in an agitated reactor, it is recommended that the actual reaction temperature for using bio-catalysts should not be close to its upper-use temperature determined by TGA analysis.

In terms of the examination of metal particle deposition on the bacteria, electron microscopy showed the Gram-negative bacteria to accommodate more evenly distributed and smaller metal particles in comparison with the Gram-positive bacteria. In order to estimate the metal particle size, CO chemisorption, TEM method, and XRD were employed. CO chemisorption was unsuitable for bio-derived materials. A good agreement was achieved on the average particle size of Pd by the TEM measurements and the crystallite size of Pd by XRD technology, giving the particle size of ~4 nm for the 5 wt%Pd on the strain of *E. coli*.

Chapter 7

Conclusions and Future Work Recommendations

7.1 Conclusions

A biological method was successfully applied to manufacture biomass-supported monometallic Pd or bimetallic AuPd nanoparticles with controllable particle size. Current work has demonstrated certain catalytic activities of bio-catalysts in three-phase hydrogenation and oxidation reactions, along with some of the key strengths and some weaknesses, which are listed as follows:

2-pentyne Hydrogenation Using Bio-Pd Catalysts

- Under optimum conditions (4 ml of 2-pentyne in 150 ml of isopropanol as solvent, catalyst loading of $0.375 \text{ mg(Pd).ml(2-pentyne)}^{-1}$, $T= 40 \text{ }^\circ\text{C}$, $p_{H_2} = 2 \text{ bar}$, $N= 1000 \text{ rpm}$) [270], complete hydrogenation of 2-pentyne was achieved within 40 mins using a 2wt%Pd/*E. coli* catalyst. The observed maximum yield of the major product *cis*-2-pentene was $18.1 \pm 0.4 \times 10^{-2} \text{ mol.l}^{-1}$ after ~30 mins, followed by its further isomerisation to *trans*-2-pentene or hydrogenation to pentane.
- The catalytic performance of bio-Pd/*E. coli* was compared with that of conventional Pd/ Al_2O_3 under identical operating conditions ($T= 40 \text{ }^\circ\text{C}$, $p_{H_2} = 2 \text{ bar}$, $N= 1000 \text{ rpm}$). The 2-pentyne consumption rate decreased in the order of catalysts: 5wt%Pd/*E. coli* > 2wt%Pd/ Al_2O_3 > 2wt%Pd/*E. coli* close to 5wt%Pd/ Al_2O_3 . At 100% conversion of 2-pentyne, bio-Pd/*E. coli* catalysts selectively produced higher amounts of *cis*-2-pentene and lower yields of *trans*-2-pentene than Pd/ Al_2O_3 catalysts at equal Pd loadings.

- A kinetic model of 2-pentyne hydrogenation was established based on the Langmuir-Hinshelwood type relationship and the *cis-trans* isomerisation following the Horiuti-Polanyi mechanism. The irreversible reaction of 2-pentyne to give *cis*-2-pentene is assumed to be the surface reaction control. All the model parameters were simultaneously estimated using a Solver function of MS Excel software, obtaining a good fit between the experimental and predicted concentration profiles.
- The model-estimated rate constants indicated a 7.6-fold faster hydrogenation of a carbon-carbon triple bond (C≡C) than that of a double bond (C=C) in 2-pentyne hydrogenation, being $22.3 \times 10^{-3} \text{ mol.g}^{-1}.\text{s}^{-1}$ and $2.9 \times 10^{-3} \text{ mol.g}^{-1}.\text{s}^{-1}$ respectively. The predicted adsorption coefficients were $28.48 \times 10^{-3} \text{ m}^3.\text{mol}^{-1}$ for 2-pentyne and $12.20 \times 10^{-3} \text{ m}^3.\text{mol}^{-1}$ for 2-pentene. This suggests a much stronger adsorption of alkyne compared to that of alkene on palladium active sites. In other words, the presence of 2-pentyne could prevent the re-adsorption of the product 2-pentene, which would be further hydrogenated to pentane or converted to its *trans*-isomer.

Soybean Oil Hydrogenation Using Pd/Al₂O₃ Catalyst

- Using 150 mg 5wt%Pd/Al₂O₃ catalyst in 150 ml soybean oil (solvent-free) at a temperature of 100 °C and hydrogen pressure of 5 bar with a stirring speed of 800 rpm, *cis*-C18:3 was completely depleted within 1.5 hours; *cis*-C18:2 showed a conversion of $96.80 \pm 1.31\%$ after 2 hours; the observed maximum yield of *cis*-C18:1 was $1.02 \pm 0.02 \text{ mol.l}^{-1}$ after ~1 hour.
- The minimum stirring speed (N_m) for complete particle suspension was found to be 279.0 rpm for a catalyst (5wt%Pd/Al₂O₃) loading of $0.001 \text{ g(catalyst).ml(oil)}^{-1}$ in the present Baskerville autoclave reactor at 100 °C.

- Mass transfer limitation studies revealed that the reaction was not mass transfer controlled with a stirring rate of 800 rpm and above (other conditions: 150 ml soybean oil solvent-free, catalyst loading of $0.05 \text{ mg(Pd).ml(oil)}^{-1}$, $T= 100 \text{ }^\circ\text{C}$, $p_{H_2} = 5 \text{ bar}$), thus a chemically-controlled regime is assured.
- A simplified mechanistic kinetic Model 1 (by lumping isomers of the same chemical formula as one product) was proposed based on a Langmuir-Hinshelwood type relation. Model 1 predicted the trends of trienic (C18:3), dienic (C18:2), monoenic (C18:1) and saturated (C18:0) fatty acids distribution closely as a function of the reaction time.
- In Model 2, a reversible *cis-trans* isomerisation was considered following the Horiuti-Polanyi mechanism and a good fit was obtained between the experimental and predicted concentration profiles. A hydrogen reaction order of 2.24 and rate constant of $3.09 \text{ mol.g}^{-1}.\text{h}^{-1}$ were predicted for the *cis*-isomer to react (forwards), and 0.11 and $1.68 \text{ mol.g}^{-1}.\text{h}^{-1}$ for the *trans*-isomer to react (backwards). The hydrogen order and rate constant for the hydrogenation of the carbon-carbon double bond (C=C) were estimated as 0.5 and $4.80 \text{ mol.g}^{-1}.\text{h}^{-1}$ respectively.
- The activation energy of soybean oil hydrogenation in the present system was found to be 37.8 kJ.mol^{-1} over a 5wt%Pd/ Al_2O_3 catalyst under 5 bar of hydrogen.

Soybean Oil Hydrogenation Using Bio-Pd Catalysts

- Under the same operating conditions (catalyst loading of $0.05 \text{ mg(Pd).ml(oil)}^{-1}$, solvent free, $T= 100 \text{ }^\circ\text{C}$, $p_{H_2} = 5 \text{ bar}$, $N= 800 \text{ rpm}$), soybean oil hydrogenation using 5wt%Pd/*E. coli* was slower than that using 5wt%Pd/ Al_2O_3 , achieving a *cis*-C18:2 conversion of ~45.52% after 5 hours and within 1 hour respectively.

- The lower catalytic activity of bio-Pd catalyst, compared with Pd/Al₂O₃, was attributed to a lower availability of palladium active sites. It is postulated that only those Pd particles that erupted onto the cell membrane through particle growth were able to contribute active sites for the reaction; Pd particles beneath the cell wall and occluded intracellular Pd depositions were clearly observed by TEM.
- Bio-Pd catalyst has the property of suppressing the formation of undesired *trans*-C18:1 and C18:0 at an equal production of *cis*-C18:1 compared with Pd/Al₂O₃. At a *cis*-C18:1 yield of 1.03±0.04 mol.l⁻¹, 5wt%Pd/*E. coli* produced *trans*-C18:1 of 0.26±0.03 mol.l⁻¹ and C18:0 of 0.19±0.00 mol.l⁻¹. In contrast, along with a maximum *cis*-C18:1 yield of 1.07±0.02 mol.l⁻¹, 5wt%Pd/Al₂O₃ gave *trans*-C18:1 of 0.52±0.02 mol.l⁻¹ and C18:0 of 0.34±0.06 mol.l⁻¹.
- The lower yield of *trans*-C18:1 and saturated C18:0 using bio-Pd catalyst, compared with Pd/Al₂O₃, can be attributed to the formed smaller palladium particle size on *E. coli*. TEM measurements revealed that a loading of 5 wt%Pd on *E. coli* gave an average Pd particle size of 4.31 nm, while a Pd crystallite size of 4.12 nm was estimated using Scherrer's equation from obtained X-ray powder diffraction data. An active particle diameter of 12.77 nm for 5wt%Pd/Al₂O₃ was determined by CO pulse chemisorption analysis.
- The decay of catalytic activity of 5wt%Pd/*E. coli* catalyst in soybean oil hydrogenation at 150 °C implied the possibility of catalyst deactivation. TGA analysis revealed the onset of 5wt%Pd/*E. coli* catalyst decomposition at ~175 °C. A stirring speed of 800 rpm in current reactor is suggested to cause potential attrition which further accelerates the damage to the bio-catalyst at an operating temperature close to its decomposition temperature.

- 5wt%Pd/*E. coli* showed a similar catalytic activity to 5wt%Pd/*D. desulfuricans* in soybean oil hydrogenation under the same conditions. The choice between using *E. coli* and *D. desulfuricans* for manufacturing bio-Pd is then governed by ease of biomass growth and economic considerations, which is easier and cheaper for *E. coli*.
- The conversion rates of both *cis*-C18:3 and *cis*-C18:2 were increased by ~30% by using formate-reduced 5wt%Pd/*E. coli* as compared to H₂-reduced 5wt%Pd/*E. coli* in soybean oil hydrogenation under the same conditions ($T= 100\text{ }^{\circ}\text{C}$, $p_{\text{H}_2} = 5\text{ bar}$, $N= 800\text{ rpm}$), with no difference shown in terms of the formation of *cis*-C18:1.

Bio-AuPd in Aerobic Oxidation of Benzyl Alcohol

- Under a dead-end operating mode using an original Parr autoclave, the reaction rate of benzyl alcohol oxidation using compressed air over a 2.5wt%Au2.5wt%Pd/*E. coli* catalyst was found to level off quickly attributed to limited oxygen availability ($m_{\text{catalyst}}= 25\text{ mg}$, $V_{\text{alcohol}}= 40\text{ ml}$, solvent-free, $T= 110\text{ }^{\circ}\text{C}$, $p_{\text{air}}= 5\text{ bar}$, $N= 1200\text{ rpm}$).
- Reactor modifications were established to supply the reaction system with a continuous air flow. In comparison with the original dead-end system, the modified flow-through system showed a higher benzyl alcohol consumption rate along with a higher selectivity to the desired product benzaldehyde.
- A portion of AuPd/*E. coli* catalyst was pre-reduced *ex-situ* under hydrogen at 393 K. Similar activities were observed in oxidation of benzyl alcohol under identical conditions ($m_{\text{catalyst}}= 7\text{ mg}$, $V_{\text{alcohol}}= 40\text{ ml}$, solvent-free, $T= 100\text{ }^{\circ}\text{C}$, $p_{\text{air}}= 5\text{ bar}$, $F_{\text{air}}= 100\text{ ml}\cdot\text{min}^{-1}$, $N= 1200\text{ rpm}$) over the *ex-situ* reduced and untreated AuPd/*E. coli*. This implied that bio-AuPd catalyst was well maintained in an active condition under the normal storage, as air-dried, ground material, with no need for re-activation prior to use.

- The reaction rate of benzyl alcohol oxidation over bio-AuPd catalyst was found to be zero order in oxygen when above a critical oxygen concentration, being independent of concentration and mass transfer rates. Within the set reaction of 7 hours in this study, reactions with 200 ml.min⁻¹ and 350 ml.min⁻¹ were not mass-transfer controlled. An average of 1423±20 turnovers per hour under the air flow rates above 200 ml.min⁻¹ was obtained.
- The amount of 2.5wt% Au2.5wt% Pd/*E. coli* catalyst should be below 100 mg to ensure the reaction being predominantly in the kinetic regime under the tested reaction conditions ($V_{alcohol}$ = 40 ml, solvent-free, T = 110 °C, p_{air} = 5 bar, F_{air} = 200 ml.min⁻¹, N = 1200 rpm).
- The activation energy was estimated as 71.8 kJ.mol⁻¹ for benzyl alcohol oxidation over a 2.5wt% Au2.5wt% Pd/*E. coli* catalyst under 5 bar of air.
- Comparing bio-2.5wt% Au2.5wt% Pd catalysts on different bacterial biomass (*Arthrobacter oxydans*, *Escherichia coli*, *Micrococcus luteus*, and *Rhodobacter sphaeroides*) in benzyl alcohol oxidation under the same reaction conditions, the Gram-negative bacteria (*R. sphaeroides*, *E. coli*) prepared bio-catalysts showed significantly higher catalytic activity than Gram-positive (*A. oxydans*, *M. luteus*) supported ones. The highest benzyl alcohol conversion after 7 hours was observed in the case of 2.5wt% Au2.5wt% Pd/*E. coli*, achieving 11.7±0.5% at a steady benzyl alcohol consumption rate of 0.16±0.01 mol.l⁻¹.hr⁻¹.
- 2.5wt% Au2.5wt% Pd/*R. sphaeroides* gave a higher alcohol consumption rate than 2.5wt% Au2.5wt% Pd/*E. coli* during the initial 2 hours, but the rate of the former gradually tailed off. This implied the potential deactivation of AuPd/*R. sphaeroides* catalyst (continuous 7 hours at 110 °C and high-speed mechanical stirring of 1200

rpm). The upper-use temperature of AuPd/*R. sphaeroides* catalyst should not exceed 125 °C (by TGA analysis) and its deactivation is suggested to be accelerated by the high-speed agitation at an operating temperature close to its decomposition temperature.

- Increasing the metal loading from 0.5wt% Au0.5wt%Pd, 1wt% Au1wt%Pd to 2.5wt% Au2.5wt%Pd on *E. coli* provides increased availability of active AuPd alloy on the cell surface though particle growth which, as a result, appears to be associated with the improved catalytic performance. Catalyst with a high loading of 25wt% Au25wt%Pd on *E. coli* was shown by TEM to have large metal clusters which gave a poor catalytic activity in benzyl alcohol oxidation (lower benzyl alcohol conversion and benzaldehyde selectivity).
- Altering the weight ratios to form 1wt% Au4wt%Pd, 2.5wt% Au2.5wt%Pd and 4wt% Au1wt%Pd on *E. coli*, the catalytic activity in benzyl alcohol oxidation was found in the order as: 4wt% Au1wt%Pd < 1wt% Au4wt%Pd < 2.5wt% Au2.5wt%Pd. XRD patterns suggested smaller crystallite sizes of Pd than Au, and the crystallinity of the Pd was destroyed by the addition of a small amount of Au (20% of the total metal mass).
- 2.5wt% Au2.5wt%Pd/*E. coli* demonstrated catalytic activities in the oxidation of other alcohols (*e.g.* 1-phenylethanol, 1-octanol, 2-octanol, and 1,4-butanediol), and was shown to be less active for the oxidation of secondary alcohols than primary alcohols.

7.2 Future Work Recommendations

This study has clearly demonstrated that biogenic metallic nanoparticles possess specific catalytic properties in both partial hydrogenation and aerobic oxidation reactions. Due to financial, equipment and time constraint, several experiments/analysis could not be performed in the scope of this work and hence are recommended as future work. They are as follows:

- Where the reaction and characterisation results have been produced by bio-catalyst from one single preparation, at least one more separate bio-catalyst preparation needs to be done and tested in the reaction to validate the reproducibility of bio-catalysts in a statistical manner. In the present study key results are shown using two independent preparations and percentage variations between them are stated.
- Bio-Pd/*E. coli* catalyst showed a lower level of *cis-trans* isomerisation and saturation than a conventional Pd/ Al_2O_3 catalyst in soybean oil hydrogenation attributed to the advantage of smaller Pd particles on *E. coli*, but a lower activity due to the limited availability of active sites. The palladium loading on bio-catalyst could carefully be altered (*e.g.* 8 wt%, 10 wt%, 15 wt%, or 20 wt%) with the aim to find a trade-off between *cis-trans* production and overall catalytic activity.
- Further modifications can be done to the oxidation reaction system for improvements, such as replacing the metering valve with mass flow controller for more accurate flow rate control. A probe to measure oxygen concentration in the liquid could be useful to monitor oxygen consumption thus to understand oxygen mass transfer during the oxidation reactions and obtain accurate concentrations for kinetic modelling studies.

- Based on the conversion rates obtained in preliminary oxidation experiments using different alcohols, further investigations into the catalytic behaviour of biogenic Au/Pd NPs should be explored in the oxidation of other alcohols.
- Further developments of the bio-catalysts will seek to improve the catalyst reproducibility, lifetime (*e.g.* stability against heating and mechanical attrition), and up-scaling of the production process. If these conditions are fulfilled, an economically feasible and effective full scale technology can be developed.
- Having established the utility of biogenic NPs the economic scaled-up production needs to be addressed. The utility of biorecycled Pd NPs in catalysis is shown in Appendix 8.5 and the utility of using bacteria sourced from another process in Appendix 8.2. Large quantities of waste bacteria are produced industrially and future studies would look to the study of pre-commercial strains used for example a primary protein or antibiotics production for utility for ‘second life’ in manufacturing catalytic nanoparticles.

Reference List

- [1] J.W. Geus and A. Dillen, Preparation of supported catalysts by deposition-precipitation, in: G. Ertl, H. Knozinger, F. Schuth, and J. Weitkamp (Eds.), *Handbook of Heterogeneous Catalysis*, (2008) 428-467.
- [2] J.W. Geus and A. Dillen, General considerations and types of catalyst, in: R.A. Sheldon and H.V. Bekkum (Eds.), *Fine Chemicals Through Heterogeneous Catalysis*, Wiley, (2001).
- [3] O. Deutschmann, H. Knozinger, K. Kochloefl, and T. Turek, *Heterogeneous Catalysis and Solid Catalysts*, Wiley-VCH, (2009).
- [4] B. Gutsche, H. Rößler, and S. Würkert, Heterogeneous catalysis in oleochemistry, in: G. Ertl, H. Knozinger, F. Schuth, and J. Weitkamp (Eds.), *Handbook of Heterogeneous Catalysis*, (2008) 3329-3359.
- [5] J. Booyens, C.C. Louwrens, and I.E. Katzeff, The role of unnatural dietary *trans* and *cis* unsaturated fatty-acids in the epidemiology of coronary-artery disease, *Medical Hypotheses*, 25 (1988) 175-182.
- [6] W.B. Rizzo, P.A. Watkins, M.W. Phillips, D. Cranin, B. Campbell, and J. Avigan, Oleic-acid lowers fibroblast saturated C22-26 fatty-acids, *Neurology*, 36 (1986) 357-361.
- [7] G.J. Hutchings, Nanocrystalline gold and gold palladium alloy catalysts for chemical synthesis, *Chemical Communications*, (2008) 1148-1164.
- [8] R.A. Sheldon, I. Arends, and U. Hanefeld, Catalytic oxidation, in: R.A. Sheldon, I. Arends, and U. Hanefeld (Eds.), *Green Chemistry and Catalysis*, Wiley-VCH, (2007) 133-222.
- [9] G. Gainelli and G. Gardillo, *Chromium oxidations in organic chemistry*, Springer, (1984).
- [10] U.R. Pillai and E. Sahle-Demessie, Oxidation of alcohols over Fe³⁺/montmorillonite-K10 using hydrogen peroxide, *Applied Catalysis A-General*, 245 (2003) 103-109.
- [11] B.A. Steinhoff, S.R. Fix, and S.S. Stahl, Mechanistic study of alcohol oxidation by the Pd(OAc)₂/O₂/DMSO catalyst system and implications for the development of improved aerobic oxidation catalysts, *J. Am. Chem. Soc.*, 124 (2002) 766-767.
- [12] G.J. Ten Brink, I.W.C.E. Arends, and R.A. Sheldon, Catalytic conversions in water. Part XXI: Mechanistic investigations on the palladium-catalysed aerobic oxidation of alcohols in water, *Advanced Synthesis & Catalysis*, 344 (2002) 355-369.
- [13] E. Santacesaria, P. Parrella, M.S. Diserio, and G. Borrelli, Role of mass-transfer and kinetics in the hydrogenation of rapeseed oil on a supported palladium catalyst, *Applied Catalysis A-General*, 116 (1994) 269-294.
- [14] C. Schuth and M. Reinhard, Hydrodechlorination and hydrogenation of aromatic compounds over palladium on alumina in hydrogen-saturated water, *Applied Catalysis B-Environmental*, 18 (1998) 215-221.
- [15] J. Cookson, The preparation of palladium nanoparticles, *Platinum Metals Review*, 56 (2012) 83-98.
- [16] C. Parmeggiani and F. Cardona, Transition metal based catalysts in the aerobic oxidation of alcohols, *Green Chemistry*, 14 (2012) 547-564.
- [17] H. Hori, T. Teranishi, Y. Nakae, Y. Seino, M. Miyake, and S. Yamada, Anomalous magnetic polarisation effect of Pd and Au nano-particles, *Physics Letters A*, 263 (1999) 406-410.
- [18] P. Mulvaney, L.M. Liz-Marzan, M. Giersig, and T. Ung, Silica encapsulation of quantum dots and metal clusters, *J. Mater. Chem.*, 10 (2000) 1259-1270.

- [19] T. Taniyama, T. Sato, E. Ohta, and M. Takeda, Intraparticle structure of Pd fine particles, *Physica B*, 213 (1995) 254-256.
- [20] J.R. Lloyd, P. Yong, and L.E. Macaskie, Enzymatic recovery of elemental palladium by using sulfate-reducing bacteria, *Applied and Environmental Microbiology*, 64 (1998) 4607-4609.
- [21] N.J. Creamer, K. Deplanche, T.J. Snape, I.P. Mikheenko, P. Yong, D. Samyahumbi, J. Wood, K. Pollmann, S. Selenska-Pobell, and L.E. Macaskie, A biogenic catalyst for hydrogenation, reduction and selective dehalogenation in non-aqueous solvents, *Hydrometallurgy*, 94 (2008) 138-143.
- [22] I.P. Mikheenko. Nanoscale palladium recovery, The University of Birmingham, Thesis, (2004).
- [23] K. Deplanche. New nanocatalysts made by bacteria from metal solutions and recycling of metal wastes, The University of Birmingham, Thesis, (2008).
- [24] J.A. Bennett, N.J. Creamer, K. Deplanche, L.E. Macaskie, I.J. Shannon, and J. Wood, Palladium supported on bacterial biomass as a novel heterogeneous catalyst: A comparison of Pd/Al₂O₃ and bio-Pd in the hydrogenation of 2-pentyne, *Chemical Engineering Science*, 65 (2010) 282-290.
- [25] J.A. Bennett, I.P. Mikheenko, K. Deplanche, I.J. Shannon, J. Wood, and L.E. Macaskie, Nanoparticles of palladium supported on bacterial biomass: New re-usable heterogeneous catalyst with comparable activity to homogeneous colloidal Pd in the Heck reaction, *Applied Catalysis B-Environmental*, 140 (2013) 700-707.
- [26] P. Yong, N.A. Rowson, J.P.G. Farr, I.R. Harris, and L.E. Macaskie, Bioreduction and biocrystallisation of palladium by *Desulfovibrio desulfuricans* NCIMB 8307, *Biotechnology and Bioengineering*, 80 (2002) 369-379.
- [27] V. Baxter-Plant, I.P. Mikheenko, and L.E. Macaskie, Sulphate-reducing bacteria, palladium and the reductive dehalogenation of chlorinated aromatic compounds, *Biodegradation*, 14 (2003) 83-90.
- [28] A.N. Mabbett, P. Yong, J.P.G. Farr, and L.E. Macaskie, Reduction of Cr(VI) by 'palladised' - biomass of *Desulfovibrio desulfuricans* ATCC 29577, *Biotechnology and Bioengineering*, 87 (2004) 104-109.
- [29] A.N. Mabbett, D. Sanyahumbi, P. Yong, and L.E. Macaskie, Biorecovered precious metals from industrial wastes: Single-step conversion of a mixed metal liquid waste to a bioinorganic catalyst with environmental application, *Environmental Science & Technology*, 40 (2006) 1015-1021.
- [30] N.J. Creamer, I.P. Mikheenko, P. Yong, K. Deplanche, D. Sanyahumbi, J. Wood, K. Pollmann, M. Merroun, S. Selenska-Pobell, and L.E. Macaskie, Novel supported Pd hydrogenation bionanocatalyst for hybrid homogeneous/heterogeneous catalysis, *Catalysis Today*, 128 (2007) 80-87.
- [31] K. Deplanche, J.A. Bennett, I.P. Mikheenko, J. Omajali, A.S. Wells, R.E. Meadows, J. Wood, and L.E. Macaskie, Catalytic activity of biomass-supported Pd nanoparticles: Influence of the biological component in catalytic efficacy and potential application in 'green' synthesis of fine chemicals and pharmaceuticals, *Applied Catalysis B: Environmental*, 147 (2014) 651-665.
- [32] F.L. Bernardis, R.A. Grant, and D.C. Sherrington, A review of methods of separation of the platinum-group metals through their chloro-complexes, *Reactive & Functional Polymers*, 65 (2005) 205-217.
- [33] L.B. Hunt and F.M. Liver, Availability of the platinum metals: A survey of productive resources in relation to industrial uses, *Platinum Metals Review*, 13 (1969) 126-138.
- [34] Z. Xiao and A.R. Laplante, Characterising and recovering the platinum group minerals: A review, *Minerals Engineering*, 17 (2004) 961-979.

- [35] A. Cowley. Platinum 2013 interim review: Johnson Matthey's latest market review of supply and demand for the platinum group metals, Johnson Matthey, (2013).
- [36] D. McDonald and L.B. Hunt, The growth of industrial catalysis with the platinum metals: A history of platinum and its allied metals, The Priory Press, (1982) 385-402.
- [37] T.B. Flanagan and W.A. Oates, The palladium-hydrogen system, Annual Review of Materials Science, 21 (1991) 269-304.
- [38] T. Graham, On the occlusion of hydrogen gas by metals, Proceedings of the Royal Society of London, 16 (1867) 422-427.
- [39] Palladium hydride, Online Source from Wikipedia, 29-4-2013.
- [40] R. Wolf and C. Mansour. The amazing metal sponge, Projects in Scientific Computing, Pittsburgh Supercomputing Center, (1995).
- [41] S. Horinouchi, Y. Yamanoi, T. Yonezawa, T. Mouri, and H. Nishihara, Hydrogen storage properties of isocyanide-stabilized palladium nanoparticles, Langmuir, 22 (2006) 1880-1884.
- [42] M. Yamauchi, R. Ikeda, H. Kitagawa, and M. Takata, Nanosize effects on hydrogen storage in palladium, Journal of Physical Chemistry C, 112 (2008) 3294-3299.
- [43] S. Mubeen, T. Zhang, B. Yoo, M.A. Deshusses, and N.V. Myung, Palladium nanoparticles decorated single-walled carbon nanotube hydrogen sensor, Journal of Physical Chemistry C, 111 (2007) 6321-6327.
- [44] P. Tobiska, O. Hugon, A. Trouillet, and H. Gagnaire, An integrated optic hydrogen sensor based on SPR on palladium, Sensors and Actuators B-Chemical, 74 (2001) 168-172.
- [45] H.J. Chen, G. Wei, A. Ispas, S.G. Hickey, and A. Eychmuller, Synthesis of palladium nanoparticles and their applications for surface-enhanced Raman Scattering and electrocatalysis, Journal of Physical Chemistry C, 114 (2010) 21976-21981.
- [46] D. McDonald and L.B. Hunt, The discovery and early history of catalysis: A History of Platinum and its Allied Metals, The Priory Press, (1982) 219-234.
- [47] S. De-Corte, T. Hennebel, B. De-Gusseme, W. Verstraete, and N. Boon, Bio-palladium: From metal recovery to catalytic applications, Microbial Biotechnology, 5 (2012) 5-17.
- [48] A. Moores and F. Goettmann, The plasmon band in noble metal nanoparticles: An introduction to theory and applications, New J. Chem., 30 (2006) 1121-1132.
- [49] W. Eberhardt, Clusters as new materials, Surface Science, 500 (2002) 242-270.
- [50] S.V. Vonsovskii, Magnetism, Wiley, (1974).
- [51] T. Taniyama, E. Ohta, and T. Sato, Ferromagnetism of Pd fine particles, Physica B, 237 (1997) 286-288.
- [52] T. Taniyama, E. Ohta, and T. Sato, Observation of 4d ferromagnetism in free-standing Pd fine particles, Europhysics Letters, 38 (1997) 195-200.
- [53] D. Mendoza, F. Morales, R. Escudero, and J. Walter, Magnetisation studies in *quasi* two-dimensional palladium nanoparticles encapsulated in a graphite host, Journal of Physics-Condensed Matter, 11 (1999) L317-L322.
- [54] S.H. Overbury, P.A. Bertrand, and G.A. Somorjai, Surface composition of binary-systems: Prediction of surface phase-diagrams of solid-solutions, Chem. Rev., 75 (1975) 547-560.
- [55] T.V. Choudhary and D.W. Goodman, Oxidation catalysis by supported gold nano-clusters, Topics in Catalysis, 21 (2002) 25-34.
- [56] E.M. Holt, G.J. Kelly, and F. King, Catalyst design and manufacture, in: J.M. Winterbottom and M.B. King (Eds.), Reactor Design for Chemical Engineers, Stanley Thornes, (1999) 276-300.

- [57] E. Marceau, X. Carrier, M. Che, O. Clause, and C. Marcilly, Ion exchange and impregnation, in: G. Ertl, H. Knozinger, F. Schuth, and J. Weitkamp (Eds.), *Handbook of Heterogeneous Catalysis*, (2008) 467-484.
- [58] Z.P. Qu, W.X. Huang, S.T. Zhou, H. Zheng, X.M. Liu, M.J. Cheng, and X.H. Bao, Enhancement of the catalytic performance of supported-metal catalysts by pretreatment of the support, *Journal of Catalysis*, 234 (2005) 33-36.
- [59] Catalyst support. Online Source fom Wikipedia, 18-7-2013.
- [60] J.M. Winterbottom and M.B. King, *Reactor design for chemical engineers*, Stanley Thornes, (1999).
- [61] S.T. Gulati, Ceramic catalyst supports for gasoline fuel, in: A. Cybulski and J.A. Moulijn (Eds.), *Structured Catalysts and Reactors*, CRC Press, (2005) 21-66.
- [62] B. Nohair, C. Especel, G. Lafaye, P. Marecot, L.C. Hoang, and J. Barbier, Palladium supported catalysts for the selective hydrogenation of sunflower oil, *Journal of Molecular Catalysis A-Chemical*, 229 (2005) 117-126.
- [63] M.B. Fernandez, J.F. Sanchez, G.M. Tonetto, and D.E. Damiani, Hydrogenation of sunflower oil over different palladium supported catalysts: Activity and selectivity, *Chemical Engineering Journal*, 155 (2009) 941-949.
- [64] N. Marin-Astorga, G. Pecchi, J.L.G. Fierro, and P. Reyes, Alkynes hydrogenation over Pd-supported catalysts, *Catalysis Letters*, 91 (2003) 115-121.
- [65] D.I. Enache, J.K. Edwards, P. Landon, B. Solsona-Espriu, A.F. Carley, A.A. Herzing, M. Watanabe, C.J. Kiely, D.W. Knight, and G.J. Hutchings, Solvent-free oxidation of primary alcohols to aldehydes using Au-Pd/TiO₂ catalysts, *Science*, 311 (2006) 362-365.
- [66] S. Meenakshisundaram, E. Nowicka, P.J. Miedzak, G.L. Brett, R.L. Jenkins, N. Dimitratos, S.H. Taylor, D.W. Knight, D. Bethell, and G.J. Hutchings, Oxidation of alcohols using supported gold and gold-palladium nanoparticles, *Faraday Discuss*, 145 (2010) 341-356.
- [67] H.J. Freund, J. Libuda, M. Baumer, T. Risse, and A. Carlsson, Cluster, facets, and edges: Site-dependent selective chemistry on model catalysts, *Chemical Record*, 3 (2003) 181-200.
- [68] E. Auer, A. Freund, J. Pietsch, and T. Tacke, Carbons as supports for industrial precious metal catalysts, *Applied Catalysis A-General*, 173 (1998) 259-271.
- [69] X.Z. Jiang, S.J. Yang, and S.H. Wu, Supported Palladium Catalysts: a comparison of solvated metal atom impregnated and conventionally prepared catalysts, *Platinum Metals Rev*, 37 (1993) 72-75.
- [70] P. Gallezot, Selective oxidation with air on metal catalysts, *Catalysis Today*, 37 (1997) 405-418.
- [71] L. Prati, A. Villa, C. Campione, and P. Spontoni, Effect of gold addition on Pt and Pd catalysts in liquid phase oxidations, *Topics in Catalysis*, 44 (2007) 319-324.
- [72] K. Sasaki, M. Shao, and R. Adzic, Dissolution and stabilisation of platinum in oxygen cathodes, in: F.N. Büchi, M. Inaba, and T.J. Schmidt (Eds.), *Polymer Electrolyte Fuel Cell Durability*, Springer, (2009) 7-27.
- [73] G.R. Bamwenda, S. Tsubota, T. Nakamura, and M. Haruta, The influence of the preparation methods on the catalytic activity of platinum and gold supported on TiO₂ for CO oxidation, *Catalysis Letters*, 44 (1997) 83-87.
- [74] C.H. Bartholomew and R.J. Farrauto, *Fundamentals of Industrial Catalytic Processes*, (2005).
- [75] J. Haber, *Manual on catalyst characterisation*, *Pure and Applied Chemistry*, 63 (1991) 1227-1246.

- [76] B. Delmon, Reactions during catalyst activation, in: G. Ertl, H. Knozinger, F. Schuth, and J. Weitkamp (Eds.), *Handbook of Heterogeneous Catalysis*, (2008) 655-676.
- [77] G.J. Hutchings, Heterogeneous catalysts: Discovery and design, *J. Mater. Chem.*, 19 (2009) 1222-1235.
- [78] J.K. Edwards, B.E. Solsona, P. Landon, A.F. Carley, A. Herzing, C.J. Kiely, and G.J. Hutchings, Direct synthesis of hydrogen peroxide from H₂ and O₂ using TiO₂-supported Au-Pd catalysts, *Journal of Catalysis*, 236 (2005) 69-79.
- [79] H. Mounzer. Heterogeneous oxidation of alcohols. The University of Birmingham, Thesis, (2009).
- [80] G.A. Martin, C. Mirodatos, and H. Praliaud, Chemistry of silica-supported catalysts: Preparation, activation and reduction, *Applied Catalysis*, 1 (1981) 367-382.
- [81] B. Delmon, P. Grange, P.A. Jacobs, and G. Poncelet, Preparation of catalysts II, (1977) 81.
- [82] A.M. Ruppert and B.M. Weckhuysen, Active phase-support interactions, in: H. Knozinger, F. Schuth, and J. Weitkamp (Eds.), *Handbook of Heterogeneous Catalysis*, (2008) 1178-1188.
- [83] H. Praliaud and G.A. Martin, Evidence of a strong metal-support interaction and of Ni-Si alloy formation in silica-supported nickel-catalysts, *Journal of Catalysis*, 72 (1981) 394-396.
- [84] R. Frety, L. Tournayan, M. Primet, G. Bergeret, M. Guenin, J.B. Baumgartner, and A. Borgna, Influence of the reduction temperature on the properties of silica-supported nickel-catalysts, *Journal of the Chemical Society-Faraday Transactions*, 89 (1993) 3313-3318.
- [85] P. Miedziak, M. Sankar, N. Dimitratos, J.A. Lopez-Sanchez, A.F. Carley, D.W. Knight, S.H. Taylor, C.J. Kiely, and G.J. Hutchings, Oxidation of benzyl alcohol using supported gold-palladium nanoparticles, *Catalysis Today*, 164 (2011) 315-319.
- [86] Y.G. Sun and Y.N. Xia, Shape-controlled synthesis of gold and silver nanoparticles, *Science*, 298 (2002) 2176-2179.
- [87] J.E. Millstone, S. Park, K.L. Shuford, L.D. Qin, G.C. Schatz, and C.A. Mirkin, Observation of a quadrupole plasmon mode for a colloidal solution of gold nanoprisms, *J. Am. Chem. Soc.*, 127 (2005) 5312-5313.
- [88] Y.J. Xiong and Y.N. Xia, Shape-controlled synthesis of metal nanostructures: The case of palladium, *Advanced Materials*, 19 (2007) 3385-3391.
- [89] B. Lim, M.J. Jiang, J. Tao, P.H.C. Camargo, Y.M. Zhu, and Y.N. Xia, Shape-controlled synthesis of Pd nanocrystals in aqueous solutions, *Advanced Functional Materials*, 19 (2009) 189-200.
- [90] W.Y. Yu, M.H. Liu, H.F. Liu, and J.M. Zheng, Preparation of polymer-stabilised noble metal colloids, *Journal of Colloid and Interface Science*, 210 (1999) 218-221.
- [91] D. Berger, G.A. Traistaru, B.S. Vasile, I. Jitaru, and C. Matei, Palladium nanoparticles synthesis with controlled morphology obtained by polyol method, *U.P.B. Sci. Bull*, 72 (2010) 113-120.
- [92] N.R. Jana, L. Gearheart, and C.J. Murphy, Seeding growth for size control of 5-40 nm diameter gold nanoparticles, *Langmuir*, 17 (2001) 6782-6786.
- [93] L.H. Lu, H.S. Wang, S.Q. Xi, and H.J. Zhang, Improved size control of large palladium nanoparticles by a seeding growth method, *J. Mater. Chem.*, 12 (2002) 156-158.
- [94] W.X. Niu, Z.Y. Li, L.H. Shi, X.Q. Liu, H.J. Li, S. Han, J. Chen, and G.B. Xu, Seed-mediated growth of nearly monodisperse palladium nanocubes with controllable sizes, *Crystal Growth & Design*, 8 (2008) 4440-4444.

- [95] C.J. Murphy, T.K. San, A.M. Gole, C.J. Orendorff, J.X. Gao, L. Gou, S.E. Hunyadi, and T. Li, Anisotropic metal nanoparticles: Synthesis, assembly, and optical applications, *Journal of Physical Chemistry B*, 109 (2005) 13857-13870.
- [96] C.J. Murphy and N.R. Jana, Controlling the aspect ratio of inorganic nanorods and nanowires, *Advanced Materials*, 14 (2002) 80-82.
- [97] Y.H. Chen, H.H. Hung, and M.H. Huang, Seed-mediated synthesis of palladium nanorods and branched nanocrystals and their use as recyclable Suzuki Coupling reaction catalysts, *J. Am. Chem. Soc.*, 131 (2009) 9114-9121.
- [98] D.M. Ledwith, A.M. Whelan, and J.M. Kelly, A rapid, straight-forward method for controlling the morphology of stable silver nanoparticles, *J. Mater. Chem.*, 17 (2007) 2459-2464.
- [99] L. Lu, A. Kobayashi, K. Tawa, and Y. Ozaki, Silver nanoplates with special shapes: Controlled synthesis and their surface plasmon resonance and surface-enhanced Raman scattering properties, *Chemistry of Materials*, 18 (2006) 4894-4901.
- [100] S.E. Habas, H. Lee, V. Radmilovic, G.A. Somorjai, and P. Yang, Shaping binary metal nanocrystals through epitaxial seeded growth, *Nature Materials*, 6 (2007) 692-697.
- [101] F.R. Fan, D.Y. Liu, Y.F. Wu, S. Duan, Z.X. Xie, Z.Y. Jiang, and Z.Q. Tian, Epitaxial growth of heterogeneous metal nanocrystals: From gold nano-octahedra to palladium and silver nanocubes, *J. Am. Chem. Soc.*, 130 (2008) 6949-6951.
- [102] T. Hennebel, B. De Gussemé, N. Boon, and W. Verstraete, Biogenic metals in advanced water treatment, *Trends in Biotechnology*, 27 (2009) 90-98.
- [103] S.E. Davis, M.S. Ide, and R.J. Davis, Selective oxidation of alcohols and aldehydes over supported metal nanoparticles, *Green Chemistry*, 15 (2013) 17-45.
- [104] S.T. Sie, Consequences of catalyst deactivation for process design and operation, *Applied Catalysis A-General*, 212 (2001) 129-151.
- [105] J.A. Moulijn, A.E. Diepen, and F. Kapteijn, Deactivation and regeneration, in: G. Ertl, H. Knozinger, F. Schuth, and J. Weitkamp (Eds.), *Handbook of Heterogeneous Catalysis*, (2008) 1-18.
- [106] P. Dufresne, Hydroprocessing catalysts regeneration and recycling, *Applied Catalysis A-General*, 322 (2007) 67-75.
- [107] C.H. Bartholomew, Mechanisms of catalyst deactivation, *Applied Catalysis A-General*, 212 (2001) 17-60.
- [108] A.P. Markusse, B.F.M. Kuster, and J.C. Schouten, Platinum catalysed aqueous methyl alpha-D-glucopyranoside oxidation in a multiphase redox-cycle reactor, *Catalysis Today*, 66 (2001) 191-197.
- [109] M. Guisnet and F.R. Ribeiro, Deactivation and regeneration of solid catalysts, in: M. Guisnet and F.R. Ribeiro (Eds.), *Deactivation and Regeneration of Zeolite Catalysts*, Imperial College Press, 9 (2011) 3-17.
- [110] R.A. Sheldon and J. Dakka, Heterogeneous catalytic oxidations in the manufacture of fine chemicals, *Catalysis Today*, 19 (1994) 215-245.
- [111] T. Mallat and A. Baiker, Oxidation of alcohols with molecular-oxygen on platinum metal-catalysts in aqueous-solutions, *Catalysis Today*, 19 (1994) 247-283.
- [112] J.D. Grunwaldt, C. Keresszegi, T. Mallat, and A. Baiker, *In situ* EXAFS study of Pd/Al₂O₃ during aerobic oxidation of cinnamyl alcohol in an organic solvent, *Journal of Catalysis*, 213 (2003) 291-295.

- [113] C. Keresszegi, J.D. Grunwaldt, T. Mallat, and A. Baiker, *In situ* EXAFS study on the oxidation state of Pd/Al₂O₃ and Bi-Pd/Al₂O₃ during the liquid-phase oxidation of 1-phenylethanol, *Journal of Catalysis*, 222 (2004) 268-280.
- [114] Z. Gogova and J. Hanika, Reactivation of a palladium catalyst during glucose oxidation by molecular oxygen, *Chemical Papers*, 63 (2009) 520-526.
- [115] H.E. Van Dam, A.P.G. Kieboom, and H. Van Bekkum, Pt/C oxidation catalysts, Part I: Effect of carrier structure on catalyst deactivation during the oxidation of glucose 1-phosphate into glucuronic acid 1-phosphate, *Applied Catalysis*, 33 (1987) 361-372.
- [116] H.E. Van Dam, P. Duijverman, A.P.G. Kieboom, and H. Van Bekkum, Pt/C oxidation catalysts, Part II: Oxidation of glucose 1-phosphate into glucuronic acid 1-phosphate using diffusion stabilised catalysts, *Applied Catalysis*, 33 (1987) 373-382.
- [117] V.R. Gangwal, J. van-der Schaaf, B.F.M. Kuster, and J.C. Schouten, Influence of pH on noble metal catalysed alcohol oxidation: Reaction kinetics and modelling, *Journal of Catalysis*, 229 (2005) 389-403.
- [118] V.R. Gangwal, B.G.M. van Wachem, B.F.M. Kuster, and J.C. Schouten, Platinum catalysed aqueous alcohol oxidation: Model-based investigation of reaction conditions and catalyst design, *Chemical Engineering Science*, 57 (2002) 5051-5063.
- [119] C. Hardacre, E.A. Mullan, D.W. Rooney, and J.M. Thompson, Use of a rotating disc reactor to investigate the heterogeneously catalysed oxidation of cinnamyl alcohol in toluene and ionic liquids, *Journal of Catalysis*, 232 (2005) 355-365.
- [120] B. Fillion, B.I. Morsi, K.R. Heier, and R.M. Machado, Kinetics, gas-liquid mass transfer, and modeling of the soybean oil hydrogenation process, *Industrial & Engineering Chemistry Research*, 41 (2002) 697-709.
- [121] T. Mallat and A. Baiker, Oxidation of alcohols with molecular oxygen on solid catalysts, *Chem. Rev.*, 104 (2004) 3037-3058.
- [122] A.A. Herzing, A.F. Carley, J.K. Edwards, G.J. Hutchings, and C.J. Kiely, Microstructural development and catalytic performance of Au-Pd nanoparticles on Al₂O₃ supports: The effect of heat treatment temperature and atmosphere, *Chemistry of Materials*, 20 (2008) 1492-1501.
- [123] C.H. Bartholomew, Sintering kinetics of supported metals: Perspectives from a generalised power-law approach, *Catalyst Deactivation 1994*, 88 (1994) 1-18.
- [124] J.Y. Shin, B.S. Lee, Y. Jung, S.J. Kim, and S.G. Lee, Palladium nanoparticles captured onto spherical silica particles using a urea cross-linked imidazolium molecular band, *Chemical Communications*, (2007) 5238-5240.
- [125] N. Dimitratos, A. Villa, D. Wang, F. Porta, D.S. Su, and L. Prati, Pd and Pt catalysts modified by alloying with Au in the selective oxidation of alcohols, *Journal of Catalysis*, 244 (2006) 113-121.
- [126] A. Villa, D. Wang, N. Dimitratos, D.S. Su, V. Trevisan, and L. Prati, Pd on carbon nanotubes for liquid phase alcohol oxidation, *Catalysis Today*, 150 (2010) 8-15.
- [127] G.J. Hutchings, Promotion in heterogeneous catalysis: A topic requiring a new approach? *Catalysis Letters*, 75 (2001) 1-12.
- [128] B.E. Koel and J. Kim, Promoters and poisons, in: G. Ertl, H. Knozinger, F. Schuth, and J. Weitkamp (Eds.), *Handbook of Heterogeneous Catalysis*, (2008) 1593-1624.
- [129] J.A. Rodriguez, Bimetallic model catalysts, in: G. Ertl, H. Knozinger, F. Schuth, and J. Weitkamp (Eds.), *Handbook of Heterogeneous Catalysis*, (2008) 1298-1309.
- [130] N. Dimitratos, A. Villa, D. Wang, F. Porta, D.S. Su, and L. Prati, Pd and Pt catalysts modified by alloying with Au in the selective oxidation of alcohols, *Journal of Catalysis*, 244 (2006) 113-121.

- [131] R. Ferrando, J. Jellinek, and R.L. Johnston, Nanoalloys: From theory to applications of alloy clusters and nanoparticles, *Chem. Rev.*, 108 (2008) 845-910.
- [132] N. Toshima and T. Yonezawa, Bimetallic nanoparticles-novel materials for chemical and physical applications, *New J. Chem.*, 22 (1998) 1179-1201.
- [133] W.X. Zhang, C.B. Wang, and H.L. Lien, Treatment of chlorinated organic contaminants with nanoscale bimetallic particles, *Catalysis Today*, 40 (1998) 387-395.
- [134] E.M. Crabb and R. Marshall, Properties of alumina supported Pd-Fe and Pt-Fe catalysts prepared using surface organometallic chemistry, *Applied Catalysis A-General*, 217 (2001) 41-53.
- [135] V.K. Tzitzios and V. Georgakilas, Catalytic reduction of N₂O over Ag-Pd/Al₂O₃ bimetallic catalysts, *Chemosphere*, 59 (2005) 887-891.
- [136] R. Massard, D. Uzio, C. Thomazeau, C. Pichon, J.L. Rousset, and J.C. Bertolini, Strained Pd overlayers on Ni nanoparticles supported on alumina and catalytic activity for buta-1,3-diene selective hydrogenation, *Journal of Catalysis*, 245 (2007) 133-143.
- [137] S.J. Kim, S.D. Oh, S. Lee, and S.H. Choi, Radiolytic synthesis of Pd-M (M= Ag, Ni, and Cu)/C catalyst and their use in Suzuki-type and Heck-type reaction, *Journal of Industrial and Engineering Chemistry*, 14 (2008) 449-456.
- [138] P.A. Sermon, G.C. Bond, and P.B. Wells, Hydrogenation of alkenes over supported gold, *Journal of the Chemical Society-Faraday Transactions I*, 75 (1979) 385-394.
- [139] M. Haruta, T. Kobayashi, H. Sano, and N. Yamada, Novel gold catalysts for the oxidation of carbon-monoxide at a temperature far below 0 °C, *Chemistry Letters*, (1987) 405-408.
- [140] M. Haruta, N. Yamada, T. Kobayashi, and S. Iijima, Gold catalysts prepared by coprecipitation for low-temperature oxidation of hydrogen and of carbon-monoxide, *Journal of Catalysis*, 115 (1989) 301-309.
- [141] G.J. Hutchings, Vapor-phase hydrochlorination of acetylene: Correlation of catalytic activity of supported metal chloride catalysts, *Journal of Catalysis*, 96 (1985) 292-295.
- [142] A.S.K. Hashmi and G.J. Hutchings, Gold catalysis, *Angewandte Chemie-International Edition*, 45 (2006) 7896-7936.
- [143] P. Landon, J. Ferguson, B.E. Solsona, T. Garcia, A.F. Carley, A.A. Herzing, C.J. Kiely, S.E. Golunski, and G.J. Hutchings, Selective oxidation of CO in the presence of H₂, H₂O and CO₂ via gold for use in fuel cells, *Chemical Communications*, (2005) 3385-3387.
- [144] A. Abad, P. Concepcion, A. Corma, and H. Garcia, A collaborative effect between gold and a support induces the selective oxidation of alcohols, *Angewandte Chemie-International Edition*, 44 (2005) 4066-4069.
- [145] A.K. Sinha, S. Seelan, S. Tsubota, and M. Haruta, A three-dimensional mesoporous titanasilicate support for gold nanoparticles: Vapor-phase epoxidation of propene with high conversion, *Angewandte Chemie-International Edition*, 43 (2004) 1546-1548.
- [146] M.D. Hughes, Y.J. Xu, P. Jenkins, P. McMorn, P. Landon, D.I. Enache, A.F. Carley, G.A. Attard, G.J. Hutchings, F. King, E.H. Stitt, P. Johnston, K. Griffin, and C.J. Kiely, Tunable gold catalysts for selective hydrocarbon oxidation under mild conditions, *Nature*, 437 (2005) 1132-1135.
- [147] J.M. Campelo, T.D. Conesa, M.J. Gracia, M.J. Jurado, R. Luque, J.M. Marinas, and A.A. Romero, Microwave facile preparation of highly active and dispersed SBA-12 supported metal nanoparticles, *Green Chemistry*, 10 (2008) 853-858.
- [148] M. Turner, V.B. Golovko, O.P.H. Vaughan, P. Abdulkin, A. Berenguer-Murcia, M.S. Tikhov, B.F.G. Johnson, and R.M. Lambert, Selective oxidation with dioxygen by gold nanoparticle catalysts derived from 55-atom clusters, *Nature*, 454 (2008) 981-U31.

- [149] J.E. Bailie and G.J. Hutchings, Promotion by sulfur of gold catalysts for crotyl alcohol formation from crotonaldehyde hydrogenation, *Chemical Communications*, (1999) 2151-2152.
- [150] Y. Segura, N. Lopez, and J. Perez-Ramirez, Origin of the superior hydrogenation selectivity of gold nanoparticles in alkyne plus alkene mixtures: Triple- versus double-bond activation, *Journal of Catalysis*, 247 (2007) 383-386.
- [151] A. Corma, C. Gonzalez-Arellano, M. Iglesias, and F. Sanchez, Gold nanoparticles and gold(III) complexes as general and selective hydrosilylation catalysts, *Angewandte Chemie-International Edition*, 46 (2007) 7820-7822.
- [152] A. Corma and P. Serna, Chemoselective hydrogenation of nitro compounds with supported gold catalysts, *Science*, 313 (2006) 332-334.
- [153] H.Y. Zhang, Y. Xie, Z.Y. Sun, R.T. Tao, C.L. Huang, Y.F. Zhao, and Z.M. Liu, *In situ* loading ultrafine AuPd Particles on ceria: Highly active catalyst for solvent-free selective oxidation of benzyl alcohol, *Langmuir*, 27 (2011) 1152-1157.
- [154] J.A. Lopez-Sanchez, N. Dimitratos, P. Miedziak, E. Ntainjua, J.K. Edwards, D. Morgan, A.F. Carley, R. Tiruvalam, C.J. Kiely, and G.J. Hutchings, Au-Pd supported nanocrystals prepared by a *sol* immobilisation technique as catalysts for selective chemical synthesis, *Physical Chemistry Chemical Physics*, 10 (2008) 1921-1930.
- [155] B.E. Solsona, J.K. Edwards, P. Landon, A.F. Carley, A. Herzing, C.J. Kiely, and G.J. Hutchings, Direct synthesis of hydrogen peroxide from H₂ and O₂ using Al₂O₃ supported Au-Pd catalysts, *Chemistry of Materials*, 18 (2006) 2689-2695.
- [156] P. Landon, P.J. Collier, A.F. Carley, D. Chadwick, A.J. Papworth, A. Burrows, C.J. Kiely, and G.J. Hutchings, Direct synthesis of hydrogen peroxide from H₂ and O₂ using Pd and Au catalysts, *Physical Chemistry Chemical Physics*, 5 (2003) 1917-1923.
- [157] J.K. Edwards, B. Solsona, P. Landon, A.F. Carley, A. Herzing, M. Watanabe, C.J. Kiely, and G.J. Hutchings, Direct synthesis of hydrogen peroxide from H₂ and O₂ using Au-Pd/Fe₂O₃ catalysts, *J. Mater. Chem.*, 15 (2005) 4595-4600.
- [158] H. Nitani, M. Yuya, T. Ono, T. Nakagawa, S. Seino, K. Okitsu, Y. Mizukoshi, S. Emura, and T.A. Yamamoto, Sonochemically synthesised core-shell structured Au-Pd nanoparticles supported on α -Fe₂O₃ particles, *Journal of Nanoparticle Research*, 8 (2006) 951-958.
- [159] A.M. Venezia, L.F. Liotta, G. Pantaleo, V. La Parola, G. Deganello, A. Beck, Z. Koppány, K. Frey, D. Horvath, and L. Gucci, Activity of SiO₂ supported gold-palladium catalysts in CO oxidation, *Applied Catalysis A-General*, 251 (2003) 359-368.
- [160] D.T. Tran, I.P. Jones, J.A. Preece, R.L. Johnston, K. Deplanche, and L.E. Macaskie, Configuration of microbially synthesised Pd-Au nanoparticles studied by STEM-based techniques, *Nanotechnology*, 23 (2012).
- [161] K. Deplanche, M.L. Merroun, M. Casadesus, D.T. Tran, I.P. Mikheenko, J.A. Bennett, J. Zhu, I.P. Jones, G.A. Attard, J. Wood, S. Selenska-Pobell, and L.E. Macaskie, Microbial synthesis of core/shell gold/palladium nanoparticles for applications in green chemistry, *Journal of the Royal Society Interface*, 9 (2012) 1705-1712.
- [162] L.O. Paz-Borbon, R.L. Johnston, G. Barcaro, and A. Fortunelli, Structural motifs, mixing, and segregation effects in 38-atom binary clusters, *Journal of Chemical Physics*, 128 (2008).
- [163] F. Pittaway, L.O. Paz-Borbón, R.L. Johnston, H. Arslan, R. Ferrando, C. Mottet, G. Barcaro, and A. Fortunelli, Theoretical studies of palladium-gold nanoclusters: Pd-Au clusters with up to 50 atoms, *J. Phys. Chem. C*, 113 (2009) 9141-9152.
- [164] M.O. Nutt, J.B. Hughes, and M.S. Wong, Designing Pd-on-Au bimetallic nanoparticle catalysts for trichloroethene hydrodechlorination, *Environmental Science & Technology*, 39 (2005) 1346-1353.

- [165] B.E. Solsona, J.K. Edwards, P. Landon, A.F. Carley, A. Herzing, C.J. Kiely, and G.J. Hutchings, Direct synthesis of hydrogen peroxide from H₂ and O₂ using Al₂O₃ supported Au-Pd catalysts, *Chemistry of Materials*, 18 (2006) 2689-2695.
- [166] M.S. Chen, D. Kumar, C.W. Yi, and D.W. Goodman, The promotional effect of gold in catalysis by palladium-gold, *Science*, 310 (2005) 291-293.
- [167] L. Prati, A. Villa, F. Porta, D. Wang, and D.S. Su, Single-phase gold/palladium catalyst: The nature of synergistic effect, *Catalysis Today*, 122 (2007) 386-390.
- [168] Y.L. Lam, J. Criado, and M. Boudart, Enhancement by inactive gold of rate of H₂-O₂ reaction on active palladium: Ligand effect, *Nouveau Journal de Chimie-New Journal of Chemistry*, 1 (1977) 461-466.
- [169] D.L. Weissman-Wenocur and W.E. Spicer, Comparison between the catalytic activities of Pd(111) and Pd-Au(111) for water synthesis, *Surface Science*, 133 (1983) 499-515.
- [170] K. Deplanche, I.P. Mikheenko, J.A. Bennett, M. Merroun, H. Mounzer, J. Wood, and L.E. Macaskie, Selective oxidation of benzyl-alcohol over biomass-supported Au/Pd bioinorganic catalysts, *Topics in Catalysis*, 54 (2011) 1110-1114.
- [171] W. De Windt, P. Aelterman, and W. Verstraete, Bioreductive deposition of palladium(0) nanoparticles on *Shewanella oneidensis* with catalytic activity towards reductive dechlorination of polychlorinated biphenyls, *Environmental Microbiology*, 7 (2005) 314-325.
- [172] K.G. Todar. Online source from The New Microbial World, (2013).
- [173] U.B. Sleytr, H. Bayley, M. Sara, A. Breitwieser, S. Kupcu, C. Mader, S. Weigert, F.M. Unger, P. Messner, B. JahnSchmid, B. Schuster, D. Pum, K. Douglas, N.A. Clark, J.T. Moore, T.A. Wittingham, S. Levy, I. Frithsen, J. Pankovc, P. Beale, H.P. Gillis, D.A. Choutov, and K.P. Martin, Applications of S-layers, *Fems Microbiology Reviews*, 20 (1997) 151-175.
- [174] T.J. Beveridge, Structures of Gram-negative cell walls and their derived membrane vesicles, *Journal of Bacteriology*, 181 (1999) 4725-4733.
- [175] P. Demchick and A.L. Koch, The permeability of the wall fabric of *Escherichia coli* and *Bacillus subtilis*, *Journal of Bacteriology*, 178 (1996) 768-773.
- [176] M.D. Redwood, K. Deplanche, V.S. Baxter-Plant, and L.E. Macaskie, Biomass-supported palladium catalysts on *Desulfovibrio desulfuricans* and *Rhodobacter sphaeroides*, *Biotechnology and Bioengineering*, 99 (2008) 1045-1054.
- [177] K. Deplanche, I. Caldelari, I.P. Mikheenko, F. Sargent, and L.E. Macaskie, Involvement of hydrogenases in the formation of highly catalytic Pd(0) nanoparticles by bioreduction of Pd(II) using *Escherichia coli* mutant strains, *Microbiology-Sgm*, 156 (2010) 2630-2640.
- [178] T. Hennebel, S. Van Nevel, S. Verschuere, S. De Corte, B. De Gusseme, C. Cuvelier, J.P. Fitts, D. van der Lelie, N. Boon, and W. Verstraete, Palladium nanoparticles produced by fermentatively cultivated bacteria as catalyst for diatrizoate removal with biogenic hydrogen, *Applied Microbiology and Biotechnology*, 91 (2011) 1435-1445.
- [179] Difference on the cell wall structure between the Gram-positive and Gram-negative bacteria. Online source, The McGraw-Hill Companies, (2013).
- [180] I. De Vargas, D. Sanyahumbi, M.A. Ashworth, C.M. Hardy, and L.E. Macaskie, Use of X-ray photoelectron spectroscopy to elucidate the mechanism of palladium and platinum biosorption by *Desulfovibrio desulfuricans* biomass, 16th International Biohydrometallurgy Symposium, (2005) 605-616.
- [181] I.P. Mikheenko, M. Rousset, S. Dementin, and L.E. Macaskie, Bioaccumulation of palladium by *Desulfovibrio fructosivorans* wild-type and hydrogenase-deficient strains, *Applied and Environmental Microbiology*, 74 (2008) 6144-6146.

- [182] S. Harrad, M. Robson, S. Hazrati, V.S. Baxter-Plant, K. Deplanche, M.D. Redwood, and L.E. Macaskie, Dehalogenation of polychlorinated biphenyls and polybrominated diphenyl ethers using a hybrid bioinorganic catalyst, *Journal of Environmental Monitoring*, 9 (2007) 314-318.
- [183] P. Yong, M. Paterson-Beedle, I.P. Mikheenko, and L.E. Macaskie, From bio-mineralisation to fuel cells: Biomanufacture of Pt and Pd nanocrystals for fuel cell electrode catalyst, *Biotechnology Letters*, 29 (2007) 539-544.
- [184] K. Deplanche, T.J. Snape, S. Hazrati, S. Harrad, and L.E. Macaskie, Versatility of a new bioinorganic catalyst: Palladised cells of *Desulfovibrio desulfuricans* and application to dehalogenation of flame retardant materials, *Environmental Technology*, 30 (2009) 681-692.
- [185] A.C. Humphries, K.P. Nott, L.D. Hall, and L.E. Macaskie, Continuous removal of Cr(VI) from aqueous solution catalysed by palladised biomass of *Desulfovibrio vulgaris*, *Biotechnology Letters*, 26 (2004) 1529-1532.
- [186] S. De Corte, T. Hennebel, J.P. Fitts, T. Sabbe, V. Biznuk, S. Verschuere, D. van der Lelie, W. Verstraete, and N. Boon, Biosupported bimetallic Pd-Au nanocatalysts for dechlorination of environmental contaminants, *Environmental Science & Technology*, 45 (2011) 8506-8513.
- [187] S. De Corte, T. Sabbe, T. Hennebel, L. Vanhaecke, B. De Gussemme, W. Verstraete, and N. Boon, Doping of biogenic Pd catalysts with Au enables dechlorination of diclofenac at environmental conditions, *Water Research*, 46 (2012) 2718-2726.
- [188] T.S.A. Heugebaert, S. De Corte, T. Sabbe, T. Hennebel, W. Verstraete, N. Boon, and C.V. Stevens, Biodeposited Pd/Au bimetallic nanoparticles as novel Suzuki catalysts, *Tetrahedron Letters*, 53 (2012) 1410-1412.
- [189] B. Hosseinkhani, L.S. Sobjerg, A.E. Rotaru, G. Emtiazi, T. Skrydstrup, and R.L. Meyer, Microbially supported synthesis of catalytically active bimetallic Pd-Au nanoparticles, *Biotechnology and Bioengineering*, 109 (2012) 45-52.
- [190] M.O. Nutt, K.N. Heck, P. Alvarez, and M.S. Wong, Improved Pd-on-Au bimetallic nanoparticle catalysts for aqueous-phase trichloroethene hydrodechlorination, *Applied Catalysis B-Environmental*, 69 (2006) 115-125.
- [191] N.J. Creamer, V.S. Baxter-Plant, J. Henderson, M. Potter, and L.E. Macaskie, Palladium and gold removal and recovery from precious metal solutions and electronic scrap leachates by *Desulfovibrio desulfuricans*, *Biotechnology Letters*, 28 (2006) 1475-1484.
- [192] K. Deplanche and L.E. Macaskie, Biorecovery of gold by *Escherichia coli* and *Desulfovibrio desulfuricans*, *Biotechnology and Bioengineering*, 99 (2008) 1055-1064.
- [193] R.L. Jack, A. Dubini, T. Palmer, and F. Sargent, Common principles in the biosynthesis of diverse enzymes, *Biochemical Society Transactions*, 33 (2005) 105-107.
- [194] F. Sargent, N.R. Stanley, B.C. Berks, and T. Palmer, Sec-independent protein translocation in *Escherichia coli*: A distinct and pivotal role for the TatB protein, *Journal of Biological Chemistry*, 274 (1999) 36073-36082.
- [195] J.R. Lloyd, C.L. Harding, and L.E. Macaskie, Tc(VII) reduction and accumulation by immobilised cells of *Escherichia coli*, *Biotechnology and Bioengineering*, 55 (1997) 505-510.
- [196] J.R. Lloyd, G.H. Thomas, J.A. Finlay, J.A. Cole, and L.E. Macaskie, Microbial reduction of technetium by *Escherichia coli* and *Desulfovibrio desulfuricans*: Enhancement via the use of high-activity strains and effect of process parameters, *Biotechnology and Bioengineering*, 66 (1999) 122-130.
- [197] P.A. Gravil and H. Toulhoat, Hydrogen, sulphur and chlorine coadsorption on Pd(111): A theoretical study of poisoning and promotion, *Surface Science*, 430 (1999) 176-191.
- [198] D.R. Alfonso, A.V. Cugini, and D.S. Sholl, Density functional theory studies of sulfur binding on Pd, Cu and Ag and their alloys, *Surface Science*, 546 (2003) 12-26.

- [199] N. Semagina, A. Renken, and L. Kiwi-Minsker, Palladium nanoparticle size effect in 1-hexyne selective hydrogenation, *Journal of Physical Chemistry C*, 111 (2007) 13933-13937.
- [200] O.M. Wilson, M.R. Knecht, J.C. Garcia-Martinez, and R.M. Crooks, Effect of Pd nanoparticle size on the catalytic hydrogenation of allyl alcohol, *J. Am. Chem. Soc.*, 128 (2006) 4510-4511.
- [201] N. Dimitratos, F. Porta, and L. Prati, Au, Pd (mono and bimetallic) catalysts supported on graphite using the immobilisation method: Synthesis and catalytic testing for liquid phase oxidation of glycerol, *Applied Catalysis A-General*, 291 (2005) 210-214.
- [202] Z. Hou, N. Theyssen, A. Brinkmann, and W. Leitner, Biphasic aerobic oxidation of alcohols catalysed by poly(ethylene glycol)-stabilised palladium nanoparticles in supercritical carbon dioxide, *Angewandte Chemie-International Edition*, 44 (2005) 1346-1349.
- [203] G.H. Jonker. Hydrogenation of edible oils and fats, Thesis, University of Groningen, The Netherlands, (1999).
- [204] Y.H. Hui, *Bailey's industrial oil and fat products*, Wiley-Interscience, (1996).
- [205] E. Bernardini, *Vegetable oils and fats processing*, Interstampa, (1982).
- [206] P.A. Ramachandran and R.V. Chaudhari, *Three-phase catalytic reactors*, Gordon and Breach Science Publishers, (1983).
- [207] D.R. Erickson, E.H. Pryde, O.L. Brekke, T.L. Mounts, and R.A. Falb, *Handbook of soy oil processing and utilisation*, American Soybean Association and the American Oil Chemists' Society, (1980).
- [208] B. Fillion and B.I. Morsi, Gas-liquid mass-transfer and hydrodynamic parameters in a soybean oil hydrogenation process under industrial conditions, *Industrial & Engineering Chemistry Research*, 39 (2000) 2157-2168.
- [209] I.A. Brouwer, A.J. Wanders, and M.B. Katan, Effect of animal and industrial *trans* fatty acids on HDL and LDL cholesterol levels in humans: A quantitative review, *Plos One*, 5 (2010).
- [210] L. Hooper, C.D. Summerbell, R. Thompson, D. Sills, F.G. Roberts, H. Moore, and G.D. Smith, Reduced or modified dietary fat for preventing cardiovascular disease, *Cochrane Database of Systematic Reviews*, (2011).
- [211] W.A. Cordova and P. Harriott, Mass-transfer resistances in palladium-catalysed hydrogenation of methyl linoleate, *Chemical Engineering Science*, 30 (1975) 1201-1206.
- [212] K. Tsuto, P. Harriott, and K.B. Bischoff, Intraparticle mass-transfer effects and selectivity in palladium-catalysed hydrogenation of methyl linoleate, *Industrial & Engineering Chemistry Fundamentals*, 17 (1978) 199-205.
- [213] J. Horiuti and M. Polanyi, Exchange reactions of hydrogen on metallic catalysts, *Transactions of the Faraday Society*, 30 (1934) 1164-1172.
- [214] R.O. Feuge, Hydrogenation of glyceride oils, in: P.H. Emmett (Ed.), *Catalysis III: Hydrogenation and Dehydrogenation*, Reinhold Publishing Corporation, (1955) 413-451.
- [215] P. van der Plank and H.J. van Oosten, Study of the mechanism of double-bond isomerisation in methyl 9-octadecenoates, *Journal of Catalysis*, 38 (1975) 223-230.
- [216] I. Heertje, G.K. Koch, and W.J. Wosten, Mechanism of heterogeneous catalytic *cis-trans* isomerisation and double-bond migration of octadecenoates, *Journal of Catalysis*, 32 (1974) 337-342.
- [217] W.F. Hoelderich, Environmentally benign manufacturing of fine and intermediate chemicals, *Catalysis Today*, 62 (2000) 115-130.
- [218] R. Sheldon and H.V. Bekkum, Introduction, in: R. Sheldon and H.V. Bekkum (Eds.), *Fine Chemicals through Heterogeneous Catalysis*, Wiley-VCH, (2001) 1-12.

- [219] V.R. Gangwal. Platinum catalysed alcohol oxidation: Kinetics, reaction engineering, and process design, Thesis, Technische Universiteit Eindhoven, (2005).
- [220] K. Mori, T. Hara, T. Mizugaki, K. Ebitani, and K. Kaneda, Hydroxyapatite-supported palladium nanoclusters: A highly active heterogeneous catalyst for selective oxidation of alcohols by use of molecular oxygen, *J. Am. Chem. Soc.*, 126 (2004) 10657-10666.
- [221] J. Chen, Q.H. Zhang, Y. Wang, and H.L. Wan, Size-dependent catalytic activity of supported palladium nanoparticles for aerobic oxidation of alcohols, *Advanced Synthesis & Catalysis*, 350 (2008) 453-464.
- [222] F. Porta, L. Prati, M. Rossi, S. Coluccia, and G. Martra, Metal sols as a useful tool for heterogeneous gold catalyst preparation: Reinvestigation of a liquid phase oxidation, *Catalysis Today*, 61 (2000) 165-172.
- [223] L. Prati and M. Rossi, Gold on carbon as a new catalyst for selective liquid phase oxidation of diols, *Journal of Catalysis*, 176 (1998) 552-560.
- [224] L. Prati and G. Martra, New gold catalysts for liquid phase oxidation, *Gold Bulletin*, 32 (1999) 96-101.
- [225] G.C. Bond and D.T. Thompson, Catalysis by gold, *Catalysis Reviews-Science and Engineering*, 41 (1999) 319-388.
- [226] H.F. Guo, A. Al-Hunaiti, M. Kemell, S. Rautiainen, M. Leskela, and T. Repo, Gold catalysis outside nanoscale: Bulk gold catalyses the aerobic oxidation of π -activated alcohols, *Chemcatchem*, 3 (2011) 1872-1875.
- [227] W.H. Fang, J.S. Chen, Q.H. Zhang, W.P. Deng, and Y. Wang, Hydrotalcite-supported gold catalyst for the oxidant-free dehydrogenation of benzyl alcohol: Studies on support and gold size effects, *Chemistry-A European Journal*, 17 (2011) 1247-1256.
- [228] D.I. Enache, D.W. Knight, and G.J. Hutchings, Solvent-free oxidation of primary alcohols to aldehydes using supported gold catalysts, *Catalysis Letters*, 103 (2005) 43-52.
- [229] A. Villa, C.E. Chan-Thaw, G.M. Veith, K.L. More, D. Ferri, and L. Prati, Au on nanosized NiO: A cooperative effect between Au and nanosized NiO in the base-free alcohol oxidation, *Chemcatchem*, 3 (2011) 1612-1618.
- [230] I.V. Delidovich, O.P. Taran, L.G. Matvienko, A.N. Simonov, I.L. Simakova, A.N. Bobrovskaya, and V.N. Parmon, Selective oxidation of glucose over carbon-supported Pd and Pt catalysts, *Catalysis Letters*, 140 (2010) 14-21.
- [231] D.I. Enache, J.K. Edwards, P. Landon, B. Solsona-Espriu, A.F. Carley, A.A. Herzing, M. Watanabe, C.J. Kiely, D.W. Knight, and G.J. Hutchings, Solvent-free oxidation of primary alcohols to aldehydes using Au-Pd/TiO₂ catalysts, *Science*, 311 (2006) 362-365.
- [232] K. Yamaguchi and N. Mizuno, Scope, kinetics, and mechanistic aspects of aerobic oxidations catalysed by ruthenium supported on alumina, *Chemistry-A European Journal*, 9 (2003) 4353-4361.
- [233] M. Besson and P. Gallezot, Selective oxidation of alcohols and aldehydes on metal catalysts, *Catalysis Today*, 57 (2000) 127-141.
- [234] C. Keresszegi, T. Burgi, T. Mallat, and A. Baiker, On the role of oxygen in the liquid-phase aerobic oxidation of alcohols on palladium, *Journal of Catalysis*, 211 (2002) 244-251.
- [235] J.H.J. Kluytmans, A.P. Markusse, B.F.M. Kuster, G.B. Marin, and J.C. Schouten, Engineering aspects of the aqueous noble metal catalysed alcohol oxidation, *Catalysis Today*, 57 (2000) 143-155.
- [236] V.R. Gangwal, J. van der Schaaf, B.F.M. Kuster, and J.C. Schouten, Catalyst performance for noble metal catalysed alcohol oxidation: Reaction-engineering modelling and experiments, *Catalysis Today*, 96 (2004) 223-234.

- [237] B.N. Zope, D.D. Hibbitts, M. Neurock, and R.J. Davis, Reactivity of the gold/water interface during selective oxidation catalysis, *Science*, 330 (2010) 74-78.
- [238] S.E. Davis, B.N. Zope, and R.J. Davis, On the mechanism of selective oxidation of 5-hydroxymethylfurfural to 2,5-furandicarboxylic acid over supported Pt and Au catalysts, *Green Chemistry*, 14 (2012) 143-147.
- [239] S. Mori, M. Takubo, K. Makida, T. Yanase, S. Aoyagi, T. Maegawa, Y. Monguchi, and H. Sajiki, A simple and efficient oxidation of alcohols with ruthenium on carbon, *Chemical Communications*, (2009) 5159-5161.
- [240] X.M. Yang, X.N. Wang, and J.S. Qiu, Aerobic oxidation of alcohols over carbon nanotube-supported Ru catalysts assembled at the interfaces of emulsion droplets, *Applied Catalysis A-General*, 382 (2010) 131-137.
- [241] K. Yamaguchi and N. Mizuno, Scope, kinetics, and mechanistic aspects of aerobic oxidations catalysed by ruthenium supported on alumina, *Chemistry-A European Journal*, 9 (2003) 4353-4361.
- [242] R.A. Sheldon and J.K. Kochi, *Metal-catalysed oxidations of organic compounds*, Academic Press, (1981).
- [243] G. An, H. Ahn, K.A. De Castro, and H. Rhee, Pd/C and NaBH₄ in basic aqueous alcohol: An efficient system for an environmentally benign oxidation of alcohols, *Synthesis-Stuttgart*, (2010) 477-485.
- [244] A.E. Diepen and J.A. Moulijn, Reactors, in: R.A. Sheldon and H.V. Bakkum (Eds.), *Fine Chemicals through Heterogeneous Catalysis*, Wiley-VCH, (2001) 45-60.
- [245] F. Kapteijn and J.A. Moulijn, Laboratory catalytic reactors: Aspects of catalyst testing, in: G. Ertl, H. Knozinger, F. Schuth, and J. Weitkamp (Eds.), *Handbook of Heterogeneous Catalysis*, Wiley-VCH (2008) 2019-2045.
- [246] T.N. Zwietering, Suspending of solid particles in liquid by agitators, *Chemical Engineering Science*, 8 (1958) 244-253.
- [247] A.W. Neinow, Suspension of solid particles in turbine agitated baffled vessels, *Chemical Engineering Science*, 23 (1968) 1453-1459.
- [248] A.W. Nienow, Agitated vessel particle-liquid mass-transfer: A comparison between theories and data, *The Chemical Engineering Journal*, 9 (1975) 153-160.
- [249] M.B. Fernandez, G.M. Tonetto, G.H. Crapiste, and D.E. Damiani, Revisiting the hydrogenation of sunflower oil over a Ni catalyst, *Journal of Food Engineering*, 82 (2007) 199-208.
- [250] Y. Kawase, T. Araki, K. Shimizu, and H. Miura, Gas-liquid mass transfer in three-phase stirred tank reactors: Newtonian and non-Newtonian fluids, *Canadian Journal of Chemical Engineering*, 75 (1997) 1159-1164.
- [251] R.V. Chaudhari, R.V. Gholap, G. Emig, and H. Hofmann, Gas-liquid mass-transfer in dead-end autoclave reactors, *Canadian Journal of Chemical Engineering*, 65 (1987) 744-751.
- [252] H. Yagi and F. Yoshida, Gas absorption by Newtonian and non-Newtonian fluids in sparged agitated vessels, *Industrial & Engineering Chemistry Process Design and Development*, 14 (1975) 488-493.
- [253] D.N. Miller, Scale-up of agitated vessels gas-liquid mass-transfer, *AIChE Journal*, 20 (1974) 445-453.
- [254] P.H. Calderbank and M.B. MooYoung, The continuous phase heat and mass-transfer properties of dispersions, *Chemical Engineering Science*, 16 (1961) 39-54.
- [255] H.S. Fogler, *Elements of chemical reaction engineering*, Prentice Hall, (2005).

- [256] K.B. Kushalkar and V.G. Pangarkar, Particle-liquid mass-transfer in 3-phase mechanically agitated contactors, *Industrial & Engineering Chemistry Research*, 33 (1994) 1817-1820.
- [257] P.M. Armenante and D.J. Kirwan, Mass-transfer to microparticles in agitated systems, *Chemical Engineering Science*, 44 (1989) 2781-2796.
- [258] D.M. Levins and Glastonb.J.R., Application of Kolmogoroff's theory to particle-liquid mass-transfer in agitated vessels, *Chemical Engineering Science*, 27 (1972) 537-542.
- [259] M.A. Gutierrezortiz, A. Castano, M.P. Gonzalezmarcos, J.I. Gutierrezortiz, and J.R. Gonzalezvelasco, Influence of operational variables on the catalytic behaviour of Pt/alumina in the slurry-phase hydrogenation of phenol, *Industrial & Engineering Chemistry Research*, 33 (1994) 2571-2577.
- [260] G.F. Froment and K.B. Bischoff, *Chemical reactor analysis and design*, John Wiley & Sons, (1979).
- [261] P.B. Weisz and C.D. Prater, Interpretation of measurements in experimental catalysis, *Advances in Catalysis*, 6 (1954) 143-196.
- [262] R.L. Orozco, M.D. Redwood, P. Yong, I. Caldelari, F. Sargent, and L.E. Macaskie, Towards an integrated system for bio-energy: Hydrogen production by *Escherichia coli* and use of palladium-coated waste cells for electricity generation in a fuel cell, *Biotechnology Letters*, 32 (2010) 1837-1845.
- [263] P. Yong, N.A. Rowson, J.P.G. Farr, I.R. Harris, and L.E. Macaskie, Biloaccumulation of palladium by *Desulfovibrio desulfuricans*, *Journal of Chemical Technology and Biotechnology*, 77 (2002) 593-601.
- [264] Charlot G., *Dosages Absorptiométriques des Elements Minéraux*, Masson, (1978).
- [265] Y. Fujita, I. Mori, and T. Matsuo, Spectrophotometric determination of gold(III) by an association complex formation between gold-thiamine and phloxine, *Analytical Sciences*, 15 (1999) 1009-1012.
- [266] R. Dicosimo and G.M. Whitesides, Oxidation of 2-propanol to acetone by dioxygen on a platinised electrode under open-circuit conditions, *Journal of Physical Chemistry*, 93 (1989) 768-775.
- [267] A.B. Ross, J.M. Jones, M.L. Kubacki, and T. Bridgeman, Classification of macroalgae as fuel and its thermochemical behaviour, *Bioresource Technology*, 99 (2008) 6494-6504.
- [268] G.I. Goldstein, D.E. Newbury, P. Echilin, D.C. Joy, C. Fiori, and E. Lifshin, *Scanning electron microscopy and X-ray microanalysis*, Plenum Press, (1981).
- [269] A.L. Patterson, The Scherrer formula for X-ray particle size determination, *Physical Review*, 56 (1939) 978-982.
- [270] J.A. Bennett, R.P. Fishwick, R. Spence, J. Wood, J.M. Winterbottom, S.D. Jackson, and E.H. Stitt, Hydrogenation of 2-pentyne over Pd/Al₂O₃ catalysts: Effect of operating variables and solvent selection, *Applied Catalysis A-General*, 364 (2009) 57-64.
- [271] A. Molnar, A. Sarkany, and M. Varga, Hydrogenation of carbon-carbon multiple bonds: chemo-, regio- and stereo-selectivity, *Journal of Molecular Catalysis A-Chemical*, 173 (2001) 185-221.
- [272] L. Cerveny and V. Ruzicka, Competitive catalytic-hydrogenation in the liquid-phase on solid catalysts, *Catalysis Reviews-Science and Engineering*, 24 (1982) 503-566.
- [273] L. Cerveny, Palladium catalysts in hydrogenation reactions, *Chemical Engineering Communications*, 83 (1989) 31-63.
- [274] X.C. Guo and R.J. Madix, Selective hydrogenation and H-D exchange of unsaturated-hydrocarbons on Pd(100)-P(1×1)-H(D), *Journal of Catalysis*, 155 (1995) 336-344.

- [275] T. Ouchaib, J. Massardier, and A. Renouprez, Competitive hydrogenation of butadiene and butene on palladium and platinum catalysts, *Journal of Catalysis*, 119 (1989) 517-520.
- [276] P. Sautet and J.F. Paul, Low-temperature adsorption of ethylene and butadiene on platinum and palladium surfaces: A theoretical-study of the di σ/π competition, *Catalysis Letters*, 9 (1991) 245-260.
- [277] M. Varga, A. Molnar, M. Mohai, I. Bertoti, M. Janik-Czachor, and A. Szummer, Selective hydrogenation of pentynes over PdZr and PdCuZr prepared from amorphous precursors, *Applied Catalysis A-General*, 234 (2002) 167-178.
- [278] J. Wood, L. Bodenes, J. Bennett, K. Deplanche, and L.E. Macaskie, Hydrogenation of 2-butyne-1,4-diol using novel bio-palladium catalysts, *Industrial & Engineering Chemistry Research*, 49 (2010) 980-988.
- [279] A. Bruehwiler, N. Semagina, M. Grasmann, A. Renken, L. Kiwi-Minsker, A. Saaler, H. Lehmann, W. Bonrath, and F. Roessler, Three-phase catalytic hydrogenation of a functionalised alkyne: Mass-transfer and kinetic studies with *in situ* hydrogen monitoring, *Industrial & Engineering Chemistry Research*, 47 (2008) 6862-6869.
- [280] M.L. Toebes, J.A. Van-Dillen, and K.P. De-Jong, Synthesis of supported palladium catalysts, *Journal of Molecular Catalysis A: Chemical*, 173 (2001) 75-98.
- [281] A.J. Haighton, K. Vanputte, and L.F. Vermaas, Determination of solid contents of fats by wide-line Nuclear Magnetic-Resonance: Signal of liquid oils, *Journal of the American Oil Chemists Society*, 49 (1972) 153-&.
- [282] A.E. Bailey, *Bailey's industrial oil and fat products*, John Wiley & Sons, (1979).
- [283] I.V. Deliy, N.V. Maksimchuk, R. Psaro, N. Ravasio, V. Dal-Santo, S. Recchia, E.A. Paukshtis, A.V. Golovin, and V.A. Semikolenov, Kinetic peculiarities of *cis/trans* methyl oleate formation during hydrogenation of methyl linoleate over Pd/MaO, *Applied Catalysis A-General*, 279 (2005) 99-107.
- [284] M.B. Smith, *March's advanced organic chemistry: Reactions, mechanisms, and structure*, Wiley, (2013).
- [285] L. Bern, J.O. Lidefelt, and N.H. Schoon, Mass-transfer and scale-up in fat hydrogenation, *Journal of the American Oil Chemists Society*, 53 (1976) 463-466.
- [286] P.H. Calderbank. Physical rate processes in industrial fermentation, I: The interfacial area in gas-liquid contacting with mechanical agitation. *Chemical Engineering Research and Design* 36 (1958) 440-463.
- [287] M.Y. Chang and B.I. Morsi, Mass-transfer in a three-phase reactor operating at elevated pressures and temperatures, *Chemical Engineering Science*, 47 (1992) 1779-1790.
- [288] M.Y. Chang and B.I. Morsi, Mass-transfer characteristics of gases in aqueous and organic liquids at elevated pressures and temperatures in agitated reactors, *Chemical Engineering Science*, 46 (1991) 2639-2650.
- [289] C. Perego and S. Peratello, Experimental methods in catalytic kinetics, *Catalysis Today*, 52 (1999) 133-145.
- [290] H. Hichri, A. Accary, and J. Andrieu, Kinetics and slurry-type reactor modeling during catalytic-hydrogenation of ortho-cresol on Ni/SiO₂, *Chemical Engineering and Processing*, 30 (1991) 133-140.
- [291] G. Roberts, *Catalysis in organic synthesis*, Academic Perss, (1976).
- [292] J.M. Winterbottom, Three-phase reactors, in: J.M. Winterbottom and M.B. King (Eds.), *Reactor Design for Chemical Engineers*, Stanley Thornes, (1999) 344-375.

- [293] R.V. Chaudhari, M.G. Parande, P.A. Ramachandran, P.H. Brahme, H.G. Vadgaonkar, and R. Jaganathan, Hydrogenation of butynediol to *cis*-butenediol catalysed by Pd-Zn-CaCO₃: Reaction-kinetics and modeling of a batch slurry reactor, *AIChE Journal*, 31 (1985) 1891-1903.
- [294] K.R. Westerterp, W.P.M. Van Swaaij, and A.A.C.M. Beenackers, *Chemical reactor design and operation*, John Wiley & Sons, (1987).
- [295] L. Bern, M. Hell, and N.H. Schön, Kinetics of hydrogenation of rapeseed oil, II: Rate equations of chemical reactions, *Journal of the American Oil Chemists Society*, 52 (1975) 391-394.
- [296] A.F. Perez-Cadenas, F. Kapteijn, M.M.P. Zieverink, and J.A. Moulijn, Selective hydrogenation of fatty acid methyl esters over palladium on carbon-based monoliths structural control of activity and selectivity, *Catalysis Today*, 128 (2007) 13-17.
- [297] A.J. Dijkstra, Kinetics and mechanism of the hydrogenation process: The state of the art, *European Journal of Lipid Science and Technology*, 114 (2012) 985-998.
- [298] A.E. Bailey, Theory and mechanics of the hydrogenation of edible fats, *Journal of the American Oil Chemists Society*, 26 (1949) 596-601.
- [299] K. Belkacemi and S. Hamoudi, Low *trans* and saturated vegetable oil hydrogenation over nanostructured Pd/*silica* catalysts: Process parameters and mass-transfer features effects, *Industrial & Engineering Chemistry Research*, 48 (2009) 1081-1089.
- [300] M. Plourde, K. Belkacemi, and J. Arul, Hydrogenation of sunflower oil with novel Pd catalysts supported on structured silica, *Industrial & Engineering Chemistry Research*, 43 (2004) 2382-2390.
- [301] L.E. Macaskie, A.C. Humphries, I.P. Mikheenko, V.S. Baxter-Plant, K. Deplanche, M.D. Redwood, J.A. Bennett, and J. Wood, Use of *Desulfovibrio* and *Escherichia coli* Pd-nanocatalysts in reduction of Cr(VI) and hydrogenolytic dehalogenation of polychlorinated biphenyls and used transformer oil, *Journal of Chemical Technology and Biotechnology*, 87 (2012) 1430-1435.
- [302] D.I. Enache, D. Barker, J.K. Edwards, S.H. Taylor, D.W. Knight, A.F. Carley, and G.J. Hutchings, Solvent-free oxidation of benzyl alcohol using titanic-supported gold-palladium catalysts: Effect of Au-Pd ratio on catalytic performance, *Catalysis Today*, 122 (2007) 407-411.
- [303] G. Li, D.I. Enache, J. Edwards, A.F. Carley, D.W. Knight, and G.J. Hutchings, Solvent-free oxidation of benzyl alcohol with oxygen using zeolite-supported Au and Au-Pd catalysts, *Catalysis Letters*, 110 (2006) 7-13.
- [304] A.M. Abend, L. Chung, R.T. Bibart, M. Brooks, and D.G. McCollum, Concerning the stability of benzyl alcohol: Formation of benzaldehyde dibenzyl acetal under aerobic conditions, *Journal of Pharmaceutical and Biomedical Analysis*, 34 (2004) 957-962.
- [305] S.H. Hansen and L.K. Sydnes, Photochemical oxidation of benzyl alcohol, *Acta Chemica Scandinavica*, 43 (1989) 395-398.
- [306] R.V. Chaudhari and P.A. Ramachandran, Influence of mass-transfer on zero-order reaction in a catalytic slurry reactor, *Industrial & Engineering Chemistry Fundamentals*, 19 (1980) 201-206.
- [307] P.A. Ramachandran and R.V. Chaudhari, *Three-phase catalytic reactors*, Gordon and Breach Science Publishers, (1983).
- [308] M. Bankmann, R. Brand, B.H. Engler, and J. Ohmer, Forming of high surface-area TiO₂ to catalyst supports, *Catalysis Today*, 14 (1992) 225-242.

- [309] H. Tsunoyama, H. Sakurai, Y. Negishi, and T. Tsukuda, Size-specific catalytic activity of polymer-stabilised gold nanoclusters for aerobic alcohol oxidation in water, *Journal of the American Chemical Society*, 127 (2005) 9374-9375.
- [310] K. Raveendran, A. Ganesh, and K.C. Khilar, Pyrolysis characteristics of biomass and biomass components, *Fuel*, 75 (1996) 987-998.
- [311] N.S. Babu, N. Lingaiah, R. Gopinath, P.S.S. Reddy, and P.S.S. Prasad, Characterisation and reactivity of alumina-supported Pd catalysts for the room-temperature hydrodechlorination of chlorobenzene, *Journal of Physical Chemistry C*, 111 (2007) 6447-6453.
- [312] S.W. Weller, Kinetics of heterogeneous catalysed-reactions, *Catalysis Reviews-Science and Engineering*, 34 (1992) 227-280.
- [313] R.J. Grau, A.E. Cassano, and M.A. Baltanas, Kinetics of methyl oleate catalytic-hydrogenation with quantitative-evaluation of *cis-trans* isomerisation equilibrium, *Industrial & Engineering Chemistry Process Design and Development*, 25 (1986) 722-728.
- [314] G. Gut, J. Kosinka, A. Prabucki, and A. Schuerch, Kinetics of the liquid-phase hydrogenation and isomerisation of sunflower seed oil with nickel catalysts, *Chemical Engineering Science*, 34 (1979) 1051-1056.
- [315] U.K. Singh and M.A. Vannice, Liquid-phase hydrogenation of citral over Pt/SiO₂ catalysts I: Temperature effects on activity and selectivity, *Journal of Catalysis*, 191 (2000) 165-180.
- [316] R.J. Grau, A.E. Cassano, and M.A. Baltanas, Solution of a complex reaction network: The methyl-linoleate catalytic hydrogenation, *Chemical Engineering Communications*, 58 (1987) 17-36.
- [317] J. Marangozis, O.B. Keramidas, and G. Pappasvas, Rate and mechanism of hydrogenation of cottonseed oil in slurry reactors, *Industrial & Engineering Chemistry Process Design and Development*, 16 (1977) 361-369.
- [318] M.T. Rodrigo, L. Daza, and S. Mendioroz, Nickel supported on natural silicates: Activity and selectivity in sunflower seed oil hydrogenation, *Applied Catalysis A-General*, 88 (1992) 101-114.
- [319] J.J. Zwicky and G. Gut, Kinetics, poisoning and mass transfer effects in liquid-phase hydrogenations of phenolic compounds over a palladium catalyst, *Chemical Engineering Science*, 33 (1978) 1363-1369.
- [320] G.H. Graaf, E.J. Stamhuis, and A.A.C.M. Beenackers, Kinetics of low-pressure methanol synthesis, *Chemical Engineering Science*, 43 (1988) 3185-3195.
- [321] G.H. Graaf, J.G.M. Winkelman, E.J. Stamhuis, and A.A.C.M. Beenackers, Kinetics of the 3-phase methanol synthesis, *Chemical Engineering Science*, 43 (1988) 2161-2168.
- [322] J.W. Veldsink, M.J. Bouma, N.H. Schoon, and A.A.C.M. Beenackers, Heterogeneous hydrogenation of vegetable oils: A literature review, *Catalysis Reviews-Science and Engineering*, 39 (1997) 253-318.
- [323] PGM price, Online source, (2013).
- [324] P. Yong, I.P. Mikheenko, K. Deplanche, M.D. Redwood, and L.E. Macaskie, Biorefining of precious metals from wastes: An answer to manufacturing of cheap nanocatalysts for fuel cells and power generation *via* an integrated biorefinery? *Biotechnology Letters*, 32 (2010) 1821-1828.
- [325] Changes to landfill tax rates, Online source, (2013).
- [326] S. Dimitriadis, N. Nomikou, and A.P. Mchale, Pt-based electro-catalytic materials derived from biosorption processes and their exploitation in fuel cell technology, *Biotechnology Letters*, 29 (2007) 545-551.

Chapter 8

Appendices

Additional information not covered elsewhere in the thesis, and parts of work not yet ready for publication, or prepared jointly with others, are presented as a series of Appendices.

8.1 Kinetic Models of Hydrogenation Reactions

For the establishment of the rate expressions in this study, the application of Langmuir-Hinshelwood-Hougen-Watson (LHHW) kinetics is a fundamental approach, which consists of a rate-determining reaction step (usually a surface reaction step, *i.e.* the insertion of hydrogen atoms in hydrogenation) combined with Langmuir adsorption of reactants and products [312].

8.1.1 Rate Equation Derivation of 2-Pentyne Hydrogenation

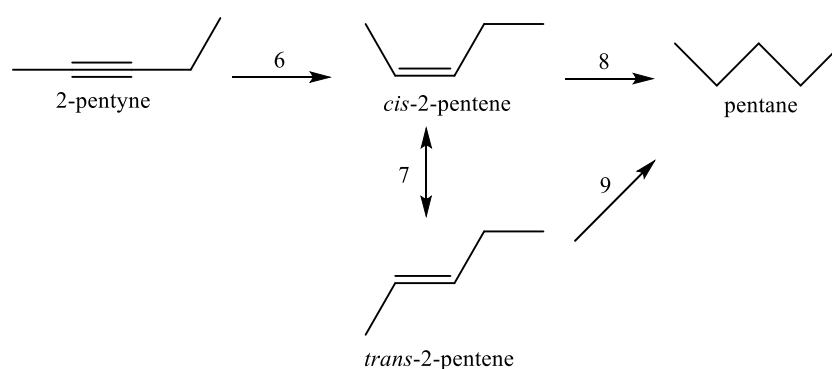
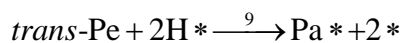
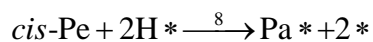
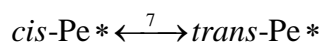
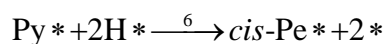
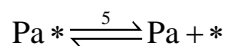
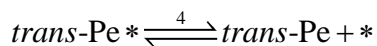
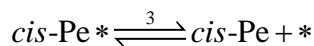
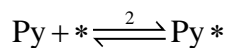
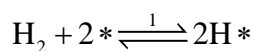


Figure 8.1 The overall integral reaction network of 2-pentyne hydrogenation.

As has been introduced in §4.2, Figure 8.1 depicts the overall integral reaction pathways in the 2-pentyne hydrogenation. Accordingly the elementary steps on the catalyst surface were described as follows:



where Py, *cis*-Pe, *trans*-Pe, and Pa denote 2-pentyne, *cis*-2-pentene, *trans*-2-pentene, and pentane correspondingly.

To derive the rate equations, the following assumptions are applied:

i) Adsorption at equilibrium:

The dissociative adsorption of hydrogen on the catalyst surface (Step 1) was assumed, *i.e.* molecular hydrogen is adsorbed onto the catalyst surface and split into two adsorbed hydrogen atoms. At the dissociative equilibrium hydrogen adsorption, there is:

$$k_H[\text{H}_2]\theta_*^2 = k_{-H}\theta_{H*}^2$$

$$\theta_{H*} = \sqrt{\frac{k_H}{k_{-H}}[\text{H}_2]} \cdot \theta_* = \sqrt{K_H[\text{H}_2]} \cdot \theta_*$$

θ_H denotes the surface fraction of the adsorption site bonded to H atom, with the according concentration as $[\text{H}_2]$. θ_* is the fraction of vacant active sites. k_H and k_{-H} are the adsorption rate constant and desorption rate constant, correspondingly K_H (equals to the fraction of k_H/k_{-H}) denotes the adsorption coefficient of the hydrogen adsorption step.

Likewise, the adsorption of the other component reaches the equilibrium, in which the adsorption constants for *cis*- and *trans*- double bonds in pentene are considered to be equal (*i.e.* $K_{cis\text{-Pe}}=K_{trans\text{-Pe}}=K_{\text{Pe}}$) [313,314]. The following equation can be derived (taking step 3 as an example, a full list is provided in Table 8.1):

$$k_3[\text{cis-Pe}]\theta_* = k_{-3}\theta_{cis\text{-Pe}*}$$

$$\theta_{cis\text{-Pe}*} = \frac{k_3}{k_{-3}}[\text{cis-Pe}]\theta_* = K_{\text{Pe}}[\text{cis-Pe}]\theta_*$$

The mass balance of the mole fractions of all components at the surface ($\sum\theta_i=1$) thus read:

$$\theta_{\text{Py}*} + \theta_{cis\text{-Pe}*} + \theta_{trans\text{-Pe}*} + \theta_{\text{Pa}*} + \theta_{\text{H}*} + \theta_* = 1$$

by substituting Equation 8-1 ~ 8-5 in Table 8.1, the above equation becomes,

$$\theta_* = \frac{1}{K_{Py}[Py] + K_{Pe}[cis-Pe] + K_{Pe}[trans-Pe] + K_{Pa}[Pa] + \sqrt{K_H[H_2]} + 1}$$

The starting material for 2-pentyne hydrogenation was 4 ml 2-pentyne in 150 ml 2-propanol, giving an initial 2-pentyne concentration $[Py]_0$ equal to $0.2707 \text{ kmol.m}^{-3}$. While the dissolved concentration of hydrogen in bulk 2-propanol was assumed to approach its value at saturation (under the optimum condition in the absence of gas-liquid limitations) and estimated to be $0.0084 \text{ kmol.m}^{-3}$ as reported by Wood *et al.* [278], taking also into consideration a weak hydrogen adsorption on Pt group metals [315], that is, $K_H[H_2] \ll 1$ and can be neglected in the denominator of θ_* , the above equation may be simplified as:

$$\theta_* = \frac{1}{K_{Py}[Py] + K_{Pe}[cis-Pe] + K_{Pe}[trans-Pe] + K_{Pa}[Pa] + 1}$$

ii) Surface reaction steps:

The irreversible reaction of 2-pentyne to give *cis*-2-pentene is assumed to be the surface reaction control [24], thus the relevant rate equation is derived below:

$$r_6 = k_6 \theta_{Py} \theta_{H^*}^2 = k_6 K_{Py}[Py] \theta_* K_H[H_2] \theta_*^2 = k'_{Py} K_{Py}[Py] \theta_*^3$$

It is suggested that both *cis*- and *trans*-isomers are equally hydrogenated during the hydrogenation [120,313,316], in other words, equal hydrogenation rate constants of *cis*-pentene (Step 8) and *trans*-pentene (Step 9) $k_8=k_9$. Taking Step 8 as an example,

$$r_8 = k_8 \theta_{cis-Pe} \theta_{H^*}^2 = k_8 K_{Pe}[cis-Pe] \theta_* K_H[H_2] \theta_*^2 = k'_{Pe} K_{Pe}[cis-Pe] \theta_*^3$$

likewise, $r_9 = k'_{Pe} K_{Pe}[trans-Pe] \theta_*^3$

The rate constants k'_{Pe} and k'_{Py} in the above equations incorporate hydrogen concentration K_H and adsorption coefficient $[\text{H}_2]$, k_7 and k_{-7} represent the reversible rate constants of *cis-trans* isomerisation in step 7 (Figure 8.1); K_i denotes the adsorption coefficient of each component.

Table 8.1 Elementary reaction steps and rate equations in the 2-pentyne hydrogenation.

Step	Elementary reaction	Equations	No.
1	$\text{H}_2 + 2* \xrightleftharpoons{1} 2\text{H}*$	$\theta_{\text{H}*} = \sqrt{K_{\text{H}}[\text{H}_2]} \cdot \theta_*$	8-1
2	$\text{Py} + * \xrightleftharpoons{2} \text{Py}*$	$\theta_{\text{Py}*} = K_{\text{Py}}[\text{Py}]\theta_*$	8-2
3	$\text{cis-Pe} * \xrightleftharpoons{3} \text{cis-Pe} + *$	$\theta_{\text{cis-Pe}*} = K_{\text{Pe}}[\text{cis-Pe}] \cdot \theta_*$	8-3
4	$\text{trans-Pe} * \xrightleftharpoons{4} \text{trans-Pe} + *$	$\theta_{\text{trans-Pe}*} = K_{\text{Pe}}[\text{trans-Pe}] \cdot \theta_*$	8-4
5	$\text{Pa} * \xrightleftharpoons{5} \text{Pa} + *$	$\theta_{\text{Pa}*} = K_{\text{Pa}}[\text{Pa}] \cdot \theta_*$	8-5
6	$\text{Py} * + 2\text{H} * \xrightarrow{6} \text{cis-Pe} * + 2*$	$r_6 = k'_{\text{Py}} K_{\text{Py}}[\text{Py}]\theta_*^3$	8-6
7	$\text{cis-Pe} * \xrightleftharpoons{7} \text{trans-Pe} *$	$r_7 = (k_7 K_{\text{Pe}}[\text{cis-Pe}] - k_{-7} K_{\text{Pe}}[\text{trans-Pe}])\theta_*$	8-7
8	$\text{cis-Pe} + 2\text{H} * \xrightarrow{8} \text{Pa} * + 2*$	$r_8 = k'_{\text{Pe}} K_{\text{Pe}}[\text{cis-Pe}]\theta_*^3$	8-8
9	$\text{trans-Pe} + 2\text{H} * \xrightarrow{9} \text{Pa} * + 2*$	$r_9 = k'_{\text{Pe}} K_{\text{Pe}}[\text{trans-Pe}]\theta_*^3$	8-9

The reaction scheme in Figure 4.1 clearly shows that apart from the case of the initial reactant 2-pentyne, the observed reaction rates of all the other compositions are composed of the contributions of several reaction paths respectively. Accordingly, the overall reaction rate of the key component during the course of the 2-pentyne hydrogenation was expressed individually as follows (numbered as Equations 4-2 ~ 4-5 in Chapter 4):

$$\frac{\partial \text{Py}}{\partial t} = m(-r_6) = -mk'_{\text{Py}} K_{\text{Py}}[\text{Py}]\theta_*^3$$

$$\begin{aligned} \frac{\partial \text{cis-Pe}}{\partial t} &= m(r_6 - r_7 - r_8) \\ &= m\left\{k'_{\text{Py}} K_{\text{Py}}[\text{Py}]\theta_*^3 - (k_7 K_{\text{Pe}}[\text{cis-Pe}] - k_{-7} K_{\text{Pe}}[\text{trans-Pe}])\theta_* - k'_{\text{Pe}} K_{\text{Pe}}[\text{cis-Pe}]\theta_*^3\right\} \end{aligned}$$

$$\frac{\partial \text{trans-Pe}}{\partial t} = m(r_7 - r_9) = mK_{\text{Pe}} \left\{ (k_7[\text{cis-Pe}] - k_{-7}[\text{trans-Pe}])\theta_* - k'_{\text{Pe}}[\text{trans-Pe}]\theta_*^3 \right\}$$

$$\frac{\partial \text{Pa}}{\partial t} = m(r_8 + r_9) = mk'_{\text{Pe}} K_{\text{Pe}} ([\text{cis-Pe}] + [\text{trans-Pe}])\theta_*^3$$

8.1.2 Kinetics Models of Soybean Oil Hydrogenation

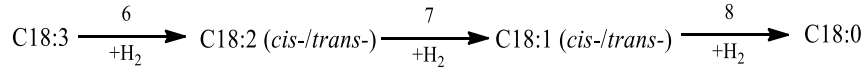
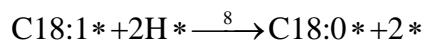
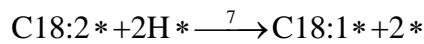
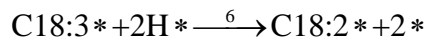
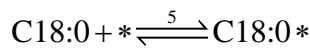
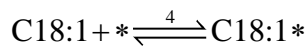
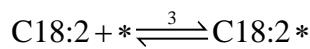
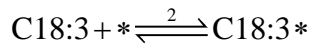
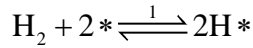
Model 1

Figure 8.2 The reaction scheme of soybean oil hydrogenation based on Model 1 [298].

Accordingly, the elementary steps are presented below:



A Langmuir-Hinshelwood based adsorption kinetic relation was used to determine the reaction rate along with the following assumptions:

i) Non-competitive adsorption between H_2 and fatty acids molecules, in other words dissociated hydrogen atoms and fatty acid double bonds are independently adsorbed on different catalyst sites [13,313,314,317,318]. In the liquid phase, the fatty acids are present in large excess and, because of the steric effects with the fatty acid owing to the large molecular size, they cannot completely cover the surface and bare palladium sites are available for dissociative chemisorption of small hydrogen [317]. However the fatty acids are assumed to compete for the same sites. The mass balances of the mole fractions of hydrogen and fatty acids respectively at the surface ($\sum \theta_i = 1$) thus read:

$$\theta_H + \theta_* = 1$$

$$\theta_{\text{C18:3}} + \theta_{\text{C18:2}} + \theta_{\text{C18:1}} + \theta_{\text{C18:0}} + \theta_* = 1$$

Thereafter, the hydrogen fraction at the surface when dissociative equilibrium hydrogen adsorption is:

$$\theta_H = \frac{\sqrt{K_H[H_2]}}{1 + \sqrt{K_H[H_2]}}$$

On the other hand, for the equilibrium adsorption constants of the fatty acids K_i ($i=0, 1, 2, 3$, corresponding to C18:0, C18:1, C18:2, and C18:3), a ratio of $K_3:K_2:K_1=3:2:1$ was assumed corresponding to the adsorption probabilities of trienic, dienic, and monoenic fatty acids, and these adsorption constants are hardly affected by temperature in the range examined [13,120].

When the fatty acids reach adsorption equilibrium, there is:

$$\theta_* = \frac{1}{1 + K_3[C18:3] + K_2[C18:2] + K_1[C18:1] + K_0[C18:0]}$$

ii) The hydrogenation of double bonds of polyenes can be described by the same rate equation equations expressed for monenes, *i.e.* hydrogenation rate constants of the double bond are independent of the degree of saturation (all denote as k). The observed different reactivity of polyenes stems from the corresponding adsorption difference, *e.g.* greater reactivity of the C18:3 than C18:2 stems from the strong adsorption of C18:3 relative to C18:2 only [203].

iii) As is discussed in §2.4.1, the addition of hydrogen atoms to the unsaturated bond (C=C) is considered as a two-step addition, which is well-known as the Horiuti-Polanyi mechanism [213]. The first hydrogen insertion to form a half-hydrogenated surface intermediate is assumed to be the rate-determining step, however difference need to be noted between the hydrogenation of polyenic and monoenic (C18:1) fatty acids [297]. The half-hydrogenated surface intermediate after the first hydrogen insertion to polyenic (C18:3H* for C18:3 and C18:2H* for C18:2) is tied to the catalyst by the residual double bond and awaits the second addition of a hydrogen atom. Therefore this rate is proportional to θ_H . However, the half-

hydrogenated surface intermediate from the monoene reacting with an adsorbed hydrogen atom (C18:1H* for C18:1) lacks a residual double bond and therefore readily dissociates and leaves again, which leading to an equilibrium in which the concentration of the this intermediate (C18:1H*) is proportional to the concentrations of the reagents forming this intermediate (C18:1* and H*). Its saturation rate is proportional to its concentration ($\theta_{\text{C18:1}^*}$) and the hydrogen atom concentration (θ_{H}) and since C18:1H* itself is proportional to θ_{H} , the rate of monoene saturation is therefore proportional to θ_{H}^2 . Accordingly, there the rate equations for step 6~8:

$$r_6 = kK_3[\text{C18:3}]\theta_*\theta_{\text{H}}, \quad r_7 = kK_2[\text{C18:2}]\theta_*\theta_{\text{H}}$$

$$\text{while } r_8 = kK_1[\text{C18:1}]\theta_*\theta_{\text{H}}^2$$

From these assumptions, a full list of the elementary reaction steps and the corresponding rate equations is presented in Table 8.2.

Table 8.2 Elementary reaction steps and rate equations in the soybean hydrogenation for Model 1.

Step	Elementary reaction	Equations	No.
1	$\text{H}_2 + 2* \xrightleftharpoons{1} 2\text{H}^*$	$\theta_{\text{H}} = \frac{\sqrt{K_{\text{H}}[\text{H}_2]}}{1 + \sqrt{K_{\text{H}}[\text{H}_2]}}$	8-10
2	$\text{C18:3} + * \xrightleftharpoons{2} \text{C18:3}^*$	$\theta_{\text{C18:3}^*} = K_3[\text{C18:3}]\theta_*$	8-11
3	$\text{C18:2} + * \xrightleftharpoons{3} \text{C18:2}^*$	$\theta_{\text{C18:2}^*} = K_2[\text{C18:2}]\theta_*$	8-12
4	$\text{C18:1} + * \xrightleftharpoons{4} \text{C18:1}^*$	$\theta_{\text{C18:1}^*} = K_1[\text{C18:1}]\theta_*$	8-13
5	$\text{C18:0} + * \xrightleftharpoons{5} \text{C18:0}^*$	$\theta_{\text{C18:0}^*} = K_0[\text{C18:0}]\theta_*$	8-14
6	$\text{C18:3}^* + 2\text{H}^* \xrightarrow{6} \text{C18:2}^* + 2*$	$r_6 = kK_3[\text{C18:3}]\theta_*\theta_{\text{H}}$	8-15
7	$\text{C18:2}^* + 2\text{H}^* \xrightarrow{7} \text{C18:1}^* + 2*$	$r_7 = kK_2[\text{C18:2}]\theta_*\theta_{\text{H}}$	8-16
8	$\text{C18:1}^* + 2\text{H}^* \xrightarrow{8} \text{C18:0}^* + 2*$	$r_8 = kK_1[\text{C18:1}]\theta_*\theta_{\text{H}}^2$	8-17

Thereafter the following partial differential equation for each composition in Model 1 can be derived (numbered as 4-15 ~ 4.18 in Chapter 4):

$$\frac{\partial C_{18:3}}{\partial t} = m(-r_6) = -mkK_3[C_{18:3}]\theta_*\theta_H$$

$$\frac{\partial C_{18:2}}{\partial t} = m(r_6 - r_7) = mk(K_3[C_{18:3}] - K_2[C_{18:2}])\theta_*\theta_H$$

$$\frac{\partial C_{18:1}}{\partial t} = m(r_7 - r_8) = mk(K_2[C_{18:2}]\theta_H - K_1[C_{18:1}]\theta_H^2)\theta_*$$

$$\frac{\partial C_{18:0}}{\partial t} = mr_8 = mkK_1[C_{18:1}]\theta_*\theta_H^2$$

Model 2

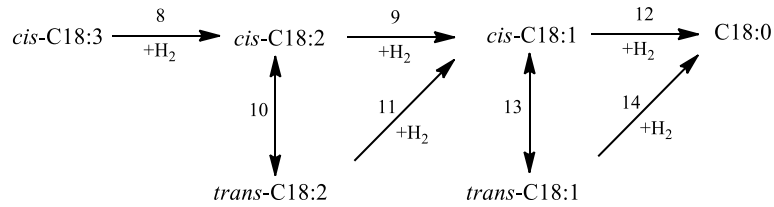
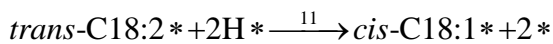
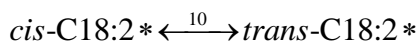
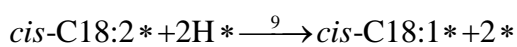
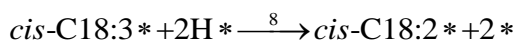
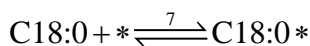
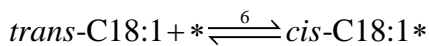
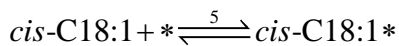
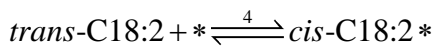
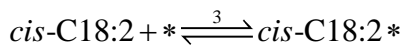
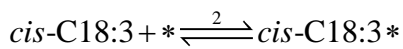
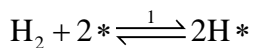
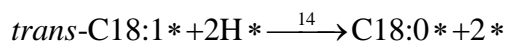
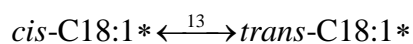
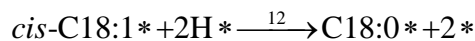


Figure 8.3 The reaction scheme of soybean oil hydrogenation based on Model 2.

For the soybean oil contains only small amount of *cis*-C18:3 which being quickly reacted, its *cis-trans* isomerisation was not counted in the reaction network. Likewise, the elementary steps of soybean oil hydrogenation on the catalyst surface based on Model 2 were described as follows:





For the establishment of the rate equations, all the assumptions in Model 1 were applied in Model 2 along with the additional assumptions below:

i) In this Model 2, the *cis-trans* isomerisation results from the easy rotation of the single bond remaining in the half-hydrogenated surface intermediate which is formed after the insertion of first hydrogen atom to the unsaturated double bond, based on the well-known Horiuti-Polanyi mechanism [297]. The surface occupation of the half-hydrogenated intermediate is negligible compared to that of bulk components in the (competitive) adsorption for vacant surface sites [319-321], due to the high reactivity. Thus in deriving LHHW-type rate equations, surface intermediates are neglected [312]. On the other hand, both *cis* and *trans* fatty acids of the same degree of saturation are adsorbed identically on the catalyst surface [313,314], *e.g.* K_I represents the adsorption constant of both the *cis*- and *trans*-isomer of monoene.

ii) It is assumed the formation of the half hydrogenated surface intermediate, *i.e.* the first hydrogen insertion, as the rate-determining step. Both *cis* and *trans*, and that the adsorbed double bond could isomerise at the catalyst surface [314]. Furthermore, although hydrogen is not consumed in isomerisation, the hydrogen concentration affects the *cis-trans* formation [322]. The hydrogen orders for the isomerisation reactions are assumed to be different, presented as γ for *cis*-isomer to react (forwards) and δ for *trans*-isomer to react (backwards), correspondingly k_i and k_{-i} as the isomerisation rate constants.

From these assumptions, the transformation rate equations of the elementary reaction steps in Model 2 are derived and listed in Table 8.3.

Table 8.3 Elementary reaction steps and rate equations in the soybean hydrogenation for Model 2.

Step	Elementary reaction	Equations	No.
1	$H_2 + 2* \xrightleftharpoons{1} 2H*$	$\theta_H = \frac{\sqrt{K_H[H_2]}}{1 + \sqrt{K_H[H_2]}}$	8-10
2	$cis-C18:3 + * \xrightleftharpoons{2} cis-C18:3*$	$\theta_{cis-C18:3*} = K_3[cis-C18:3]\theta_*$	8-18
3	$cis-C18:2 + * \xrightleftharpoons{3} cis-C18:2*$	$\theta_{cis-C18:2*} = K_2[cis-C18:2]\theta_*$	8-19
4	$trans-C18:2 + * \xrightleftharpoons{4} trans-C18:2*$	$\theta_{trans-C18:2*} = K_2[trans-C18:2]\theta_*$	8-20
5	$cis-C18:1 + * \xrightleftharpoons{5} cis-C18:1*$	$\theta_{cis-C18:1*} = K_1[cis-C18:1]\theta_*$	8-21
6	$trans-C18:1 + * \xrightleftharpoons{6} trans-C18:1*$	$\theta_{trans-C18:1*} = K_1[trans-C18:1]\theta_*$	8-22
7	$C18:0 + * \xrightleftharpoons{7} C18:0*$	$\theta_{C18:0*} = K_0[C18:0]\theta_*$	8-23
8	$cis-C18:3* + 2H* \xrightarrow{8} cis-C18:2* + 2*$	$r_8 = kK_3[cis-C18:3]\theta_*\theta_H$	8-24
9	$cis-C18:2* + 2H* \xrightarrow{9} cis-C18:1* + 2*$	$r_9 = kK_2[cis-C18:2]\theta_*\theta_H$	8-25
10	$cis-C18:2* \xrightleftharpoons{10} trans-C18:2*$	$r_{10} = (k_i[cis-C18:2] - k_{-i}[trans-C18:2])K_2\theta_H^\gamma\theta_*$	8-26
11	$trans-C18:2* + 2H* \xrightarrow{11} cis-C18:1* + 2*$	$r_{11} = kK_2[trans-C18:2]\theta_*\theta_H$	8-27
12	$cis-C18:1* + 2H* \xrightarrow{12} C18:0* + 2*$	$r_{12} = kK_1[cis-C18:1]\theta_*\theta_H^2$	8-28
13	$cis-C18:1* \xrightleftharpoons{13} trans-C18:1*$	$r_{13} = (k_i[cis-C18:1] - k_{-i}[trans-C18:1])K_1\theta_H^\delta\theta_*$	8-29
14	$trans-C18:1* + 2H* \xrightarrow{14} C18:0* + 2*$	$r_{14} = kK_1[trans-C18:1]\theta_*\theta_H^2$	8-30

The mass balance for each component is given by the following differential equations (numbered as 4-19 ~ 4-24 in Chapter 4):

$$\begin{aligned}
\frac{\partial C18:3}{\partial t} &= m(-r_8) \\
&= -mkK_3[cis-C18:3]\theta_*\theta_H \\
\frac{\partial cis-C18:2}{\partial t} &= m(r_8 - r_9 - r_{10}) \\
&= m\left\{(K_3[cis-C18:3] - K_2[cis-C18:2])k\theta_H - (k_i[cis-C18:2] - k_{-i}[trans-C18:2])K_2\theta_H^\gamma\right\}\theta_* \\
\frac{\partial trans-C18:2}{\partial t} &= m(r_{10} - r_{11}) \\
&= mK_2\left\{(k_i[cis-C18:2] - k_{-i}[trans-C18:2])K_2\theta_H^\gamma - k[trans-C18:2]\theta_H\right\}\theta_* \\
\frac{\partial cis-C18:1}{\partial t} &= m(r_9 + r_{11} - r_{12} - r_{13}) \\
&= mkK_2([cis-C18:2] + [trans-C18:2])\theta_*\theta_H - mK_1\left\{k[cis-C18:1]\theta_H^2 + (k_i[cis-C18:1] - k_{-i}[trans-C18:1])\theta_H^\delta\right\}\theta_* \\
\frac{\partial trans-C18:1}{\partial t} &= m(r_{13} - r_{14}) \\
&= mK_1\left\{(k_i[cis-C18:1] - k_{-i}[trans-C18:1])\theta_H^\delta - k[trans-C18:1]\theta_H^2\right\}\theta_* \\
\frac{\partial C18:0}{\partial t} &= m(r_{12} + r_{14}) \\
&= mkK_1([cis-C18:1] + [trans-C18:1])\theta_*\theta_H^2
\end{aligned}$$

8.2 Towards Economic Bio-Catalyst Production

The economic feasibility is one determining factor for bio-catalyst applications in pilot-scale and full-scale. Several costs need to be taken into account during the manufacturing of bio-catalysts, *e.g.* the costs of precious metal salts, culturing the bacteria, and the hydrogen as the reducing agent. This section presents some preliminary findings and perspectives based on the above three types of costs, for designing a cost-effective technology to manufacture precious metal nanoparticles with catalytic activity.

8.2.1 Production of Catalyst from ‘Surrogate’ and Real Wastes

Conventional supported precious metal catalysts are usually prepared using metal salts as precursors, of which the cost can be approximately £90,000 kg⁻¹, as listed in Table 8.4 the current market prices of some precious metal salts. The limited abundance of precious metals coupled with the increasing demand in industry applications (see literature review §2.2) brings about their volatile prices (Figure 8.4), while arousing research interests on the recovery and recycling of these metals.

Table 8.4 Commercial prices of some precious metal salts. ^a

Commercial precious metal salt	CAS ^b	Price (£) ^c	Supplier
palladium(II) sodium chloride (Na ₂ PdCl ₄)	13820-53-6	79.8 (1 g)	Sigma-Aldrich
		110.0 (1 g)	Alfa Aesar
		409.0 (5 g)	
potassium platinum(II) chloride (K ₂ PtCl ₄)	10025-99-7	94.9 (1 g)	Sigma-Aldrich
		331.0 (5 g)	
		91.7 (1 g)	Alfa Aesar
		374.0 (5 g)	
gold(III) chloride hydrate (HAuCl ₄ ·nH ₂ O)	27988-77-8	97.1 (500 mg)	Sigma-Aldrich
		440.0 (5 g)	
		83.6 (1 g)	Alfa Aesar
		312.0 (5 g)	

^a all 99.99% trace metals basis. ^b CAS: Chemical Abstracts Service number. ^c Price unit: Great Britain Pounds.

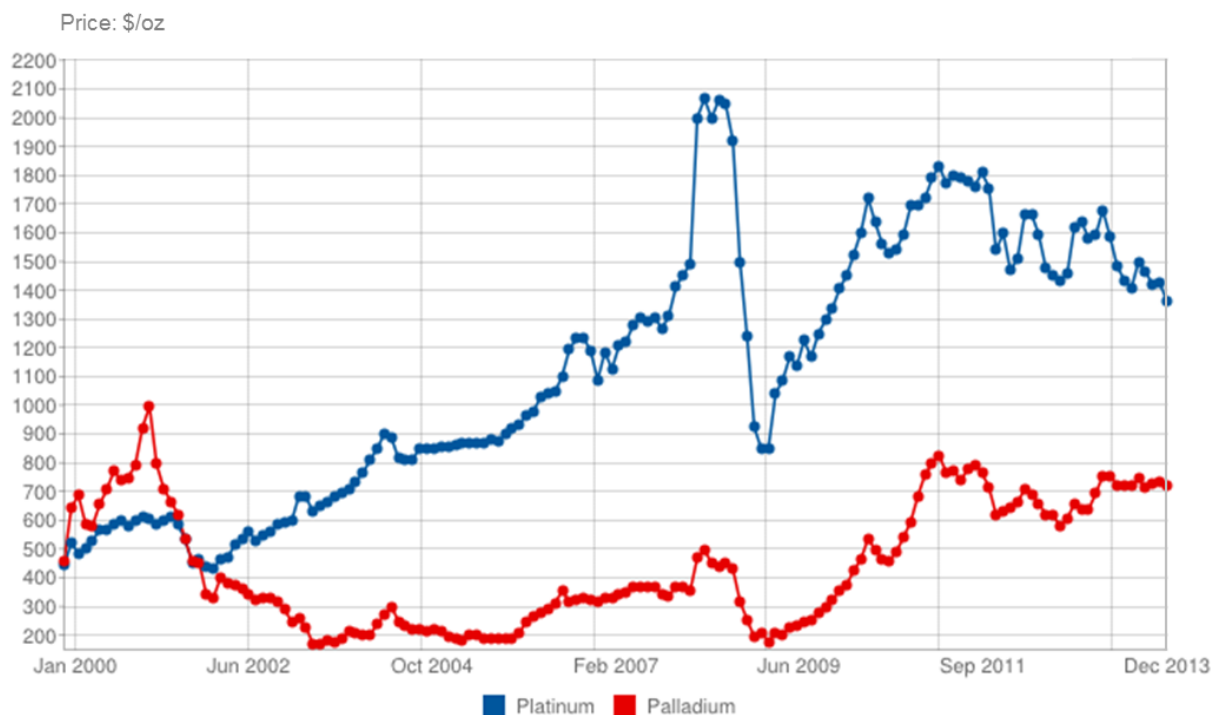


Figure 8.4 Price chat of platinum and palladium showing monthly averages (US\$ per troy oz, 1 \$= ~0.61 £) between January 2000 and December 2013. (Online source from Johnson Matthey Base [323])

Following a pioneering study by Mabbett *et al.* (below) that proved the catalytic efficacy of bio-Pd made from a waste source, it was suggested that if the Pd, for example, is recovered from a Pd(II) containing waste stream or leachate, the cost of palladium catalyst preparation can be 70% lower than by using a pure palladium salt [47]. Studies have shown the extended application of the recovered metals. For instance, Mabbett *et al.* [29] produced bioinorganic catalyst by single-step reduction of platinum group metals (PGM) from industrial waste solution onto biomass of *Desulfovibrio desulfuricans*; such bio-recycled catalyst was shown to have good catalytic activity in reducing Cr(VI) to Cr(III). While Yong *et al.* [324] showed that a fuel cell anode constructed from waste precious metals produced more power than an anode fabricated from bio-Pd alone. Another two-step approach has been developed using *E. coli* cells to recover precious metals from model solutions (containing 2 mM Pd(II) and Pt(IV)) and then subsequently real leachates into effective catalyst and the work is accepted for publication (Appendix 8.4). As the first step, the resting *E. coli* cells were palladised with a Pd loading of 2 wt% following the procedure described in §3.3.2. The pre-metallised cells

(i.e. 2wt%Pd/*E. coli*) then functioned as chemical catalysts in the reductive recovery of precious metals from acidic solutions of 2 mM Pd(II) and Pt(IV), forming 16wt%PdPt/*E. coli*. The catalytic performance of biofabricated PdPt catalyst was examined in the hydrogenation of 2-pentyne ($T= 40\text{ }^{\circ}\text{C}$, $p_{\text{H}_2} = 2\text{ bar}$, $N= 1000\text{ rpm}$) and compared with a conventional Pd/ Al_2O_3 catalyst, the former showing comparable activity and more than 3-fold enhanced selectivity towards the desired *cis*-pentene product. It is concluded that the biorefining of waste precious metals into new catalysts has high potential.

8.2.2 Production of Catalyst Using ‘Second-Life’ Bacteria

Another cost consideration is highlighted in the culturing of the bacteria, for example the market price of nutrient broth no.2 used for *E. coli* growth in the present laboratory is £61.0 kg^{-1} (Sigma-Aldrich, UK). On the other hand today’s industry produces large amounts of waste bacteria from the production of pharmaceuticals, proteins, antibiotics and biochemicals. Disposal of such waste carries financial burdens, e.g. the landfill tax in UK is currently £72 per tonne and there is a trend to increase (Table 8.5). Transporting waste to landfill incurs additional costs (diesel, CO_2 emissions *etc.*), while methane production from landfills is a significant addition to atmospheric greenhouse gases. It was suggested that the overall cost of culturing and subsequent handlings of the bacteria can amount to £840 kg^{-1} cell dry weight [47] which is clearly unfeasible for a process; a more realistic cost is £40 kg^{-1} cell dry weight (J. Clipsham; Catalytic Technologies Management Ltd.; personal communication to Prof L.E. Macaskie).

Table 8.5 Changes to landfill tax rates (Online source from HM Revenue and Customs [325]).

Date of change	Standard rate (£ per tonne)
01.10.96	7
01.04.99	10
01.04.00	11
01.04.01	12
01.04.02	13
01.04.03	14
01.04.04	15
01.04.05	18
01.04.06	21
01.04.07	24
01.04.08	32
01.04.09	40
01.04.10	48
01.04.11	56
01.04.12	64
01.04.13	72

If waste biomass ('second-life' bacteria) can be used as nanocatalyst support [262,326], this would mitigate against the costs of culturing of bacteria, biomass waste disposal and hence the overall cost. Accordingly, attempts were carried to manufacture bio-Pd catalyst using 'second-life' *E. coli* cells harvested from a 4-litre fermentation bioreactor after 3 weeks of hydrogen production [262]. The harvested cells were divided for two different treatments (noted as A and B) to active cells before palladisation as described in §3.3.1. The Pd catalysts were made by the H₂-promoted reduction of appropriate amounts of Pd(II) from Na₂PdCl₄ to give final loadings of 5 wt% palladium on biomass as described in §3.3.2.

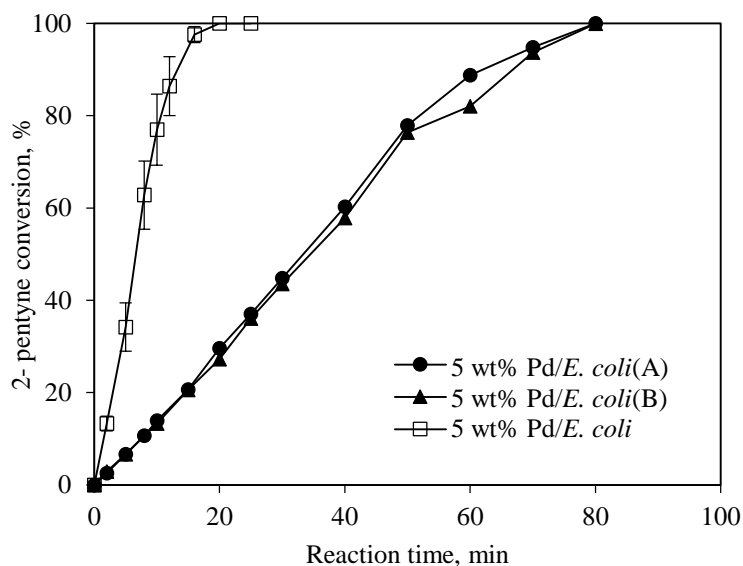


Figure 8.5 2-pentyne conversion profiles versus reaction time over different catalysts. Reaction conditions were: 30 mg of 5 wt% bio-Pd; 4 ml of 2-pentyne in 150 ml of isopropanol as solvent; $T = 40\text{ }^{\circ}\text{C}$; $p_{H_2} = 2\text{ bar}$; $N = 1000\text{ rpm}$. Open symbol: specially-grown *E. coli*. Filled symbols: ‘second-life’ *E. coli* treated by method A or B (see §3.3.1). Where error bars are shown these were calculated as mean \pm standard error of the mean from at least three experiments, bio-Pd catalysts were from two separate preparations. Where no error bars are shown the data were averaged from two experiments with a reproducibility of within 10%, catalyst was from one single preparation.

The resulting bio-Pd catalysts, noted as 5 wt%Pd/*E. coli*(A) and 5 wt%Pd/*E. coli*(B) were tested in the hydrogenation of 2-pentyne ($T = 40\text{ }^{\circ}\text{C}$, $p_{H_2} = 2\text{ bar}$, $N = 1000\text{ rpm}$) and compared with the 5 wt% bio-Pd using specially-grown *E. coli* cells. Figure 8.5 compares the 2-pentyne conversion as a function of reaction time over these 3 bio-Pd catalysts. It is clearly observed that the two bio-Pd catalysts from fermenting *E. coli* cells (A and B) gave very similar 2-pentyne conversions but the rate of 2-pentyne conversion was ~ 6 -fold lower than the bio-Pd catalyst from specially-grown *E. coli* cells. The reason behind this may attribute to various hypotheses, e.g. that the matrix of *E. coli* cells may change after the fermentation process or the proportions of hydrogenases, or their precise localisations or indeed an unknown factor(s), which could bring an effect on the localisations and size of the Pd nanoparticles and ultimately their catalytic performance in 2-pentyne hydrogenation. The difference between palladium depositions on specially-grown and ‘second-life’ *E. coli* cells

can be examined using characterisation techniques such as electron microscopy and XRD; however this is not covered in this study due to time constraints.

In addition to the above factors, the cost of the hydrogen donor for reducing the metal ions (*e.g.* Pd(II) to Pd(0), Pt(IV) to Pt(0), and Au(III) to Au(0) onto the biomass) also needs to be included. There are several well-established technologies for producing or extracting hydrogen, such as steam reforming and electrolysis. Reducing the cost of these production technologies is the primary challenge for hydrogen production to make the resulting hydrogen cost competitive with conventional transportation fuels [8]. Instead of using an external hydrogen supply, a less expensive alternative could potentially use fermentative bacteria to produce H₂ *in situ* [47] during the manufacturing process of bio-Pd catalyst, thus the cost of H₂ can be omitted. Making use of biohydrogen and also the bacteria that produced it carries a ‘penalty’ of lower activity of the bio-Pd (above) but a greater range of target reactions should be examined.

8.3 Calculations

8.3.1 Agitator Reynolds Number and Power Consumption

The agitator Reynolds number (Re) was estimated using the following expression (Equation 8-31), with the corresponding parameters listed in Table 8.6.

$$\text{Re} = \frac{Nd_I^2 \rho_L}{\mu_L} \quad 8-31$$

Table 8.6 Parameters used for the calculation of the agitator Reynolds number (Re) in this study.

substrate	Hydrogenation in Baskerville		Oxidation in Parr
	2-pentyne (in isopropanol)	soybean oil	benzyl alcohol
stirrer diameter (d_I , cm)	5.84	5.84	2.06
stirring speed (N , s ⁻¹)	16.67	8.33~20	20
density (ρ_L , g.cm ⁻³)	0.786	0.865	1.044
viscosity (μ_L , g.cm ⁻¹ .s ⁻¹)	0.018	0.067	0.055

A gas-free liquid was considered for hydrogenation reactions in Baskerville autoclave under dead-end operation, power consumption for agitation per unit mass (P) was estimated using the expression below [206]:

$$P = \frac{N_P N^3 d_I^5 \rho_L}{m} \quad 8-32$$

For the oxidation reactions under a constant air flow in Parr autoclave, a correction factor (ψ) [206] for power consumption was applied in the presence of gas bubbles, thus power consumption per unit mass was estimated as:

$$P = \psi \frac{N_P N^3 d_I^5 \rho_L}{m} \quad 8-33$$

8.3.2 Air Flow Rate Calculation in Parr Autoclave

In order to precisely monitor the introducing air flow rate in the alcohol oxidation, a metering valve from HOKE Incorporated (Series no. 1335G4Y, Figure 8.6 a) was installed as part of the air flow controlling set up in the modified Parr autoclave. The fine metering control is achieved by the 18-turn displacement of stem (1°), of which the flow coefficient C_v is obtained from the reference flow curve determined by the manufacture (Figure 8.6 b). Meanwhile the micrometering vernier handle provides visual control and repeatable stem settings; in addition the 316 stainless steel material allows the operating temperature range from -54°C to 232°C and maximum operating pressure of 345 bar at 21°C .

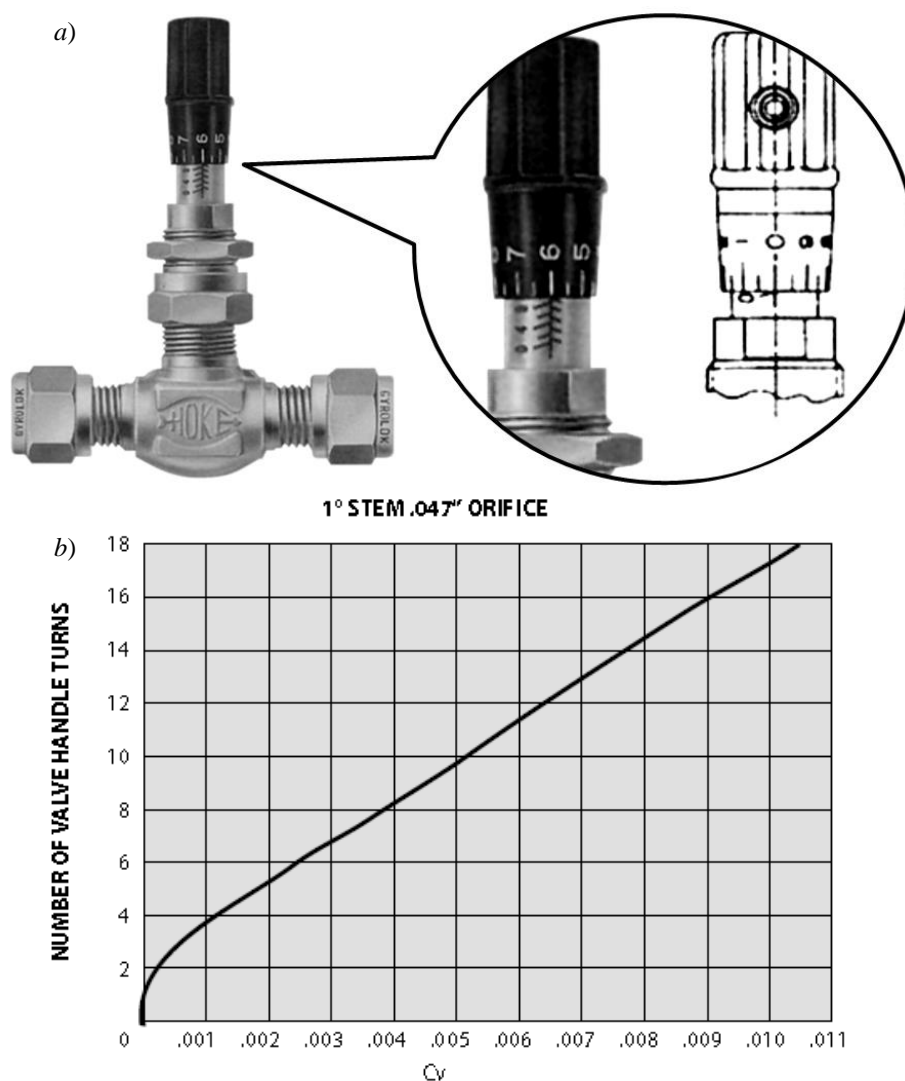


Figure 8.6 a) Image of the Hoke metering valve (Series no. 1335G4Y) for adjusting air flow rate in this study. b) Reference flow curve of C_v vs. handle turns for Hoke metering valve (Series no. 1335G4Y).

The flow chart of the flow rate controlling set up in the modified Parr autoclave is demonstrated in Figure 8.7. Symbols used in the flow chart are: q = flow rate, C_v = flow coefficient, p_1 = inlet pressure, psia, p_2 = outlet pressure, psia.

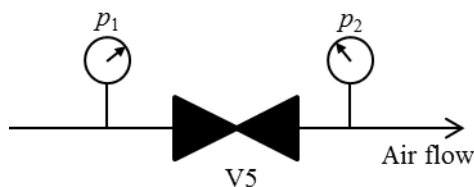


Figure 8.7 Flow chart of the air flow rate controlling set up in the modified Parr autoclave system.

To determine the flow of a gas @ 70 °F (21 °C), the following formula obtained from the manufacturer's brochure was applied:

$$SCFH = 1360C_v \sqrt{\frac{(\Delta p)(p_1)}{(460 + T)(S.G.)}} \quad 8-34$$

where: Δp = pressure drop ($p_1 - p_2$), SCFH= flow in standard cubic feet per hour, T = temperature in °F, and S.G.= specific gravity of gas where air= 1.0 @ 70 °F (21 °C) and 14.7 psia.

Under successful control of this metering valve, the air flow rates examined in the alcohol oxidation reaction were 100 ml.min⁻¹, 200 ml.min⁻¹, and 350 ml.min⁻¹ at room temperature of 70 °F (21 °C) and reaction pressure of 5 bar. The corresponding parameters were fully listed in Table 8.7.

Table 8.7 Air flow rates examined in this study and the corresponding parameters appeared for the calculation using Equation 8-34.

Air flow rate, ml.min ⁻¹	Turns *	Flow coefficient, C_v	Temperature, °F	Pressure drop Δp , psia
100	6.22	0.0026	70	$p_1 = 88.94$
200	10.84	0.0056		$p_2 = 88.20$
350	16.17	0.0091		

* Turns were read accurately from the from the micrometer vernier handle.

8.4 Conferences and Additional Publications

Conference Posters

- Poster: Application of Novel Bio-Pd Catalyst in Hydrogenation Reactions.

Conference: ISCRE 22: 22nd International Symposium on Chemical Reaction Engineering.

Maastricht, The Netherlands, September 2012.

- Poster: Hydrogenation of Soybean Oil Using Bio-Pd Catalyst. ^a

Conference: Hybrid Materials 2011: 2nd International Conference on Multifunctional, Hybrid & Nanomaterials.

Strasbourg, France, March 2011.

^a This poster was also presented in ‘The 17th Joint Annual Conference of CSCST & SCI-CS, Oxford University, UK, 2010’. (Awarded with the third prize)

Conference Presentation

- Talk: Selective Oxidation of Benzyl Alcohol Using Novel Au/Pd Bioinorganic Catalyst.

Conference: The 18th Joint Annual Conference of CSCST-SCI.

University of Cambridge, United Kingdom, September 2011.

Additional Publications

- A.J. Murry, S.M. Taylor, **J. Zhu**, J. Wood, and L.E. Macaskie, A Novel biorefinery: Biorecovery of precious metals from spent automotive catalyst leachates into new catalysts effective in metal reduction and in the hydrogenation of 2-pentyne, Minerals Engineering (manuscript accepted for publication).

- K. Deplanche, M.L. Merroun, M. Casadesus, D.T. Tran, I.P. Mikheenko, J.A. Bennett, **J. Zhu**, I.P. Jones, G.A. Attard, J. Wood, S. Selenska-Pobell, and L.E. Macaskie, Microbial synthesis of core/shell gold/palladium nanoparticles for applications in green chemistry, *Journal of the Royal Society Interface*, 9 (2012) 1705-1712.